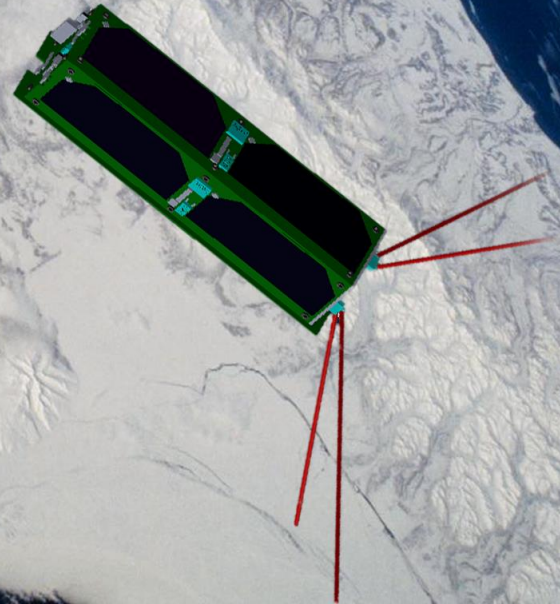
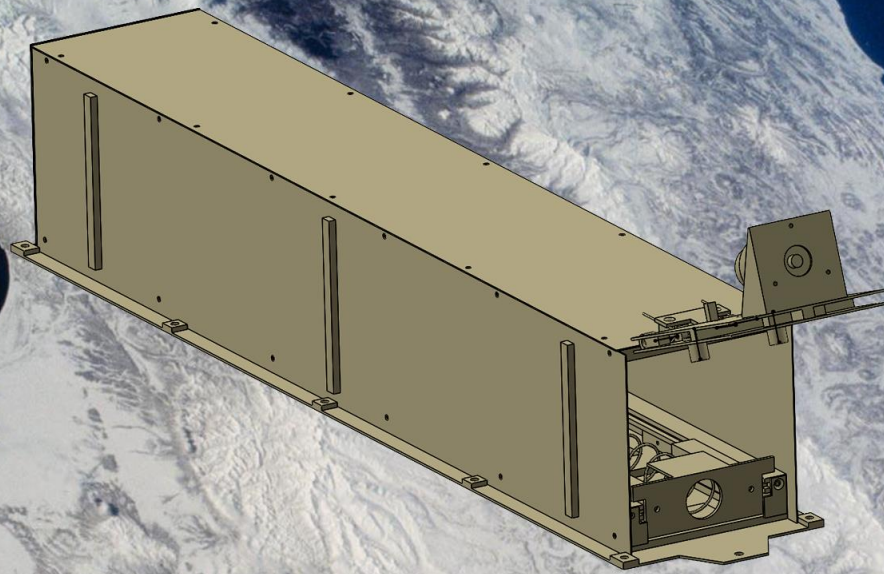


# POCKETQUBE DEPLOYMENT SYSTEM



ASHVIJ NARAYANAN

 TU Delft

# PocketQube Deployment System

By

Ashvij Narayanan

in partial fulfilment of the requirements for the degree of

**Master of Science**  
in Aerospace Engineering

at the Delft University of Technology,  
to be defended publicly on Wednesday June 8, 2022 at 1:30 PM.

Supervisor:	M.S. Uludag	
Thesis committee:	Dr. J. Guo	TU Delft
	I. Uriol Balbín	TU Delft

An electronic version of this thesis is available at <http://repository.tudelft.nl/>.

Cover Page Credits: NASA

# Preface

Spacecraft technology in the past six decades has demonstrated applications in remote sensing, telecommunication, and resource management to name a few. The past 20 years have seen the growth of CubeSats particularly for constellation based applications. However, the barrier to entry for players in the space industry is enormous due to the capital required to get to orbit.

Taking advantage of the rapid progress in the commercial electronics industry, the Space Engineering research group at TU Delft has set a vision to miniaturize spacecraft systems and sub-systems. It has led to the conception of a new spacecraft standard for the Picosatellite class called the PocketQube.

This study aims to enable greater access to space by reduction of PocketQube mission cost, the chief contributor to which is the total launch mass. Through the research conducted, cost reduction was achieved by minimization of deployment system mass.

*Ashvij Narayanan  
Delft, May 2022*

# Acknowledgements

During the course of this thesis, I have not only gained exposure to the rigorous standards required to conduct research but also to some wonderful individuals that have immensely helped me in my personal growth.

Firstly, I would like to thank M. Sevket Uludag, Stefano Speretta, and Silvana Radu for their continued guidance during the course of this research. I would also like to thank Juan Garcia and Ralph Sloopweg from ISISPACE for their review on the preliminary PocketQube Deployment System design. For their inputs on launch vehicle load characteristics, I am grateful to Ashish James from ISRO and Erdinc Yakut from GUMUSH Aerospace & Defense.

I express my sincere thanks to Dr. Chantal Cappelletti from GAUSS Srl for her inputs on PocketQube standards and to Dr. Alexander van Zuijlen from Aerodynamics research group for providing access to high performance computing. Lastly, I would like to thank members of the Ansys Community Forum and all vendors contacted for the design of deployment system.

*Ashvij Narayanan  
Delft, May 2022*

# Abstract

To enable greater access to space, this study aims to develop a cost-effective PocketQube Deployment System capable of deploying multiple PocketQubes from various launch vehicles. Mission cost, of which launch cost is a significant driver, can be reduced by minimizing deployment system mass. This can be achieved by structural analyses of single and multi pod configurations using finite element method. A metric called '*deployer ratio*', defined as the ratio of payload and deployer mass, is introduced to compare the effectiveness of CubeSat and PocketQube deployers. From the perspective of deployer mass and mission cost, it was observed that it is more efficient to launch PocketQubes from a multi pod deployer rather than a single pod deployer. Although the estimated launch cost for PocketQubes is currently equivalent to commercial manufacturers, further cost reduction is possible by optimizing the mass of such a multi pod deployer.

# Table of Contents

<b>TABLE OF CONTENTS</b>	<b>I</b>
<b>LIST OF FIGURES</b>	<b>V</b>
<b>LIST OF TABLES</b>	<b>VIII</b>
<b>ACRONYMS</b>	<b>X</b>
<b>SYMBOLS</b>	<b>XII</b>
<b>1 INTRODUCTION</b>	<b>1</b>
1.1 RESEARCH OBJECTIVE .....	2
1.2 RESEARCH QUESTIONS .....	2
1.3 RESEARCH METHODOLOGY .....	2
<b>2 LITERATURE STUDY</b>	<b>4</b>
2.1 HERITAGE OVERVIEW .....	4
2.1.1 POCKETQUBES .....	4
2.1.2 CUBESAT DEPLOYERS .....	5
2.1.3 CUBESAT DEPLOYMENT VELOCITY .....	6
2.1.4 MULTI POD CUBESAT DEPLOYER FOOTPRINT .....	7
2.1.5 POCKETQUBE DEPLOYERS .....	7
2.1.6 RELEASE MECHANISM.....	8
2.2 POCKETQUBE STANDARD .....	9
2.3 AXIS DEFINITION.....	9
2.3.1 POCKETQUBE .....	10
2.3.2 POCKETQUBE DEPLOYMENT SYSTEM .....	10
2.3.3 LAUNCH VEHICLE.....	10
2.4 POCKETQUBE DEPLOYMENT SYSTEM REQUIREMENTS .....	10
2.4.1 POCKETQUBE STANDARD REQUIREMENTS .....	11
2.4.2 LAUNCH VEHICLE REQUIREMENTS .....	11
2.4.3 GENERAL REQUIREMENTS .....	12
2.5 SYSTEM COST BREAKDOWN .....	13
2.6 LAUNCH COST COMPARISON.....	14
2.7 CUBESAT DEPLOYER MASS COMPARISON.....	16
2.8 MATERIAL SELECTION .....	17
2.9 RELEASE MECHANISM SELECTION.....	19
2.10 POD CONFIGURATION STUDY.....	21
<b>3 LAUNCH ENVIRONMENT</b>	<b>24</b>
3.1 TERMINOLOGY .....	24
3.2 LAUNCH VEHICLE LOADS.....	25
3.2.1 QUASI-STATIC ACCELERATION .....	26
3.2.2 SINUSOIDAL VIBRATIONS .....	26
3.2.3 RANDOM VIBRATION .....	27
3.2.4 ACOUSTIC VIBRATION.....	29
3.2.5 SHOCK.....	29
3.3 NATURAL FREQUENCY REQUIREMENT.....	29
3.4 DESIGN LOADS .....	30
<b>4 SYSTEM DESIGN</b>	<b>31</b>

<b>4.1</b>	<b>PIN PULLER SELECTION .....</b>	<b>31</b>
<b>4.2</b>	<b>ALUMINIUM ALLOY SELECTION .....</b>	<b>32</b>
<b>4.3</b>	<b>SPRINGS .....</b>	<b>33</b>
4.3.1	POCKETQUBE DEPLOYMENT ENERGY .....	33
4.3.2	MAIN SPRING SPECIFICATION .....	34
4.3.3	POCKETQUBE DEPLOYMENT VELOCITY MODEL VALIDATION .....	35
4.3.4	MAIN SPRING ANALYSIS .....	36
4.3.5	PRACTICAL CONSIDERATION .....	39
4.3.6	FRICITION EFFECT ON DEPLOYMENT VELOCITY .....	40
4.3.7	TORSION SPRING .....	42
4.3.8	SEPARATION SPRING.....	44
<b>4.4</b>	<b>DOOR ASSEMBLY.....</b>	<b>46</b>
4.4.1	DOOR RETAINER MECHANISM .....	47
4.4.2	PUSH BACK MECHANISM.....	48
<b>4.5</b>	<b>PUSHER PLATE ASSEMBLY.....</b>	<b>49</b>
4.5.1	PUSHER PLATE.....	50
4.5.2	PUSHER PLATE GUIDE .....	50
4.5.3	PUSHER PLATE STOPPER.....	51
4.5.4	PUSHER PLATE LOAD ANALYSIS .....	52
<b>4.6</b>	<b>GUIDE MECHANISM.....</b>	<b>53</b>
4.6.1	DIMENSIONING CONSIDERATION.....	53
<b>4.7</b>	<b>POD DIMENSIONS .....</b>	<b>55</b>
<b>4.8</b>	<b>POCKETQUBE SEPARATION DISTANCE .....</b>	<b>56</b>
<b>4.9</b>	<b>SINGLE POD SYSTEM CONFIGURATION.....</b>	<b>58</b>
<b>4.10</b>	<b>MULTIPLE POD SYSTEM .....</b>	<b>59</b>
4.10.1	FOOTPRINT ANALYSIS .....	59
4.10.2	CONFIGURATION STUDY .....	59
<b>5</b>	<b>STRUCTURAL ANALYSIS .....</b>	<b>61</b>
<b>5.1</b>	<b>VIBRATION THEORY &amp; STRUCTURAL ANALYSIS OVERVIEW .....</b>	<b>61</b>
5.1.1	STATIC ANALYSIS .....	61
5.1.2	MODAL ANALYSIS .....	61
5.1.3	HARMONIC ANALYSIS .....	62
5.1.4	RANDOM VIBRATION ANALYSIS .....	63
<b>5.2</b>	<b>STRUCTURAL ANALYSIS METHODOLOGY.....</b>	<b>64</b>
5.2.1	MODEL PREPARATION METHODS.....	64
5.2.2	FINITE ELEMENT MODEL DEFINITION.....	65
5.2.3	FEM ANALYSIS SOLUTION SCHEMATIC.....	67
5.2.4	METHOD SELECTION.....	68
<b>5.3</b>	<b>FEM VALIDATION.....</b>	<b>69</b>
5.3.1	SOLVER VALIDATION .....	69
5.3.2	METHOD VALIDATION.....	70
<b>5.4</b>	<b>MESH SENSITIVITY STUDY .....</b>	<b>71</b>
<b>5.5</b>	<b>DESIGN ACCEPTANCE CRITERIA .....</b>	<b>72</b>
<b>5.6</b>	<b>LONGITUDINAL DESIGN PROGRESSION .....</b>	<b>73</b>
5.6.1	VERSION 1 .....	74
5.6.2	VERSION 2 .....	75
<b>5.7</b>	<b>LATERAL DESIGN PROGRESSION.....</b>	<b>76</b>
5.7.1	VERSION 1 .....	76
5.7.2	VERSION 2 .....	77
5.7.3	VERSION 3 .....	77
<b>5.8</b>	<b>SENSITIVITY TO PQ MASS DISTRIBUTION.....</b>	<b>79</b>
<b>5.9</b>	<b>PQ CENTRE OF MASS SENSITIVITY STUDY .....</b>	<b>80</b>

<b>5.10</b>	<b>PARAMETRIC STUDY .....</b>	<b>81</b>
5.10.1	RESULT SUMMARY .....	83
<b>5.11</b>	<b>SINGLE POD RESULT SUMMARY.....</b>	<b>85</b>
<b>5.12</b>	<b>MULTI POD DESIGN PROGRESSION .....</b>	<b>86</b>
5.12.1	VERSION 1 .....	87
5.12.2	VERSION 2 .....	88
5.12.3	VERSION 3 .....	89
5.12.4	VERSION 4 .....	90
5.12.5	VERSION 5 .....	91
<b>5.13</b>	<b>MULTI POD RESULT SUMMARY .....</b>	<b>92</b>
<b>6</b>	<b><u>FINAL DESIGN</u></b>	<b>95</b>
<b>6.1</b>	<b>POCKETQUBE ORDER IN POD .....</b>	<b>95</b>
<b>6.2</b>	<b>SINGLE POD .....</b>	<b>97</b>
<b>6.3</b>	<b>MULTIPLE POD.....</b>	<b>98</b>
6.3.1	STRUCTURAL CHANGES FROM SINGLE POD .....	98
6.3.2	DEPLOYER FOOTPRINT .....	98
6.3.3	DEPLOYMENT SEPARATION.....	99
6.3.4	DEPLOYMENT SEQUENCE.....	101
6.3.5	POWER REQUIREMENT .....	101
<b>6.4</b>	<b>SAFETY FEATURES .....</b>	<b>102</b>
<b>6.5</b>	<b>ADDITIONAL FEATURES .....</b>	<b>102</b>
<b>6.6</b>	<b>MASS BUDGET.....</b>	<b>103</b>
<b>6.7</b>	<b>DEPLOYER MASS COMPARISON .....</b>	<b>103</b>
<b>6.8</b>	<b>COST BUDGET.....</b>	<b>104</b>
<b>6.9</b>	<b>DEPLOYER CHOICE .....</b>	<b>106</b>
<b>6.10</b>	<b>DEPLOYER COST COMPARISON.....</b>	<b>107</b>
<b>7</b>	<b><u>PROTOTYPING AND TESTING</u></b>	<b>109</b>
<b>7.1</b>	<b>STRUCTURE PROTOTYPING .....</b>	<b>109</b>
<b>7.2</b>	<b>MAIN SPRING CHARACTERIZATION TEST .....</b>	<b>110</b>
7.2.1	TEST METHOD AND SETUP .....	110
7.2.2	CHARACTERIZATION TEST RESULT.....	111
<b>7.3</b>	<b>DOOR DEPLOYMENT TEST.....</b>	<b>112</b>
7.3.1	TEST METHOD AND SETUP .....	112
7.3.2	RESULT .....	114
<b>8</b>	<b><u>SYSTEM INTEGRATION AND ENVIRONMENTAL TEST PLAN</u></b>	<b>117</b>
<b>8.1</b>	<b>SYSTEM INTEGRATION .....</b>	<b>117</b>
8.1.1	PROTOTYPING LESSONS.....	117
<b>8.2</b>	<b>FASTENERS .....</b>	<b>118</b>
<b>8.3</b>	<b>INTEGRATION COST METHODOLOGY.....</b>	<b>120</b>
<b>8.4</b>	<b>ENVIRONMENTAL TEST PLAN.....</b>	<b>120</b>
<b>9</b>	<b><u>CONCLUSION AND RECOMMENDATIONS</u></b>	<b>122</b>
<b>9.1</b>	<b>THESIS SUMMARY .....</b>	<b>122</b>
<b>9.2</b>	<b>CONCLUSION .....</b>	<b>123</b>
<b>9.3</b>	<b>RECOMMENDATIONS.....</b>	<b>124</b>
<b>10</b>	<b><u>REFERENCES</u></b>	<b>126</b>
<b>11</b>	<b><u>APPENDIX</u></b>	<b>134</b>
<b>11.1</b>	<b>APPENDIX A (STRUCTURAL ANALYSIS RESULTS) .....</b>	<b>142</b>
11.1.1	SINGLE POD LONGITUDINAL VERSION 1 .....	142



11.1.2	SINGLE POD LONGITUDINAL VERSION 2 .....	143
11.1.3	SINGLE POD LATERAL VERSION 1 .....	144
11.1.4	SINGLE POD LATERAL VERSION 2 .....	145
11.1.5	SINGLE POD LATERAL VERSION 3 .....	146
11.1.6	MULTI POD FINAL VERSION .....	151
<b>11.2</b>	<b>APPENDIX B (ESTIMATOR SCRIPTS) .....</b>	<b>155</b>
11.2.1	DEPLOYMENT VELOCITY ESTIMATOR SCRIPT .....	155
11.2.2	DOOR DEPLOYMENT TIME ESTIMATOR SCRIPT .....	156
<b>11.3</b>	<b>APPENDIX C (SYSTEM INTEGRATION PROCEDURE).....</b>	<b>157</b>
11.3.1	DOOR ASSEMBLY .....	157
11.3.2	SINGLE POD .....	157
11.3.3	MULTI POD .....	158

# List of Figures

FIGURE 1: WORK BREAKDOWN STRUCTURE.....	3
FIGURE 2: P-POD DEPLOYER [12].....	5
FIGURE 3: ISIPOD 3U DEPLOYER [14].....	5
FIGURE 4: NRCSD 3U DEPLOYER [15].....	6
FIGURE 5: CSD 3U DEPLOYER [16]. ....	6
FIGURE 6: CUBESAT LAUNCHERS [3]. ....	6
FIGURE 7: MULTI POD CUBESAT DEPLOYER FOOTPRINT COMPARISON [19], [16], [14]. ....	7
FIGURE 8: ALBAPOD [21]. ....	8
FIGURE 9: FOSSA PQ DEPLOYER [23]. ....	8
FIGURE 10: POCKETQUBE AXIS DEFINITION [2]. ....	10
FIGURE 11: POCKETQUBE DEPLOYMENT SYSTEM AXIS DEFINITION. ....	10
FIGURE 12: LAUNCH VEHICLE AXIS DEFINITION. ....	10
FIGURE 13: PDS COST BREAKDOWN.....	13
FIGURE 14: SPECIFIC LAUNCH COST FOR DIFFERENT LAUNCH VEHICLES [34], [35], [36].....	15
FIGURE 15: LAUNCH FREQUENCY OF RELEVANT LAUNCH VEHICLES [35], [37].....	15
FIGURE 16: MASS COMPARISON BETWEEN CUBESAT DEPLOYERS [13], [14], [16], [38]. ....	16
FIGURE 17: ASHBY CHART FOR COMMONLY USED MATERIALS [39]. ....	17
FIGURE 18: MATERIAL STRENGTH AND STIFFNESS COMPARED WITH DENSITY [40], [41], [42], [43], [44].....	18
FIGURE 19: POSSIBLE COMBINATIONS OF POCKETQUBES IN DEPLOYER. ....	23
FIGURE 20: ACCELERATION PROFILE OF APOLLO 17 (LEFT) AND STS 121 MISSION [52]. ....	26
FIGURE 21: LAUNCH VEHICLE SINUSOIDAL VIBRATION [53], [54], [55], [56], [65]. ....	27
FIGURE 22: RANDOM VIBRATIONS OF DIFFERENT LAUNCH VEHICLES [17], [51], [53], [54], [57], [55], [56]. ....	28
FIGURE 23: SHOCK RESPONSE SPECTRUM [53], [54], [57], [55], [56].....	29
FIGURE 24: ALUMINIUM ALLOY YIELD STRENGTH [42]. ....	32
FIGURE 25: FLAT-WIRE WAVE SPRING [82]. ....	34
FIGURE 26: SPIRAL SPRING [83]. ....	34
FIGURE 27: MAIN SPRING ENERGY VARIATION ALONG ITS STROKE. ....	35
FIGURE 28: EQUIVALENT FORCE INVARIANCE TO POCKETQUBE MASS. ....	36
FIGURE 29: OPERATION WINDOW OF MAIN SPRING [85]. ....	37
FIGURE 30: VELOCITY AND ACCELERATION IMPARTED ON SPACECRAFT ALONG STROKE. ....	37
FIGURE 31: DEPLOYMENT VELOCITY AND TIME VARIATION WITH SPACECRAFT MASS. ....	38
FIGURE 32: DEPLOYMENT VELOCITY UNCERTAINTY DUE TO SPRING TOLERANCE. ....	38
FIGURE 33: DEPLOYMENT VELOCITY ACCOUNTING DEPLOYED SPACECRAFT.....	39
FIGURE 34: DEPLOYMENT VELOCITY VARIATION FOR PQS REMOVED FROM POD.....	40
FIGURE 35: DEPLOYMENT VELOCITY AND SYSTEM ENERGY VARIATION ACCOUNTING FRICTION. ....	41
FIGURE 36: EFFECT OF FRICTION ON DEPLOYMENT VELOCITY. ....	42
FIGURE 37: TORSION SPRING ENERGY VARIATION ALONG ITS ROTATION. ....	43
FIGURE 38: DOOR ANGULAR VELOCITY AND TIME VARIATION WITH ROTATION.....	44
FIGURE 39: DOOR DEPLOYMENT TIME VARIATION WITH ITS MASS. ....	44
FIGURE 40: SEPARATION VELOCITY COMPARISON BETWEEN CUBESAT AND POCKETQUBE.....	45
FIGURE 41: DOOR ASSEMBLY WITH EXPLODED VIEW.....	46
FIGURE 42: DOOR ASSEMBLY IN STOWED AND DEPLOYED CONDITIONS. ....	46
FIGURE 43: DOOR TOP.....	46
FIGURE 44: DOOR BOTTOM.....	47
FIGURE 45: DOOR BRACKET.....	47
FIGURE 46: HINGE 1 AND 2.....	47
FIGURE 47: DOOR RETAINER PLATE.....	48
FIGURE 48: DOOR RETAINER PIN.....	48
FIGURE 49: PUSHER PLATE ASSEMBLY WITH EXPLODED VIEW.....	49
FIGURE 50: PUSHER PLATE. ....	50
FIGURE 51: PUSHER PLATE GUIDE WITH DIMENSIONAL TOLERANCE.....	51

FIGURE 52: PUSHER PLATE STOPPING MECHANISM. ....	52
FIGURE 53: PUSHER PLATE LOAD ANALYSIS. ....	52
FIGURE 54: GUIDE MECHANISM DEFORMATION AT -40 °C. ....	53
FIGURE 55: GUIDE MECHANISM DEFORMATION AT +80 °C. ....	54
FIGURE 56: POCKETQUBE ALLOWABLE APPENDAGE IN X & Y DIRECTIONS WITH POD INTERNAL DIMENSIONS. ....	55
FIGURE 57: SEPARATION DISTANCE FOR DIFFERENT DEPLOYMENT DIRECTIONS (WITH ILLUSTRATION). ....	57
FIGURE 58: SEPARATION DISTANCE VARIATION WITH MAGNITUDE OF DEPLOYMENT VELOCITY. ....	58
FIGURE 59: SINGLE POD CONFIGURATION (ILLUSTRATION FOR REFERENCE). ....	58
FIGURE 60: MULTI POD PDS PRELIMINARY FOOTPRINT ANALYSIS. ....	59
FIGURE 61: CONFIGURATION STUDY FOR MULTIPLE POD STRUCTURAL ELEMENTS (SKELETON VIEW). ....	60
FIGURE 62: MID-PLANE METHOD BLOCK DIAGRAM. ....	65
FIGURE 63: 3D MESH METHOD BLOCK DIAGRAM. ....	65
FIGURE 64: MESH ELEMENT TYPES [109]. ....	66
FIGURE 65: STRUCTURAL ANALYSIS SOLUTION SCHEMATIC. ....	67
FIGURE 66: GEOMETRIES USED FOR 2D AND 3D METHODS. ....	68
FIGURE 67: VALIDATION OF FINITE ELEMENT MODEL [94]. ....	70
FIGURE 68: MESH SENSITIVITY STUDY. ....	71
FIGURE 69: INITIAL STRUCTURAL DESIGN WITH L BRACKETS. ....	73
FIGURE 70: INITIAL STRUCTURAL DESIGN WITH INTEGRATED VERTICAL BRACKETS. ....	73
FIGURE 71: GUIDE MECHANISM HAVING COMBINED VERTICAL RIBS. ....	74
FIGURE 72: STRUCTURAL ELEMENT DESIGN LONGITUDINAL VERSION 1. ....	74
FIGURE 73: STRUCTURAL ELEMENT DESIGN LONGITUDINAL VERSION 2. ....	75
FIGURE 74: STRUCTURAL ELEMENT DESIGN LATERAL VERSION 1. ....	76
FIGURE 75: STRUCTURE DESIGN LATERAL VERSION 3. ....	78
FIGURE 76: PQ MASS DISTRIBUTION SENSITIVITY STUDY. ....	79
FIGURE 77: PQ CENTRE OF MASS SENSITIVITY STUDY. ....	81
FIGURE 78: PARAMETRIC STUDY -Y PANEL THICKNESS. ....	82
FIGURE 79: PARAMETRIC STUDY -Y PANEL THICKNESS. ....	82
FIGURE 80: PARAMETRIC STUDY -Z PANEL THICKNESS. ....	83
FIGURE 81: PARAMETRIC STUDY +Y PANEL THICKNESS. ....	83
FIGURE 82: PARAMETRIC STUDY +X PANEL THICKNESS. ....	83
FIGURE 85: PARAMETRIC STUDY GUIDE MECHANISM THICKNESS (PARAMETER 1 & 2). ....	83
FIGURE 83: PARAMETRIC STUDY RIB HORIZONTAL THICKNESS. ....	83
FIGURE 84: PARAMETRIC STUDY -X PANEL THICKNESS. ....	83
FIGURE 86: PARAMETRIC STUDY RIB THICKNESS. ....	83
FIGURE 87: PARAMETRIC STUDY CORRELATION MATRIX. ....	84
FIGURE 88: PARAMETRIC STUDY CORRELATION MATRIX LEGEND. ....	84
FIGURE 89: SINGLE POD RESULT SUMMARY. ....	85
FIGURE 90: RANDOM INPUT PSD LEVELS FOR MULTI POD PDS. ....	86
FIGURE 91: STRUCTURAL ELEMENT DESIGN MULTI POD VERSION 1. ....	87
FIGURE 92: MODAL ANALYSIS RESULTS LONGITUDINAL MULTI POD VERSION 1. ....	88
FIGURE 93: STRUCTURAL ELEMENT DESIGN MULTI POD VERSION 2. ....	88
FIGURE 94: MODAL ANALYSIS RESULTS MULTI POD VERSION 2. ....	89
FIGURE 95: STRUCTURAL ELEMENT DESIGN MULTI POD VERSION 3. ....	89
FIGURE 96: MODAL ANALYSIS RESULTS MULTI POD VERSION 3. ....	90
FIGURE 97: STRUCTURAL ELEMENT DESIGN MULTI POD VERSION 4. ....	90
FIGURE 98: MODAL ANALYSIS RESULTS MULTI POD VERSION 4. ....	91
FIGURE 99: STRUCTURAL ELEMENT DESIGN MULTI POD VERSION 5. ....	91
FIGURE 100: MODAL ANALYSIS RESULTS MULTI POD VERSION 5. ....	92
FIGURE 101: MULTI POD RESULT SUMMARY. ....	93
FIGURE 102: POSSIBLE PERMUTATIONS OF POCKETQUBES IN DEPLOYER (SPECIFIC CASE). ....	96
FIGURE 103: RELATIVE VELOCITIES OF LAUNCH VEHICLE AND DEPLOYED POCKETQUBES (REFER FIGURE 102). ....	96
FIGURE 104: HARNESS ROUTING SINGLE POD. ....	98
FIGURE 105: MULTI POD DEPLOYER FINAL FOOTPRINT COMPARISON. ....	99
FIGURE 106: POCKETQUBE SEPARATION DISTANCE VARIATION. ....	99
FIGURE 107: DEPLOYMENT VELOCITY ANGULAR SEPARATION ESTIMATE. ....	100
FIGURE 108: MULTI POD DEPLOYMENT SEQUENCE. ....	101

FIGURE 109: ADDITIONAL APPENDAGE VOLUME IN -Z DIRECTION. ....	103
FIGURE 110: MASS COMPARISON BETWEEN POCKETQUBE AND CUBESAT DEPLOYERS [13], [14], [16], [38]...	104
FIGURE 111: POCKETQUBE DEPLOYMENT SYSTEM COST DIVISION. ....	105
FIGURE 112: COST BREAK EVEN BETWEEN SYSTEMS. ....	106
FIGURE 113: BREAK EVEN COST FOR DIFFERENT LAUNCH VEHICLES. ....	106
FIGURE 114: LAUNCH COST COMPARISON PER KILOGRAM [118], [119], [120]. ....	107
FIGURE 115: LAUNCH COST PER SPACECRAFT COMPARISON PER [118], [119], [120]. ....	108
FIGURE 116: PDS STRUCTURE 3D PRINTING. ....	109
FIGURE 117: MAIN SPRING CHARACTERIZATION TEST SETUP. ....	111
FIGURE 118: SPRING CHARACTERIZATION TEST RESULTS OVERLAID ON OPERATION WINDOW. ....	112
FIGURE 119: BLOCK DIAGRAM SHOWING SEQUENCE OF DOOR DEPLOYMENT TEST. ....	113
FIGURE 120: IMAGES OF THE SETUP USED FOR DOOR DEPLOYMENT TEST. ....	113
FIGURE 121: START AND END FRAMES OF DOOR DEPLOYMENT TEST. ....	114
FIGURE 122: DIAGRAM INDICATING COMPONENTS OF GRAVITY INFLUENCING DOOR DEPLOYMENT TEST. ...	115
FIGURE 123: INFLUENCE OF GRAVITY ON TIME FOR DOOR DEPLOYMENT. ....	115
FIGURE 124: GRAVITY INFLUENCE ON DOOR DEPLOYMENT FORCE AND ANGULAR VELOCITY. ....	116
FIGURE 125: MAIN SPRING DRAWING SHOWING TOLERANCE [85]. ....	136
FIGURE 126: MODAL ANALYSIS RESULTS VERSION 1 – LONGITUDINAL CONFIGURATION. ....	142
FIGURE 127: MODAL ANALYSIS RESULTS VERSION 2 – LONGITUDINAL CONFIGURATION. ....	143
FIGURE 128: MODAL ANALYSIS RESULTS VERSION 1 – LATERAL CONFIGURATION. ....	144
FIGURE 129: MODAL ANALYSIS RESULTS VERSION 2 – LATERAL CONFIGURATION. ....	145
FIGURE 130: MODAL ANALYSIS RESULTS VERSION 3 – LATERAL CONFIGURATION. ....	146
FIGURE 131: DEFORMATION, INDUCED STRESS SINUSOIDAL X EXCITATION. ....	146
FIGURE 132: SINUSOIDAL FREQUENCY RESPONSE X EXCITATION. ....	147
FIGURE 133: DIRECTIONAL DEFORMATION, INDUCED STRESS RANDOM X EXCITATION. ....	147
FIGURE 134: RANDOM FREQUENCY RESPONSE X EXCITATION. ....	147
FIGURE 135: DEFORMATION, INDUCED STRESS QUASI-STATIC X EXCITATION. ....	148
FIGURE 136: DEFORMATION, INDUCED STRESS SINUSOIDAL Y EXCITATION. ....	148
FIGURE 137: SINUSOIDAL FREQUENCY RESPONSE Y EXCITATION. ....	148
FIGURE 138: DIRECTIONAL DEFORMATION, INDUCED STRESS RANDOM Y EXCITATION. ....	149
FIGURE 139: RANDOM FREQUENCY RESPONSE Y EXCITATION. ....	149
FIGURE 140: DEFORMATION, INDUCED STRESS QUASI-STATIC Y EXCITATION. ....	149
FIGURE 141: DEFORMATION, INDUCED STRESS SINUSOIDAL Z EXCITATION. ....	150
FIGURE 142: SINUSOIDAL FREQUENCY RESPONSE Z EXCITATION. ....	150
FIGURE 143: DIRECTIONAL DEFORMATION, INDUCED STRESS RANDOM Z EXCITATION. ....	150
FIGURE 144: RANDOM FREQUENCY RESPONSE Z EXCITATION. ....	151
FIGURE 145: DEFORMATION, INDUCED STRESS QUASI-STATIC Z EXCITATION. ....	151
FIGURE 146: DEFORMATION, INDUCED STRESS SINUSOIDAL X EXCITATION. ....	151
FIGURE 147: SINUSOIDAL FREQUENCY RESPONSE X EXCITATION. ....	151
FIGURE 148: DIRECTIONAL DEFORMATION, INDUCED STRESS RANDOM X EXCITATION. ....	152
FIGURE 149: DEFORMATION, INDUCED STRESS QUASI-STATIC X EXCITATION. ....	152
FIGURE 150: DEFORMATION, INDUCED STRESS SINUSOIDAL Y EXCITATION. ....	152
FIGURE 151: SINUSOIDAL FREQUENCY RESPONSE Y EXCITATION. ....	153
FIGURE 152: DIRECTIONAL DEFORMATION, INDUCED STRESS RANDOM Y EXCITATION. ....	153
FIGURE 153: DEFORMATION, INDUCED STRESS QUASI-STATIC Y EXCITATION. ....	153
FIGURE 154: DEFORMATION, INDUCED STRESS SINUSOIDAL Z EXCITATION. ....	154
FIGURE 155: SINUSOIDAL FREQUENCY RESPONSE Z EXCITATION. ....	154
FIGURE 156: DIRECTIONAL DEFORMATION, INDUCED STRESS RANDOM Z EXCITATION. ....	154
FIGURE 157: DEFORMATION, INDUCED STRESS QUASI-STATIC Z EXCITATION. ....	155

# List of Tables

TABLE 1: DETAILS OF FIRST POCKETQUBES LAUNCHED [9], [10].....	5
TABLE 2: DEPLOYMENT VELOCITY AND FORCE OF CUBESAT DEPLOYERS.....	7
TABLE 3: RELEASE MECHANISMS USED IN CANISTER DEPLOYERS.....	8
TABLE 4: POCKETQUBE DIMENSIONS AND MASS [2].....	9
TABLE 5: PDS SYSTEM LEVEL REQUIREMENTS.....	11
TABLE 6: POCKETQUBE STANDARD REQUIREMENTS.....	11
TABLE 7: LAUNCH VEHICLE REQUIREMENTS.....	11
TABLE 8: PDS GENERAL REQUIREMENTS.....	12
TABLE 9: MATERIAL SELECTION TRADE-OFF.....	18
TABLE 10: RELEASE MECHANISM TRADE-OFF.....	20
TABLE 11: POD CONFIGURATION TRADE-OFF.....	22
TABLE 12: ACCELERATION LOADS OF VARIOUS LAUNCH VEHICLES [53], [54], [55], [56], [57].....	26
TABLE 13: NATURAL FREQUENCY REQUIREMENT.....	30
TABLE 14: NASA RECOMMENDED FLIGHT HARDWARE DESIGN FACTORS OF SAFETY [51].....	30
TABLE 15: PIN PULLER DETAILS [71], [72], [73], [74].....	31
TABLE 16: DEPLOYMENT CHARACTERISTICS BASED ON SPRING TOLERANCE.....	38
TABLE 17: PRACTICAL CONSIDERATION FOR PDS.....	40
TABLE 18: THERMAL DEFORMATION AT GUIDE RAIL SURFACE.....	54
TABLE 19: GUIDE RAIL AND PQ BACKPLATE CLEARANCE.....	54
TABLE 20: MODAL RESULT SUMMARY – LONGITUDINAL VERSION 1.....	74
TABLE 21: MODAL RESULT SUMMARY – LONGITUDINAL VERSION 2.....	75
TABLE 22: MODAL RESULT SUMMARY – LATERAL VERSION 1.....	77
TABLE 23: MODAL RESULT SUMMARY – LATERAL VERSION 2.....	77
TABLE 24: MODAL RESULT SUMMARY – LATERAL VERSION 3.....	78
TABLE 25: STRUCTURAL ANALYSIS RESULT SUMMARY SINGLE POD LATERAL.....	78
TABLE 26: DESIGN MARGIN OF SAFETY – SINGLE POD.....	79
TABLE 27: CONFIGURATION RESULTS FOR MULTI POD VERSION 1.....	87
TABLE 28: STRUCTURAL ANALYSIS RESULT SUMMARY MULTI POD PDS.....	93
TABLE 29: DESIGN MARGIN OF SAFETY – MULTI POD.....	94
TABLE 30: POCKETQUBE DEPLOYMENT SYSTEM COST BREAKDOWN.....	104
TABLE 31: EXPERIMENTAL RESULTS OF DOOR DEPLOYMENT TEST.....	114
TABLE 32: EXPECTED RESULTS FOR DOOR ASSEMBLY MADE OF ALUMINIUM ALLOY.....	116
TABLE 33: NASA RECOMMENDED TEST FACTORS AND DURATIONS [51].....	120
TABLE 34: MATERIAL PHYSICAL PROPERTIES.....	134
TABLE 35: SINUSOIDAL ACCELERATION OF DIFFERENT LAUNCH VEHICLES.....	134
TABLE 36: RANDOM VIBRATION $G_{RMS}$ FOR LAUNCH VEHICLES.....	134
TABLE 37: DESIGN LOADS ACCOUNTING FOR NASA RECOMMENDED FOS.....	134
TABLE 38: COST CORRECTION TO 2021 US\$ ACCOUNTING INFLATION.....	135
TABLE 39: LAUNCH COST ESTIMATE FOR A KILOGRAM OF SPACE HARDWARE.....	135
TABLE 40: CHEMICAL COMPOSITION LIMITS FOR ALUMINIUM ALLOYS [42].....	135
TABLE 41: MECHANICAL PROPERTIES OF ALUMINIUM ALLOY [42].....	136
TABLE 42: SPECIFICATION OF MAIN SPRING [85].....	136
TABLE 43: DEPLOYMENT VELOCITY BASED ON LOCATION IN POD.....	136
TABLE 44: SPECIFICATION OF TORSION SPRINGS.....	137
TABLE 45: SPECIFICATION OF DOOR RETAINER SPRING.....	137
TABLE 46: SPECIFICATION OF PUSH BACK SPRING.....	137
TABLE 47: MINIMUM SEPARATION DISTANCE FOR DEPLOYMENT VELOCITY OF 1 M/S.....	137
TABLE 48: PROPERTIES OF CANTILEVER BEAM USED FOR SOLVER VALIDATION [94].....	137
TABLE 49: MODAL ANALYSIS COMPARISON FOR FEM METHODS.....	138
TABLE 50: STATIC AND DYNAMIC ANALYSIS COMPARISON FOR FEM METHODS.....	138
TABLE 51: COMPARISON OF SOLVER RESULTS BASED ON BEAM THEORY.....	138

TABLE 52: CHANGES IN BASELINE PARAMETER VALUES BASED ON STUDY. ....	139
TABLE 53: SENSITIVITY OF PQ MASS DISTRIBUTION.....	139
TABLE 54: POCKETQUBE DEPLOYMENT VELOCITY BASED ON POSITION IN POD (SPECIFIC CASE). ....	139
TABLE 55: MASS BUDGET (SINGLE POD).....	140
TABLE 56: MASS BUDGET (MULTI POD). ....	140
TABLE 57: COMBINATION OF WEIGHTS USED FOR SPRING CHARACTERIZATION.....	141
TABLE 58: RECOMMENDED TOLERANCE DURING TESTING [51]. ....	141

# Acronyms

AIT	Assembly Integration and Testing
ATV	Automated Transfer Vehicle
CAD	Computer Aided Design
CDS	CubeSat Design Specification
CFRP	Carbon Fibre Reinforced Polymers
CNC	Computer Numeric Control
CoM	Centre of Mass
CSD	Canisterized Satellite Dispenser
dB	Decibel
EMC	Electromagnetic Compatibility
ESA	European Space Agency
FEA	Finite Element Analysis
FEM	Finite Element Method
FOS	Factor of Safety
FPS	Frames per Second
GC	Geometric Centre
GTO	Geostationary Transfer Orbit
HTV	H-II Transfer Vehicle
ICD	Interface Control Document
ISIS	Innovative Solutions In Space B.V.
ISRO	Indian Space Research Organization
JAXA	Japan Aerospace Exploration Agency
JEM	Japanese Experiment Module
J-SSOD	JEM Small Satellite Orbital Deployer
LEO	Low Earth Orbit
LV	Launch Vehicle
MoO <sub>3</sub>	Molybdenum Trioxide
MoS	Margin of Safety
MoS <sub>2</sub>	Molybdenum Disulphide
MPC	Multi-Point Constraint
MRFOD	Morehead Rome Femto Orbital Deployer

NASA	National Aeronautics and Space Administration
NRCSD	NanoRacks CubeSat Deployer
PDS	PocketQube Deployment System
PLA	Polylactic Acid
P-POD	Poly-Picosatellite Orbital Deployer
PQ	PocketQube
PSD	Power Spectral Density
PSLV	Polar Satellite Launch Vehicle
RBF	Remove Before Flight
RMS	Root Mean Square
SMA	Shape Memory Alloy
SRS	Shock Response Spectrum
STS	Space Transportation System
TVAC	Thermo-Vacuum



# Symbols

Symbol	Description	Unit
$\{\dot{X}\}$	Velocity Vector	m/s
$\{\ddot{X}\}$	Acceleration Vector	m/s <sup>2</sup>
$[C]$	Damping Matrix	Ns/m
$[K]$	Stiffness Matrix	N/m
$[M]$	Mass Matrix	kg
$\{D\}$	Unit Displacement Vector in Coordinate System	-
$\{f(t)\}$	External Load Vector	N
$\{\phi\}_i$	Eigen Vector of i <sup>th</sup> mode	-
$\{X\}$	Displacement Vector	m
$a_d$	Linear acceleration at door's centre of mass	m/s <sup>2</sup>
$a_i$	Acceleration at i <sup>th</sup> iteration	m/s <sup>2</sup>
$a_{PQ}$	Acceleration on PocketQubes due to main spring	m/s <sup>2</sup>
$A_t$	Nominal stress area on Fastener	m <sup>2</sup>
$b$	Beam Width	m
$C_B$	Battery Capacity	J
$CoM_{PQ}$	Centre of Mass of PocketQube	m
$CoM_{Stack}$	Centre of Mass of PQ stack in pod	m
$d$	Fastener Nominal Diameter	m
$d_{CoM}$	Distance between door rotation axis and its CoM	m
$DOD$	Depth of Discharge	-
$d_p$	Fastener Pitch Diameter	m
$d_r$	Fastener Minor Diameter	m
$d_s$	Stopping Distance	m
$dx$	Discretization of main spring stroke length	m
$d\theta$	Discretization of door rotation angle	rad
$E$	Young's Modulus	Pa
$E_P$	Potential Energy of Spring	J
$F_a$	Axial Force on Fastener	N
$F_{eq}$	Equivalent Force of Main Spring	N
$F_g$	Force of gravity on door	N
$F_j$	Maximum preload applied to a fastener	N
$F_{MS}$	Force exerted by main spring	N
$f_n$	Natural Frequency	Hz
$F_p$	Proof load of Fastener material	N
$F_s$	Stopping Force	N

$F_{sh}$	Shear Force on Fastener	N
$F_{TS}$	Force exerted by torsion springs	N
$F_{\mu}$	Friction force	N
$g$	Acceleration due to gravity	m/s <sup>2</sup>
$G$	Shear Modulus	Pa
$h$	Beam Height	m
$h_o$	Orbital Height	m
$I$	Area moment of Inertia of Beam	m <sup>4</sup>
$I_d$	Moment of inertia of door	kgm <sup>2</sup>
$J_p$	Polar moment of Inertia	m <sup>4</sup>
$K$	Nut factor	-
$k$	Torsional Constant	m <sup>4</sup>
$k_{MS}$	Main Spring Constant	N/m
$k_{TS}$	Torsion Spring Constant	Nm/rad
$L$	Beam Length	m
$m$	Beam Mass	kg
$M_b$	Bending Moment on Fastener	Nm
$m_d$	Mass of door assembly	kg
$M_{eff,i}$	Effective Mass of i <sup>th</sup> mode	-
$m_{PDS}$	Total PDS mass including payload	kg
$m_{pp}$	Mass of Pusher Plate Assembly	kg
$m_{PQ}$	Mass of PocketQube	kg
$m_{Stack}$	Total mass of PQ in pod	kg
$N$	Normal force	N
$N_d$	Number of pod deployments	-
$p$	Pitch of metric thread	m
$P$	PocketQube Unit	-
$P_e$	Electrical Power Required	W
$P_{\mu}$	Ratio of normal and main spring force	-
$R_b$	Bending load ratio on Fastener	-
$R_E$	Radius of Earth	m
$R_s$	Shear load ratio on Fastener	-
$R_t$	Tensile load ratio on Fastener	-
$s$	Stroke length of main spring	m
$T_b$	Torque to be applied on Fastener	Nm
$t_{dep}$	Time required for PocketQube Deployment	s
$T_e$	Time for Release Mechanism Actuation	s
$t_P$	Orbital Period	s
$T_{TS}$	Torque produced by torsion springs	Nm
$U$	CubeSat Unit	-

$u_{MS}$	Initial velocity of main spring	m/s
$v_{dep}$	Deployment Velocity	m/s
$v_i$	Velocity at $i^{\text{th}}$ iteration	m/s
$v_{MS}$	Final velocity of main spring	m/s
$x$	Deflection of Spring	m
$y_i$	Complex Modal Coordinate of $i^{\text{th}}$ mode	-
$\alpha_d$	Angular acceleration of door	rad/s <sup>2</sup>
$\alpha_j$	Angular Acceleration of door at $j^{\text{th}}$ iteration	rad/s <sup>2</sup>
$\gamma_i$	Participation Factor of $i^{\text{th}}$ mode	-
$\zeta$	Damping Ratio	-
$\theta$	Rotation angle of door	rad
$\mu$	Coefficient of friction	-
$\mu_E$	Gravitational Parameter of Earth	m <sup>3</sup> /s <sup>2</sup>
$\sigma_p$	Proof stress of Fastener material	Pa
$\sigma_y$	Yield stress of material	Pa
$\tau_y$	Shear yield stress of material	Pa
$\Omega$	Harmonic Excitation Frequency	rad/s
$\omega_{df}$	Final angular velocity of door	rad/s
$\omega_{di}$	Initial angular velocity of door	rad/s
$\omega_i$	Natural Frequency of $i^{\text{th}}$ mode	rad/s
$\omega_j$	Angular velocity of door at $j^{\text{th}}$ iteration	rad/s

# 1.

## Introduction

Delft University of Technology has set a vision for miniaturization of spacecraft components and subsystems. With such a vision comes the challenge of developing new miniaturized systems and technologies essential for nominal operation of such spacecraft.

Miniaturization of spacecraft bears a massive advantage to the space industry. One such example is the development of distributed space sensor networks. PocketQube class of spacecraft have the potential to be industry drivers in enabling inexpensive access to space by further reducing the required resources. Reduction in capital required for the development of PocketQubes will result in empowering small scale manufacturers to take part in the spacecraft development process and facilitate large scale deployment of such PocketQubes. Therefore, large numbers of PocketQubes can be placed in orbit for a fraction of the cost required by traditional constellations of artificial spacecraft.

A test bed for the miniaturised systems on a PocketQube is a small spacecraft called Delfi-PQ. The PocketQube platform is a new concept of standardized spacecraft small enough to fit in an average sized pocket [1]. A PocketQube is similar to the CubeSat however, it is one step further reduction in size, volume, and mass. Each PocketQube unit (P unit) is one half of the dimension of CubeSat unit (50 mm) on each side and thereby one eighth in volume [2].

Technically, a PocketQube is a miniaturized satellite where all its subsystems are confined within a volume of 50 x 50 x 50 mm cube form factor called PocketQube (P) units. Many such PocketQube (P) units can be stacked in various configurations to make up a single PocketQube spacecraft similar to the CubeSat (U) units [1]. PocketQubes utilize the progress in miniaturization of the commercial electronics industry and thus are smaller in size. Therefore, as a result of this progress, PocketQubes which are smaller in size and mass can replace CubeSats without a compromise on the quality of the spacecraft mission.

In orbit utilization of standardised small spacecraft such as CubeSats and PocketQubes are expected to increase exponentially in the coming decade [3]. PocketQubes are envisioned to be deployed in large numbers similar to the growth of CubeSat constellations in recent years [4]. Further, with private space companies like SpaceX and Rocket Lab aiming to develop completely reusable launch vehicles, spacecraft launch costs in the coming decade are expected to decrease considerably.

Additionally, the development of dedicated kick stages like the Photon module by Rocket Lab expand the reach of small spacecraft into interplanetary space [5]. Spacecraft constellations deployed in interplanetary space can have applications related to planetary resource exploration, low-frequency radio telescopes [6], and emerging swarm technologies.

Similar to CubeSats, the PocketQube standard offers standardization of spacecraft dimensions and interfaces [2]. With such spacecraft standardization, deployers are designed to accommodate spacecraft of different sizes that conform to the standard and to be

interchangeable. Due to these merits, pod based deployer configuration used for deployment of CubeSats is also the best suited configuration for PocketQubes.

In order to cater to this projected demand of PocketQubes, a necessity arises to develop a suitable spacecraft deployer, which can deploy large numbers of PocketQube to orbit. In this study therefore, different configurations of PocketQube deployment system are analyzed to compare their system performance. Based on the performance of configurations, suitable design options are explored to minimize launch cost for PocketQubes enabling greater access to space.

## 1.1 Research Objective

***‘To design a cost-effective, modular PocketQube deployment system capable of deploying multiple PocketQubes in a mission, and to be able to adapt to different launch vehicles’.***

Following the current research available in previous works elaborated in Chapter 2, the requirement for a PocketQube Deployment System that arises is to be cost-effective, modular, and able to adapt to different launch vehicles. The research objective therefore is to design a PocketQube Deployment System that is :

1. Cost-effective as spacecraft launch cost is a significant portion of its overall cost. By ensuring that the deployment system design is cost-effective, overall cost to orbit for PocketQubes can be reduced.
2. Modular so as to allow for flexible use of resources. Such a modular system can incorporate design changes with minimum changes to deployer structure design and is aimed at procured components.
3. Able to adapt to multiple launch vehicle interfaces. Such a design will not only provide launch vehicle flexibility, but also be able to choose an economical launch vehicle on market to reduce total cost.

## 1.2 Research Questions

The objective of this thesis has been described in detail in the previous section. In order to achieve the set objectives, some questions have to be researched. They are :

1. What measures are best suited to reduce total cost to orbit for PocketQubes?
2. What is the best suited deployer configuration for deployment of one or more PocketQubes?
3. What is the best suited system configuration that can be integrated to multiple launch vehicles?

## 1.3 Research Methodology

Having defined the objective of research to be conducted in this study, this section details the methodology followed to achieve the defined objective. Figure 1 shows the work breakdown structure for this study. The research work conducted in this study will be in 5 phases as shown in Figure 1.

A literature study shall be conducted to determine current state-of-the-art in spacecraft deployers. Requirements for the PocketQube deployment system shall be derived from research objective set previously with an intent to reduce PocketQube mission cost. Deployer mass for different manufacturers shall be compared and system costs shall be analyzed. System

level trade-off studies shall be conducted to choose suitable solutions for the deployment system.

Following phase 1, launch vehicle loads shall be analyzed to arrive at design loads and stiffness requirements of the system in Chapter 3. Subsequently, an analysis of the non-structural aspect of the PocketQube Deployment System (PDS) shall begin in Chapter 4. Non-structural element design will focus on design of springs, door assembly, pusher plate assembly, guide mechanism, and pod dimensioning. Further, effect of deployment velocity on separation distance between spacecraft and launch vehicle shall be analyzed. Following which, system configurations for single pod and multi pod deployment systems are to be explored.

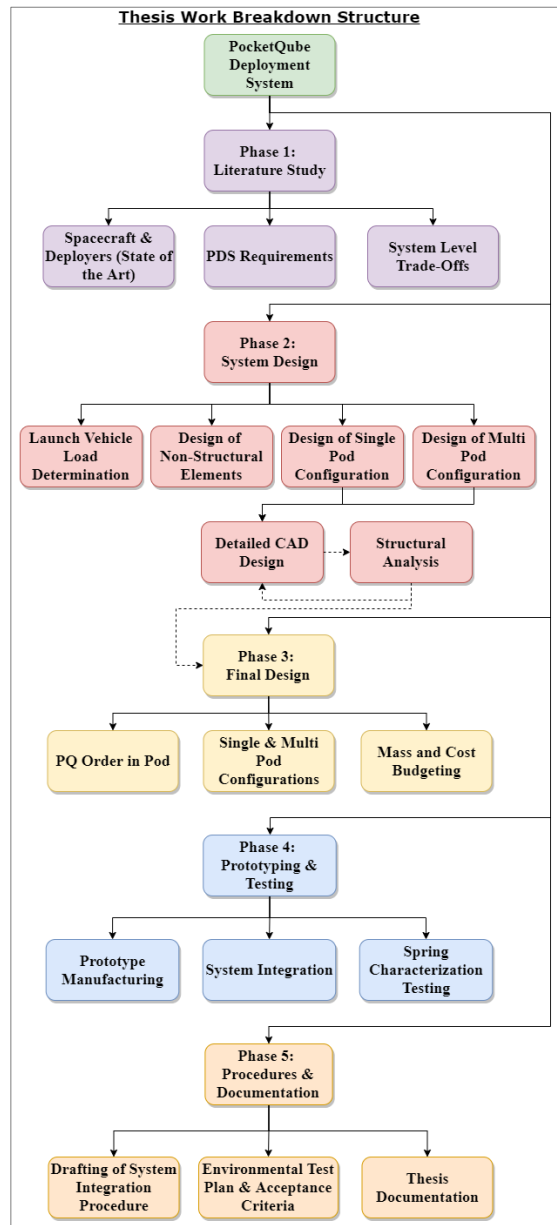


Figure 1: Work Breakdown Structure.

The chapter on research introduction is completed. Literature study will be discussed in the next chapter.

Following the configuration study of systems, structural analysis shall be performed using finite element method in Chapter 5. Validation of finite element methodology shall be realized prior to the analysis of PDS configurations.

Structural sensitivity analysis shall be performed to analyze the system sensitivity to different spacecraft parameters. Parametric study shall be conducted to determine design variables that affect system stiffness properties.

Final design of the different configurations of PDS shall be based on results obtained from structural analysis. For the final design of single and multi pod configurations, system mass and cost is estimated. Further, PDS mass and cost are to be compared with existing commercial deployers in Chapter 6.

System prototyping is envisioned to identify potential design flaws in system design and integration. Spring characterization testing shall be conducted to validate spring performance models and manufacturer specifications in Chapter 7.

Finally, integration and environmental testing procedures shall be authored for ease of future work on PocketQube deployers in Chapter 8. Lastly, documentation of the thesis work is completed.

# 2.

## Literature Study

This chapter is focused on the discussion concerning the heritage of PocketQubes, CubeSat deployers, PocketQube deployers, and release mechanisms used on pod based deployers. The chapter also details the requirements of PocketQube deployment system, system cost breakdown, launch cost assessment, and design trade-off studies.

### 2.1 Heritage Overview

This section will investigate the existing technologies of satellite deployment systems which have been proven for space applications. Traditionally, for spacecraft ranging between 100 to 6000 kg in mass, deployment has been carried out using clamp bands, Marman clamps and motorised light band systems as hold down mechanism which are actuated using a pyrotechnic actuator [7], [8].

Since the development of CubeSats, canister based satellite deployer units are in use. In canister deployers, spacecraft are held within the deployer envelope (unlike other separation mechanisms) and are released utilizing the potential energy stored in a compressed mechanical spring. The spacecraft is set in motion by the use of a release door which itself is actuated using a release mechanism. During deployment, the spacecraft is guided using rails which ensure low rotation rates on spacecraft post deployment. This form of deployer design has the advantage of spacecraft standardization and therefore spacecraft interchangeability.

Since the PocketQube and the PocketQube Standard are a derivative of CubeSats, it is logical to utilize a canister based deployer solution for PocketQube deployments.

#### 2.1.1 PocketQubes

As of July 2021, there have been a total of 13 PocketQubes (PQ) which have been deployed into Earth orbit. The first four were launched on a Russian launch vehicle onboard the UniSat-5 spacecraft manufactured by Gauss SRL on 21 November 2013 [9], [10]. The four PocketQubes were T-LogoQube, \$50Sat, QubeScout-S1, and WREN. Of the four PocketQubes, only two were successful in contacting the ground stations on Earth. Table 1 lists the details of the PocketQubes launched on UniSat-5 mission.

Out of the four PocketQubes launched in 2013 we can conclude that T-LogoQube and \$50Sat had mission success. T-LogoQube was operational for two months after launch and the reason for loss of mission is not known. \$50Sat was operational for 20 months after launch and its outage was attributed to a power system failure. Power failure was speculated to be due to low bus voltage values indicated in the last packets of telemetry received. Hence, a solar panel failure due to spluttering is thought to be the reason for the outage [9].

A further 6 PQs were launched by Alba Orbital on December 6, 2019 and 3 PQs were launched in March of 2021 by Gauss SRL. Recently in January 2022, several PQs were deployed on Transporter 3 rideshare mission [11].

Table 1: Details of first PocketQubes launched [9], [10].

PocketQube	T-LogoQube	\$50Sat	QubeScout-S1	WREN
<b>Developer</b>	Sonoma State University and Morehead State University	Amateur Developers	University of Maryland, Baltimore	STADOKO UG
<b>Payload</b>	Magnetometer	PocketQube Technology Demonstrator	Super Fine Sun Sensor	4 micro Pulsed Plasma thrusters
<b>Mass</b>	450 g	-	400 g	250 g
<b>Units</b>	3 P	1.5 P	2 P	1 P
<b>Current Status</b>	Inactive	Inactive	Inactive	Inactive
<b>Operational Period</b>	2 months	20 months	-	None
<b>Reason for outage</b>	Not known	Loss of power due to solar panel spluttering	-	Failed to contact ground

### 2.1.2 CubeSat Deployers

Several universities and private entities have developed and commercially operated CubeSat deployers in the past two decades. Some of the frequently used CubeSat deployers are listed below.

1. P-POD [12] – The deployer was developed by California Polytechnic State University in collaboration with Stanford University. It has a capacity of 3U and has a flight heritage since June 2003. Different versions of P-POD (Mk I, II and III) have successfully launched more than 50 times and have deployed 98 CubeSats into orbit [12], [13].

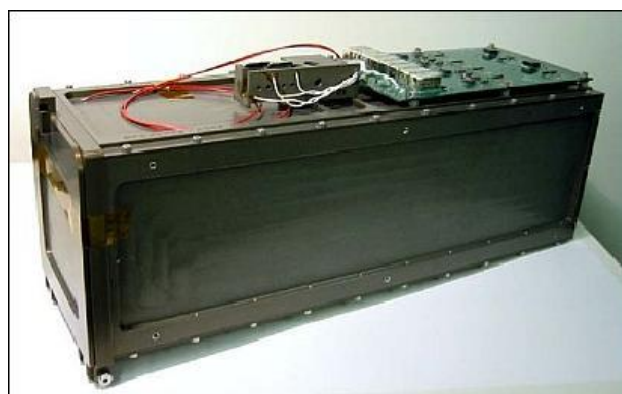


Figure 2: P-POD deployer [12].

2. ISIPOD CubeSat Deployer [14] – This deployer is developed by ISIS based in Delft, Netherlands. This deployer can accommodate any satellite following the CubeSat standard from 1U up to 16U. The deployer has various standard capacity of 3U, 6U, 12U and 16U. The ISIPOD has a flight heritage since 2013 and has deployed a total of 101 satellites in a single launch on 15 February 2017. This deployer system is highly versatile as it has demonstrated adaptability to different launch vehicles.



Figure 3: ISIPOD 3U deployer [14].



3. NanoRacks CubeSat Deployer (NRCSD) [15] – This deployer is developed by NanoRacks, USA. It has a maximum capacity of 6U in a single canister and can accommodate up to 12U per launch. This deployer has a fixed orbit of deployment as spacecraft are deployed from the International Space Station. However, in April 2019 NRCSD was used to deploy Lemur spacecraft on a PSLV launch vehicle to a polar earth orbit.



Figure 4: NRCSD 3U deployer [15].

4. Canisterized Satellite Dispenser (CSD) [16] – This deployer is developed by Planetary System Corporation, USA. Its capacity ranges from 1U to 12U and has a flight heritage since September 2013. Since then it has launched multiple times with a 100 percent success rate. It is a highly versatile deployer system as it can be integrated to the launch vehicle on any of its faces.

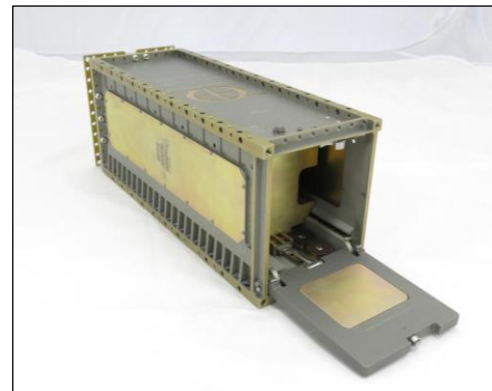


Figure 5: CSD 3U deployer [16].

Figure 6 shows the share of launch vehicles that have been used to deploy CubeSats into orbit. Of the launch vehicles shown, Dnepr has since been retired and Minotaur is to be exclusively used to deploy satellites belonging to United States Military. From Figure 6, it is evident that Atlas V, PSLV and Soyuz are the preferred launch vehicles for CubeSats. However, this study was conducted in 2018, since then few new launch vehicles have been attractive for small satellites. SpaceX with their ride share program and dedicated small satellite launch vehicles have become operational since. A detailed analysis on launch vehicles and associated costs is performed in Section 2.6.

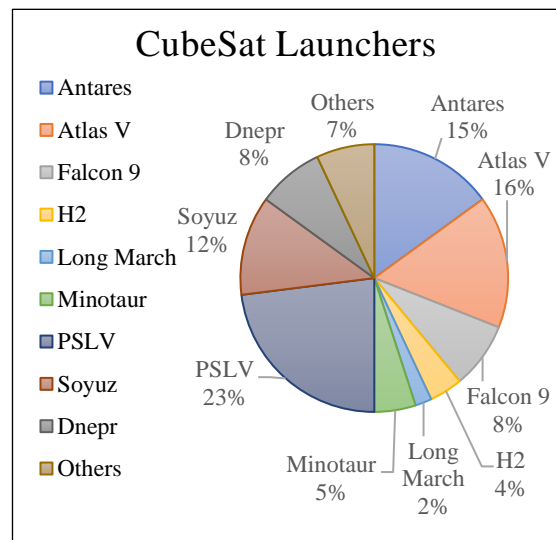


Figure 6: CubeSat Launchers [3].

### 2.1.3 CubeSat Deployment Velocity

Having discussed various CubeSat deployers and their characteristics, it is important to compare typical deployment velocities for these deployers. Deployment velocity is critical as it dictates the separation between launch vehicle and deployed spacecraft. Deployment velocity plays a direct role in defining the mechanical properties of the compression spring used to energize spacecraft for deployment.

Table 2: Deployment velocity and force of CubeSat Deployers.

Deployer Type	Deployment Velocity (m/s)	Deployment Spring Force (N)
NanoRacks CubeSat Deployer [15]	0.5 to 2.0	-
JAXA Small Satellite ICD [17]	1.1 to 1.7	46.5
Canisterized Satellite Dispenser [18]	0.7 to 1.6	-
P-POD [13]	2.0	44.4
EXOPOD [19]	1.14 to 1.64	-

Deployment force and velocities for different CubeSat deployers are listed in Table 2. It is seen from the table that the deployment velocity ranges between 0.5 and 2 m/s. Based on these values, the required deployment velocity for PocketQubes is set to be 2 m/s.

#### 2.1.4 Multi Pod CubeSat Deployer Footprint

In this section, different CubeSat deployers are compared to analyze typical launch vehicle footprints. This study focuses on 12U CubeSat deployers from different manufacturers. 12U is considered as it is the most common type of multi pod CubeSat deployer in use. Reasoning behind the usage of 12U CubeSat deployers is discussed in Section 2.7.

Deployer footprints of CubeSat deployers are overlaid one over the other and shown in Figure 7.

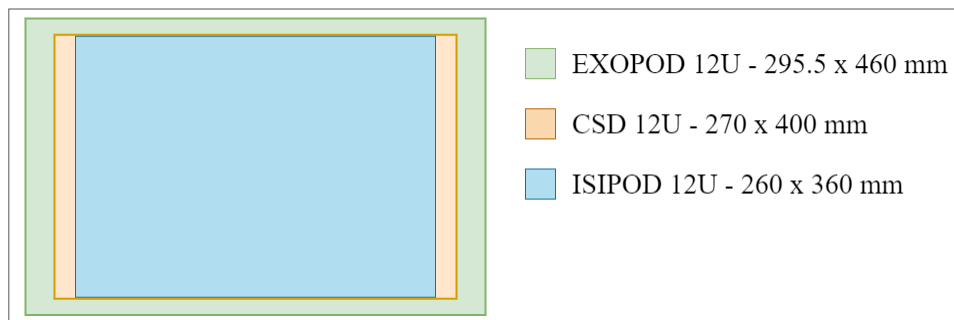


Figure 7: Multi pod CubeSat deployer footprint comparison<sup>A</sup> [19], [16], [14].

Footprint analysis of multi pod CubeSat deployers offers a starting point for the multi pod PocketQube deployment system. The multi pod CubeSat deployers in use are adaptable to multiple launch vehicles. Therefore, designing the multi pod PocketQube deployer with a footprint area similar to these deployers, PocketQube deployer compatibility to various launch vehicles is ensured.

#### 2.1.5 PocketQube Deployers

Having seen various CubeSat deployers and their characteristics, this section investigates PocketQube deployers currently in operation. In the recent past, there have been three commercial companies which have developed a deployer intended for PocketQubes, namely, Gauss SRL, Alba Orbital Ltd, and FOSSA Systems. Gauss SRL have developed a PocketQube deployment system on a satellite based delivery system. This deployer is an ad-hoc deployer that was flown onboard the Unisat-5 spacecraft and followed the MRFOD standard [20]. Satellites listed in Table 1 were all launched from Unisat-5 on 21 November 2013 on a Russian launch vehicle. However, no further information is available on this deployer.

<sup>A</sup> Footprint dimensions of ISIPOD inferred using CubeSat standard dimensions.

Alba Orbital Ltd. has developed a PocketQube deployment system which is shown in Figure 8. The deployment system is currently designed for 6P volume in a pod and to be integrated to the final stage of a launch vehicle. AlbaPOD having a 6P pod envelope and a maximum launch capacity of 96P for constellation deployment is a new direction of development for Alba Orbital. On 6 December 2019, a single pod deployer from Alba Orbital successfully deployed 6 PocketQubes (1P) from Electron launch vehicle [11].



Figure 8: AlbaPOD [21].

Recently, FOSSA Systems deployed 6 PQs on Transporter 3 rideshare mission [22]. The deployer has a total envelope of 8P units, with each pod having 4P volume as shown in Figure 9. The deployment system is actuated using two doors to deploy 8P unlike the AlbaPOD which uses a single door for 6P units.



Figure 9: FOSSA PQ Deployer [23].

The main difference between the two PocketQube standards (MRFOD and PocketQube standard) is the physical dimensions of PQ back plate. In this thesis only the PocketQube standard is considered and hence the deployer is designed for this standard. Information on PocketQube standard is provided in Section 2.2

### 2.1.6 Release Mechanism

This section focuses on overview of release mechanisms used for actuation in small spacecraft and canister deployers. Release mechanism is a critical system as it ensures opening of pod door which in turn actuates the spacecraft held within. Different release mechanisms used in pod based deployers are listed in Table 3.

Table 3: Release mechanisms used in canister deployers.

Release Mechanism	Users
Wire Cutter	P-Pod Mk I [13], ISIPOD [14]
Solenoid Pin Puller	P-Pod Mk II [12], AlbaPOD [21], FOSSA Systems [23]
DC Brush Motor	CSD [16]
SMA Release	ISRO Nanosatellites [24]

Wire cutter mechanism is the simplest mechanism of them all. It utilizes a nichrome burn wire to melt a restraining wire typically made up of a material like nylon [25]. Melting the restraining wire actuates the mechanism.

Solenoid pin pullers are commercially available release mechanisms qualified for space applications. The working principle behind the pin puller is that a pin made out of a ferromagnetic material is enclosed by a tightly wound conductor. Passing current through the conductor develops a magnetic field around it causing the pin to actuate. A spring load is added to hold the pin in place when the solenoid is disconnected from the circuit [26].

Shape Memory Alloy (SMA) based release mechanism is similar to the burn wire release. A heating element causes the SMA made of nitinol to contract in length (negative coefficient of thermal expansion). This contraction causes the hold down mechanism to release. Once heating is turned off, the SMA in time reverts back to its state before actuation therefore allowing for the mechanism to be reused if necessary.

DC brush motor mechanism is actuated electrically by commanding rotation of the motor. All other mechanisms discussed call for a torsion spring to provide the required energy for door actuation.

Wire cutter has been extensively used for antenna deployments in CubeSats and has been proven as a reliable deployment mechanism with hundreds of on orbit deployments [11], [27]. Pin puller is the next commonly used system. Apart from pod based deployers, pin pullers are used for solar panel deployments in spacecraft [28] and quick release mechanisms in the defence industry. Pin pullers have demonstrated high reliability with successful deployments of PocketQubes to orbit.

DC brush motor mechanism has proved to be a reliable mechanism used on the CSD system by Planetary System Corporation for multiple deployments. SMA based release mechanism is a novel system, however, with respect to reliability it can be assumed that mechanism reliability will be similar to wire cutter as the principle of actuation is similar for both mechanisms.

The trade-off analysis for PDS release mechanism is discussed in Section 2.9.

## 2.2 PocketQube Standard

Having discussed the heritage of standard spacecraft and their deployers, this section details the standard for PocketQubes. PocketQube class of spacecraft was introduced by Prof. Twiggs from Morehead State University in 2009. During initial phase of development of PocketQubes a standard called the MRFOD standard was introduced [29]. First four PocketQubes launched in 2013 followed the MRFOD standard.

However in 2018, a new standard was introduced for PocketQubes with collaboration from TU Delft, Alba Orbital Ltd., and GAUSS SRL. The main difference between the two standards are the physical dimensions of the backplate [30]. Physical dimensions and maximum allowed mass for spacecraft of different unit sizes according to the PocketQube standard are shown in Table 4.

*Table 4: PocketQube dimensions and mass [2].*

<b>PocketQube Units (P)</b>	<b>External dimensions without backplate (mm)</b>	<b>Sliding backplate dimension (mm)</b>	<b>Mass (kg)</b>
1P	50 x 50 x 50	58 x 64 x 1.6	0.25
2P	50 x 50 x 114	58 x 128 x 1.6	0.5
3P	50 x 50 x 178	58 x 192 x 1.6	0.75

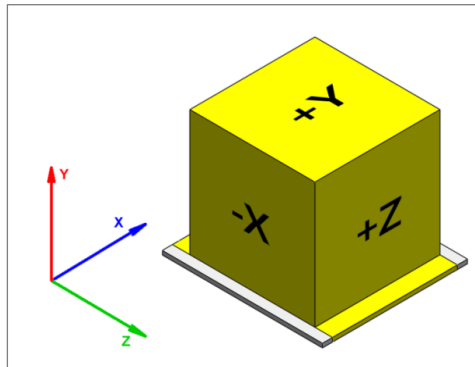
Apart from the physical dimensions and mass properties of PocketQubes mentioned in Table 4, the location of centre of mass is restricted by the standard. For PocketQubes of all unit sizes, the location of its centre of mass shall not exceed 10 mm from its geometric centre (GC) in stowed condition (*PQ-Mass-04*) [2].

## 2.3 Axis Definition

In this section of the report, axis definition of PocketQube, PocketQube Deployment System (PDS), and launch vehicles have been described. As PDS need to interface with both PocketQubes and launch vehicles it will be essential to describe the orientation of the respective systems for seamless interfacing of components. Based on the axis definition of the

PocketQube Deployment System (PDS) and launch vehicle, respective mounting directions are discussed in Chapter 4.

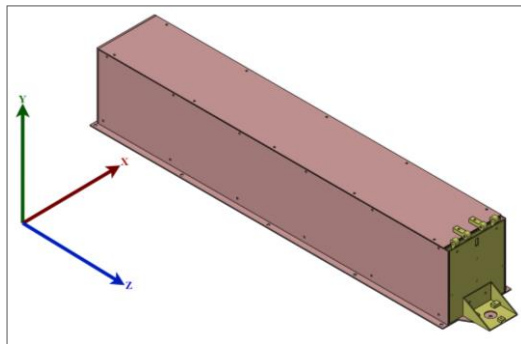
### 2.3.1 PocketQube



The axis definition of PocketQubes is shown in Figure 10. It is evident from the figure that the backplate of PQ is present on its -Y face. It is this face that will be in contact with the guide mechanism on the PDS. Further, the separation springs will be mounted on the backplate facing the -Z face. The direction of deployment for PocketQubes will be towards +Z face.

Figure 10: PocketQube axis definition [2].

### 2.3.2 PocketQube Deployment System



PocketQube Deployment System follows the same coordinate system as the PocketQube themselves. The axis definition of the deployment system is shown in Figure 11. All further description of the PocketQube Deployment System will adhere to this coordinate system unless specified otherwise.

Figure 11: PocketQube Deployment System Axis Definition.

### 2.3.3 Launch Vehicle

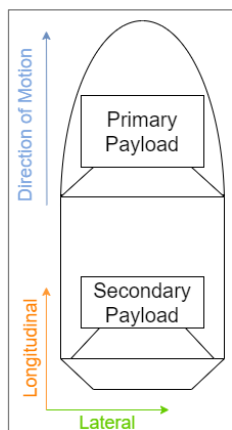


Figure 12 describes the axis definition of launch vehicles. Terminology is important because loads for the components mounted on launch vehicle are described using these axes. Typically for launch vehicles, longitudinal axis is the axis parallel to velocity vector and lateral axes are the ones perpendicular to the velocity vector.

PDS will be designed to be integrated onto the launch vehicle on all three of its axes for modularity. Hence, resultant launch vehicle loads in longitudinal and lateral axes are considered for PDS design.

Figure 12: Launch Vehicle axis definition.

## 2.4 PocketQube Deployment System Requirements

In this section the requirements for PocketQube Deployment System are listed and the rationale behind the requirements are discussed. Defining the requirements of the system at this stage of the study is important because it dictates the design choices and decisions accordingly. The requirements are classified into system level requirements and further requirements are derived from PocketQube standard, launch vehicle and general space environmental considerations.

System requirements for PocketQube Deployment System are listed in Table 5. Based on the requirements discussed in Table 5, further requirements are derived based on their origin and are elaborated upon in following sections.

*Table 5: PDS system level requirements.*

<b>Requirement Identifier</b>	<b>Description</b>	<b>Rationale</b>
<b>PDS-SYS-001</b>	The PDS shall be compliant with the PocketQube Standard.	PDS has to comply with the electrical and mechanical interfaces as prescribed by the PocketQube Standard.
<b>PDS-SYS-002</b>	The PDS shall be compliant with launch vehicle requirements.	PDS has to interface with the launch vehicle and has to meet all requirements set by it.
<b>PDS-SYS-003</b>	The PDS shall be compliant with general requirements set for space systems.	PDS has to operate in extreme pressure, temperature and radiation environments. Therefore PDS design has to account for these environmental constraints.

#### 2.4.1 PocketQube Standard Requirements

Requirements for the PDS which are derived from the PocketQube standard are listed in Table 6.

*Table 6: PocketQube standard requirements.*

<b>Requirement Identifier</b>	<b>Description</b>	<b>Rationale</b>
<b>PDS-PQS-001</b>	The PDS shall accommodate all the physical dimensions as required by the PocketQube Standard.	The deployment system is developed to accommodate any PocketQube which follows the PocketQube standard.
<b>PDS-PQS-002</b>	The PDS shall accommodate all electrical interfaces as required by the PocketQube Standard.	Deployment switches are critical for power on of PocketQubes. PDS shall ensure that deployment switches are only turned on after separation with the deployer.
<b>PDS-PQS-003</b>	The least volume of PocketQube that the PDS shall accommodate is 3P.	It is not practical to design and develop a deployment system merely to launch a 1P or 2P PocketQube.

#### 2.4.2 Launch Vehicle Requirements

Requirements for the PDS which are derived from launch vehicle are listed in Table 7.

*Table 7: Launch vehicle requirements.*

<b>Requirement Identifier</b>	<b>Description</b>	<b>Rationale</b>
<b>PDS-LVR-001</b>	The mechanical and electrical interface of PDS and launch vehicle shall be compatible with each other.	It ensures that the PDS and launcher can physically and electrically integrate with each other.
<b>PDS-LVR-002</b>	No pyrotechnics and hazardous materials shall be used for the PocketQube Deployment System.	PocketQubes are intended to be launched as secondary payloads and the use of pyrotechnics or any other hazardous materials can pose

		danger to primary payloads and other secondary payloads.
<b>PDS-LVR-003</b>	The release door/mechanism shall be able to withstand the launch vehicle dynamic and transient loads.	It is critical that the door stays closed during the launch phase of a mission and does not actuate unless triggered by a launch vehicle command.
<b>PDS-LVR-004</b>	The PDS release mechanism shall ensure that no parts coming from the separation process shall contaminate the payload or other payloads.	During the separation process there may be other payloads which are yet to be deployed by the launcher and ejected material may damage these payloads.
<b>PDS-LVR-005</b>	The PDS structure natural frequencies shall be above the minimum natural frequency specified by the launch vehicle.	The launch loads and the testing criteria for qualification will be provided by the launch vehicle (discussed in Chapter 3).
<b>PDS-LVR-006</b>	The PDS structure shall withstand the quasi-static loads induced by the launch vehicle acceleration.	
<b>PDS-LVR-007</b>	The PDS structure shall withstand the harmonic excitations induced by the launch vehicle.	
<b>PDS-LVR-008</b>	The PDS structure shall withstand the random vibration loads induced by the launch vehicle.	
<b>PDS-LVR-009</b>	The PDS structure shall withstand the shock loads induced by the launch vehicle.	
<b>PDS-LVR-010</b>	The PDS outer dimension/footprint shall comply with the footprint of a 12 U/16 U CubeSat deployer.	It makes the integration of multiple pod PDS and launcher simple as the interface for 12 U/16 U CubeSat deployer can be accommodated by variety of launch vehicles.

### 2.4.3 General Requirements

General requirements for the PDS is described in Table 8.

*Table 8: PDS general requirements.*

<b>Requirement Identifier</b>	<b>Description</b>	<b>Rationale</b>
<b>PDS-GEN-001</b>	The choice of material for PocketQube guide rail shall ensure no jamming of the spacecraft inside the PDS.	For a metallic surface, anodization is recommended in order to avoid cold fusion of material. Sliding contact surfaces must be sufficiently lubricated for easy movement of PocketQubes.
<b>PDS-GEN-002</b>	The PDS shall be able to withstand overall temperature range of $-40\text{ }^{\circ}\text{C}$ to $+80\text{ }^{\circ}\text{C}$ .	Typically for satellites in LEO, temperature ranges are as mentioned. The deployer mission lifetime will be short and therefore these temperature ranges will be sufficient for its purpose.

		For PocketQubes intended for deep space missions, the deployer will not be attached to a launch vehicle but to a spacecraft or a kick stage which would possess thermal management systems.
<b>PDS-GEN-003</b>	The deployer's structural material shall prevent spacecraft charging.	If the deployer encounters any unintended currents it should ensure the spacecraft are isolated from these runaway events.
<b>PDS-GEN-004</b>	The designed PDS shall not weigh more than 1kg for a PocketQube of 3P.	The PDS structure has to withstand loads imposed upon it, however, in doing so it must also be optimised for mass.
<b>PDS-GEN-005</b>	PDS shall be designed to be reusable.	Overall cost for the PDS can be reduced if the system can be reused with minimum refurbishments. With launch vehicles moving towards complete hardware reusability, PDS design shall therefore account for this in near future.

Having defined the requirements for the PocketQube Deployment System, a breakdown of system cost is discussed in Section 2.5.

## 2.5 System Cost Breakdown

Cost breakdown for the PocketQube Deployment System is shown in Figure 13. Total system cost can be broken down into 5 major categories:

1. Procurement Cost
2. Manufacturing Cost
3. Assembly and Integration Cost
4. Environmental Test Cost
5. Launch Cost

Detailed discussion on overall system cost for the PDS configurations is carried out in Section 6.8.

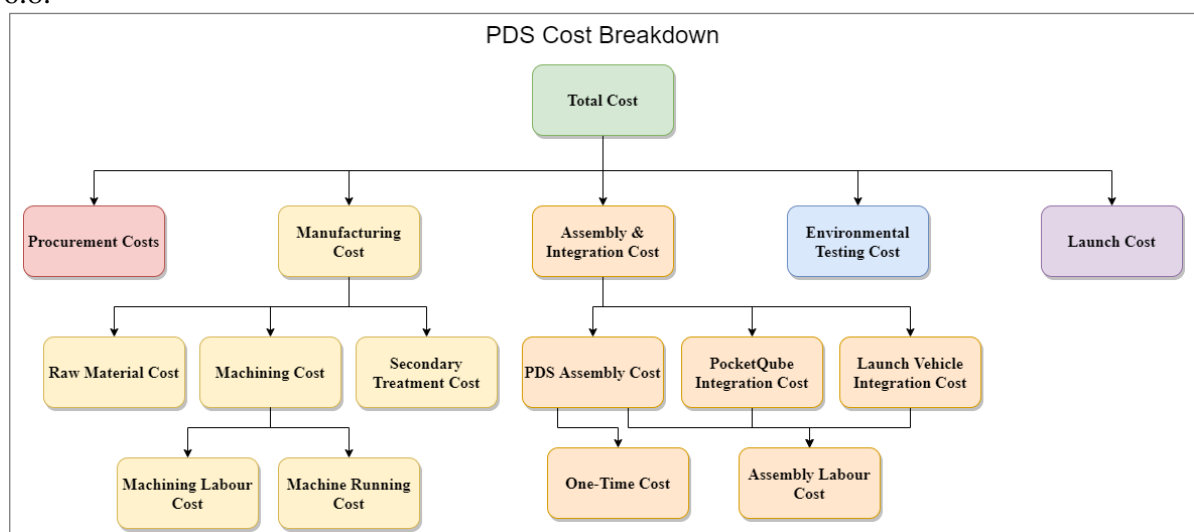


Figure 13: PDS Cost Breakdown.



**Procurement Cost:** Procurement cost includes all components of the PDS that have to be procured from external vendors. The items in this list include various springs, release mechanism, fasteners, and secondary locking solutions. All of the items have a fixed price set by their respective manufacturers. Procurement costs for different components are shown in Table 30.

**Manufacturing Cost:** Manufacturing cost includes cost of raw materials, machining of components and cost for secondary treatments for material. Machining costs can further be divided into machine running time cost and machining labour cost. Machine running cost is the cost incurred due to the machining time of the component and is only dependent on complexity of manufactured part. Machining labour cost is the cost paid for CNC machine programming, tool path registry and others. For mass production, machining labour cost are negligible due to economies of scale. Launch vehicles demand secondary treatments on metallic components to achieve corrosion and wear resistance. Anodization process also provide electrical isolation which is necessary for fault isolation in system electronics.

**Assembly and Integration Cost:** Assembly and integration costs can further be divided into PDS assembly cost, PocketQube and launch vehicle integration cost. PDS assembly cost has two components, a one-time investment cost to produce PDS assembly and integration fixtures for ease of integration and a recurring labour cost for a technician. Further, fit checks and integration of PocketQubes onto PocketQube Deployment System will incur recurring labour cost and so do the system assembly onto launch vehicle. Hourly cost for an average mechanical technician in Delft, The Netherlands is about 21.33 US\$ [31]. Methodology involved in estimating integration cost is discussed in Section 8.3, with estimates found in Table 30.

**Environmental Test Cost:** It is stipulated that PDS flight models have to undergo system environmental testing to prove workmanship. These tests include simulating launch vibration in three mutually perpendicular axes, and thermo-vacuum cycling of the test object. Therefore, environmental test costs are a recurring cost. Environmental testing cost although recurring will not vary between CubeSats and PDS as they fall under the same category (nanosatellites) for these tests. An estimated cost for environmental testing in 2017 for a 3U CubeSat was around 25,000 € [27], [32], [33]. For further cost budgeting this value will be considered for environmental testing.

**Launch Cost:** A detailed overview of launch costs has been discussed in Section 2.6.

## 2.6 Launch Cost Comparison

Launch cost is a significant percentage of the overall cost of any space system. A trend of decreasing launch costs has been observed in the recent years driven by partial reusability of launch vehicles [34]. Although space companies like SpaceX and Rocket Lab are aiming to further reduce launch costs, it is critical for a space systems designer to optimise their design to minimize launch cost.

Figure 14 shows the variation of launch cost per kilogram for different launch vehicles. The cost of small satellite launch vehicles indicated in Figure 14 are projected costs. As of July 2021, two micro-launchers are operational, namely, Rocket Lab's Electron and Virgin Orbit's LauncherOne. It is evident that specific cost of small satellite launch vehicles is on average higher than other launch vehicles that have high payload capacity. Although Figure 14 provides

a general estimate of the specific launch cost for a space component, it is hard to average the launch cost as it is highly dependent on the launch vehicle used to get to orbit.

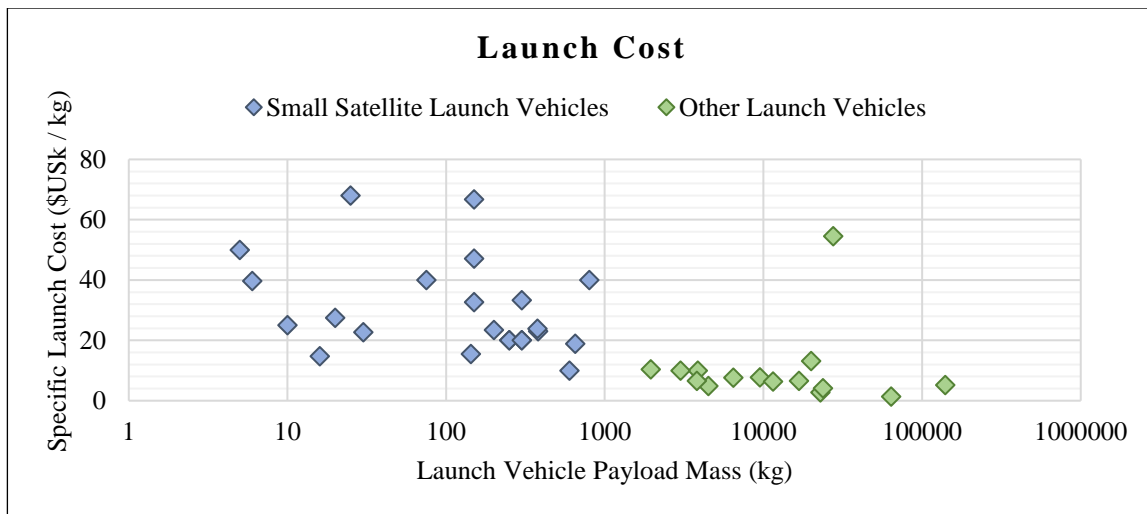


Figure 14: Specific launch cost for different launch vehicles [34], [35], [36].

In order to normalise the average specific cost to orbit of different launch vehicles, a normalization factor of launch frequency per year is calculated for currently operational and popular launch vehicles. Launch frequency is an effective cost normalization tool as it determines the market price for spacecraft launches based on demand and supply. Average normalized cost is calculated using Equation (1) where n is the number of launch vehicles considered.

$$\text{Average Normalized Cost} = \frac{\sum_{i=1}^n (\text{Specific Launch Cost})_i * (\text{Launch Frequency})_i}{n} \quad (1)$$

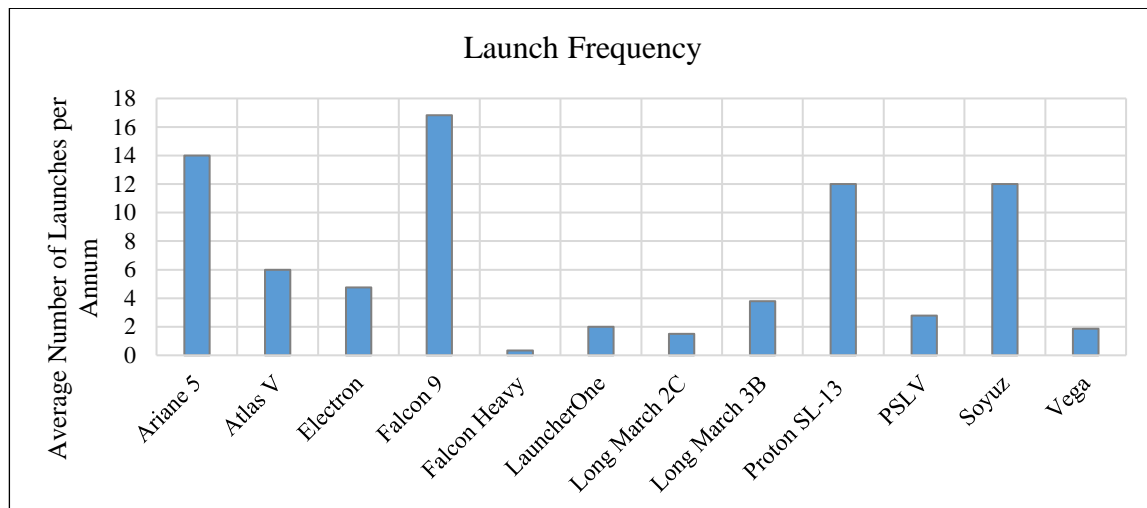


Figure 15: Launch frequency of relevant launch vehicles [35], [37].

Figure 15 shows the launch frequency of relevant launch vehicles. Based on Figure 15, Table 39 is generated showing the normalized cost per kilogram for launch hardware. Table 39 has been updated to 2021 US\$ by accounting for inflation, the calculation of which is shown in Table 38.

As seen in Table 39, the average specific launch cost is just 10,957.71 US\$ which is remarkably low. However, the average normalized cost provides a better estimate on current rates for launch of space hardware. For further cost analysis in this thesis, a rounded value of 62,000

US\$ per kilogram is considered as specific launch cost based on normalization discussed above.

## 2.7 CubeSat Deployer Mass Comparison

Having discussed the characteristics and heritage of CubeSat deployers, it is important to classify them based on their mass. Mass of deployer is chosen as a comparison parameter considering it drives spacecraft launch cost as discussed in Section 2.6. Deployment system as any space bound component shall consider minimizing its mass during the design process. Further, the launch cost of a deployment system is projected onto the spacecraft mission cost and having high launch cost will restrict low cost access to space which is detrimental to the objective of this study.

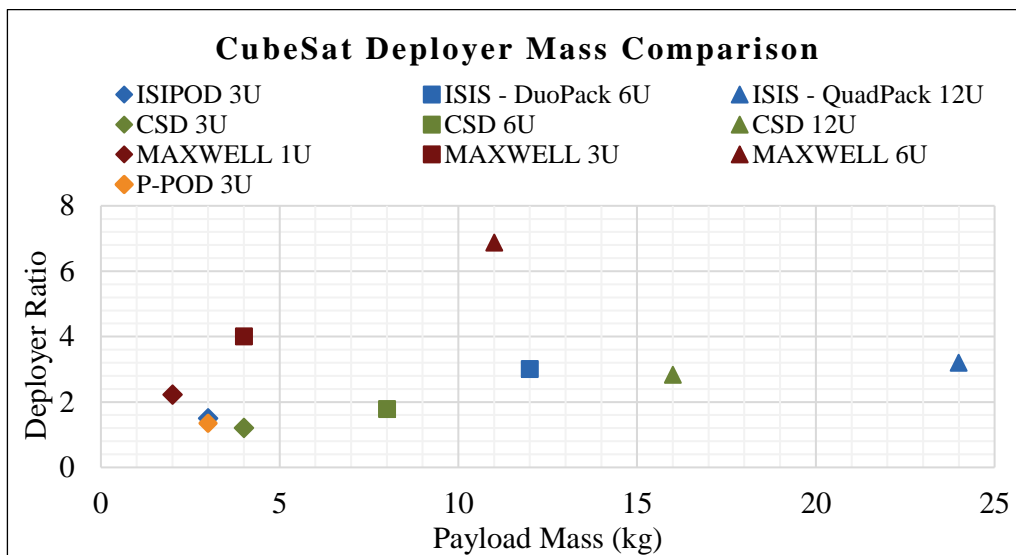


Figure 16: Mass comparison between CubeSat deployers [13], [14], [16], [38].

In order to characterize the deployers based on mass and compare deployment systems from different manufacturers, a term called deployer ratio is introduced in this study. Deployer ratio is calculated using Equation (2).

$$Deployer Ratio = \frac{Payload Mass}{Deployer Mass} \quad (2)$$

The distribution of deployer ratio along payload mass for different CubeSat deployers is graphically represented in Figure 16. High deployer ratio is preferred for deployers as it indicates a deployer that is optimized for system mass which minimizes its launch cost. It is also noticed in Figure 16 that maxwell deployers from Rocket Labs have higher deployer ratio compared to other CubeSat deployer manufacturers. This trend was traced to the use of Carbon Fibre Reinforced Polymers (CFRP) as the structure material of this deployer whereas, other deployers utilized aluminium alloy. Discussion on the choice of material for PDS structure is carried out in Section 2.8.

From Figure 16 it is observed that for the same manufacturer, with an increase in payload capacity deployer ratio increases. Hence, from a mass perspective it is optimum to deploy CubeSats from a multiple pod deployer. Therefore, in order to deploy large numbers of PocketQubes it is logical to use a deployer with high payload capacity rather than multiple deployers with lower capacity. Hence, a multiple pod deployer is preferred over a single pod deployer for large spacecraft deployment numbers.

## 2.8 Material Selection

In this section a comparative analysis is conducted to select suitable materials for use on the PDS structural components. The considerations for the choice of materials are listed below.

1. Sufficient strength and stiffness to withstand launch environment and qualification tests (**PDS-LVR-005** to **PDS-LVR-009**).
2. Low density to reduce structure mass (**PDS-GEN-004**).
3. Retention of mechanical properties over the operation range of PDS (**PDS-GEN-002**).
4. Not degrade or de-gas in vacuum conditions.
5. High corrosion resistance, non-toxic and easy to handle.

Having enumerated the considerations underlying the choice of materials for the PDS, a graphical representation of material stiffness of common materials is shown in Figure 17. Materials present on a line represented in Figure 17 have uniform specific stiffness performance for the shapes mentioned.

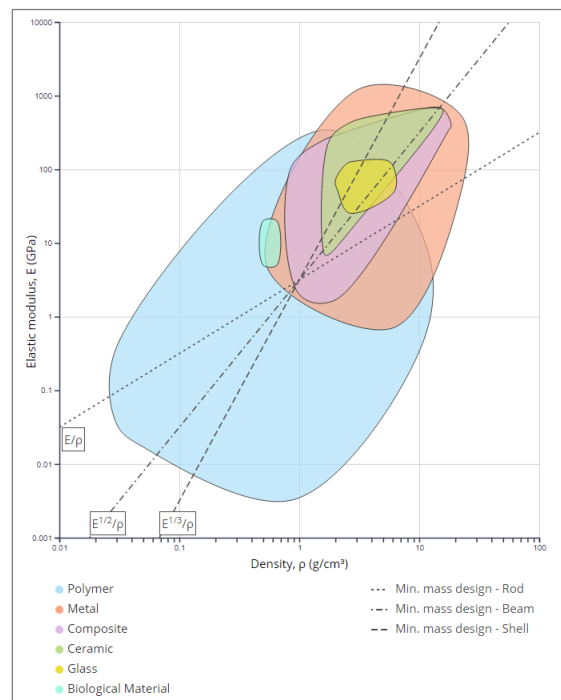


Figure 17: Ashby chart for commonly used materials [39].

Further, material properties of a few materials that meet the considerations are shown in Figure 18. Stiffness and strength are critical properties of a material, as system stiffness greatly determines its dynamic characteristics and material strength determines the maximum load a material can withstand without adverse effects.

From a space bound system perspective, material stiffness properties would take precedence over strength for the design to meet launch vehicle natural frequency requirement. Purely from this perspective it would be ideal to manufacture PDS structure from Beryllium. However, other considerations have to be had before choosing a suitable material and a design trade-off analysis is conducted to choose a satisfying material for the structural design of the PDS.

The criteria chosen for material trade-off in the order of priority are Material Density, Strength, Stiffness, Raw Material and Manufacturing Cost, and Secondary Considerations. Material density defines system mass which affects launch cost as discussed previously. By choosing a material with low density, PQ mission cost is reduced. Hence, material density has the highest weightage of 30%.

Material strength and stiffness are important properties which determine the system response to external loading conditions. It is critical for the PDS structure to be made of a stiff material to limit deformation due to launch vehicle dynamic loading and it has a score of 25%. Material strength of structure defines if the PDS withstands the launch forces without permanent deformation and it is desirable that strength be as high as possible. It has a weightage of 20%.

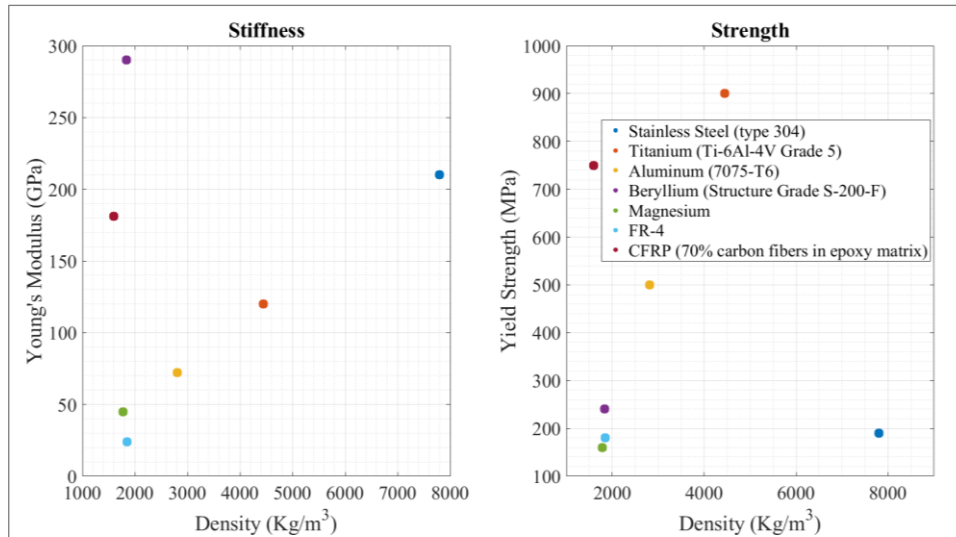


Figure 18: Material strength and stiffness compared with density [40], [41], [42], [43], [44].<sup>B</sup>

Raw material and manufacturing cost of the chosen material include the cost for raw materials and all costs in the process of converting the raw material to final structural components that are ready for integration. It accounts for machinability, secondary treatments for metals and fibre layup, setting of binding material for composites. For composite materials it also accounts for initial capital investment required for the manufacturing of composites. Raw material and manufacturing cost therefore has a weightage of 17.5%. Weightage of manufacturing cost is just 17.5% because PDS manufacturing cost is only fraction of total system cost details of which can be found in Section 6.8.

Further, considerations that are specific to certain materials are taken into account under secondary considerations. Secondary consideration has a weightage of 7.5%. Material selection trade-off is shown in Table 9. The material strength, stiffness and density property scores in the trade-off table are normalized values shown in Figure 18 for the different materials.

Table 9: Material selection trade-off.

		Material Options						
Criteria	Weight (%)	Stainless Steel	Titanium	Aluminium	Beryllium	Magnesium	CFRP	FR-4
Material Density	30	25	55	85	90	95	95	95
Material Stiffness	25	66	50	40	98	17	60	20
Material Strength	20	20	90	50	25	15	75	18
Raw Material and Manufacturing Cost	17.5	98	50	95	30	50	10	80
Secondary Considerations	7.5	90	90	90	20	60	90	95
<b>Total Score</b>	<b>100</b>	<b>51.9</b>	<b>62.5</b>	<b>68.88</b>	<b>63.25</b>	<b>49</b>	<b>67</b>	<b>58.23</b>

**Legend**

Highly Desirable	Less Desirable

The property scores for the raw material and manufacturing cost for steel, aluminium and FR-4 are high as they are extensively used in various engineering applications due to low material cost. Titanium has a score of 50 as it is an expensive metal to source and its machining costs are high.

<sup>B</sup> Composite material properties (FR-4, CFRP) are along fibre orientation.

Similarly for beryllium, raw material cost is high and further precautions have to be taken during machining to avoid dispersion of small particles. Hence it is given a score of 30. Although magnesium is readily available, it costs more than steel and aluminium. Magnesium alloys are hard to work with [45] and increase machining costs which gives it a score of 50.

CFRP has a low score of 10 as manufacturing costs are high. Further, manufacturing of CFRP composites require specialized tooling and machining. The investment cost into processes and machines required for manufacturing CFRP is high compared to machining of metals. This is due to the fact that general infrastructure is currently present to machine blocks of metal to design requirements and not for composite manufacturing.

Further, structural elements made of CFRP composites are highly specialized for the specific part. Different layers of carbon fibres have to be oriented along the expected stress directions to strengthen the part in those directions. Therefore, to manufacture these parts either highly specialized machinery is required or fibres have to be laid by hand (increasing labour cost). Both these methods increase costs significantly.

Secondary considerations are other considerations that are specific to beryllium and magnesium alloys. Beryllium can be toxic to humans when small particles are inhaled [46], [47]. Considering this health risk, beryllium alloys score 20. Machining magnesium is tricky because at high temperatures it can spontaneously ignite with oxygen present in air. Therefore, machining tool speeds must be low and dry machining has to be avoided at all costs to prevent accidental fires [48], [49]. Hence magnesium alloys score 60.

Based on material selection trade-off shown in Table 9, it is seen that aluminium alloys would be the best suited material to manufacture the PDS structure. Aluminium is chosen as it optimises density, material strength, material stiffness and cost.

## 2.9 Release Mechanism Selection

With the overview of release mechanisms used on small satellites and their deployers discussed in Section 2.1.6, a trade-off analysis of release mechanisms is conducted to select a suitable mechanism for the PDS. The criteria for release mechanism trade-off study are mechanism mass, system manufacturing and integration, reusability, component heritage, and handling concerns.

Pneumatic actuation is considered for the trade-off study as in recent years there is a drive towards reusable launch vehicles. Pneumatic based actuation system can be actuated multiple times based on the feed system used. For this study, a pneumatic system based on thermal decomposition of Sodium Azide is considered. This mechanism can be made low mass by eliminating the requirement for pressurized fluid storage system by instantaneous gas generation.

DC brush motor discussed in Section 2.1.6 is not considered for this study for its lengthy door actuation time and high mechanism mass. Considering number of deployments to be made for the multiple pod deployer, the deployment time is critical to reduce overall time to deploy all the PocketQubes during a mission. Details of time delay between multi pod deployments is discussed in Section 6.3.3.

Table 10: Release mechanism trade-off.

		Release Mechanism Options			
Criteria	Weight (%)	Burn Wire	Solenoid Pin Puller	Shape Memory Alloy	Pneumatic Actuation
Mechanism Mass	30	90	80	70	60
System Manufacturing and Integration	25	75	90	80	50
Reusability	20	80	100	100	80
Component Heritage	15	95	80	80	50
Handling Concerns	10	100	100	100	50
<b>Total Score</b>	<b>100</b>	<b>86</b>	<b>88.5</b>	<b>83</b>	<b>59</b>
<b>Legend</b>					
		Highly Desirable		Less Desirable	

Of the chosen criteria, mechanism mass has the highest weightage of 30. Mechanism mass is important as it contributes to the total mass of the PDS. The chosen mechanism will be used for multiple deployments on the multiple pod deployer. Hence, it is critical that mechanism mass be as low as possible to ensure low total mass.

Burn wire is the lightest of the mechanisms closely followed by pin puller and they have a score of 90 and 80 respectively. SMA and pneumatic actuation currently have high mass, however, a customized design is a possibility to obtain lower mechanism mass. Hence, they have a score of 70 and 60 respectively.

System manufacturing and integration is another critical criterion for the release mechanism. This criterion has weightage of 25 and evaluates the ease with which the release mechanism can be manufactured, integrated with PDS and tested for qualification. The restraining wire required by the burn wire mechanism needs to be replaced with every door actuation increasing its testing time and cost giving it a score of 70.

Pin puller scores 90 as it is an off the shelf component and can easily be integrated to the system. SMA mechanism scores 80 as its string length needs to be calibrated increasing its integration time. For the pneumatic actuation mechanism, a feed system is required to contain the generated gas and make it do work on a moving member to create the required actuation. Hence, due to the complications implementing this system, it has a score of 50.

PDS is designed based on the current trend of reusability of launch vehicles in mind. In the near future, with reusable launch vehicle upper stages becoming a reality, the possibility of reusing the PocketQube deployment system is high. Therefore, the release mechanism used on the PDS has to accommodate this requirement and the reusability criterion measures how easily a release mechanism can be reused. Reusability can reduce life cycle cost of PDS and has a weightage of 20%.

The pin puller and the SMA release mechanisms score high as they can be reused with minimum refurbishments required (pin needs to be reset for pin puller using a resetting tool) [28]. For burn wire, the restraining wire needs to be replaced and mechanism needs to be mechanically loaded (to maintain contact of burn and restraining wires) and shut. For

pneumatic actuation, Sodium Azide charge has to be replaced. This can be stored in a cartridge style container for easy replacement and to be in contact with heating element. For these reasons burn wire and pneumatic mechanism scores 80.

Component heritage for the release mechanism is considered as it is a single point of failure for the PDS mission objective. Heritage scores are based on total number of successful actuations that have taken place in on-orbit conditions and has a weightage of 15%. Most CubeSat deployers use a burn wire mechanism for actuation of door. Further, solar panel and antenna deployments in CubeSats also employ burn wire mechanism. Hence it has a score of 95.

Pin puller and SMA mechanisms have been proved to work in on-orbit conditions. However, the number of deployments are not as numerous as the burn wire mechanism. Hence, each have a score of 80. The pneumatic actuation system needs to be adapted for use on PDS and the system needs to be tested for on-orbit qualification. It has a score of 50.

Handling concerns has the least weightage of 10% as it is a secondary consideration for handling potentially toxic substances. Sodium Azide which is required for low mass design of pneumatic system is toxic. It requires additional safety precautions and handling expertise [50].

## 2.10 Pod Configuration Study

In Section 2.1.5 it was discussed that pod volume for the two operational PocketQube deployers vary (6P for AlbaPOD and 4P for FOSSA systems). The objective of the study was to reduce deployment system resource for identical volume of payload to be deployed. Hence, pod configuration study was conducted to figure out the optimum payload volume per pod of the PDS.

The total amount of PocketQube units to be deployed under this study was considered to be 6P units. The reason was that developing a PocketQube deployer that has a payload volume of just 3P units would be expensive in terms of structure mass and therefore drive up PQ mission cost (**PDS-PQS-003**).

Further, for this study a preliminary pod structure was considered. The structure dimensioning was according to Figure 56, considering a deployable volume of 10 mm on all faces. Two configurations were selected for the study to obtain a comparative understanding between them. The multiple door configuration considered deployment volume of 3P per pod with two pods required for deploying total of 6P payload. Single door configuration considered a deployment volume of 6P per pod with all 6P units housed within a single pod.

For the two configurations a trade-off study was conducted to find a suitable option for the optimum utilization of deployment system. The criteria considered for pod configuration trade-off study were mass, compactness, ease of integration and testing, and deployment reliability.

Configuration mass is the criterion with highest weight as it defines the deployment system mass and launch cost. Based on preliminary structure design, for aluminium alloy, about 300 grams was saved for single door configuration compared to multiple door (17,112 € per pod saved in launch cost). Hence single door configuration has a score of 80 while multiple door configuration has a score of 50.



For secondary payloads on launch vehicles, the area available for integration with the launch vehicle is limited. It is important to design the deployment system such that it occupies minimum launch vehicle surface area for a given payload volume. Provided the launch vehicle mass budget is closed, such a design will offer additional payload capacity within the same mission, hence lowering cost. Compactness is a criterion that accounts for this surface area and has 25% weight. Single door configuration scores 80 while multiple door configuration scores 60 as it would require double the surface area than the single door configuration.

Ease of integration and testing criterion accounts for time required for integration and testing activities for the two configurations. This criterion has a weightage of 20% as reducing time for integration and testing reduces the total cost by lowering labour costs. Multiple door configuration employs additional door assembly, release mechanism, pusher plate assembly, and main spring to deploy same amount of payload. It also requires electronic circuitry to stagger door deployment to avoid PocketQube collision. Therefore, multiple door configuration scores 50 and single door configuration scores 60.

Reliability is another criterion considered for comparing the configurations. A single point of failure which can cause total loss of PDS mission objective is the release mechanism. While reliability of the release mechanisms is discussed in Section 2.1.6, this criterion quantifies the probable chance of failure due to non-actuation of door assembly for a configuration as a whole. The criterion has a low weightage of 15%.

Single door configuration scores 70 while the multiple door configuration scores 60. For the single door configuration, the reason for a score of 70 is that if actuation fails, all PocketQubes in the pod (6P) will fail to deploy. For multiple door configuration, due to there being two doors to deploy same PocketQube volume, the probability of failure increases as two release events are needed giving it a score of 60.

Reliability of space systems is hard to quantify without conducting system testing for orbit conditions. Therefore, comparison of pod configurations on this criterion can only be roughly estimated by analyzing the engineering design of each pod configuration.

*Table 11: Pod configuration trade-off.*

Criteria	Weight (%)	Pod Configuration Options	
		Multiple Door Configuration	Single Door Configuration
Configuration Mass	40	50	80
Compactness	25	60	80
Ease of Integration & Testing	20	50	60
Reliability	15	60	70
<b>Total Score</b>	<b>100</b>	<b>54</b>	<b>74.5</b>
<b>Legend</b>			
	Highly Desirable		Less Desirable

Based on the pod configuration trade-off analysis it is apparent that the single door configuration has considerable benefits. For all further discussions in this thesis, the deployable volume per pod is taken to be 6P units capable of deploying 1.5 kg of spacecraft.

Figure 19 shows the various possible combinations of PocketQubes units that can be accommodated in the deployer envelope. It is to be noted that such an arrangement allows for PQ's of lower mass to be higher in the deployer envelope. The reasoning behind this decision will be discussed in detail in Section 6.1.

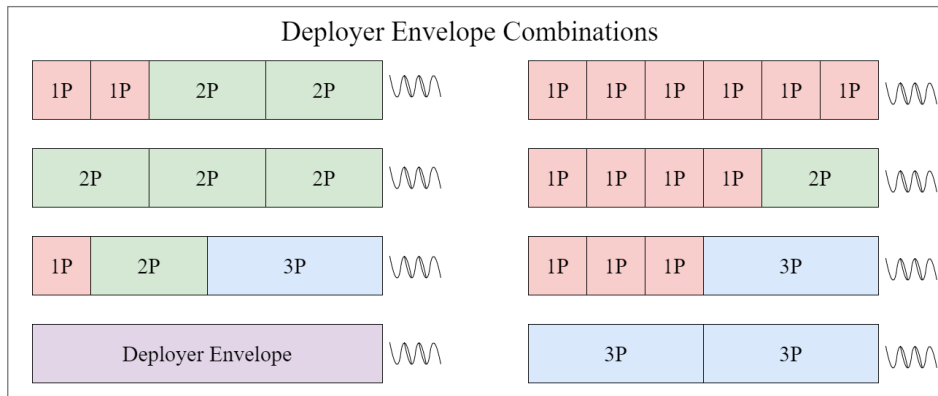


*Figure 19: Possible combinations of PocketQubes in deployer.*

# 3.

## Launch Environment

The chapter is dedicated to the discussion on the environment experienced by PocketQube deployment system during its launch phase. An overview on launch vehicle terminology is followed by description of different types of static and dynamic excitations.

For launch vehicle loads which are described, the resultant magnitude in lateral and longitudinal axes are considered as PDS is designed irrespective of its orientation of mounting on launch vehicle. Based on the determined launch vehicle loads, design loads and system frequency requirements are arrived at.

### 3.1 Terminology

Preceding the discussion on the various types of loads that a launch vehicle induces on its payload(s), it is important to understand the terms that define these loads and their amplitude levels. Depending on the loading profile of a specific launch vehicle, environment test levels are specified for payloads after considering safety margins. In order to understand these environmental test levels, we have to define the individual hardware on which the tests are to be performed. The different hardware on which environmental testing is conducted are prototype, protoflight, and flight hardware.

Prototype hardware is built to evaluate the design, manufacturing processes, and to discover potential design or production flaws. Such discoveries help rectify problems in future hardware versions. The prototype is typically subjected to the design qualification test program.

Flight hardware is the hardware used operationally in space. It is given higher level of care during handling and other ground operations compared to prototypes. It is to be noted that the flight hardware must not be over tested during the testing process [51]. Protoflight hardware is a subset of flight hardware for a new design, which is subjected to a qualification program that combine elements of prototype and flight hardware testing. A protoflight hardware is produced when the decision is taken to skip prototyping a new design, and flight hardware is manufactured in place of the prototype.

Qualification tests are the tests intended to demonstrate that the system under testing will function within the defined performance specifications under conditions more severe than expected during its life cycle. It is conducted to evaluate the system design and to uncover deficiencies in design and method of manufacturing. Acceptance tests are testes to demonstrate that the system is acceptable for flight. Typically the test levels for acceptance tests are significantly lower than qualification levels.

With a purpose to streamline the test process and to prevent over testing of space systems, NASA has defined the terminology for space system testing [51]. These design test terms are enumerated below.

1. Prototype Qualification
2. Flight Acceptance
3. Protoflight Qualification

Of the three system testing methods mentioned above, it is to be noted that two (prototype and protoflight) tests are intended to be qualification tests and acceptance test is proposed to be carried out on all hardware intended for flight.

1. **Prototype Qualification:** It is a level of environmental testing with which a specific design is subjected to conditions much severe than the system will encounter during its life cycle. The reasoning for such a test is to uncover potential flaws in design and manufacturing. Care must be taken to ensure qualification testing does not exceed design margins or introduce unrealistic modes of failure. A design is said to be qualified if the system functions within specifications when subjected to qualification testing.
2. **Flight Acceptance:** It is the verification process that demonstrates that the hardware is acceptable for flight. It serves as a quality control screening to detect defects or deficiencies that generally occur due to production.
3. **Protoflight Qualification:** Such a level of qualification is a hybrid testing scenario involving qualification and acceptance testing elements. A protoflight qualification test level will involve the application of qualification test levels for flight acceptance test durations. Protoflight qualification testing is carried out on a new design which is intended for flight hence qualifying the design and also accepting the hardware to be flight worthy.

As PocketQube Deployment System is a new design, a prototype test philosophy will be utilized for its design. Based on these test conditions, design loads will be generated to evaluate the design of PDS.

## 3.2 Launch Vehicle Loads

Payload of a launch vehicle experiences different types of structural loads. These loads are dependent on launch vehicle structure design, launch vehicle type, the phase of flight and factors which are external to the launch vehicle. The source of these loads can be due to various launch vehicle operation phenomena or interactions between the launch vehicle and its environment.

The structural loads encountered by a payload that is mounted on a launch vehicle can be classified into 5 main categories. These are listed below:

1. Quasi-Static Acceleration
2. Sinusoidal Vibrations
3. Random Vibrations
4. Acoustic Excitations
5. Shock

The different launch vehicle load types will be discussed in the following sections in detail while highlighting sources of specific loads and the levels to which these occur in specific launch vehicles.

### 3.2.1 Quasi-Static Acceleration

Acceleration loads are frequency independent loads experienced by the launch vehicle structure and its payloads. These loads generally occur due to the operation of rocket engines which are responsible for the launch vehicle ascent. The value of these loads depend on the type of launch vehicle, specific mission profile, and the ascent phase.

Acceleration loads depend on the type of launch vehicle as different launch vehicles use different types of engines in their vehicle design. The phase of flight is also a variable for the acceleration loads, as different launch vehicle stages produce variable levels of thrust. Further, mission profile is also a contributor for the acceleration loads as it dictates the rate of ascent of the launch vehicle. Atmospheric density of planet earth is maximum at sea level (where most launch sites are located) and decreases with increase in altitude. As a result, initial thrust levels need to be optimum to reduce structural loading.

Typical acceleration profile of a launch vehicle is shown in Figure 20.

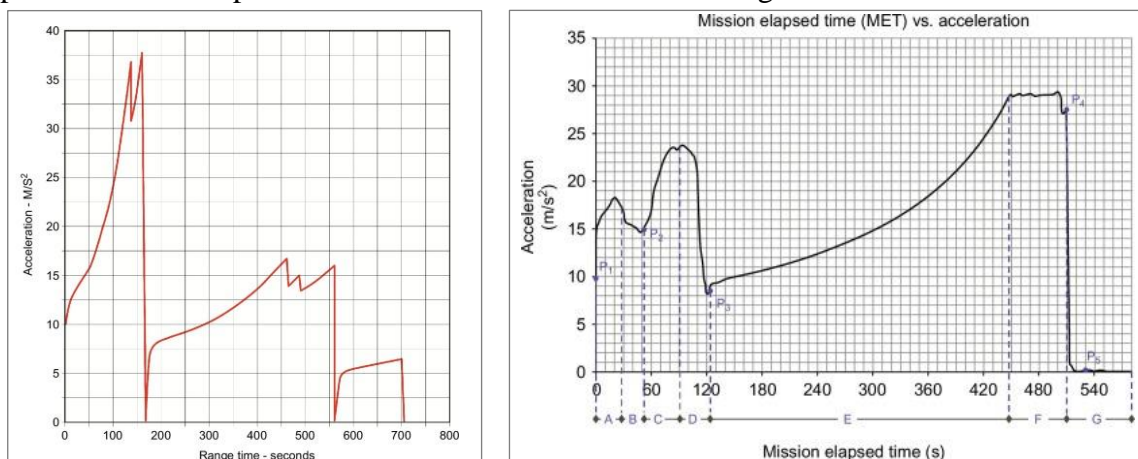


Figure 20: Acceleration Profile of Apollo 17 (left) and STS 121 mission [52].

Based on the acceleration profile of the launch vehicle, a maximum acceleration level is specified for the payloads by the launch vehicle manufacturer. It is to be observed from Figure 20, the acceleration levels of Space Shuttle and Saturn V launch vehicles do not exceed a magnitude of 4g ( $1g = 9.81 \text{ m/s}^2$ ) as these launch vehicles are human rated. However, there are launch vehicles which have higher acceleration levels, and a few launch vehicle levels are tabulated in Table 12. It is to be noted that the launch vehicles specified in Table 12 are ones which frequently transport small spacecraft and payloads.

Table 12: Acceleration loads of various launch vehicles [53], [54], [55], [56], [57].

Quasi-Static Acceleration							
Launch Vehicle	HTV	ATV	Falcon 9	PSLV	Electron	QB-50	Vega C
Acceleration (g)	8.34	12.37	8.67	7	8	13	10

### 3.2.2 Sinusoidal Vibrations

Sinusoidal vibration is a cyclic structural vibration experienced by the launch vehicle which can be expressed mathematically as a sinusoidal load. Various sources of harmonic vibrations are rocket engine chamber pressure oscillations [58], transient loads from thrust excitation [59], pogo oscillations, and propellant sloshing in liquid stages.

The amplitude of the sinusoidal vibrations depend on the launch vehicle design and the type of staging the launch vehicle (LV) uses. Generally, the harmonic excitations are expressed as

frequency dependant acceleration with the convention specifying the maximum amplitude at a particular frequency.

Chamber pressure oscillation is a cyclic phenomenon where the pressure levels in the rocket engine combustion chamber vary with time. The cause of chamber pressure oscillations can be attributed to combustion instabilities. Combustion chamber pressure oscillations will result in the rocket engine thrust variation [60]. These thrust variations will introduce structural excitations which have the same frequency as the pressure oscillations in the combustion chamber.

Transient loads from thrust excitation are short duration dynamic loads which are induced by the ignition and shutdown of rocket engines. Due to these transient effects internal stresses are developed on the launch vehicle structure which are then transmitted to its payloads.

Pogo is a type of low frequency thrust oscillation predominantly in the longitudinal direction of the launch vehicle. It is caused when pressure oscillation in propellant tanks passes through the feed systems and transforms to combustion pressure oscillations [61]. This can cause a positive feedback loop and amplification which leads to undesired acceleration loads. Pogo excitation can occur only in liquid stages and can be rectified using pogo correctors in the feed system.

Propellant sloshing is another source of low frequency oscillation which predominantly occurs in low gravity environments. Once the rocket engine is shutdown, due to its resident inertia, propellants stored in the tanks can slosh around [62], [63]. This phenomenon occurs during stage separation events and after final stage engine shutdown [64]. It can cause cyclic loading of the launch vehicle structure inducing a dynamic loading environment.

Based on all these factors and in flight measurements, the launch vehicle manufacturer provides maximum sinusoidal acceleration levels for their launch vehicles. Some of the launch vehicle dynamic acceleration levels for small payloads are listed in Table 35 and plotted in Figure 21.

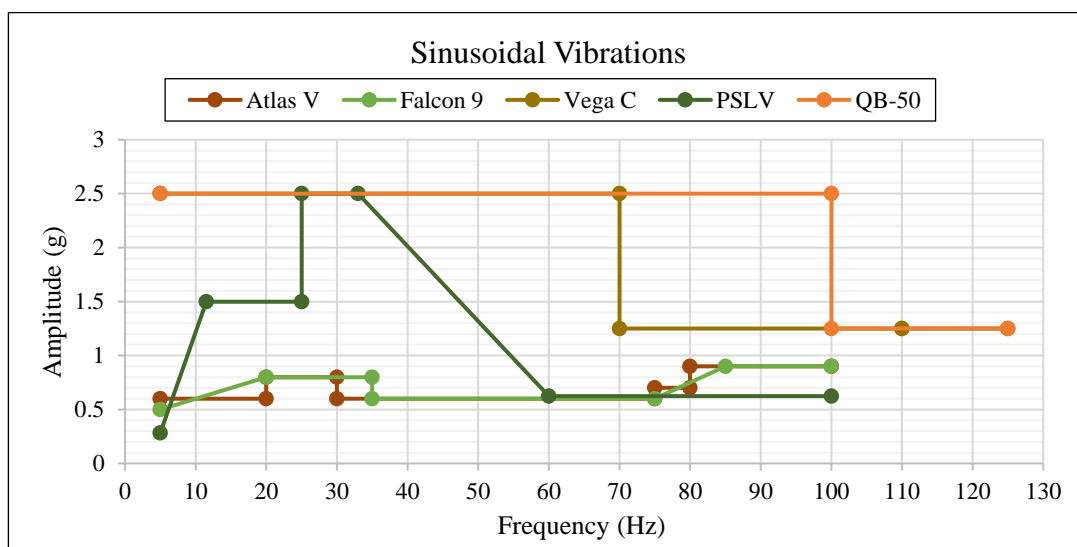


Figure 21: Launch Vehicle Sinusoidal Vibration [53], [54], [55], [56], [65].

### 3.2.3 Random Vibration

Random vibrations are random in nature. The true magnitude of such vibration is not known at a given time. However, magnitude of random excitations are expressed in statistical terms

such as mean value, standard deviation, and probability of occurrence. The different sources of such vibrations on a launch vehicle structure are acoustic noise during lift off, aerodynamic-structural response and wind excitations.

Acoustic noise during launch vehicle lift off occurs near the launch pad as the rocket engine exhaust gases are reflected from the pad infrastructure back onto the vehicle [66], [67]. Generally, launch pads are equipped with acoustic suppression systems however, they do not eliminate structural excitations. During the atmospheric phase of flight, aerodynamic loads are applied on the vehicle structure. The cause of these aerodynamic response loadings are attributed to turbulent boundary layer excitation, separated flows, wake flows, and shock waves [66]. Other sources of random vibrations are due to atmospheric winds and gusts the launcher experiences during its atmospheric phase of flight.

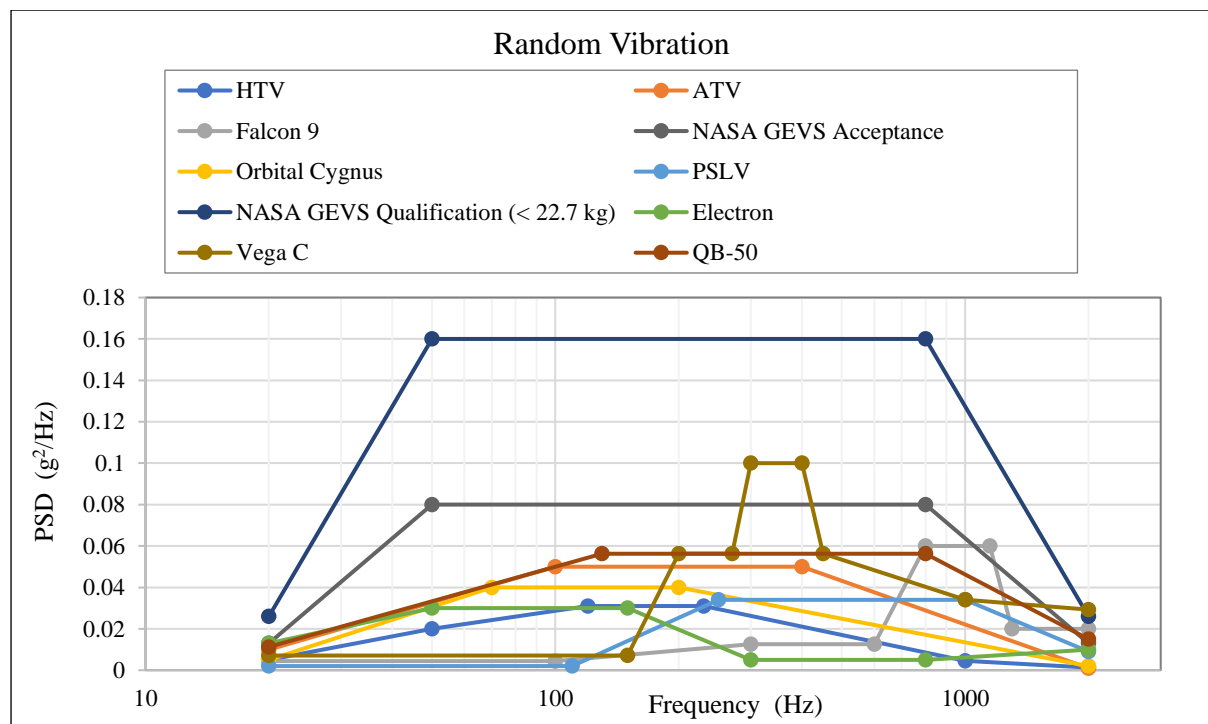


Figure 22: Random vibrations of different launch vehicles<sup>c</sup> [17], [51], [53], [54], [57], [55], [56].

Random excitations of launch vehicle are usually described in terms of Power Spectral Density (PSD) function. A PSD function is a measure of energy at a particular frequency. Therefore, a PSD of random vibrations describe the energy of excitation at a particular frequency onto the structure. Launch vehicle manufacturers specify the PSD of their launch vehicles by measuring the random accelerations the launch vehicle experiences during developmental flights. The time domain random acceleration data is converted to frequency domain by Fourier transformation. Additional margin is added to the frequency domain data and converted to a PSD curve for the payload qualification.

Table 36 and Figure 22 describe the random vibration levels for relevant launch vehicles.

<sup>c</sup> Qualification levels for system with mass less than 22.7 kg. Correction factor to be applied for mass above 22.7 kg.

### 3.2.4 Acoustic Vibration

Acoustic interactions affect the structures on a launch vehicle which have large surface area and low mass. Due to the acoustic environment close to the launch pad and during initial ascent phase of flight, acoustic interactions can excite elements like payload fairings, solar panels and large antennas.

Acoustic derived structural excitations are not relevant for the PocketQube Deployment System. For small satellites mounted on a launch vehicle, acoustic excitations will be observed as random structural excitations due to launch vehicle structural response to these loads. Hence, acoustic loads for small components are accounted for in random input PSD [66].

### 3.2.5 Shock

Shock loads are transient loads having very high amplitude and short duration. Generally in launch vehicles, the events that bring about shock excitations are during lift off, stage separation and other pyrotechnic device actuations. Shock response spectrum for launch vehicles is shown in Figure 23.

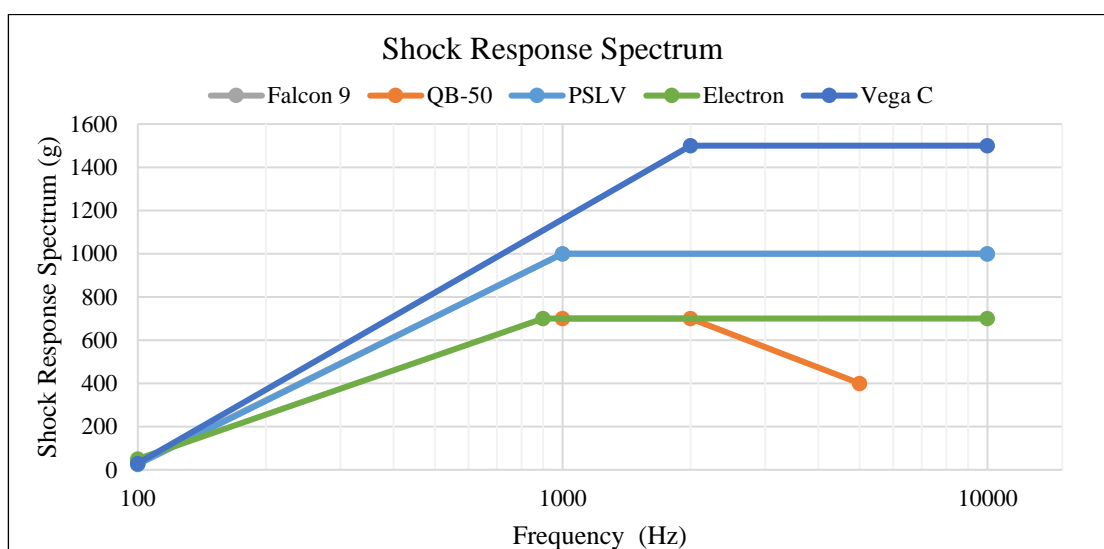


Figure 23: Shock Response Spectrum [53], [54], [57], [55], [56].

## 3.3 Natural Frequency Requirement

Having discussed the various types of static and dynamic loads that are introduced on a system due to the launch vehicle, it is important for PDS to avoid resonance due to dynamic coupling with the launch vehicle. Resonance in any component will lead to amplification of loads and therefore increasing its deformation which, further can lead to structural failure.

Steinberg's octave rule is the design guideline for minimising resonance caused as a result of dynamic system coupling [68]. It states that '*Natural frequency of chassis must be at least one octave of the natural frequency of the component*'. For the case of PDS, chassis would be the launch vehicle and the component being the deployment system. Based on this principle and considering other factors like payload mounting location and component size, generally, launch vehicles specify the lowest natural frequency of a component. Table 13 lists the natural frequency requirements for small satellites and their deployers. Based on values described it was chosen that the PDS minimum natural frequency shall be greater than 135 Hz to meet launch vehicle requirements.



Table 13: Natural Frequency Requirement.

Standard	Natural Frequency Requirement (Hz)
QB-50 [55]	> 90
JAXA Small Satellite ICD [17]	> 100
Vega-C [54]	>115
P-POD [13]	> 120
PSLV [69]	> 135

### 3.4 Design Loads

Having discussed the various types of loads exerted by the launch vehicles on its payloads in Section 3.2, in this section we evaluate the design loads based on the launch vehicle factors and recommended factors of safety for space systems. Table 14 shows the recommended factors of safety for different types of launch vehicle loads by NASA for spacecraft structures.

Table 14: NASA recommended flight hardware design factors of safety [51].

Load Type	Factor of Safety
Quasi-Static (Acceleration)	1.25
Sinusoidal Vibration	1.25
Random Vibration <sup>D</sup>	1.6 / +3dB
Shock	1.4

Based on Table 14, Factor of Safety (FOS) for different structural loads, the structural analysis input load levels are arrived at. An exception is present for the factor of safety considered for random vibrations. The FOS mentioned for random vibration in Table 14 is based on flight acceptance levels. An FOS of 1.6 is only applied if testing is carried out at less than +3dB of acceptance limit levels. For random vibration analysis, qualification levels specified in NASA environmental standard (*GSFC-STD-7000A*) is +3 dB higher than flight acceptance levels [51]. Therefore, for structural analysis, random qualification levels are considered and no further FOS is added to it. Additionally, peak system response to random load input will be evaluated as  $3\sigma$  value with a confidence level of 99.7 %.

Having seen the safety factors for the different load types, the design loads are described in Table 37 based on Table 12, Figure 21, Figure 22 and Table 14. Considering that the PDS qualification is intended regardless of its orientation with respect to launch vehicle mounting, peak loads are applied to the PDS during structural analysis in all three perpendicular directions. Detailed description of structural analysis is carried out in Chapter 5.

With the description of design loads, current chapter on launch vehicle environment is concluded. System design, structural analysis, and system testing are discussed in future chapters.

<sup>D</sup> Safety factor based on Flight Acceptance Levels.

# 4.

## System Design

The chapter will detail the design of PocketQube Deployment System. This chapter will focus on the design of component systems such as springs, door assembly, pusher plate assembly, and guide mechanism used on the deployment system.

Design of structural elements of PDS will be detailed in the following chapter, however, different system configurations for single and multi pod deployment systems are discussed here.

### 4.1 Pin Puller Selection

In this section, a market analysis is conducted on commercially available pin puller mechanisms which satisfy PDS requirements. Based on a trade-off study on release mechanism detailed in Section 2.9, the design choice for a pin puller based release mechanism was arrived at.

Pin pullers considered for the PDS are shown in Table 15. Considerations behind the market survey were pin puller mass and electrical actuation redundancy. Electrical redundancy is provided by utilizing two independent isolated current paths to command pin puller actuation. Electrical circuit redundancy is preferred in order to ensure that multiple actuation methods are possible using isolated electrical circuits. As discussed previously, failure of release mechanism would lead to PDS mission failure. Electrical redundancy is one of the ways of risk mitigation in this regard [70]. Hence, electrical actuation circuit redundancy was a prerequisite for pin puller market analysis.

Of the pin pullers mentioned in Table 15, pin puller from Tini Aerospace and from D Cubed have been used on the AlbaPOD and on FOSSA Systems PQ deployer respectively. Pin puller costs are not readily available from the manufacturers due to customer specific customizations. However for cost analysis of PDS which is discussed in Section 6.8, 5000 € is considered as unit price of pin puller mechanism based on price quote from one of the manufacturers.

*Table 15: Pin puller details [71], [72], [73], [74].*

Manufacturer	Tini	Glen Air	D Cubed	Arquimea
Part No.	P5	061-013-190	nD3PP	PPLL.012.V2.XX
Mass (g)	30	145.8	25	55
Non Actuating Shear Force (N)	444.8	1467	50	1800

Pin puller mass was the other factor considered to choose a suitable pin puller. Of the four eligible candidates, pin pullers from Glen Air and Arquimea were discarded due to high system mass. Pin puller mass for the remaining two pin pullers were similar, however, ability to withstand side load for pin puller manufactured by Tini Aerospace was far greater than one manufactured by D Cubed. Therefore, Tini Aerospace pin puller with part number P5 was chosen for the PDS release mechanism. However, side loads experienced by the pin puller pin

will be estimated by structural analysis in Chapter 5 to ensure loads are within acceptable limits.

## 4.2 Aluminium Alloy Selection

In previous sections of this report, a comparative study was conducted to evaluate a suitable material for PDS structural components. The conclusion from the study was that aluminium alloy is best suited for structural components. Details of this study is found in Section 2.7.

Desirable properties for the choice of aluminium alloy are high specific stiffness, high resistance to corrosion and low cost. Strength and corrosion properties of aluminium are highly dependent on combination of alloying elements used. Alloy strength is a parameter which is used to specify the alloy selection for deployer structural components (similar stiffness). The choice of suitable alloys will be based on structural analysis stress results. Aluminium alloy with high yield strength such as Al-2024 and Al-7075 would be preferred for components which are expected to encounter high member stress when subjected to launch vehicle loads.

Due to proximity of typical launch sites to coastal areas, corrosion in metals would be accelerated. Aluminium alloys such as Al-2024-T3, Al-7075-T6 and Al-7079-T6 are highly susceptible to stress corrosion cracking in the short transverse direction [75]. Therefore, corrosion protection measures such as anodizing, cladding, and painting are a necessity. Anodization of metallic surfaces is the common treatment method used in the aerospace industry to mitigate corrosion [76].

Anodization of aluminium alloy increases its surface hardness, corrosion and wear resistance [77]. Properties of the anodized layer is strongly affected by morphology, chemical composition and crystalline structure of the oxide generated, which depend on the electrolyte type, concentration and current density used during the anodizing process [78]. Anodizing process is classified based on thickness of oxide layer generated on the surface. Anodizing of aluminium alloys must be carried out in accordance to European Space Agency (ESA) standards (**ECSS-Q-ST-70-03C**).

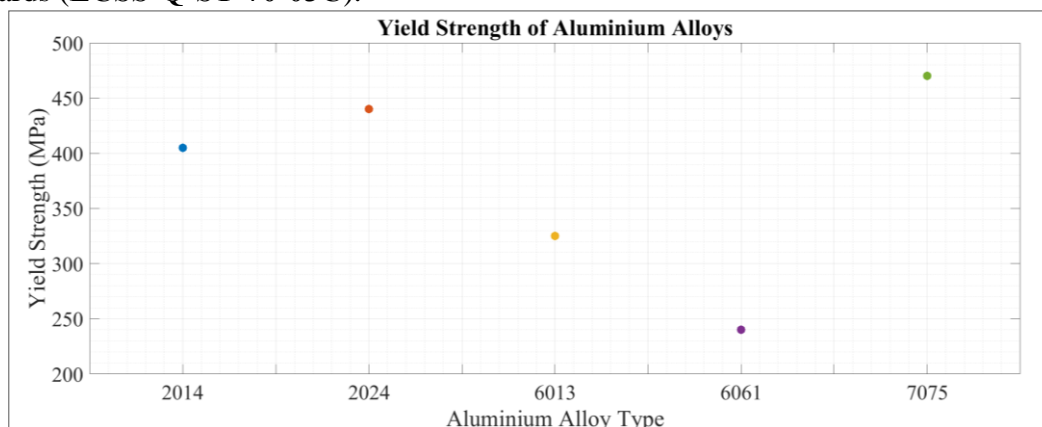


Figure 24: Aluminium alloy yield strength [42].<sup>E</sup>

In this section, aluminium alloys commonly used for spacecraft engineering applications are considered. Aluminium alloy types considered for Table 40 and Table 41 are based on European Space Agency's material standard which have high resistance to stress corrosion cracking (**ECSS-Q-ST-70-36C**) [79].

<sup>E</sup> Mechanical properties are dependent on tempering (heat treatment) process.

Alloy strength for different aluminium alloys is shown in Figure 24 with mechanical properties listed in Table 41. Raw material cost comparison between the different alloy types were highly dependent on raw material block dimensions and did not yield appreciable results. In order to compare an individual part was considered for manufacturing with different alloys. It was observed that for cost did not substantially vary between the chosen alloys<sup>F</sup> [80].

The choice of aluminium alloy used for different components of deployment system will be based on the stresses experienced by the individual members. Details of which will be discussed in Chapter 5. Alloy selection for different components of the deployment system is listed in in Table 55 and Table 56.

## 4.3 Springs

This section is dedicated to arriving at suitable spring specifications for the different springs used on the PocketQube Deployment System. Springs are the preferred form of storing potential energy which is required for various deployments present on the deployment system.

The main spring for PocketQube deployment, the torsion spring for door deployment and the separation springs for PocketQube separation are discussed. Verification models are developed for spring performance estimation to provide confidence in obtained results. Estimation performance is evaluated based on system characterization and testing in Chapter 7.

### 4.3.1 PocketQube Deployment Energy

Having established the requirement for PocketQube deployment velocity based on CubeSat heritage in Section 2.1.3, this section is dedicated to determining a suitable mechanism to provide the required deployment energy. Few mechanisms are introduced, their merits and drawbacks are discussed before choosing a suitable mechanism.

1. **Electromagnetic Rail** : This mechanism is based on linear induction motion technology. Based on Maxwell's equations on electromagnetism, a set of linear conducting coils will provide an accelerating force to a pusher mechanism made of a ferromagnetic material. This force can be utilised to provide required acceleration for PocketQube deployment.

Such a system would require energy storage devices like capacitors to build up and rapidly discharge during the spacecraft deployment process. Power electronics and switching circuits would also be required to ensure optimum use of system.

The advantage of the principle behind this mechanism is that the deployment velocity of PocketQubes can be controlled to great accuracy using a feedback mechanism. Further, the system can be tuned based on the PQ mass to be accelerated. The drawback of this system is that it does not meet Electromagnetic Compatibility (EMC) requirements set for space systems [81]. Further, such a system would likely interfere with instruments like magnetometers and magnetic torquers on PocketQubes.

Due to this limitation, an alternative method is required which would store energy in a passive mechanism. A mechanical spring would be such a system which stores its potential energy due to material elasticity. Mechanical springs are of different types and the ones suitable for PQ deployment application is discussed further.

---

<sup>F</sup> Considering manufacturing and secondary treatment.

2. **Flat-Wire Wave Spring** : Such a spring is similar to conventional spring in principle. However, the design of such a spring uses a flattened coil which is wound in a wave pattern to provide the necessary spring stiffness as shown in Figure 25. The main advantage of such a spring is that it offers excellent force to compression length ratio. For the same force, compressed length of such a spring is lower when compared to compression spring. Such springs also offer higher force linearity across its working range.



Figure 25: Flat-Wire Wave Spring [82].

However, such a spring does not offer large stroke length which is required for PQ deployment (about 400 mm). This drawback can be mitigated by spring stacking which defeats the purpose of using this variety of spring.

3. **Spiral Spring** : A spiral spring offers the advantage of constant force over its stroke length. Typical spiral springs can be found in measuring tapes which retract using this mechanism. Most designs utilize a spiral spring to provide a constant force during compression (coil retraction). However, a spring which provides force during extension is required for PQ deployment.

A possible alternative is to use spiral compression spring and invert its action. This complicates the deployment system design by requiring a spring hold-down near the door assembly. Such a hold-down mechanism could interfere with PocketQube appendage volume during the spacecraft deployment process. Owing to this drawback, a conventional compression spring is preferred.



Figure 26: Spiral Spring [83].

4. **Compression Spring** : This spring is a conventional coil wound in helical form. Force exerted by such a spring will be proportional to its deflection from rest position. Due to non-linear stiffness characteristics of helical springs at the beginning and end of their stroke, it is standard practice to exclusively utilize middle 80% of a compression spring's travel [84].

With force variation along spring length, total velocity imparted to PocketQube needs to be calculated using an estimator. Discussion on such an estimator is carried out in the next section.

#### 4.3.2 Main Spring Specification

The requirement of the PocketQube Deployment System is to deploy PocketQubes once in desired orbit. Having seen the typical deployment velocities for CubeSats in Table 2, the requirement was set to design the deployment system such that the PocketQubes deployment velocity will have a magnitude of 2 meters per second. The discussion on deployment velocity was conducted in Section 2.1.3.

Having set the deployment velocity, the spring force required to impart the desired deployment velocity needs to be calculated. The required stroke length of the spring is equal to the length of two PocketQubes of size 3P (384 mm). Applying Equations (3),(4) of motion on the Spring-PocketQube system an estimate for required spring force can be calculated. Where,  $a_{PQ}$  is the

acceleration of PocketQubes,  $m_{Stack}$  is total mass of PQ in pod,  $F_{MS}$  is the main spring force,  $s$  is the stroke length,  $u_{MS}$ , and  $v_{MS}$  are the initial and final velocity of main spring during deployment.

$$a_{PQ} = \frac{F_{MS}}{m_{Stack}} \quad (3)$$

$$v_{MS}^2 = u_{MS}^2 + 2 a_{PQ} s \quad (4)$$

However, one aspect for consideration during the calculation of deployment velocity is that the force exerted by the spring is dependent on its position. During the spring stroke, spring force exerted decreases linearly. Therefore, any calculation of velocity using equations of motion cannot be obtained as the acceleration varies with force and in turn on spring stroke.

$$v_{i+1}^2 = v_i^2 + 2 a_i dx \quad (5)$$

In order to calculate velocity of deployment the force exerted by the spring is discretized along its stroke length and the velocity is calculated using by numerical integration. Equation (5) is the first-order discretized version of Equation (4) where,  $v_i$ ,  $a_i$  are the velocity and acceleration at  $i^{th}$  iteration respectively, and  $dx$  is the discretized length. It was found that a discretized length of  $1 \times 10^{-3}$  meters was optimal to minimize error and computation time.

### 4.3.3 PocketQube Deployment Velocity Model Validation

The deployment velocity model described by Equation (5) needs to be validated in order to ensure any further analysis of deployment velocity carried out would be accurate. The two independent ways employed for validating the deployment velocity model are energy and momentum balance checks.

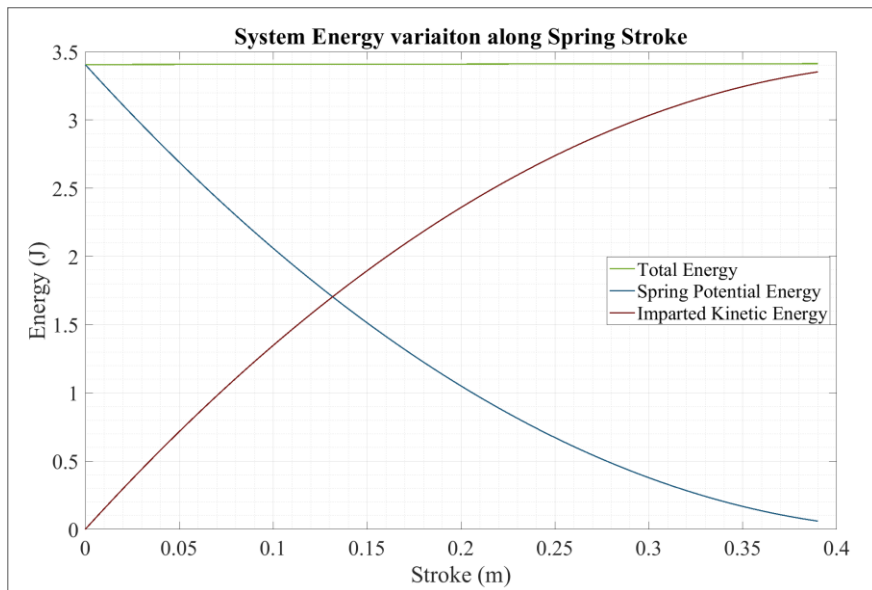


Figure 27: Main spring energy variation along its stroke.

**Energy Balance:** Potential energy of spring is given by Equation (6) where,  $E_P$  is spring potential energy,  $x$  is the deflection measured from rest position, and  $k_{MS}$  is spring constant of main spring.

$$E_P = \frac{1}{2} k_{MS} x^2 \quad (6)$$

Kinetic energy imparted on the PocketQubes due to spring action is given by Equation (7) where,  $E_K$  is kinetic energy and  $v$  is the velocity of PocketQubes.

$$E_K = \frac{1}{2} m_{Stack} v^2 \quad (7)$$

Total energy in the system is given by Equation (8).

$$E = E_K + E_P \quad (8)$$

Total energy of the Spring-PocketQube system must be invariable along the stroke length of the spring. This is shown in Figure 27.

**Momentum Balance:** Momentum change in Spring-PocketQube system at start and end points of spring stroke will be conserved. General equation for change in momentum is given in Equation (9).

$$\Delta Ft = \Delta mv \quad (9)$$

We know that force exerted by the spring changes along its stroke. Therefore, an equivalence term called Equivalent Force ( $F_{eq}$ ) is introduced in this study which is given by Equation (10) where,  $v_{dep}$  is the velocity of PocketQubes after deployment, and  $t_{dep}$  is time taken for PocketQube deployment.

$$F_{eq} = m_{stack} \frac{v_{dep}}{t_{dep}} \quad (10)$$

Since force exerted by the spring is its intrinsic property, equivalent force must also be solely dependent on the spring. Therefore, equivalent force must be invariable with PocketQube mass in pod. In order to verify the deployment velocity model, PocketQube mass is varied and its effect on equivalent force is analyzed. Hence, if equivalent force does not vary with PocketQube mass in pod, the model is considered to be validated.

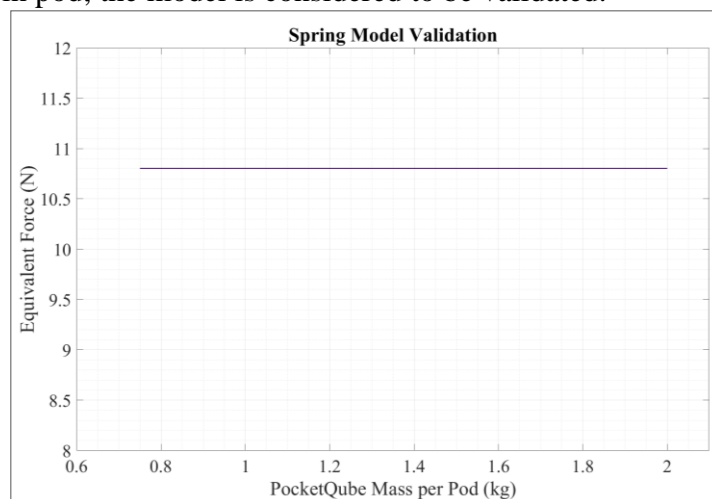


Figure 28: Equivalent force invariance to PocketQube mass.

Equivalent force invariance is shown in Figure 28. The deployment velocity model is considered validated by the invariance of total energy and equivalent force.

#### 4.3.4 Main Spring Analysis

Based on considerations of deployment velocity of 2 m/s and calculations using deployment velocity model, a specification for the main spring was arrived at and is listed in Table 42. These specifications were forwarded to a spring manufacturer and a custom spring was ordered from Tevema B.V [85]. Custom spring was chosen to minimize spring compressed length. Minimizing the compressed length has to main advantages. They are:

1. Reduced structure mass as total length of pod is decreased.
2. Lowering of system centre of mass in +Z direction.

Implications of centre of mass of pod is discussed in Chapter 5 and Section 6.1. Impact of system mass on launch cost was discussed in Section 2.6.

Main spring drawing is shown in Figure 125. Based on manufacturer defined tolerance for stroke length and spring force, a window of operation for the main spring is generated and is shown in Figure 29.

Acceleration and velocity imparted to the PocketQubes along stroke length due to the action of main spring is shown in Figure 30. Nominal spring performance is assumed, PQ mass of 1.5 kg (based on pod capacity of 6P), and a stroke length of 390 mm is considered for this analysis. Deployment velocity achieved is equal to 2.1149 m/s and time to deploy PocketQubes is 0.2937 seconds.



Figure 29: Operation window of Main Spring [85].

In Figure 30.1, PQ velocity increases steadily until the end of spring stroke is achieved. However, close to 75% of the deployment velocity is achieved in the first 25% of spring stroke. Figure 30.2 depicts the variation of acceleration with time as the spacecraft acceleration variation with stroke would be a straight line. Maximum acceleration experienced by PocketQubes is  $10.1 \text{ m/s}^2$  and at the beginning of deployment.

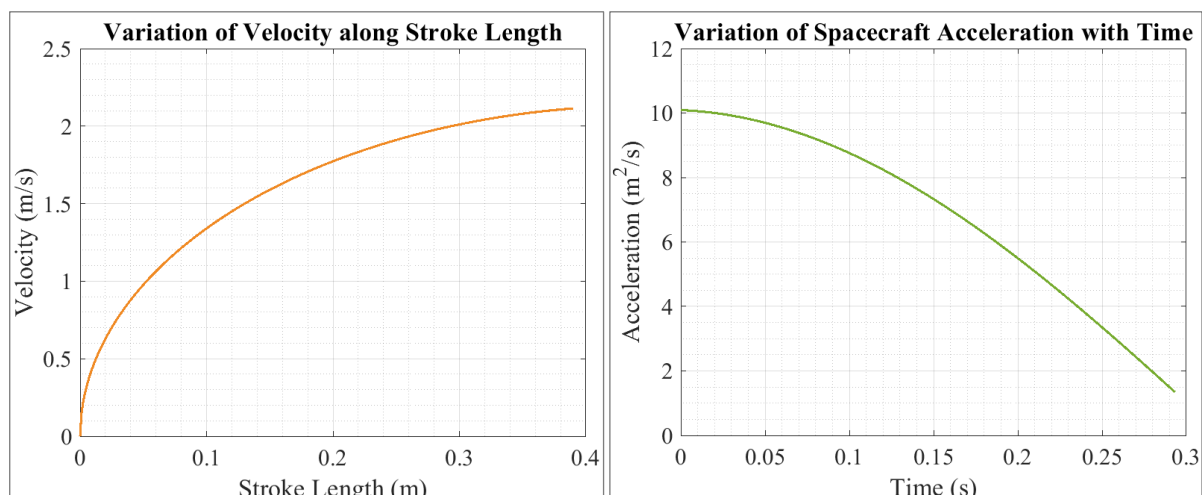


Figure 30: Velocity and acceleration imparted on spacecraft along stroke.

The previous analysis is expanded to calculate the variation of deployment velocity and time accounting for the tolerance specification of main spring. PQ mass and stroke length remain unchanged and are 1.5 kg and 390 mm respectively. The results of this analysis is tabulated in Table 16 and inferred from Figure 32.



Equivalent force changes for different tolerance limits as the spring performance (spring constant) varies and performance is lowest for lower limit. Deployment velocity of PocketQubes for lower limit tolerance is close to intended 2 m/s.

Table 16: Deployment characteristics based on spring tolerance.

Tolerance Window	Deployment Velocity (m/s)	Deployment Time (s)	Equivalent Force (N)
Nominal	2.1149	0.2937	10.8025
Upper Limit	2.2331	0.2821	11.87398
Lower Limit	1.9911	0.3068	9.734844

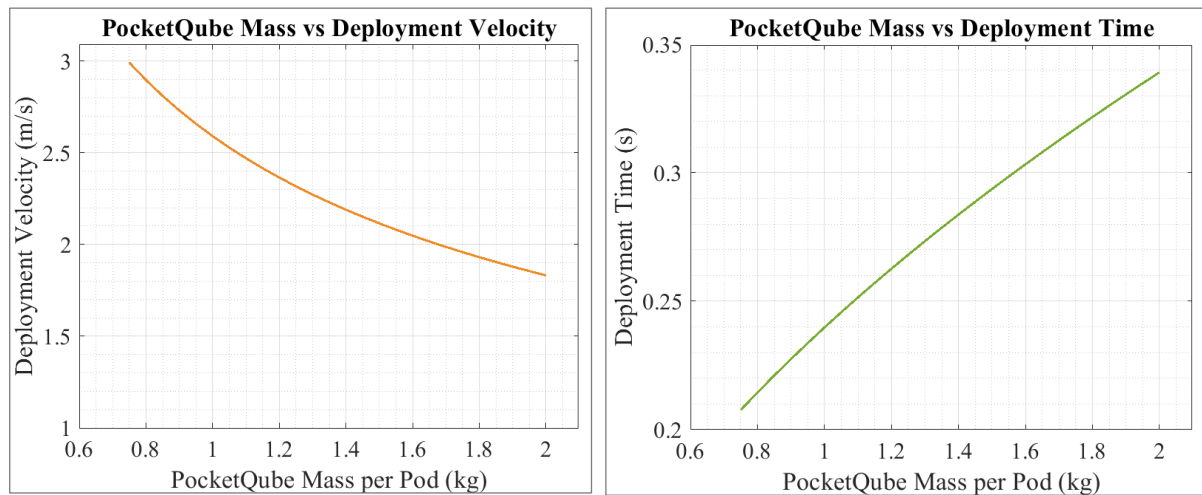


Figure 31: Deployment velocity and time variation with spacecraft mass.

For nominal spring performance, variation of deployment velocity and time with varying total PocketQube mass in pod is shown in Figure 31. Total PQ mass in pod is varied from 0.75 to 2 kg and the trendline is captured. As expected with an increase in PQ mass, deployment velocity decreases and time to deploy increases.

Further, this analysis can be extended to estimate deployment velocity when spring performance is not nominal and thus accounting for variation in spring tolerance. Deployment velocity range for varying PQ mass and spring performance is shown in Figure 32.

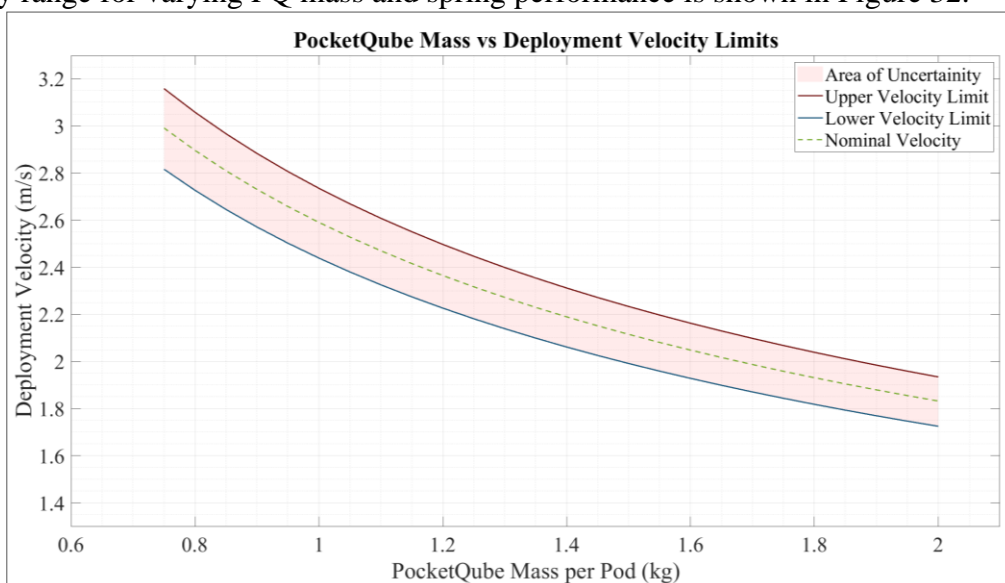


Figure 32: Deployment velocity uncertainty due to spring tolerance.

All estimations discussed above assume that the PocketQube load on main spring is constant during the spring stroke. However, once the PocketQube is completely out of the deployer pod, PQ mass on main spring decreases. The reduction in mass (load on spring) will be equal to the mass of spacecraft deployed. As different PocketQubes have different mass, the reduction in load will be based on the size of PocketQube deployed. Spacecraft size and mass information can be accessed from Section 2.2.

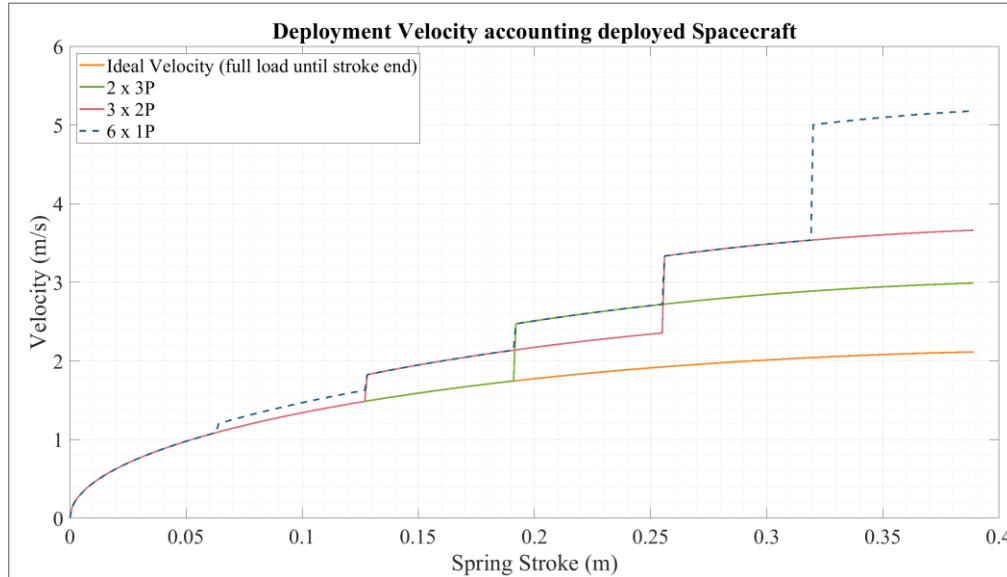


Figure 33: Deployment velocity accounting deployed spacecraft.

Spacecraft velocity imparted when considering load reduction due to deployment is shown in Figure 33. Of the 7 pod combinations shown in Figure 19, only 3 combinations are discussed here. The three combinations considered have equal size PocketQubes in pod, namely, 6x1P, 3x2P, and 2x3P. Spacecraft deployment velocities when pod is populated with PocketQubes of different sizes will be discussed in Section 6.1.

Deployment velocities based on order of PocketQubes in pod are listed in Table 43. Minimum value of spacecraft deployment velocity in Table 43 is 1.088 m/s which corresponds to the 1<sup>st</sup> PocketQube to be separated in 6 x 1P pod combination. Accounting for spring performance lower limit, deployment velocity for this PocketQube decreases to 1.046 m/s. The implication of deployment velocity on separation distance will be discussed in Section 4.8.

It is also evident from Figure 33 that the deployment velocity of PocketQube is not only dependant on size of PocketQube but also on the location of the spacecraft in pod. Detailed discussion on order of PocketQube in pod can be found in Section 6.1.

#### 4.3.5 Practical Consideration

As stated in Section 2.10, each pod of PDS will ensure a total PocketQube deployment volume of 6P units. However, due to eventualities some of the PocketQubes allotted for a given pod might be absent during final integration and a replacement spacecraft might be hard to find before PDS integration onto launch vehicle. In the given case, there would be two options for the PDS based on the type of launch vehicle used [69].

1. Consider a dummy mass replacement in place of the missing PocketQubes.
2. Consider launching remaining PocketQubes without the missing ones.

If case one is chosen, the performance of the Spring-PocketQube system would not vary, however, if case two is chosen, there would be a change in PocketQube deployment velocity. Deployment velocity changes due to the change in spring force as a result of change in main

spring compressed length (due to missing PQ). Table 17 lists the change in stroke length, deployment velocity, and time considering different numbers of PQ units are removed from pod.

*Table 17: Practical consideration for PDS.*

PocketQubes Removed (P)	Stroke Length (mm)	PQ Mass (kg)	Deployment Velocity (m/s)	Deployment Time (s)
0	390	1.5	2.1149	0.2937
1	326	1.25	1.9813	0.2631
2	262	1	1.8385	0.2292
3	198	0.75	1.6849	0.1906
4	134	0.5	1.5190	0.1449
5	70	0.25	1.3474	0.0872

Table 17 considers nominal spring performance and variation of deployment velocity with PQs removed is shown in Figure 34 considering spring tolerance.

In Figure 34 when zero P units are removed, the deployment velocity range is equal to range shown in Figure 32. The deployment velocity steadily decreases as more P units are removed as the maximum force of the main spring decreases with an increase in its compressed length. For the case when 5Ps are removed, deployment velocity does not fall below 1.15 m/s. The minimum PocketQube deployment velocity is within range of CubeSat deployment velocity shown in Table 2.

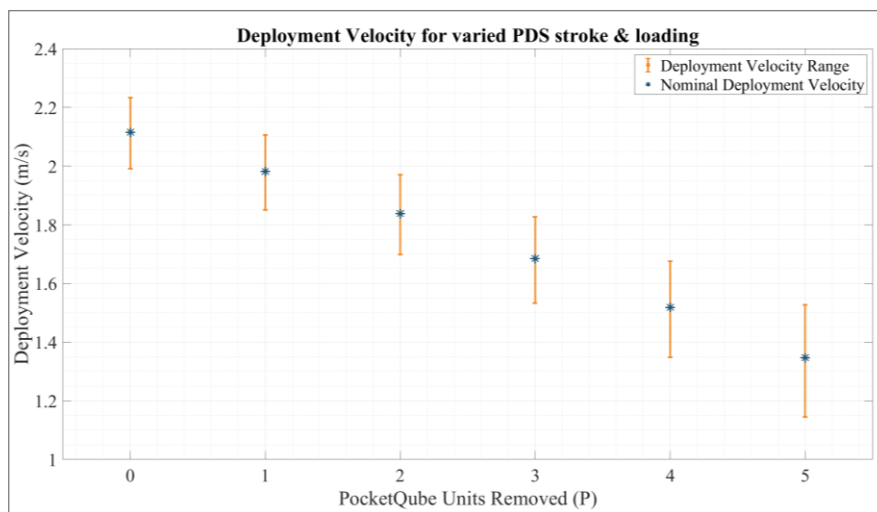


*Figure 34: Deployment velocity variation for PQs removed from pod.*

Although the deployment velocity decline is not significant enough to warrant a change in spring specification, a review is required to assess how practical it is to launch a single PQ of 1P in a pod dedicated for deploying total of 6P units.

#### 4.3.6 Friction Effect on Deployment Velocity

In all of the previous analysis of Spring-PocketQube system, friction effect between the PocketQube backplates and the deployer rails are ignored. In this section, an analysis is carried out to quantify the effect of friction between the PocketQube and PDS. As the backplates are to be manufactured with either FR-4 or aluminium alloy, for this analysis aluminium is considered as the backplate material as coefficient of friction is higher for aluminium [86], [87].

For anodized Al-6082 alloy with no lubricant, static coefficient of friction is 0.8 [88], and a maximum and average value of 0.5 and 0.79 respectively for 6061-T651 alloy [89]. For 7075 alloy, the coefficient of friction depends on the sealing solution used in the anodization process and the largest value for friction coefficient was found to be 0.8 for potassium dichromate solution [77]. Further, kinetic friction coefficient for anodized aluminium 7075-T6 alloy ranges from 0 to 0.5 [90]. Therefore for this analysis, static friction coefficient is taken to be 0.8 and kinetic friction coefficient as 0.5.

Additionally, due to engineering considerations, mainly centreline mounting error of main spring (within a radius of 5 mm), the normal force for friction is considered to be a maximum of 10% of spring force. Friction force is given by Equation (11) where  $F_\mu$  is the friction force,  $\mu$  is the coefficient of friction,  $N$  is the normal force, and  $P_\mu$  the ratio of normal force and spring force.

$$F_\mu = \mu * N = \mu * (P_\mu F_{MS}) \quad (11)$$

$P_\mu$  is varied from 1 to 10 percent and its effect on deployment velocity is analyzed. PQ mass of 1.5 kg (6P in pod), stroke length of 390 mm is considered. Figure 35 shows the influence of friction on deployment velocity and system energy for a  $P_\mu$  value of 10%. For this case, energy lost due to friction between PocketQubes and rails is around 4.9% of the total system energy and decrease in deployment velocity is negligible. Deployment velocity drops from 2.1149 to 2.006 m/s for 20%  $P_\mu$  which is double than the assumed worst case scenario.

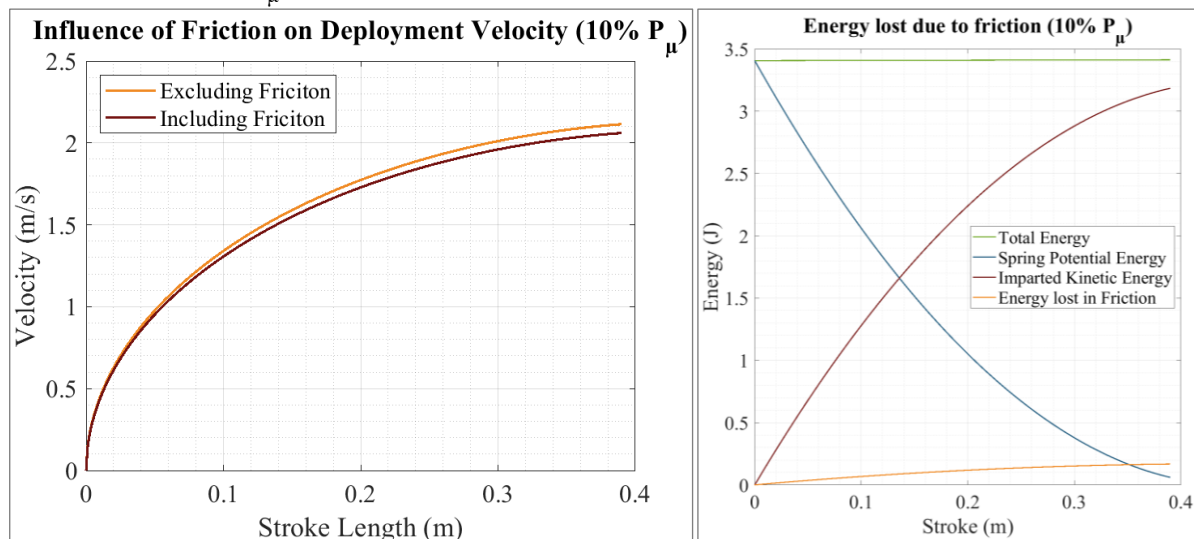


Figure 35: Deployment velocity and system energy variation accounting friction.

Further, the analysis is expanded to account for variability of PQ mass in pod. Figure 36.1 shows PocketQube deployment velocity for varying friction conditions. For better understanding of the effect of friction, Figure 36.2 is generated overlaying Figure 36.1 on Figure 32. From Figure 36.2 it is evident that the variability of spring force has a greater effect on PocketQube deployment velocity than friction effects.

It can be concluded from this analysis that even though friction adversely affects PQ deployment velocity, the absolute magnitude drop in deployment velocity is negligible and is accounted for in the deployment velocity margins taken. However, a PQ deployment test in microgravity conditions would be necessary to estimate average friction force contribution during the deployment process.

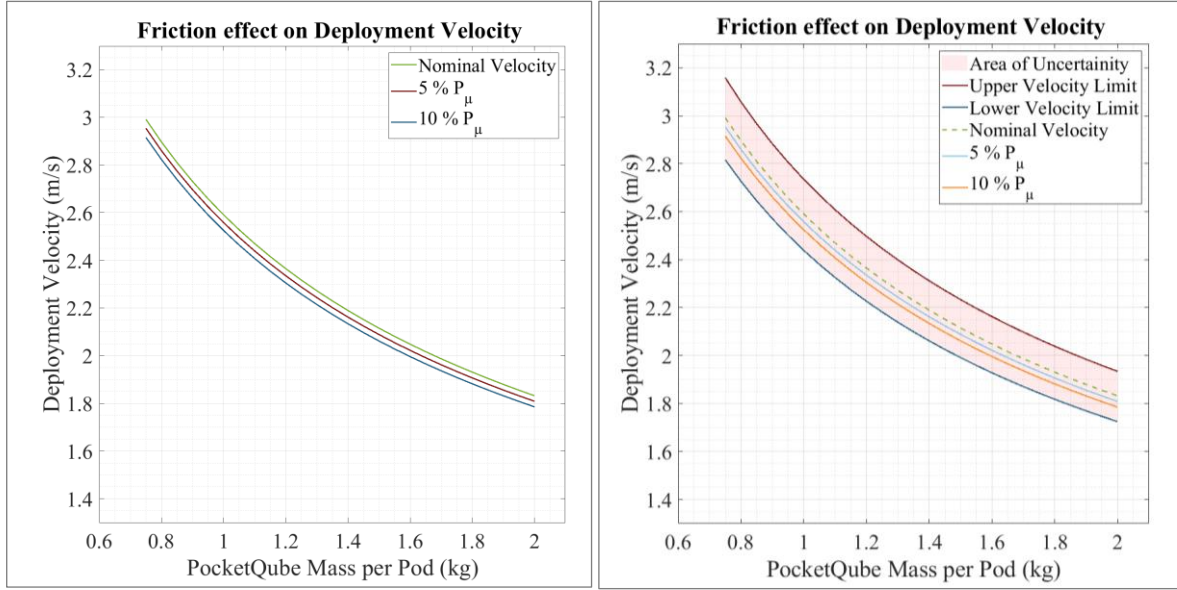


Figure 36: Effect of friction on deployment velocity.

### 4.3.7 Torsion Spring

Torsion spring is the component that provides the required force to open the PDS door. It is essential to ensure that during the deployment of PocketQubes, there is no interference between the door and the PocketQubes. The initial acceleration of the PocketQubes due to main spring in Section 4.3.4 is  $10.1 \text{ m/s}^2$ . Therefore, to avoid interference, door acceleration must be greater than  $11 \text{ m/s}^2$ . Further, for the analysis, mass of the door assembly is taken to be 90 grams based on CAD. The door is allowed to rotate to  $110^\circ$  from its locked position,  $20^\circ$  angular separation is given to ensure that there is no interference with PocketQubes.

Based on these parameters, the force needed to be exerted on the door to avoid interference is calculated using Equation (12) where,  $F_{TS}$  is torsion spring force,  $m_d$  is mass of door assembly, and  $a_d$  is linear acceleration of door.

$$F_{TS} = m_d a_d \quad (12)$$

Initial torque demanded by the door assembly is given by Equation (13) where,  $T_{TS}$  is torque provided by torsion spring,  $d_{CoM}$  is the distance between door rotation axis and door Centre of Mass (CoM).

$$T_{TS} = F_{TS} d_{CoM} \quad (13)$$

From CAD geometry in Section 4.4, door has a mass of 90 grams and distance between door rotation axis and door Centre of Mass (CoM) is 54 mm. Based on the required acceleration of door greater than  $11 \text{ m/s}^2$ , a torque value of 0.0535 Nm is to be provided by the torsion spring. A set of torsion springs are selected with their specification listed in Table 44 which apply a torque of 0.0592 Nm in stowed condition.

Relation between angular acceleration of door and torsion spring torque is given by Equation (14) where,  $\alpha_d$  is door angular acceleration,  $I_d$  is moment of inertia of door and given by Equation (15).

$$T_{TS} = I_d \alpha_d \quad (14)$$

$$I_d = m_d d_{CoM}^2 \quad (15)$$

Angular velocity imparted to the door due to the application of torsion spring torque is given by Equation (16) where,  $\omega_{di}$ ,  $\omega_{df}$  is initial and final angular velocity of door and  $\theta$  is the angular deflection of door.

$$\omega_{df}^2 = \omega_{di}^2 + 2 \alpha_d \theta \quad (16)$$

Force exerted by the torsion spring is proportional to its angular deflection from its rest position. Therefore, angular acceleration experienced by door will vary along its rotation. Similar to deployment velocity analysis in Section 4.3.4 force exerted by torsion spring is discretized along rotation of torsion spring and angular velocity is found by numerical integration using Equation (17).

$$\omega_{j+1}^2 = \omega_j^2 + 2 \alpha_j d\theta \quad (17)$$

It was found that a discretized angle ( $d\theta$ ) of  $1 \times 10^{-4}$  radians was optimal to minimize error and computation time. Having calculated the angular velocity, the time required for door actuation can be easily computed.

The model is verified by checking energy balance of the system. Potential energy of torsion spring is given by Equation (18).

$$E_p = \frac{1}{2} k_{TS} \theta^2 \quad (18)$$

Kinetic energy imparted on door assembly due to torsion spring torque is given by Equation (19).

$$E_K = \frac{1}{2} I_d \omega_d^2 \quad (19)$$

Total energy in the system is given by Equation (20).

$$E = E_K + E_p \quad (20)$$

Total energy must be invariable along the rotation of torsion spring. This is shown in Figure 37 and model is validated. It is to be noted that the spring rest position is when door is at  $90^\circ$  rotation, hence the torsion spring potential energy drops to zero beyond this position.

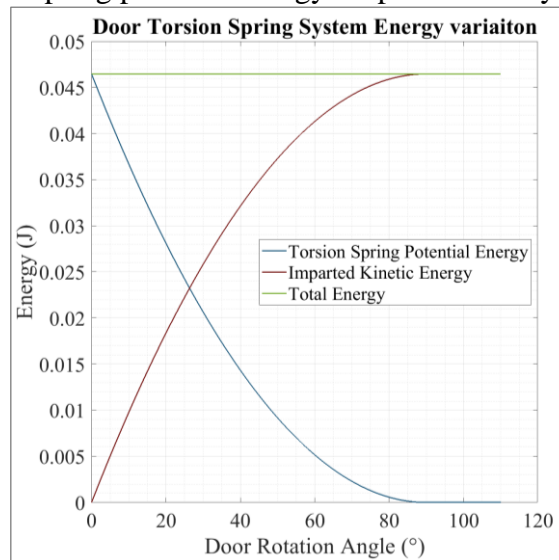


Figure 37: Torsion spring energy variation along its rotation.

Having validated the torsion spring model we can analyze the angular velocity variation with rotation angle of the door as well as the time taken for door rotation. Figure 38 shows the angular velocity and time varied with door rotation angle. It is seen in Figure 38 that the angular velocity steadily increases with the door rotation until about  $85^\circ$ , after which it remains constant. The time required for door to complete rotation of  $90^\circ$  is 0.12 seconds and for  $110^\circ$  is 0.146 seconds.

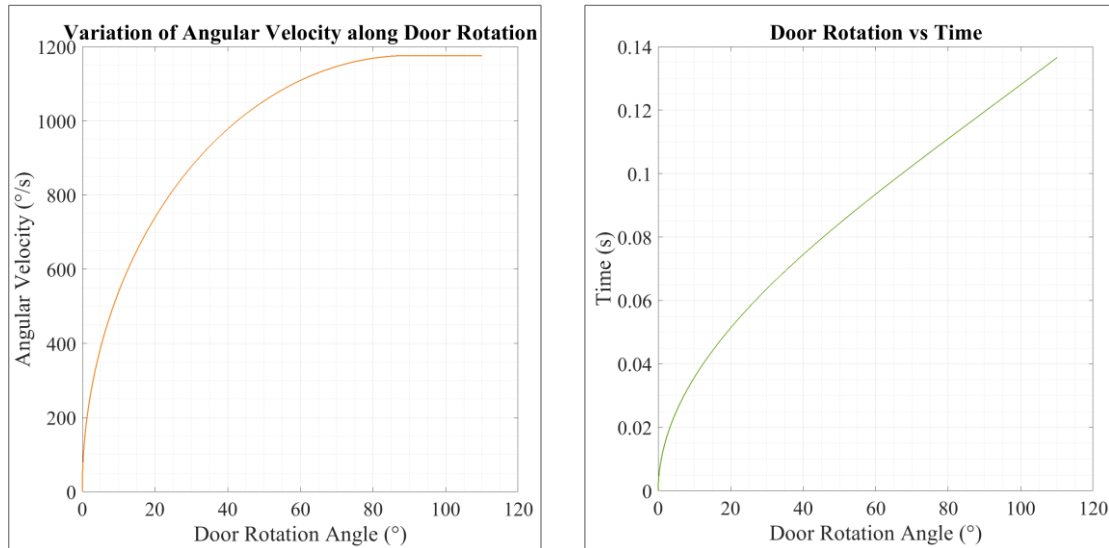


Figure 38: Door angular velocity and time variation with rotation.

Further, the analysis tool is used to quantify the door deployment time variation with door mass. For this study time required for 90° and 110° rotations are plotted against door mass in Figure 39. 90° rotation is critical because after the door rotates to 90°, there will be minimum chance of collision between door and deploying PocketQubes.

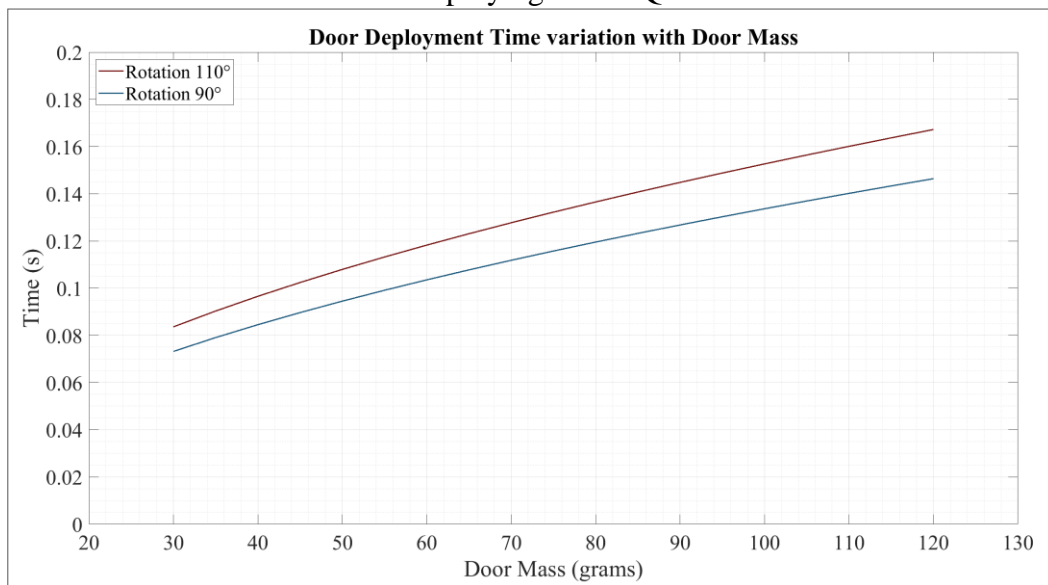


Figure 39: Door deployment time variation with its mass.

#### 4.3.8 Separation Spring

A separation spring is required to ensure separation between PocketQubes which are deployed using the same pod [91]. Separation springs would be in contact with neighbouring PocketQube backplate and be compressed once integrated into the deployment system [2]. Upon actuation of release door and ejection of spacecraft, separation springs would provide necessary force to impart separation between successive spacecraft.

Separation Spring recommended by California Polytechnique for use on CubeSats must have specifications as follows [91], [92]:

- Initial Force - 0.9 pounds (4 Newtons)
- Final Force - 0.14 pounds (0.62 Newtons)
- Spring Travel - 4 millimetres (Minimum of 2 millimetres)

- Material - Stainless Steel

Based on the above specifications, JAXA has custom developed a separation spring with part number *251D939002-1* [93].

A component manufactured by C&K switches with part number *KSU213WFLG* can be suitable as a PocketQube separation spring. Specifications of this part is given below.

- Force -  $0.7 \pm 0.5$  N
- Spring Travel -  $1.5 \pm 0.2$  mm

Similar to main compression spring as discussed in Section 4.3.4, an analysis can be conducted to evaluate performance of separation spring. Additionally, PocketQube and CubeSat separation springs are compared to verify if the selected component provides required separation velocity. By analyzing the tolerance extremities, the designer can be assured that separation spring will function satisfactorily within its window of operation.

Spacecraft mass for this analysis was considered to be 1.33 kilogram/U and 250 gram/P based on the CubeSat and PocketQube standards [92], [2]. As the standard documents require 2 separation springs per satellite, the respective force values are doubled for the analysis (no imbalance between springs). Further, as stroke length is significantly lesser than that of main spring, for numerical integration, stroke length was discretized to  $1 \times 10^{-5}$  meters to provide sufficient accuracy in predicting separation velocity. It is to be noted that CubeSat Design Specification document does not specify the requirement of a separation spring on 3U CubeSats, however, for this analysis, it is considered to employ separation springs.

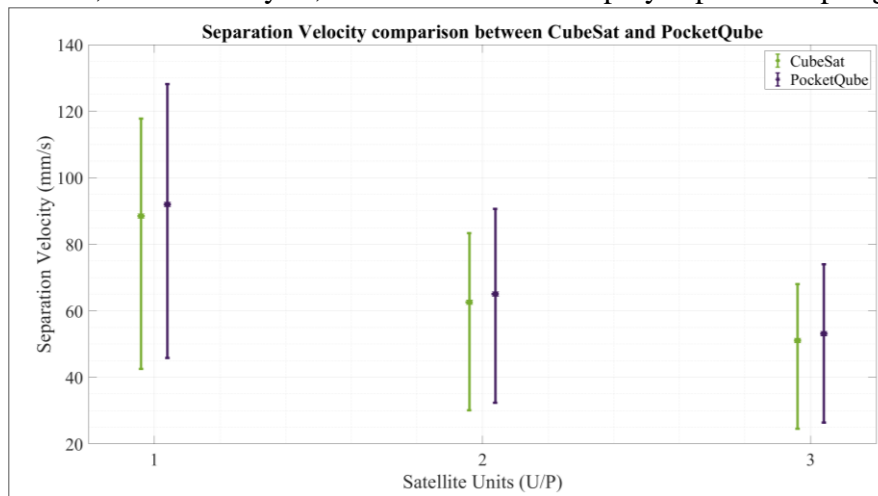


Figure 40: Separation Velocity Comparison between CubeSat and PocketQube.

The result of this analysis is shown in Figure 40, it is apparent that there is considerable overlap in separation velocity ranges of CubeSat and PocketQube. The nominal, minimum and maximum separation velocities of PocketQubes is marginally higher than respective CubeSats. Therefore, it can be concluded that performance of the selected separation spring with part number *KSU213WFLG* is satisfactory and use of this spring can be authorized with confidence.

Having seen the various characteristics of springs required by the PocketQube Deployment System, following sections are dedicated to mechanical design of parts and assemblies for the PDS.



## 4.4 Door Assembly

Door assembly plays a vital role within the PocketQube Deployment System. The role of this assembly is to ensure that PocketQubes are enclosed within the pod during launch phase of a mission. Once in orbit, the door assembly would be actuated from stowed to deployed position using pin puller. Deployment of the door assembly will set the PocketQubes in motion due to main spring action.

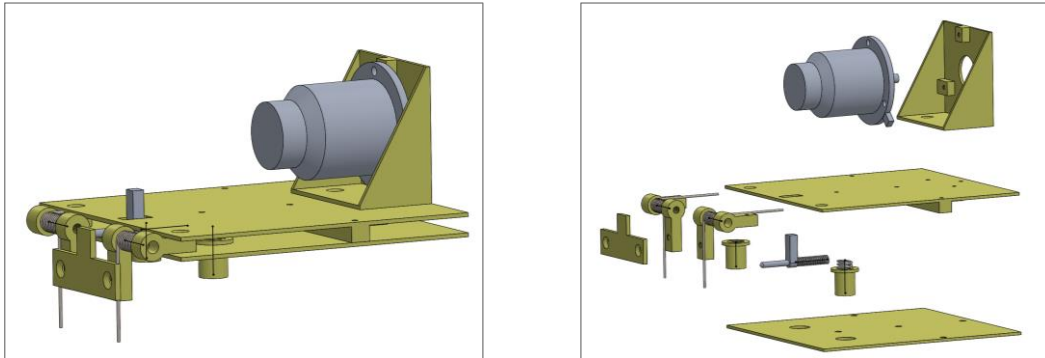


Figure 41: Door assembly with exploded view.

Components of door assembly are shown in Figure 41 with stowed and deployed views in Figure 42. Mass of the assembly was about 90 grams, with its centre of mass at a distance of 54 mm from torsion spring rotation axis. Design consideration for the different parts comprising the door assembly are discussed in detail below.

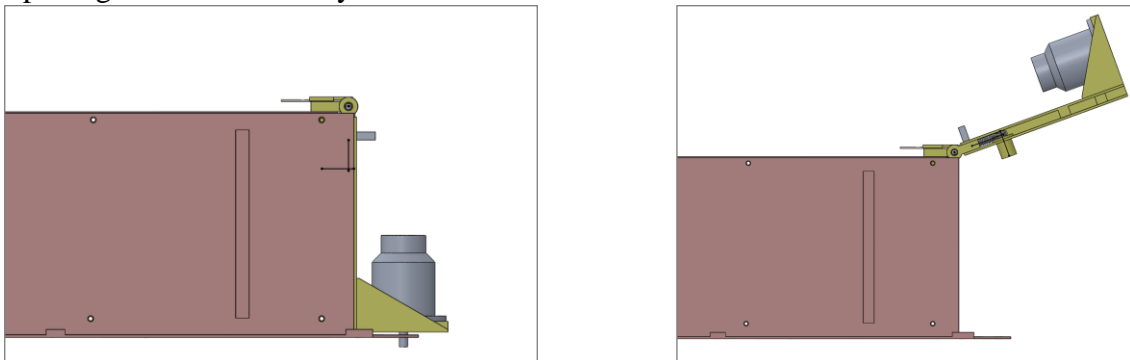


Figure 42: Door assembly in stowed and deployed conditions.

**Door Top and Bottom:** Door Top is the main component of the door assembly. It is to this part that hinge 1, door bracket, and door retainer mechanism are mounted along with the bottom door. Its length along Y axis is 80 mm and X axis is 70 mm (single pod). Ribs required for door stiffness were placed on this part as Pin Puller mass is mounted on it through the door bracket.

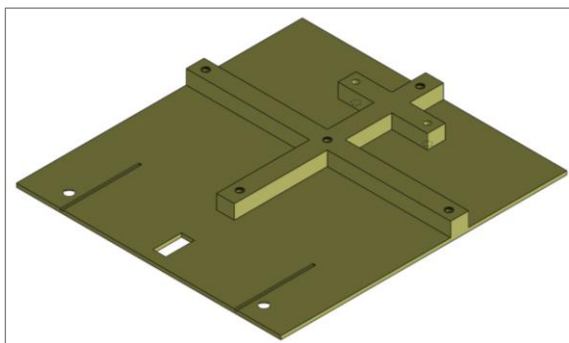


Figure 43: Door Top.

Figure 43 shows isometric view of door top showing the ribs. Two slots are placed for the torsion spring legs and a cut-out is provided for door retainer pin translation. For the first iteration only one rib running along Y axis of PDS was used with 2 fasteners joining it to door bottom. However upon analyzing modal interactions, the rib running along X axis was added and number of fasteners was increased to 5. The rib is 5 mm wide and 4 mm in height.

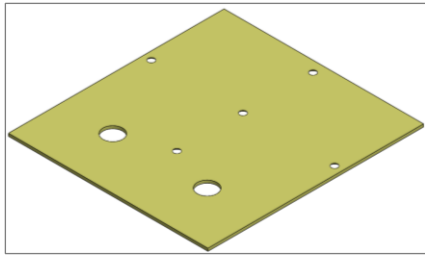


Figure 44: Door Bottom.

Door Bottom part has its dimensions equal to door top. It has countersunk holes for the 5 fasteners and 2 cut-outs for push back mechanism. Door bottom is shown in Figure 44.

**Door Bracket:** It is the part on which Pin Puller is mounted on. This part itself is mounted onto Door Top using 2 fasteners.

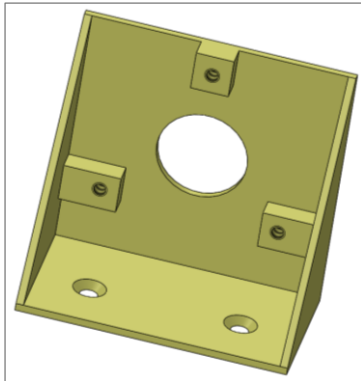
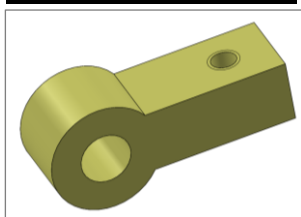


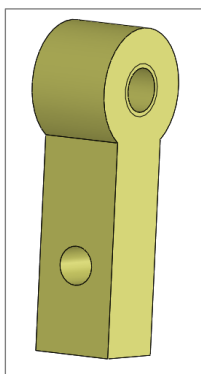
Figure 45: Door Bracket.

Pin puller is mounted in the orientation as shown in Figure 41 (Pin axis parallel to Y axis). If Pin Puller is mounted in such a way that pin is parallel to Z axis, the pod dimension along Y axis has to be increased by 16.5 mm to accommodate for PocketQube appendage volume. That would be undesirable as it will increase the mass by needing additional structural stiffening elements. Hence, door bracket is designed to mount the Pin Puller. Three boss of height 3 mm are given for Pin Puller mounting fastener threads.

**Hinge 1 and Hinge 2:**



Hinge 1 and 2 are shown in Figure 46. Hinge 1 attaches to door top on one end and on the other has a M3 clearance hole for accommodating a fastener which doubles as torsion spring spindle. This fastener attaches hinge 1 to hinge 2.



Hinge 2 has threaded interface to accommodate the M3 spindle attaching to both hinges. It attaches to PDS structure on the other end. Door retainer is attached to hinge 2.

Figure 46: Hinge 1 and 2.

**4.4.1 Door Retainer Mechanism**

Having seen the basic components and their functions for the door assembly, we discuss the design of specialized mechanisms and their functions. The function of the door retainer mechanism is to restrict any rebound motion once the door has reached its deployed position. This bounce back motion has to be restricted to avoid collision of door with PocketQubes exiting the pod. The components of this mechanism include door retainer plate, retainer pin, and a retainer spring.

### **Door Retainer Plate:**

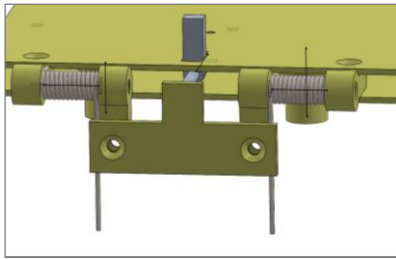


Figure 47: Door retainer plate.

Door retainer plate has two functions. One function of this plate is to act as an anchor for the two torsion springs used to provide necessary energy for door deployment. The other function is to provide the necessary gap between itself and PDS structure to allow the door retainer pin to slot into position and restrict the bounce back of door assembly.

**Door Retainer Pin:** It is the critical component that ensures the door assembly once completely actuated, does not rotate back towards the pod. This ensures the door assembly locking in place after complete actuation. End of the retainer pin is chamfered to allow for easy rotation of the door during deployment.

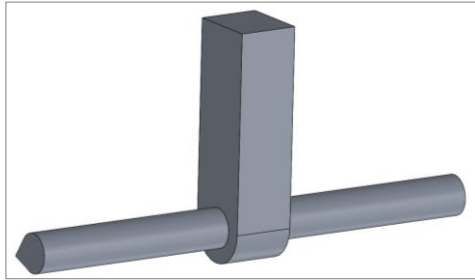


Figure 48: Door Retainer Pin.

The top is extended for ease of access during assembly of door and locking of door assembly to PDS structure. The retainer pin is spring loaded, and the spring will be extended during the door deployment sequence allowing the door assembly to lock in place.

The diameter of retainer pin is calculated taking into account stress expected to develop during said actuation. In order to calculate the stress on retainer pin, we need to calculate the door stopping force. Stopping force is given by Equation (21) where,  $F_S$  is the stopping force,  $d_S$  the stopping distance, and  $E_K$  kinetic energy imparted to door.

$$F_S = \frac{E_K}{d_S} \quad (21)$$

Energy imparted to door at end of rotation from Figure 37 is equal to 0.0467 J. Stopping distance is assumed to be 0.1 mm. As the impact is parallel to cross-sectional area of retainer pin, impact results in shear stress within the member. For a pin diameter of 2 mm the stress developed in retainer pin due to impact will be equal to 148.6 MPa.

Shear yield strength considering Von-Misses criterion is given by Equation (22) where,  $\tau_y$  and  $\sigma_y$  are the shear yield and tensile yield strength of material.

$$\tau_y = 0.577 \sigma_y \quad (22)$$

Considering Von-Misses criterion for shear failure, impact stress is well below shear yield strength for aluminium 7075 alloy. Hence retainer pin is to be manufactured using 7075 aluminium alloy.

**Door Retainer Spring:** This spring is attached to the door retainer pin. It provides the necessary force for the displacement of the door retainer pin during the door actuation. The spring is attached to the rib on door top at one end and the retainer pin on the other. The specifications for the door retainer spring is provided in Table 45.

### **4.4.2 Push Back Mechanism**

The function of the push back mechanism is to provide a counteracting force to restrict the movement of PocketQubes within the rail. In order to ensure PocketQubes are accommodated within the pod dimensions, clearance is provided in Z direction along rail. Description of this clearance is discussed in Section 4.6.1.

There is a possibility of oscillation of the main spring-PocketQube(s) system when the spacecraft are enclosed within the pod. This oscillation will be amplified if the launch vehicle loading will coincide with PQ Z axis. The spring mass system oscillation has to be avoided for two main reasons. Oscillating mass can amplify the launch vehicle loads which can cause additional structural loading, leading to increased chance of system failure. Oscillation can lead to wear of PocketQube backplate due to frictional forces arising from contact with guide rail. Wear would not be a concern for PocketQubes with metal backplates. However, for PocketQubes which utilise FR-4 backplate, delamination due to friction wear is a concern which needs further addressing.

Push back mechanism comprises of two elements i.e., a push back spring and a push back holder.

**Push Back Spring:** The specification for the push back spring is described in Table 46. By ensuring that the force balance is greater on the push back mechanism (compared to main spring) designer can ensure that the oscillation will be negligible if any.

Force is transferred from push back spring to PocketQube backplate by push back holder. Push back holder has a length of 7.5 mm measured from the door bottom and can compress by 3 mm due to push back spring stroke. Two numbers of push back spring and holders are present in the door assembly. The 3 mm clearance would provide the required clearance if PocketQube backplate dimensions exceed 384 mm (6P) in Z direction.

The next section of this study details the design of pusher plate mechanism.

## 4.5 Pusher Plate Assembly

Pusher plate assembly is an important subsystem of the PDS. The assembly has three main functions.

1. Transfer force exerted by the main spring onto PocketQube through its backplate.
2. Reduce friction between itself and guide mechanism to ensure minimum frictional loss during PocketQube deployment.
3. Withstand quasi-static forces as a result of launch vehicle acceleration in Z direction (PDS coordinate system) and PocketQube mass in pod.

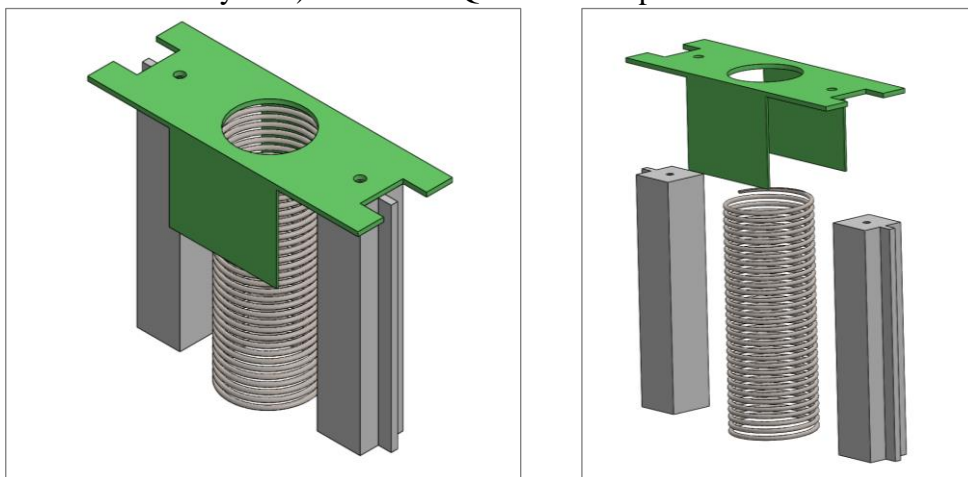


*Figure 49: Pusher plate assembly with exploded view.*

Apart from these main functions, pusher plate assembly has an additional function as a locking mechanism for the main spring during system integration and ground operations. This locking mechanism is incorporated to avoid unintentional extension of spring. Two RBF screws will

be placed on the pusher plate assembly to act as spring hold down mechanism. Details of this feature is discussed in Section 6.4.

Pusher plate assembly is shown in Figure 49. The design of individual parts of the pusher plate assembly is discussed in further sections.

#### 4.5.1 Pusher Plate

Pusher plate is the part that will be in contact with the PocketQube backplate. Pusher plate provides a flat surface on which the deployment force from main spring is transferred to PocketQubes. As pusher plate would be in contact with the PocketQube backplate, material chosen for it was aluminium alloy to prevent cold fusion (**PDS-GEN-001**).



*Figure 50: Pusher Plate.*

Pusher plate is shown in Figure 50. The circular cut-out on the pusher plate is provided to reduce mass. It was expected that the membrane stresses to be minimum at the location of cut-out. Results for which are shown in Figure 53. Skirts were added on two sides in order to restrict any lateral (Y direction) movement of the main spring. During deployment it is important to restrict lateral movement of spring on pusher plate end as it could result in change of deployment force vector.

A change in deployment force vector in lateral direction is not desirable due to its negative impact on deployment velocity of PocketQubes and increased chance of spacecraft jamming.

#### 4.5.2 Pusher Plate Guide

Pusher plate assembly must ensure minimum frictional losses during PocketQube deployment. Pusher plate guide is the part that will be in contact with the internal faces of PDS guide mechanism. It is crucial to reduce the friction between sliding surfaces and hence the material chosen for the pusher plate guide is important (**PDS-GEN-001**). In Section 4.3.6 it was seen that friction coefficient for aluminium on itself is 0.8. High coefficient of friction can lead to greater frictional losses during the deployment process. This condition is of course undesirable.

A possible alternative is to use a lubricant on the sliding surfaces which are in contact. Molybdenum Disulphide ( $\text{MoS}_2$ ) coatings have been used in spacecraft to lubricate surfaces in contact since 1960's [94]. However,  $\text{MoS}_2$  coatings degrade upon contact with water vapour [95]. As a result, during system integration, special care needs to be taken when  $\text{MoS}_2$  coatings are used and further, hermetically sealed containers are needed for transport and ground handling operations. Additionally, at low orbital altitudes,  $\text{MoS}_2$  can oxidize to Molybdenum Trioxide ( $\text{MoO}_3$ ) when exposed to atmospheric atomic oxygen.  $\text{MoO}_3$  has higher coefficient of friction and is therefore an inferior lubricant compared to  $\text{MoS}_2$  [96].

Recently, composite coatings with made of Keronite and  $\text{MoS}_2$  is deposited using plasma electrolytic oxidation method [97]. This surface coating has been developed for use in cryogenic plain sliding bearings. Keronite and  $\text{MoS}_2$  composite coating offers low sliding friction coefficient, maximum resistance to wear, minimum debris generation, vacuum compatibility, thermal shock resistance, and thermal conductivity [98]. Using this method the static coefficient of friction can be reduced to as low as 0.04 [99].

Having seen the surface coatings available for metals to reduce friction at sliding contacts, it is relevant to discuss non-metallic materials that exhibit low frictional characteristics with aluminium. One material that qualifies is a polyimide called Vespel. Vespel has low wear rate

and low coefficient of friction in vacuum and moisture-free environments. It has low outgassing properties under vacuum and at high temperatures conditions which is critical for polymers. It has been demonstrated as a successful non-metallic interface material against aluminium in the design of the electric propulsion pointing hold down and release mechanism of Bepi-Colombo spacecraft [100].

With the different methods to reduce friction coefficient between sliding surfaces discussed, it is important to choose a suitable method for the pusher plate guide. Due the degradability and handling constraints with MoS<sub>2</sub>, it was chosen that the pusher plate guide will be manufactured from Vespel.

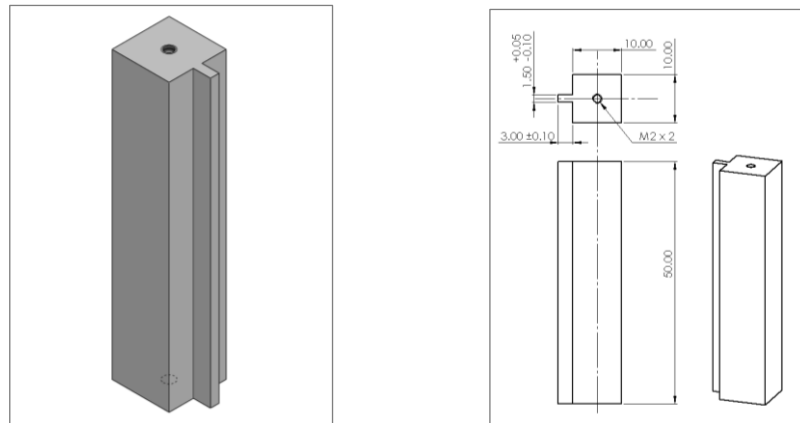


Figure 51: Pusher plate guide with dimensional tolerance.

Pusher plate guide is shown in Figure 51 including its dimensioning. The pusher plate guide has threads on its bottom surface which act as the locking mechanism for main spring during integration and ground operations. This feature is discussed in detail in Section 6.4.

#### 4.5.3 Pusher Plate Stopper

A stopping mechanism is required for the pusher plate assembly to ensure the assembly is held within the pod. It is necessary to meet launch vehicle requirement (**PDS-LVR-004**) and also avoid space debris which is projected to become a major problem in near earth environment. Current estimate for debris of dimension of a few centimetres are several hundred thousand and it is not in our interest to further increase this number [101].

Pusher plate stopper design has to ensure that it does not interfere with the deploying PocketQubes, while also ensuring that the pusher plate assembly does not move out of the bounds of PDS. Additionally, a deployment indicator is envisioned to be placed on the pusher plate stopper as it would provide PocketQube deployment status for the pod.

$$E_{PP} = \frac{1}{2} m_{PP} v^2 \quad (23)$$

From Figure 33, maximum velocity imparted to the pusher plate assembly will be 5.2 m/s. For this velocity considering mass of moving components of pusher plate assembly as 30 grams, energy imparted to this system is given by Equation (23) where  $m_{pp}$  is the mass of pusher plate assembly. Force of impact is calculated using Equation (21) assuming a stopping distance of 0.1 mm.

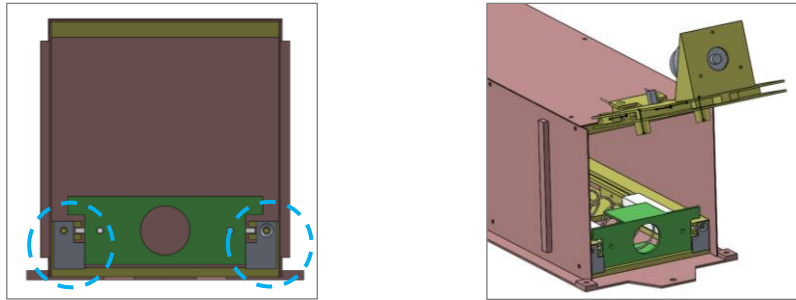


Figure 52: Pusher plate stopping mechanism.

Although the impact force is distributed between the two surfaces of the pusher plate stoppers, for dimensioning of member it is assumed all of the force acts on a single stopper. Based on this condition, impact stress is calculated in the member and for a thickness of 1 mm. Stress induced in member due to pusher plate impact was well below yield strength of the material.

Pusher plate stopper is shown in Figure 52 attached to the guide mechanism. Having discussed the design of pusher plate assembly, discussion on the load analysis of assembly is followed.

#### 4.5.4 Pusher Plate Load Analysis

In this section, an analysis is performed on the pusher plate assembly to arrive at a suitable pusher plate thickness. The assembly was fixed at lower end of pusher plate guide and input load for this study was 239 N normal of pusher plate (-Y direction in Figure 53). 239 N was arrived at factoring in PQ mass per pod (1.5 kg), launch vehicle acceleration and FOS.

Mesh was refined at fastener interface of pusher plate guide on the pusher plate and along the face of the cut out on pusher plate. The results of load analysis on pusher plate assembly is shown in Figure 53. A circular cut-out was provided on pusher plate as a mass saving measure because it was estimated that region of pusher plate would not encounter high member stresses.

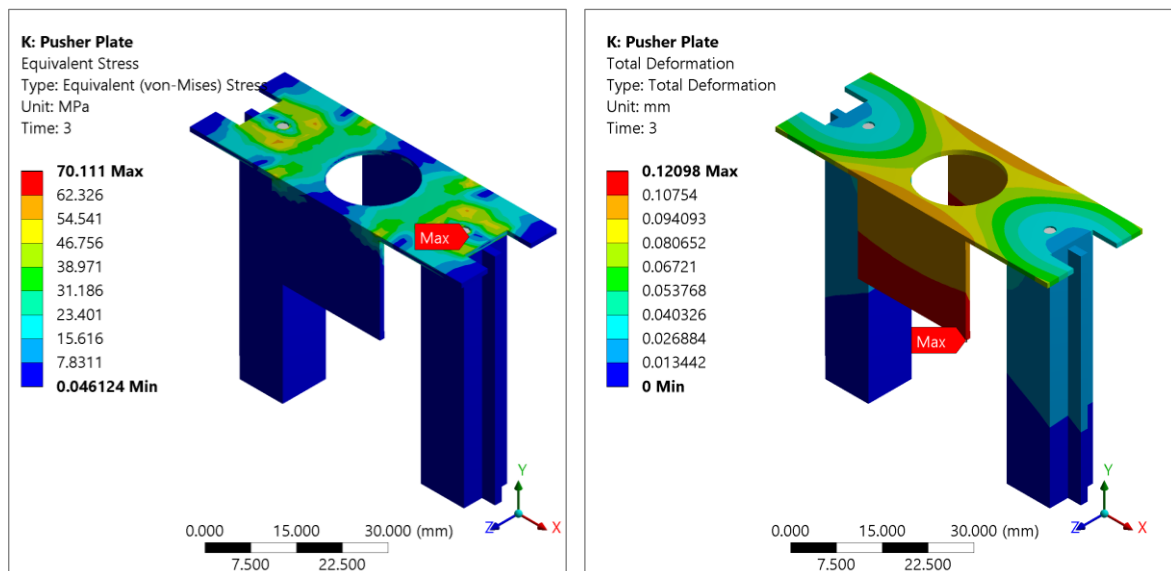


Figure 53: Pusher plate load analysis.

At first, pusher plate thickness was set to 0.5 mm for the analysis. For 0.5 mm thickness, deformation observed was 0.479 mm and stress at the interface was recorded to be 250.56 MPa. As stress induced in the member was close to yield strength of aluminium 6061 alloy, it was decided to increase the thickness of pusher plate to 1 mm. Stress results for 1 mm thickness was still close to yield strength, and thickness was increased to 1.5 mm. The results for 1.5 mm

thickness of pusher plate is shown in Figure 53, with a maximum induced stress at 70 MPa and deformation of 0.12 mm at the flange. Thickness increase of 1 mm added a mass of 1.5 grams and the circular cut out saved 0.5 grams on the pusher plate assembly.

Load analysis discussion on PDS pusher plate assembly is concluded. Design of other elements of PDS is discussed further.

## 4.6 Guide Mechanism

Guide mechanism is the part that will enclose the PQ sliding backplate. It has two main functions.

1. During launch phase of the mission, it shall be the load bearing member for PocketQubes housed within the pod.
2. During deployment phase of the mission, it shall act as the guiding member for PocketQubes to ensure smooth spacecraft deployment.

In this section, emphasis is placed on the design dimensioning of guide mechanism slot (guide rail) that houses the PocketQube backplate. The structural design for the guide mechanism as a load bearing member is discussed in Chapter 5.

### 4.6.1 Dimensioning Consideration

Dimensioning of guide rail is critical for the performance of PDS. Higher clearance between the PocketQube backplate and guide rail will allow for easier deployment of PQs. High clearance has a negative effect on the tumbling rates of the deployed spacecraft. On the other hand if tolerance is low, spacecraft rates would be lower than the high tolerance case, however, the chance of jamming of PQ backplate with guide rail increases. Backplate jamming has to be avoided at all costs as it would be detrimental to the PocketQube deploying process. Therefore, a clearance fit is envisioned for the PQ backplate-guide rail sliding mechanism.

A study on the influence of guide rail tolerance on spacecraft ejection rates has been conducted for CubeSat deployment. This analysis assumes successive elastic collisions between CubeSat and guide rail during deployment process and iteratively solves equations of motion to estimate deployment rates. However, computational load for conducting such an analysis is extremely high [102]. It is out of scope for this thesis to analyze PocketQube deployment rate dependence on guide rail tolerance.

Typically, materials change their dimensions with variation in temperature. For CubeSat deployer having a pod length of 300 mm, considering aluminium expansion rate for  $\pm 80$  °C, it was found that a tolerance between guide rails and spacecraft to be 0.5 mm on both axis. This value is the minimum gap required between the spacecraft and guide rail in order to prevent spacecraft jamming over the deployer working temperature range [103].

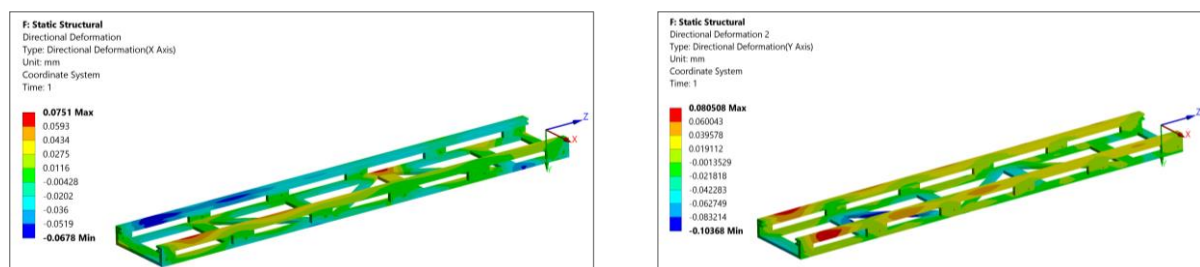


Figure 54: Guide mechanism deformation at -40 °C.



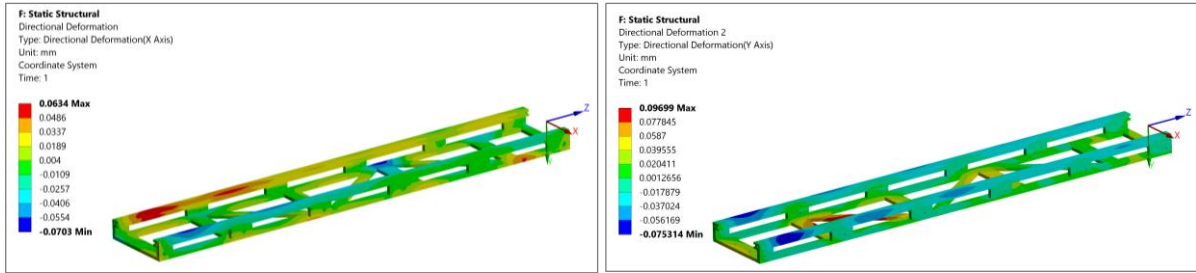


Figure 55: Guide mechanism deformation at +80 °C.

An analysis is conducted for determining the effect of thermal deformation on guide rail tolerance over the working temperature of PDS (**PDS-GEN-002**). This analysis is conducted on version 2 of lateral configuration of a single pod PDS. The reasoning for dimensional tolerancing analysis having been conducted on this model was that guide mechanism deformation is dependent on the shape of part. This version of guide mechanism was the final version and therefore most dimensions of guide mechanism were fixed at this stage of design.

Table 18: Thermal deformation at guide rail surface.

Temperature (°C)	Directional Deformation (mm)								
	X			Y			Z		
	Min	Max	Total	Min	Max	Total	Min	Max	Total
- 40	-0.0634	0.0622	0.1256	-0.0190	0.0619	0.0809	-0.017	0.0788	0.0964
80	-0.0582	0.0593	0.1175	-0.0579	0.0177	0.0757	-0.0737	0.0164	0.0901

Dimensional variation due to thermal effects on the guide mechanism is shown in Figure 54 and Figure 55. Table 18 enlists the directional deformation at guide rail due to temperature variation.

A moment arm is present between the deployment force vector and PQ CoM (due to PQ standard) along Y axis, however, along X axis the force vector is parallel to PQ CoM (assuming no main spring mounting error). Due to the presence of moment arm along Y axis, there will be an inherent tendency of PQ to rotate along Y axis. In order to minimise the angular velocity along Y axis, a stricter tolerance between the guide rail and PQ backplate is adopted in guide rail design. Table 18 shows that guide rail deformation due to temperature variation is higher along X axis compared to that of Y axis. Hence, a tighter tolerance along Y axis would not increase chances of PQ rail jamming.

Based on CubeSat deployer experience and engineering intuition, tolerance of guide rail is fixed. Dimensioning of guide rail in Y direction is  $2.2 +0.1/-0$  mm and in X axis is  $59 \pm 0.1$  mm. This will allow for a minimum clearance of 0.6 mm in Y direction and 0.8 mm in X direction. The minimum clearance in X and Y directions is sufficient assuming the PQ backplate deforms same amount as described in Table 18 but in the opposite direction.

Table 19: Guide Rail and PQ backplate clearance.

Clearance (mm)	X Axis		Y Axis	
	Min	Max	Min	Max
	0.8	1.2	0.5	0.8

The minimum and maximum dimensional clearance between the PQ backplates and guide rail are listed in Table 19. Having discussed the guide rail interface dimensioning, we determine the length of the guide mechanism required for its operation.

For dimensioning of guide mechanism in Z direction few other dimensions of parts need to be considered. The compressed length of main spring would be 50 mm, pusher plate thickness 1.5 mm, PQ backplate (6P) 384 mm, and push back mechanism on door assembly 7.5 mm. All the member dimensions have been discussed in detail in previous sections of this chapter. Further, thickness of pusher plate stopper was 1 mm and a clearance of 1 mm is provided for door assembly. Based on all these considerations, guide mechanism length of 441 mm was arrived at.

Having discussed guide rail dimensioning considerations, following section focuses on pod dimensioning.

## 4.7 Pod Dimensions

Pod dimensioning is an important factor to consider before the design of components and structural elements. PocketQube Standard states that a maximum envelope available for deployables is 7 mm normal to  $\pm X$  and  $\pm Y$  faces (*'PQ-Mech-08'*) [2]. It is necessary for PDS to meet this requirement to satisfy **PDS-PQS-001**.

However, in view of providing additional appendage volume for PocketQubes, a design choice was made to increase the limit to 10 mm on all 4 faces. The reasoning for this decision considers the fact that for PQs with high on orbit power requirements, additional solar panels can be accommodated in the volume provided. As on orbit utilization for PocketQube class of spacecraft increases, payload variety will increase. It is this trend that PDS wants to satisfy by having additional deployable volume. Additionally, it also provides increased flexibility for PQ developers. Appendage area for PocketQubes is shown in Figure 56.

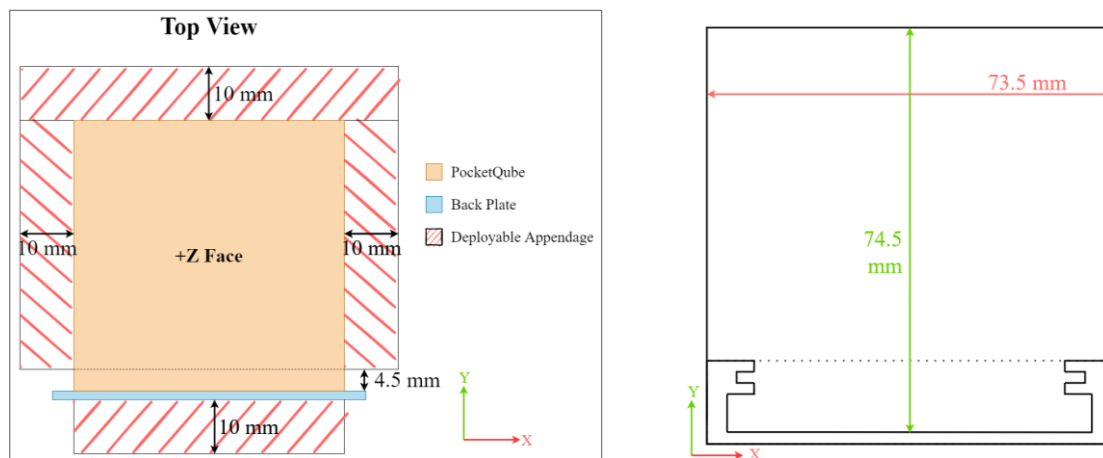


Figure 56: PocketQube allowable appendage in X & Y directions with pod internal dimensions.

Based on the appendage area described in Figure 56, pod internal dimensions in X and Y directions are arrived at. Additionally, for PDS panels on  $\pm X$  and  $\pm Y$  faces, maximum permissible deflection is taken to 1 mm normal to the face. This condition of 1 mm panel deformation will be addressed in Section 5.5. Further, to account for clearance between PocketQube backplate and guide mechanism, 1.2 mm and 0.8 mm are added to pod dimensions in X and Y directions respectively (refer Table 19). Based on these conditions, pod internal dimensions are 73.5 mm in X direction and 74.5 mm in Y direction.

Stay off area is recommended on  $\pm X$  faces of 4.5 mm from PQ backplate towards +Y face (refer Figure 56). This stay off area is present to avoid interference between appendage volume

and guide mechanism structure. Separation distance between PocketQube and launch vehicle is discussed in the next section.

## 4.8 PocketQube Separation Distance

This section is dedicated to the discussion on factors influencing the separation distance of deployed PocketQubes. Separation distance of PocketQubes is dependent on the deployment velocity of spacecraft from pod. Detailed discussion on spacecraft deployment velocity was carried out in Section 4.3.4. In Section 4.3.4, the lowest magnitude of spacecraft deployment velocity was estimated to be 1 m/s, when the first PQ in 6 x 1P configuration is deployed.

This section is dedicated to estimating the range between launch vehicle upper stage and the deployed spacecraft. It is critical to evaluate the separation distance between launch vehicle and satellites to ensure collision is avoided. In order to estimate the separation distance between spacecraft and launch vehicle, orbits of both bodies are propagated post spacecraft deployment and relative distance is estimated by comparing the positions of the bodies.

The following assumptions are made for object orbit propagation:

1. Earth centred gravity model without higher order perturbations was considered for orbit propagation.
2. Velocity change of launch vehicle due to spacecraft deployment is negligible (Launch vehicle mass much greater than deployed spacecraft).
3. Gravitational interaction between spacecraft and launch vehicle is negligible (Earth mass much greater than launch vehicle and spacecraft mass combined).

The deployment velocity vector is a factor of not only the mounting orientation of PDS with launch vehicle but also of launch vehicle attitude during spacecraft deployment. As the attitude of launch vehicle is unknown, for this study, deployment velocity orientation with respect to orbital velocity is considered. The separation distance will depend on the relative orientation of orbital and deployment velocity vectors.

To determine the dependency of separation distance with orientation of deployment velocity vector, 4 possible orientations are analyzed. They are deployment velocity parallel to:

1. Orbital velocity.
2. Orbital radius.
3. Orbital angular momentum.
4. 45° from orbital angular momentum and orbital radius.

Further, two orbits were chosen to analyze the variation of separation distance with orientation of deployment velocity vector. The orbits chosen were circular low earth orbit (LEO) at a height of 500 km, and geostationary transfer orbit (GTO) with perigee height at 200 km. Both orbits were considered at 0° inclination as separation distance is only a factor of relative distance between spacecraft and launch vehicle and not on orientation of orbit or location of objects in a certain orbit.

Circular LEO at 500 km was chosen for its popularity in rideshare missions of earth observation spacecraft (primary payload) [11]. In order to analyze the effect of eccentricity on separation distance, GTO was chosen. Perigee and orbit inclination of GTO depend on the launch vehicle and launch site respectively, however for this study, GTO inclination is assumed to be 0° and perigee height at 200 km.

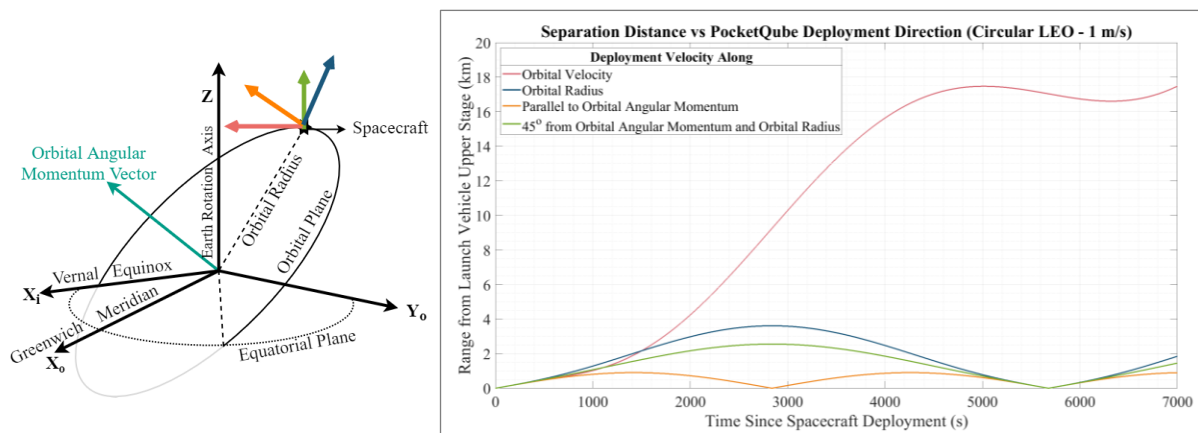


Figure 57: Separation distance for different deployment directions (with illustration).

Separation distance between launch vehicle and deployed spacecraft for different deployment velocity vector orientations in LEO are shown in Figure 57. In Figure 57, magnitude of deployment velocity does not vary for the different orientations and is equal to 1 m/s based on minimum value estimated in Section 4.3.4.

Separation distance between launch vehicle and spacecraft is highest when the deployment and orbital velocity vectors coincide. Separation distance is lowest when the deployment velocity and orbital angular momentum vectors coincide and occurs close to half the orbital period after spacecraft separation. When deployment velocity is radial to orbit, minimum separation distance occurs about one orbital period after spacecraft deployment.

The location of minimum value of separation distance is similar for both LEO and GTO and is listed in Table 47. It was also observed that the minimum separation distance increases steadily after each orbit. This is to be expected as the impulse provided to the spacecraft by PDS results in change to its orbital elements.

However, right after separation of spacecraft from launch vehicle, the range between deployed spacecraft and launch vehicle is independent of the orientation of deployment velocity. In Figure 57, it is observed that the range between deployed spacecraft and launch vehicle increased linearly below 500 seconds (8 minutes) after deployment. The linear region was observed to be about 300 seconds (5 minutes) for deployment in GTO.

Based on above observation, the distance between launch vehicle and spacecraft can be approximated as the product of deployment velocity and time since deployment. This approximation is true for both the orbits and all considered deployment orientations when time since deployment is not greater than 5 minutes.

Additionally, it is important to note that the separation distance would also be a factor of the magnitude of deployment velocity. Figure 57 considers a conservative magnitude of deployment velocity. Variation of separation distance with magnitude of deployment velocity is shown in Figure 58. The values considered for magnitude of deployment velocity for different spacecraft will be discussed in Section 6.1.

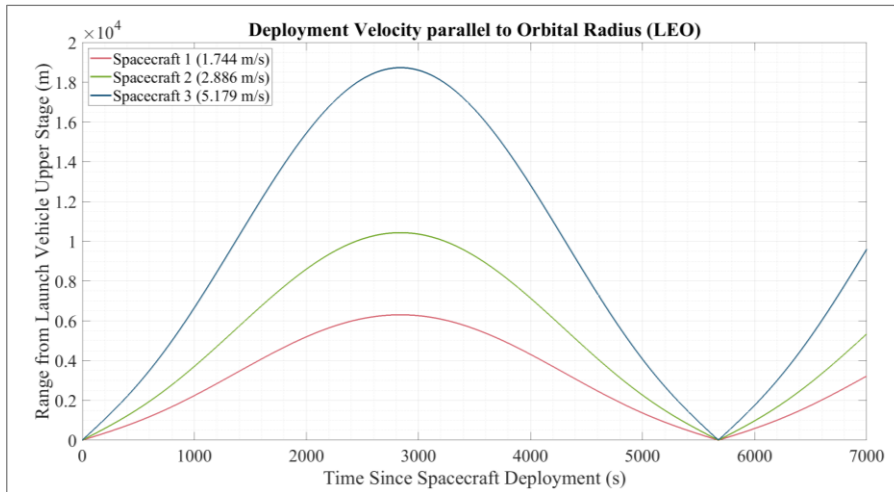


Figure 58: Separation distance variation with magnitude of deployment velocity.

Figure 58 assumes all PocketQubes are deployed at the same time. This assumption is not true as there would be time delay between PocketQube deployments from the same pod which is insignificant for this analysis.

Following sections discuss the structural configuration of single and multiple pod PocketQube Deployment System.

## 4.9 Single Pod System Configuration

Having discussed the design of various component systems of the PDS, this section details the configurations of structural elements of PDS. Two configurations are envisioned for the single pod system, namely, longitudinal and lateral configuration. The difference between the two configurations of the single pod PDS is the location of interface for mounting PDS onto launch vehicle. By changing the mounting surface, the PocketQube deployment velocity vector changes with respect to the launch vehicle.

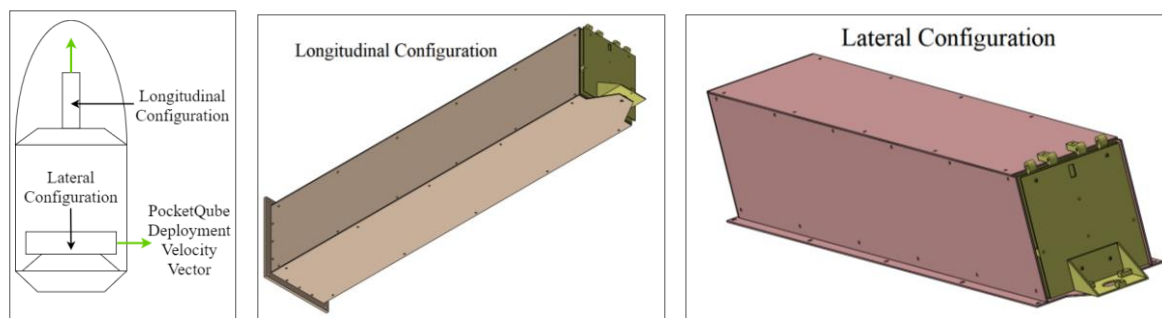


Figure 59: Single pod configuration (illustration for reference).

To better understand the difference between the configurations, let us assume that both configurations of single pod PDS are mounted to a surface perpendicular to launch vehicle velocity vector. PocketQube deployment velocity vector for longitudinal configuration will be parallel to launch vehicle longitudinal axis and for lateral configuration it will be parallel to launch vehicle lateral axis. This change in PocketQube deployment velocity vector (green arrow) is shown in Figure 59. It is to be noted that velocity vectors are dependent on mounting location and orientation. PDS design will ensure all possible mounting orientations can be accommodated by structural analysis load definition in all 3 axes.

At this stage of design of the PDS, longitudinal configuration of the PDS is the preferred design solution as it would occupy less launch vehicle surface area due to its mounting footprint being lower in comparison to lateral configuration. Detailed analysis between the configurations is carried out in Chapter 5 based on structural design.

## 4.10 Multiple Pod System

Having seen configurations of the single pod PDS, this section dwells into preliminary design of multi pod PDS. A footprint analysis is conducted based on pod dimensioning, following which structural configurations for the multi pod PDS are discussed.

### 4.10.1 Footprint Analysis

In this section, a preliminary footprint analysis for the multi pod PDS is conducted. Deployer launch vehicle footprint is an important factor to be considered for the design of multi pod PDS. PDS design has to ensure that integration to various types of launch vehicles is possible.

With this consideration, it becomes important that the multi pod PDS footprint would be such that multiple launch vehicles can integrate the design. In this regard, multi pod CubeSat deployers with a payload capacity of 12/16 U have proven to be adaptable to multiple launch vehicles. Hence, multi pod PDS is designed to match footprint of 12/16 U CubeSat deployers (**PDS-LVR-010**).

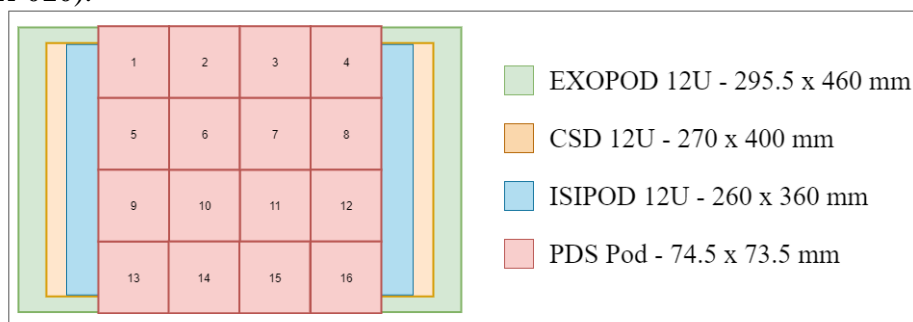


*Figure 60: Multi pod PDS preliminary footprint analysis.*

Based on CubeSat deployers' footprint shown in Figure 7 and PDS pod dimensions discussed in Section 4.7, a total of 16 pods could be accommodated in a 4x4 pattern for the multi pod PDS. The payload volume for a total of 16 pods would be 96P (24 kg). Preliminary footprint analysis for multi pod PDS is shown in Figure 60 with dimensions of individual pods being equal to dimensions shown in Figure 56.

Initial footprint analysis assumes that multi pod PDS has launch vehicle interface on -Z face and all dimensioning apart from the pod dimensions are ignored. Although ignoring other dimensions lead to dimensional inaccuracy, this analysis provides a good first approximation to multi pod PDS footprint. Different launch vehicle fixture locations are evaluated in Chapter 5 and deployer footprint dimensions of final design is discussed in Chapter 6.

### 4.10.2 Configuration Study

Having discussed the multi pod PDS footprint, this section details the structural configuration of the multi pod PDS. Configuration study is based on structural elements designed for the single pod PDS including guide mechanism and structural rib discussed in Section 5.6.2 and shown in Figure 73.

The structural configuration of the multi pod system takes into account the conclusions from single pod structural design progression discussed in Section 5.6 and Section 5.7. The 4x4 pod

pattern was arrived at in order to distribute modal mass participation proportionally along the two axes perpendicular to the deployment velocity vector. By ensuring near equal modal mass participation by structural design, the 4x4 configuration proportionally distributes system dynamic mass resulting in higher structural stiffness. Hence, the 4x4 configuration with 96 P payload capacity is the suited configuration for multi pod system accounting for launch vehicle footprint and structural dynamics.

The objective of this study was to determine an optimum orientation of structural elements required for multi pod deployer to minimise structure mass. A total of 4 pods are considered as a linear pattern of these pods (X direction) will result in forming the 96P deployable volume as discussed previously. Figure 61 shows structural element placement for a line of 4 pods within the multi pod deployer.

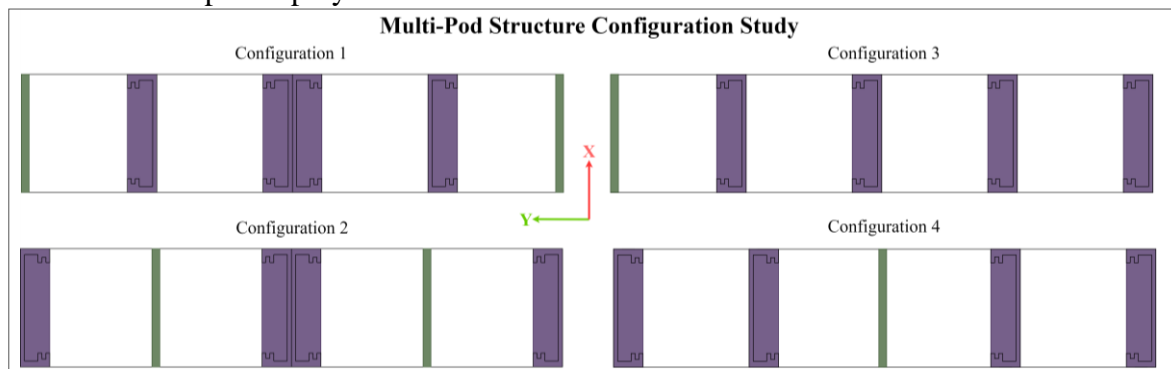


Figure 61: Configuration study for multiple pod structural elements (skeleton view).

In Figure 61, guide mechanism is coloured purple and rib green. Of the four configurations shown, it is evident that configuration 1 and 2 would require an additional rib for the same payload mass. Further, at the middle of these configurations additional spacing has to be accommodated in Y direction to allow for door deployment clearance ( $20^\circ$  each). Hence, configurations 1 and 2 are not suitable for multi pod PQ deployer.

Configurations 3 and 4 have same mass to payload ratio however, configuration 3 would be a good choice if launch vehicle interface would be on -Y face and configuration 4 for -Z face. This is to reduce distance between system centre of mass (CoM) and launch vehicle fixture surface.

Based on these considerations, detailed structural analysis of multi pod PDS is discussed in Section 5.12.

The design of component systems of PDS being completed and preliminary configuration analysis for single pod and multi pod discussed, structural analysis of PDS is discussed in following chapter.

# 5.

## Structural Analysis

This chapter is dedicated to the discussion of structural analysis of PocketQube Deployment System. The chapter will focus on theory of Finite Element Method (FEM) solver, analysis methodology, methodology validation, system structural design, and sensitivity studies.

Structural analysis is necessary in order to find a balanced solution between system stiffness, strain, stress, and natural frequency while minimizing system mass. Based on results obtained from structural analyses of PDS, final design is arrived at.

### 5.1 Vibration Theory & Structural Analysis Overview

General equation of motion for a body under vibration is given by Equation (24) where  $\{X\}$ ,  $\{\dot{X}\}$  and  $\{\ddot{X}\}$  are displacement, velocity, and acceleration vectors respectively,  $[M]$ ,  $[C]$  and  $[K]$  are respective mass, damping, and stiffness matrices and  $f(t)$  is external load(s) applied on the system.

$$[M]\{\ddot{X}\} + [C]\{\dot{X}\} + [K]\{X\} = \{F(t)\} \quad (24)$$

#### 5.1.1 Static Analysis

Static analysis by definition is conducted on a system in which system excitation and structural response are invariant with time. Hence, Equation (24) is reduced to Equation (25).

$$[K]\{X\} = \{F\} \quad (25)$$

Using Equation (25), structural displacement is estimated using matrix inversion by the FEM solver.

In further sections, dynamic analysis of structure using FEM model is discussed.

#### 5.1.2 Modal Analysis

Modal analysis is an analysis technique used to determine dynamic characteristics of structures. For a dynamic system, it is important to obtain natural frequencies and mode shapes of the structure. The analysis is conducted to meet the natural frequency requirements of launch vehicles as well as to verify if any dynamic loads coincide with the natural frequency of the structure.

Modal analysis is solved as a free and undamped vibration system. Hence Equation (24) is reduced to Equation (26).

$$[M]\{\ddot{X}\} + [K]\{X\} = \{0\} \quad (26)$$

Assuming harmonic motion of the structure, displacement vector  $\{X\}$  can be represented as shown in Equation (27) and acceleration vector  $\{\ddot{X}\}$  in Equation (28) where,  $\phi_i$  is the amplitude,  $\omega_i$  is frequency, and  $\theta_i$  is the phase angle of the harmonic oscillation.

$$\{X\} = \{\phi_i\} \{\sin(\omega_i t + \theta_i)\} \quad (27)$$

$$\{\ddot{X}\} = -\omega_i^2 \{\phi_i\} \{\sin(\omega_i t + \theta_i)\} \quad (28)$$



Substitution of Equation (27) and Equation (28) in Equation (26) and solving for the determinant in Equation (30), will compute the natural frequencies of the system.

$$([K] - \omega_i^2[M])\{\phi\}_i = \{0\} \quad (29)$$

$$\det([K] - \omega_i^2[M]) = \{0\} \quad (30)$$

Equation (30) is an eigenvalue problem and can be solved to obtain its roots. Eigenvalues correspond to the natural frequency ( $\omega_i$ ) of the structure and eigenvectors to their respective mode shapes ( $\phi_i$ ). Eigenvectors are normalized to the mass matrix, therefore, just the mode shapes have real meaning and not deformation values obtained during the solution.

Total number of modes of the system equal total degrees of freedom for that system. The natural modes of vibration are inherent to a dynamic system and are completely determined by system's physical properties such as mass, stiffness, damping, and each of their spatial distributions.

Modal analysis is a linear analysis and ignores nonlinear effects. Nonlinear effects can originate from geometrical nonlinearities (large deformation), material nonlinearities (elasto-plastic material), and contact regions. These effects result in variation of stiffness matrix during load application.

$$\gamma_i = \{\phi\}_i^T [M] \{D\} \quad (31)$$

Participation factors of the extracted modes can be calculated using Equation (31) where,  $\{D\}$  is an assumed unit displacement vector in each of the coordinate directions. Participation factor indicates the quantity of system mass excited in each coordinate direction for a given mode. For example a high value of participation factor indicates that a mode will be excited when subjected to a force in that direction.

$$M_{eff,i} = \gamma_i^2 \quad (32)$$

$$\sum_{i=1}^n \frac{M_{eff,i}}{M_{total}} \sim 1 \quad (33)$$

Effective mass for a given mode is described in Equation (32). It is recommended that the ratio of effective to total mass over the summation of all extracted modes (Equation (33)) must be greater than 0.9 for modal analysis results to be used in subsequent analyses [104]. As discussed earlier, total number of modes in a system will be equal to its total degrees of freedom, hence computation of all modes is computationally expensive and the cut off is set at 0.9 on Equation (33).

Having seen the method behind modal analysis and the requirement of modal analysis for further dynamic analysis, we discuss the methodology behind harmonic and random analysis in coming sections.

### 5.1.3 Harmonic Analysis

Harmonic analysis is used to determine steady state response of structure to harmonic excitation. Excitation force for harmonic analysis is generalized in Equation (34), where  $F$  is the amplitude of excitation force,  $\Omega$  the excitation frequency, and  $\theta$  the phase angle.

$$\{F(t)\} = F \sin(\Omega t + \theta) \quad (34)$$

General governing equation for vibration (Equation (24)) for a system under harmonic loading reduces to Equation (35).

$$[M]\{\ddot{X}\} + [C]\{\dot{X}\} + [K]\{X\} = F \sin(\Omega t + \theta) \quad (35)$$

Generalized system displacement, velocity, and acceleration due to the harmonic excitation are shown in Equations (36), (37) and (38), where,  $\{X\}$ ,  $\{\dot{X}\}$  and  $\{\ddot{X}\}$  are displacement, velocity, and acceleration vectors.

$$\{X\} = A (\cos \Omega t + j \sin \Omega t) = A e^{j\Omega t} \quad (36)$$

$$\{\dot{X}\} = A\Omega (j \cos \Omega t - \sin \Omega t) = jA\Omega e^{j\Omega t} \quad (37)$$

$$\{\ddot{X}\} = -A\Omega^2 (\cos \Omega t + j \sin \Omega t) = -A\Omega^2 e^{j\Omega t} \quad (38)$$

Substituting Equations (34), (36), (37) and (38) in Equation (35) we get Equation (39) (in complex variable notation) where,  $\{X_1\}, \{X_2\}$  are real and imaginary components of displacement vectors and  $\{F_1\}, \{F_2\}$  are real and imaginary components of excitation force vectors.

$$(-\Omega^2 [M] + j\Omega [C] + [K]) (\{X_1\} + j\{X_2\}) = (\{F_1\} + j\{F_2\}) \quad (39)$$

Using ‘Mode Superposition Method’, Equation (39) can be converted into modal form and is represented in Equation (40) where,  $\omega_i$  is natural frequency,  $y_i$  is complex modal coordinates,  $f_i$  is complex modal force, and  $\zeta_i$  is damping ratio. Equation (40) can be solved using mode superposition method which expresses the displacements as a linear combination of mode shapes.

$$(-\Omega^2 + j\Omega 2\zeta_i \omega_i + \omega_i^2) y_i = f_i \quad (40)$$

Using Equation (40) modal coordinates ( $y_i$ ) is computed and displacement is calculated using Equation (41) where,  $\{X\}$  is the displacement vector,  $n$  is total number of computed modes,  $\{\phi\}_i$ , and  $y_i$  are eigen vector and modal coordinates for a given mode respectively.

$$\{X\} = \sum_{i=1}^n \{\phi\}_i * y_i \quad (41)$$

Modal coordinates are scale factors computed by the solver to scale the contribution of each mode to the resultant displacement at specific excitation frequency,  $\Omega$ . As mode superposition method solves the equation of motion as a system of uncoupled equations, solution accuracy is dependent on whether adequate number of modes are extracted during the modal analysis. Number of modes must be sufficiently high to prevent mode truncation error. Typically, modes up to 1.5 times the interested frequency range is recommended for mode superposition method [105], [106], [107].

Further, for steady state harmonic analysis, structural response varies over the range of excitation frequencies. In this analysis, structural deformation is analyzed over the range of frequencies and stresses are evaluated for the maximum deformation state. In doing so structural response to sinusoidal excitations can be evaluated over the excitation frequency range.

Having seen the method behind harmonic analysis, random vibration analysis is discussed in the coming section.

#### 5.1.4 Random Vibration Analysis

Random vibrations are indeterministic in nature. Hence, it is mathematically described as the superposition of multiple harmonic excitations. Random excitations are assumed to follow Gaussian Distribution in occurrence. As discussed in Section 3.2.3, random excitations are expressed as PSD over the frequency range.

Random vibration analysis is conducted by determining a transfer function called the frequency response function  $H(\omega)$  across the range of frequencies and is represented by Equation (42).

The magnitude of the frequency response function by definition is the ratio of amplitudes of input and output excitations and shown in Equation (43).

$$H(\omega) = A(\omega) - iB(\omega) \quad (42)$$

$$|H(\omega)| = \sqrt{A^2 + B^2} = \frac{a_{out}}{a_{in}} \quad (43)$$

The system response to a single input PSD is given by Equation (44) where,  $S_{out}$  is the spectral density of response,  $S_{in}$  is input spectral density (PSD), and  $H(\omega)$  the transfer function.

$$S_{out}(\omega) = |H(\omega)|^2 S_{in}(\omega) \quad (44)$$

For random vibration analysis, transfer function  $H(\omega)$  is calculated using the mode superposition method [108]. The structural response will be frequency dependant and in order to estimate the average response to input PSD over all frequencies, root mean square response is estimated. Root mean square average will be one standard deviation ( $1\sigma$ ) and is given by Equation (45).

$$RMS = \sqrt{\int_0^{\infty} S(\omega) d\omega} \quad (45)$$

$3\sigma$  is calculated which accounts for 99.73% probability of occurrence. As input PSD frequency range is in the of 20 to 2000 Hz, modal analysis is carried out to find modes between 0 and 3000 Hz. These modes will further be utilized in calculating the dynamic response of the system.

Having discussed vibration theory overview and FEM solver methodology, analysis methodology and solver validation are discussed further.

## 5.2 Structural Analysis Methodology

This section of the study is dedicated to the discussion on the methodology used for FEM modelling. It details the methods used to prepare structural models for the FEM analysis, the representation of different physical elements within FEM model, and the procedure used to obtain FEM solution. Further, this section also compares different model preparation methods to choose a suitable method for analysis.

### 5.2.1 Model Preparation Methods

In this section, two different methods for preparation of CAD model for structural analysis input are discussed in detail. The two methods are:

1. Mid-Plane Method
2. 3D Mesh Method

A comparison between the methods are discussed in detail in Section 5.2.4, including their advantages and drawbacks.

#### 1. Mid-Plane Method

The licencing of Ansys program led to a limit on total number of 3D mesh elements that can be solved using the Ansys Mechanical Module. In order to overcome this drawback, at first the mid-plane method was tried to solve the Finite Element Method (FEM) model. Block diagram of the mid-plane method is shown in Figure 62.

All 3D surfaces (structural members) required for the finite element model was retained from the detailed CAD assembly. The 3D parts of the assembly were converted into 2D geometry using mid-plane sections. The 2D assembly was then imported into Ansys where material

properties of parts and their thicknesses were defined. A 2D mesh based on geometry was generated and the model was solved having defined respective boundary conditions.

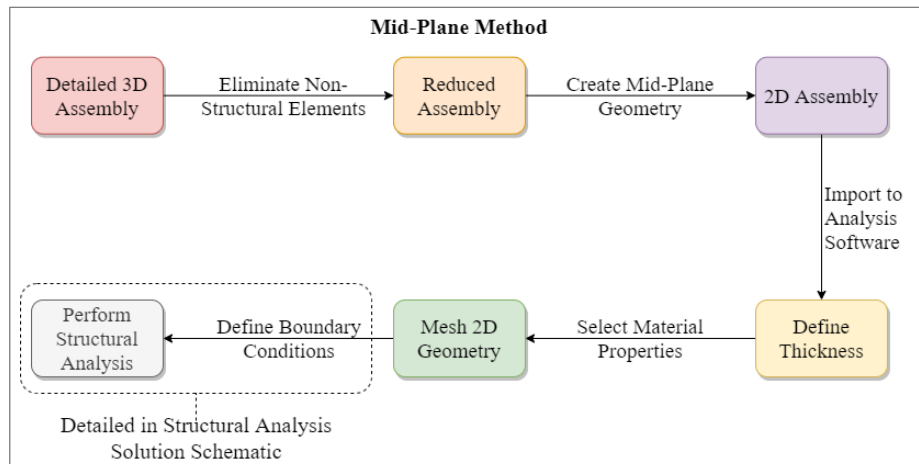


Figure 62: Mid-plane method block diagram.

## 2. 3D Mesh Method

Block diagram of 3D mesh method is shown in Figure 63. Similar to the mid-plane method, only essential elements of the assembly were retained for the finite element model. With geometry imported, the finite element model is defined within Ansys. Details of which is discussed further in Section 5.2.2.

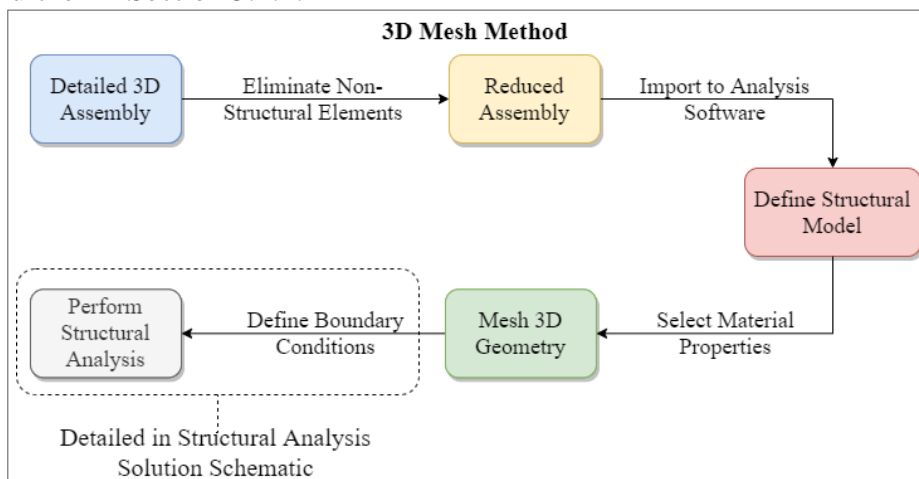


Figure 63: 3D mesh method block diagram.

To overcome the limit on total number of 3D mesh elements, two steps were introduced. The order of mesh elements were increased and an adaptive mesh was utilised. Detailed description of mesh definition is given in Section 5.2.2 under meshing.

### 5.2.2 Finite Element Model Definition

In this section, the different constituents of the finite element model are defined. Further, the description of model constituents and their relevance are discussed.

#### 1. PocketQube

PocketQubes in the finite element model will be represented as a point mass instead of a solid body in order to decrease the complexity of model. The point mass will be located at geometric centre of the representative PocketQube.

The point mass will have a mass of 250 grams per P unit in accordance to the PocketQube standard. Sensitivity of structural analysis model to different PocketQube sizes is analyzed in

detail in Section 5.8. Additionally, system sensitivity to variation in position of PQ centre of mass (CoM) is analyzed in Section 5.9.

Point mass of PocketQube is scoped onto the guide rail such that guide mechanism will be the PQ load bearing member. PocketQube point mass is scoped to the guide rail using multipoint constraint (MPC) contact and deformable constraint equations called RBE3. RBE3 contacts create constraint equations such that the motion of the master node is the average of the slave nodes. A force or moment applied at the master node is distributed to a set of slave nodes taking into account the geometry of the slave nodes as well as weighting factors.

## 2. Pin Puller

Similar to PocketQube, pin puller is represented as a point mass at its respective centre of mass. Representing pin puller as a point mass reduces total elements in the FEM model. The puller pin is scoped onto the pin puller bracket. This method although not representational of real scenario, it is a good approximation. Pin puller mass is taken to be 30 grams as discussed in Section 4.1. Within the finite element model, pin is defined as a joint for which all degrees of freedom except the pin axis are restricted.

## 3. Structure

Detailed CAD model of PDS is reduced to contain only structural members. Pusher plate assembly and other non-essential elements on door assembly are detached in the FEM model.

## 4. Mesh

Ansys Mechanical Module licencing set a limit on total number of 3D mesh elements that can be solved. In order to overcome the limitation of the total number of elements that are needed to be solved in the finite element model, a decision was taken to use mesh elements with quadratic nodes instead of linear nodes. This decision resulted in increasing the total number of nodes in the finite element model while maintaining the same number of mesh elements. Figure 64 shows the linear and quadratic element types for different mesh elements [109].

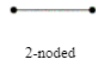
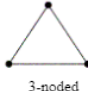
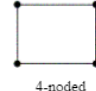
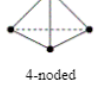


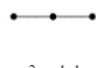
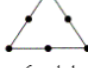
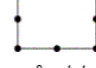
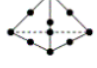
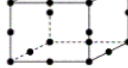
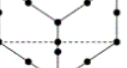
Element Order	1D	2D		3D		
	Beams	Triangles	Quadrilaterals	Tetrahedrons	Hexahedrons	Pentahedrons
Linear	 2-noded	 3-noded	 4-noded	 4-noded	 8-noded	 6-noded
Quadratic	 3-noded	 6-noded	 8-noded	 10-noded	 20-noded	 15-noded

Figure 64: Mesh element types [109].

Further, in the interest of refining the finite element analysis results, an adaptive meshing technique was utilised. As the likelihood of increased stress conditions were greater at interface joints connecting one structural member to another (place where load transfer between members occur), the meshing element size at the interface holes were chosen to be small. This adaptive meshing method resulted in refinement of analysis results at interfaces, while keeping the total number of meshing elements below the licencing requirement.

Detailed discussion on the dependence of FEM results on meshing is carried out in Section 5.4.

## 5. Fasteners

Fasteners connecting two structural members are modelled as beam elements in FEM. The beam elements have a circular cross-section with a diameter equal to the mean diameter of

respective fastener. The beam elements are connected to structural members using RBE3 contacts at both ends.

With all elements of finite element model defined, the solution schematic is discussed in succeeding section.

### 5.2.3 FEM Analysis Solution Schematic

In this section, the schematic used to obtain structural analysis solution of the PocketQube Deployment System is discussed. The pre-processing of the model until discretizing the structure into finite mesh is discussed in Sections 5.2.1 and 5.2.2. Further once the mesh is derived, the model is split into two separate analysis components i.e., dynamic and static structural analysis. The FEM analysis solution schematic is shown in Figure 65.

For static analysis, the boundary conditions (launch vehicle fixtures) and quasi-static acceleration inputs are defined. The launch vehicle input acceleration for static analysis is discussed in detail in Section 3.2.1. Once all necessary boundary conditions are defined, analysis solution is obtained to estimate deformation and structural stresses.

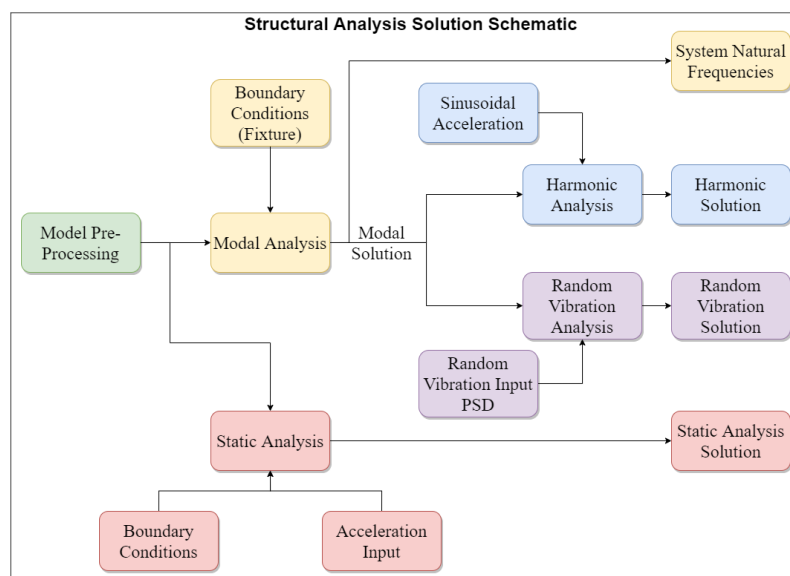


Figure 65: Structural analysis solution schematic.

For modal analysis, launch vehicle mountings are defined and the solution is obtained. The solution contains system natural frequencies and participation factors of the different modes, both of which are required for further system dynamic analyses. The number of modes to be calculated by the FEM solver was set such that natural frequencies up to 3000 Hz are captured in the solution set. 3000 Hz is selected since the random vibration PSD input frequency ranges from 20 to 2000 Hz [105]. Modal solution results are consequently utilized by harmonic and random vibration solvers to obtain system dynamic results.

Harmonic analysis is performed using modal analysis results and the sinusoidal input accelerations which are defined for various launch vehicles in Section 3.2.2. Deformations and structural stresses are obtained from the solution. Random vibration analysis is performed using modal solution and PSD inputs defined in Section 3.2.3. The probabilistic estimates of deformation and structural stresses are estimated by the solver and peak system response are evaluated to a confidence level of  $3\sigma$  following the *GSFC-STD-7000A* standard [51].

All acceleration and PSD inputs have factors of safety added to them according to Table 14.

## 5.2.4 Method Selection

In this section, the two FEM model preparation methods discussed in Section 5.2.1 are compared to choose a suitable method for structural analysis of PDS. The two geometries used for the mid-plane and 3D mesh methods are shown in Figure 66. All dimensions of the two geometries are equal and are chosen to evaluate performance of the two methods. However, thickness of different elements for the mid-plane method is defined on FEA software, whereas, for 3D mesh method it is defined on CAD software.

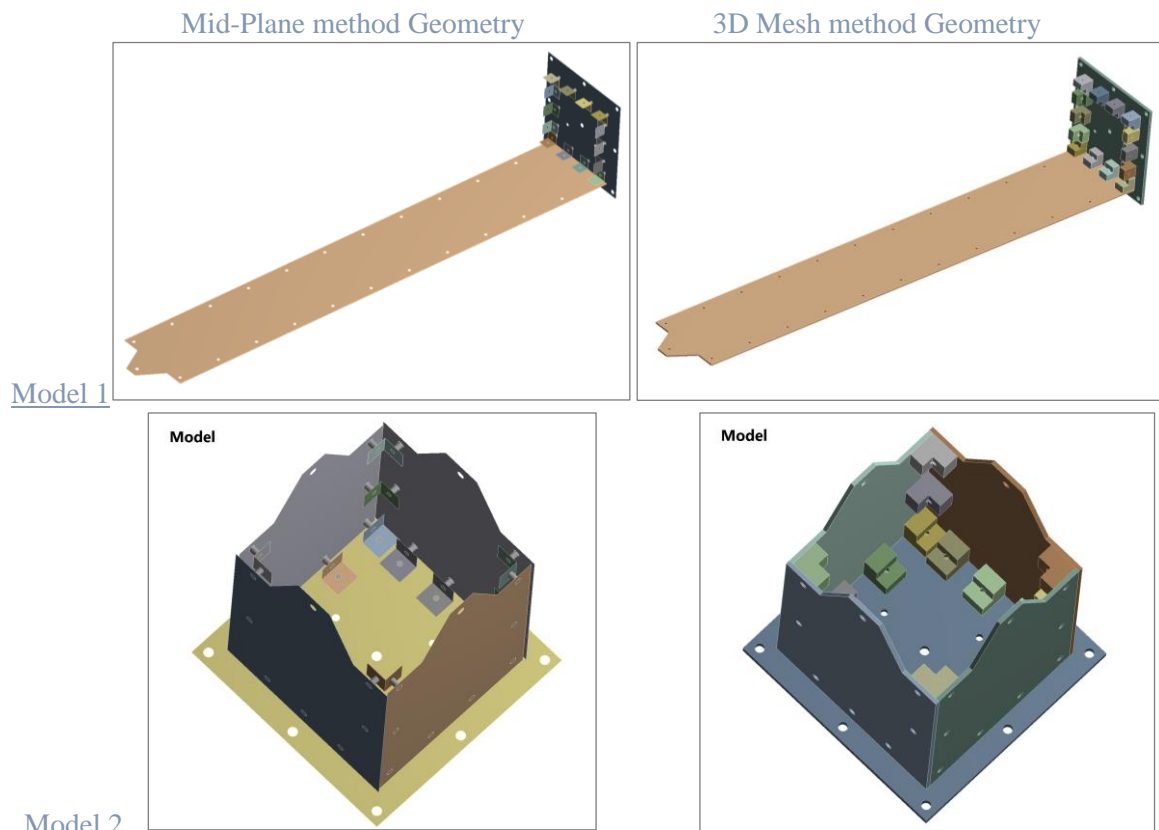


Figure 66: Geometries used for 2D and 3D methods.

Modal analysis results for the two FEM methods is shown in Table 49. As expected the mid-plane method underpredicts the natural frequencies of the validation model. This is due to the mid-plane geometry being an oversimplified geometry and the number of FEM elements through the thickness of components is unity. The average error between natural frequencies predicted by the two methods is about 10% for model 1 and 43% for model 2.

The comparison of FEM methods for static and dynamic analyses are shown in Table 50. It is observed that the error between the two methods are considerably high. The advantages and disadvantages of the two methods are discussed based on these results.

The advantage of mid-plane method is it reduces CPU resources required for obtaining analysis solution. Hence, large FEM models can be solved using limited computation resources. The method also predicts system natural frequencies with reasonable accuracy for model 1, whereas for model 2, inaccuracy is high. However, further dynamic analysis introduces large errors and is outside acceptable limits for both models. The largest drawback of mid-plane method is that the PDS will be overdesigned using this method. This overdesign will impact as an increase in structure mass and in turn have a negative consequence on system cost which is detrimental to the objective of this study.

Due to geometric complexity involved of the individual parts of PDS within the finite element model, scoping errors were noticed between geometries in the mid-plane method. These geometric scoping errors could not be handled by the solver, leading to solution errors. Hence, due to scoping errors and solution inaccuracies, mid-plane method was discarded and 3D mesh method was utilized in order to solve the finite element model.

With a detailed understanding of FEM model setup and solution schematic, next section details the validation of solver and setup methods used for structural analysis.

## 5.3 FEM Validation

As discussed on the dynamic solution methodology in Section 5.1, modal analysis methodology is critical in the FEM model as it serves as the input for both harmonic and random vibration analyses. Further, structural stresses induced due to sinusoidal/random excitations cannot be quantified during a shaker table test. Rather, a modal survey is conducted before and after dynamic structural loading to verify if permanent deformation has occurred on the test member [110]. A permanent deformation will be registered as a change in system natural frequency.

Keeping these constraints in mind, a conclusion was arrived at to validate the methodology of the finite element model in two parts. Initially, FEM solver is validated based on beam theory followed by the validation of overall method using modal analysis. By validating the modal analysis section of the FEM, the designer can have considerable confidence in the methodology utilised for overall FEM analysis.

### 5.3.1 Solver Validation

To validate the solver based on beam theory, a simple cantilever beam with a rectangular cross-section is considered. Natural frequency of a beam fixed at one end and free on the other with uniform distributed mass under bending is given by Equation (46) and under torsion is given by Equation (47) [111].

$$f_n = \left(\frac{1}{2\pi}\right) \alpha_n^2 \sqrt{\frac{E I}{m L^3}} \quad (46)$$

where, E is Young's Modulus, I is the area moment of inertia of beam cross-section, m is beam mass, and L beam length.  $\alpha_n$  is given below.

Mode	1	2	3	n>3
$\alpha_n$	1.8751	4.6941	7.8548	$(2n-1)\pi/2$

$$f_n = \left(\frac{1}{2\pi}\right) \beta_n \sqrt{\frac{Gk}{\rho J_p}} \quad (47) [111]$$

where, k is torsional constant, G is Shear Modulus,  $\rho$  is density of beam material, and  $J_p$  is polar moment of inertia of beam cross-section.  $\beta_n$  is given by Equation (48) [111], k and  $J_p$  are given by Equation (49) and Equation (50) respectively for a beam of rectangular cross-section with width b and height h.

$$\beta_n = \frac{(2n-1)}{2L} \pi \quad (48)$$

$$k = bh^3 \left( \frac{1}{3} - 0.21 \frac{h}{b} \left( 1 - \frac{h^4}{12 b^4} \right) \right) \quad (49)$$



$$J_p = \frac{bh(b^2 + h^2)}{12} \quad (50)$$

Based on properties of cantilever beam mentioned in Table 48 and Equations (46) to (50), the theoretical values for natural frequencies of the beam are calculated. Table 51 lists the numerical result obtained from Ansys mechanical solver and the theoretical results for the first 10 modes along with error of numerical results.

It was noted that the solver inaccuracy was higher in out-of-plane bending modes compared to in-plane bending and torsion modes. From Table 51, natural frequency error in modal analysis of a cantilever beam was found not to exceed a value of 5%. Hence the solver used by Ansys mechanical module is considered to be validated [112].

### 5.3.2 Method Validation

To validate the entirety of finite element model, a reference study was chosen where the authors had conducted finite element analysis as well as a vibration table test of a 1U CubeSat structure (CubeSat Kit) [113]. Upon conducting the modal survey test (sine sweep) on a shaker table, the reference team obtained the first natural frequency of 645 Hz for this structure.

To validate the FEM methodology, CAD model for 1U CubeSat Kit™ was obtained from Pumpkin Space Systems, Inc and modal analysis was conducted on this model using method described in Section 5.2.2. Modal analysis results of the model is plotted along with the reference study in Figure 67.

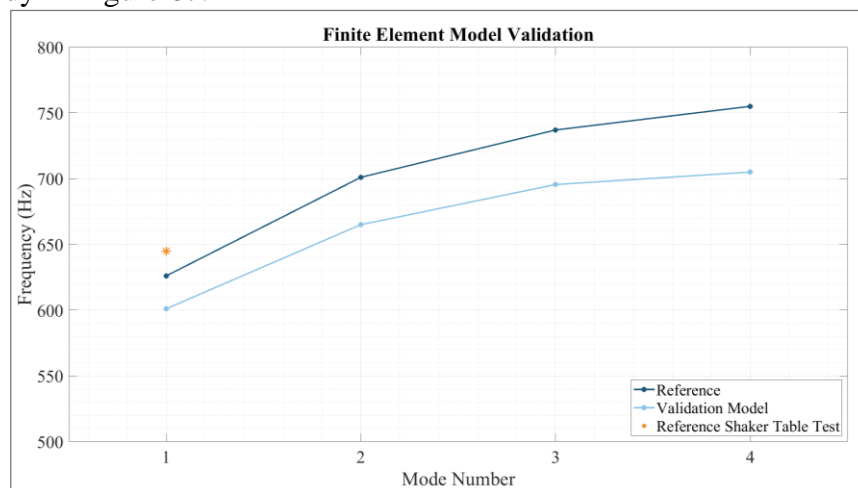


Figure 67: Validation of finite element model [94].

Figure 67 shows that the modal analysis methodology underpredicts system natural frequencies when compared to reference study values. However, the validation model follows same trend as the reference. It is also seen that reference study FEM model predicts the system frequency lower than the actual system frequency based on shaker table test.

Factors affecting the under prediction of system natural frequencies by the FEM model can be for various reasons. Some known factors are discussed below.

1. Finite element model is solved by discretizing a set of continuous bodies into discrete elements and forming constraint equations between them. Due to this inherent solving methodology a discretization error is introduced into the model [114]. This error would be dependent on the mesh element sizing of the model [115]. As element size tends to zero, the discretization error will approach zero. However, such a mesh results in large

number of elements in the model and thus high computation time. The effects of mesh element sizing on FEM results are further discussed in Section 5.4.

2. PocketQubes in the FEM are modelled as deformable point masses at their respective Centre of Mass (CoM). This modelling method results in contribution of PQ mass for modal interactions while, its stiffness is modelled as 0. However, in real scenario PQs will have inherent stiffness to deformation and will contribute to stiffening of the deployer structure.
3. As described in Section 5.2.2, bolted joints are modelled as deformable beam elements to reduce complexity of FEM. This method of reducing fastener model to beam element is found to decrease system frequency while increasing stresses generated within the fastener as well as at the joint sections [116].
4. Pre-tensioning of bolted joint is not considered for the FEM. The effect of fastener pretension is an increase in stiffness of a bolted joint. Therefore, fastener pre-tensioning contributes to the overall stiffening of the structure.

Based on Figure 67, the structural analysis results obtained will be a conservative estimate. Therefore, system natural frequencies will be underpredicted whereas, stress and strain values would be overpredicted. As a system designer this method would add additional margin of safety to design due to model behaviour. Based on these results, it can be considered that the FEM methodology is validated.

## 5.4 Mesh Sensitivity Study

Mesh sensitivity study was conducted to reason out the sensitivity of Ansys mechanical solver to changes in the mesh element size. This study was conducted on a lateral configuration model (version 2) of PDS. Goal of this study was to estimate the accuracy of solver subjected to different meshing conditions.

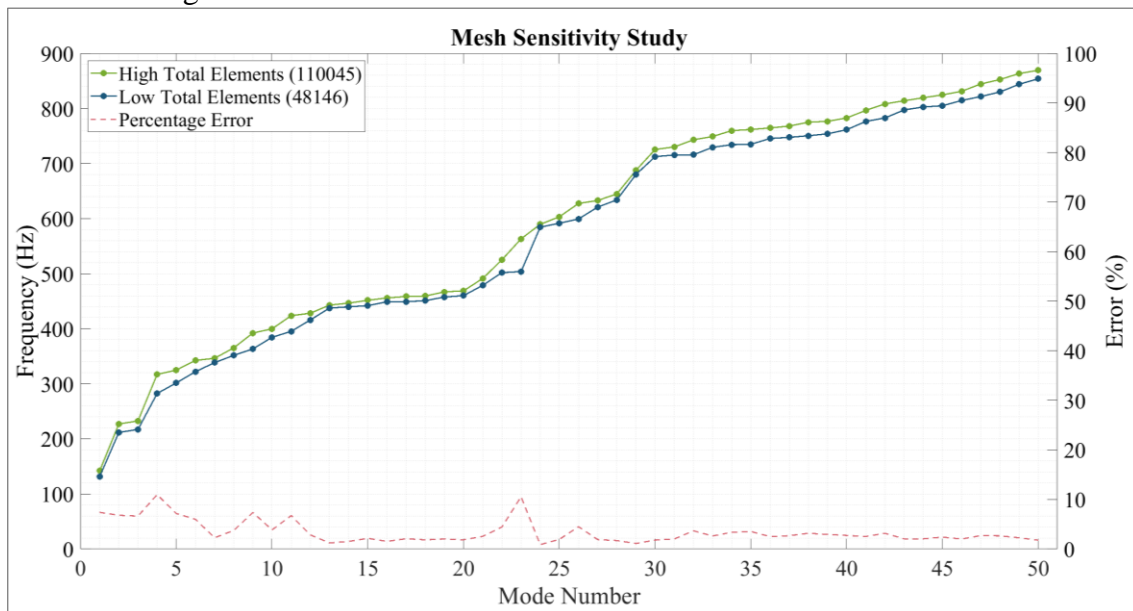


Figure 68: Mesh Sensitivity Study.

Modal analysis was chosen for this study as it serves as the input step for further FEM analysis and hence solver sensitivity to meshing is critical at this step. Total number of modes to be found was fixed at 50 and mesh element type was quadratic for this study. All other variables were also fixed between study. Solver sensitivity to total number of elements in the FEM is shown in Figure 68.

Figure 68 shows that the frequency of different modes follow similar trajectory between high and low element counts. High total elements has a smooth transition between mode frequencies however the low total elements curve is more jagged. Error in frequency is highest for mode number 23 with an inaccuracy of about 11 percent. This can be attributed to uneven stepping of low element curve compared to high elements at mode 23.

Overall the low element count underpredicts the natural frequency of the model than the high element numbers. One other parameter that changed considerably by varying element count was model solution time. For high element number (110,045) the solution time was 280 minutes and for low element number (48,146) the solution time was 72 minutes. Solution time increased by 290% with increase in element numbers.

In order to reduce model solution time and also have natural frequency estimation similar to high element number values, an adaptive meshing method was utilised. With adaptive meshing the mesh element sizing near the interface joints were reduced while maintaining the global element size the same. For M2 interface element size of 0.2 mm was used on selective panels to not exceed the maximum number count of the solver.

For this condition, the total number of elements was 52,862 (similar to low element count) and a solution time of 93 minutes (30% increase). The modal frequency curve obtained by this solution was similar to high total element curve in Figure 68 with a maximum error of 0.3% at mode 27 highlighting the advantages of adaptive meshing.

Based on these results, all structural analysis models utilized adaptive meshing technique to reduce computational requirements while maintaining high solution accuracy.

## 5.5 Design Acceptance Criteria

Having discussed the structural analysis theory, model definition, and validation, this section is dedicated to defining the acceptance criteria for structural analysis of PocketQube Deployment System.

A first consideration for acceptance of PDS design would be system natural frequency. As discussed in Section 3.3, deployment system natural frequency must meet the minimum launch vehicle requirement to avoid dynamic load amplification. The cut off frequency for the PDS was set at 135 Hz in Section 3.3.

Having met the natural frequency requirement, the structure is then evaluated to quantify the structural deformations and member stresses encountered due to launch vehicle loads. The structure is said to pass the design acceptance criteria if deformation values are within acceptable limits for the specific components and if the cumulative Margin of Safety (MoS) is positive. Margin of safety is calculated using Equation (51).

$$\text{Margin of Safety} = \frac{\text{Material Yield Strength}}{\text{Design Stress}} - 1 \quad (51)$$

Acceptable deformation values vary for different members of the PDS structure. For example, maximum permissible deformation for +X and -X panels of single pod PDS would be 1 mm. This condition is present as a clearance of 1 mm was considered between PDS structure and PocketQube appendage volume in X direction. If panel deformation exceeds this considered

clearance, there is a possibility of interference between deployment system structure and PocketQubes inside the pod which is highly undesirable.

Margin of safety can be made positive by choosing suitable material or alloy having high strength or by increasing thickness of components to reduce the induced design stress for the component.

Having discussed the acceptance criteria for structural analysis of PocketQube Deployment System, design progression of single pod and multi pod deployment systems are discussed in further sections.

## 5.6 Longitudinal Design Progression

In this section, design progression of the longitudinal configuration of single pod PDS is discussed. A detailed discussion on single pod system configurations was carried out in Section 4.9 and only structural analysis of the longitudinal configuration is discussed in this section.

Initial design of structural elements of PDS was envisioned to have multiple repeatable elements as a way of reducing manufacturing cost. For this reason, the PDS was constructed using multiple L brackets. The CAD assembly of such a design is shown in Figure 69. Guide rail dimensions which interfaces PocketQube backplate is the same as described in Section 4.6.1 with pod dimensions described in Figure 56. It is to be noted that these dimensions are not altered for all designs to ensure no interference with PocketQubes or their appendage volumes. All panels were 1 mm in thickness for the study.

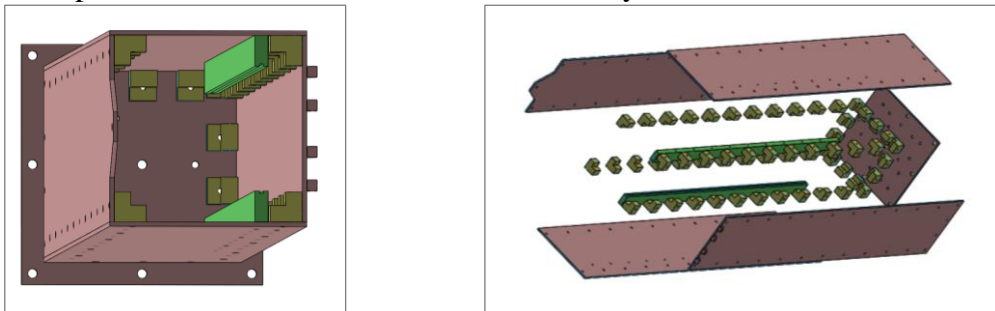


*Figure 69: Initial structural design with L brackets.*

Although this design provides for economical manufacturing, upon structural analysis it was observed that the design does not provide required stiffness to meet natural frequency requirement. To stiffen the structure, the design was modified to combine the vertical L brackets to a continuous vertical L rib as shown in Figure 70.

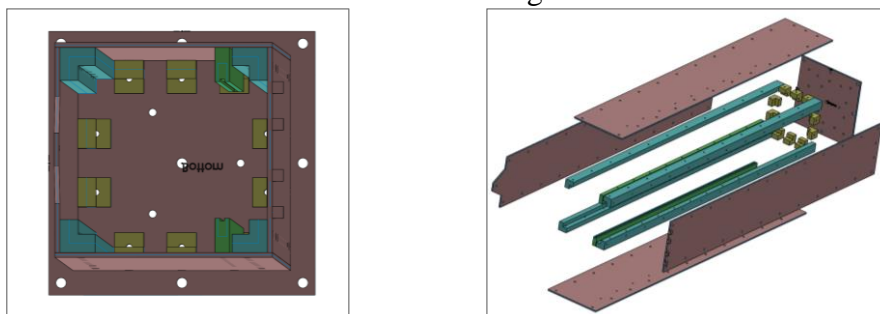


*Figure 70: Initial structural design with integrated vertical brackets.*

The modification resulted in stiffening of higher modes. However, modes 1 and 2 which are discussed in detail in later sections were not affected. Additionally, the structure mass was

increased to 1.65 kg which was highly undesirable. Based on this initial analysis, design direction for the development of structural elements of single pod configurations were cemented.

### 5.6.1 Version 1

Based on initial structural analysis results discussed previously, a decision was taken to combine the guide mechanism and vertical ribs attaching to -Y panel seen in Figure 70. By combining the three elements, overall stiffening of the structure is to be expected while reducing system mass.

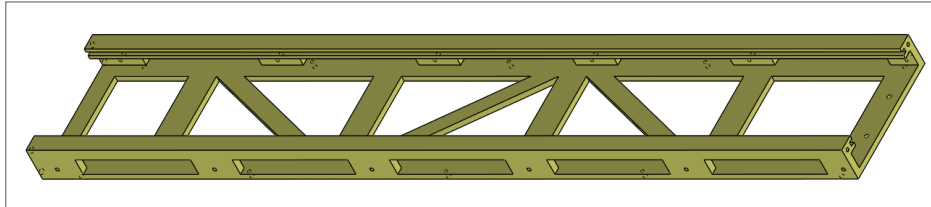


*Figure 71: Guide mechanism having combined vertical ribs.*

Figure 71 shows the guide mechanism having combined two vertical stiffeners and previous guide rail. Horizontal ribs are added to join the guide mechanism and resist deformation in X direction. Three diagonal elements are also added between the horizontal ribs to increase torsional stiffness of the member. Rectangular cut outs are present in  $\pm X$  directions as a mass saving measure. Stiffening elements are added keeping in mind that PocketQube mass is transferred to the deployment system through the guide mechanism.

Further, vertical L ribs attaching to +Y panel were removed and replaced by rib with a square cross-section of dimension 5x5 mm. 2 of such ribs were present to attach +Y panel to  $\pm X$  panels. Top and exploded views of the structure after all modifications is shown in Figure 72. The total structure mass dropped to 820 grams, which was about half the initial mass.

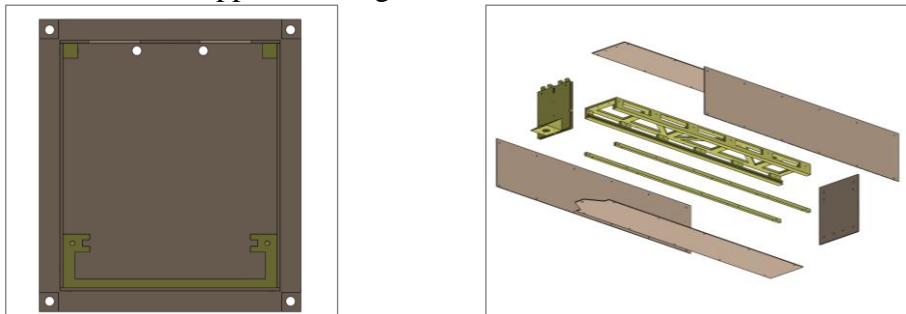


*Figure 72: Structural element design longitudinal version 1.*

The summary of modal analysis results is shown in Table 20, with modal deformations of each mode shown in Figure 126. For modal analysis results, first six natural frequencies are discussed as we are concerned of the lowest system frequencies. Once structural stiffness requirement is satisfied, further dynamic analysis is conducted by including large number of modes as discussed in Section 5.1.2.

*Table 20: Modal result summary – Longitudinal Version 1.*

Mode Number	Frequency (Hz)
1	32.309
2	35.104
3	88.463
4	94.141
5	102.59
6	105.09

As seen in Figure 126, for modes 3 to 6 having frequencies between 85 and 105 Hz, the primary deformation is in the form of panel flapping primarily in length. This can be observed in both  $\pm Y$  panels (mode 5). In order to restrict movement of the Y panels, the number of fasteners will be increased from 6 to 10. The additional fasteners will restrict panels from deformation which will increase the modal frequency.

Modes 1 and 2 are primarily bending modes in Y and X directions respectively with some torsional vibration blended in. In order to restrict torsional instability and increase modal frequency, independent ribs attaching to +Y panel will be combined.

### 5.6.2 Version 2

The changes for this version compared to the previous version was increase in number of fasteners to 10 numbers on  $\pm Y$  panels and merging of ribs. Four horizontal stiffeners were added to merge ribs in order to resist deformation in X direction. Top and exploded views of the structure after modification is shown in Figure 73. As a result of these changes, structure mass was increased to 850 grams.

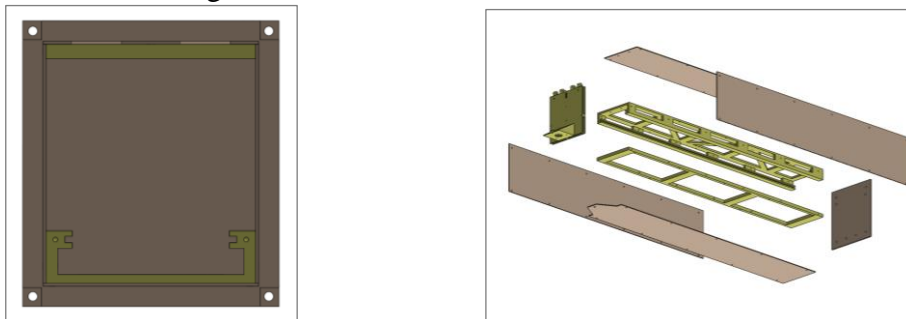


Figure 73: Structural element design longitudinal version 2.

The summary of modal analysis results is shown in Table 21, with modal deformations of each mode shown in Figure 127.

Table 21: Modal result summary – Longitudinal Version 2.

Mode Number	Frequency (Hz)
1	35.477
2	37.71
3	122.05
4	150.69
5	207.39
6	307.25

It can be seen from the modal results that a small increase in frequency of first two modes were observed. Additionally, torsional stiffness of the structure increases for the two modes and they are transformed to primary bending modes. The two modes have been converted to pure bending and similar to bending mode of a cantilever beam.

The increase in fastener numbers on Y panels has resulted in increasing system frequency. Y panel oscillations at 88 and 94 Hz frequencies increased to 311 and above 350 Hz respectively. Modes 4 and 5 although above 135 Hz requirement, are of particular interest as it is seen to excite the door assembly. The origin of this excitation was the interfacing method used to attach door assembly (threads in hinge attaching to -Y panel). As a precautionary measure, fastener attachment was shifted to guide mechanism from -Y panel for further versions to provide resistance to this form of excitation. This change caused difficulty in integration of door assembly which is further discussed in Section 7.1.

The structure model at this stage was modified to form version 1 of lateral single pod configuration. This model was the first model which had system frequency range close to the requirement. As discussed previously, the first two modes of vibration of this version would be specific to this configuration due to the nature of their deformation. Hence this structural model was chosen to be modified into version 1 of lateral configuration. Detailed discussion of this analysis is carried out in Section 5.7.1.

Design of single pod longitudinal configuration was halted at this stage. The implications of which are discussed in Section 5.11.

## 5.7 Lateral Design Progression

In this section, the design progression of the lateral configuration of single pod PDS is discussed. A detailed discussion on single pod system configurations are discussed in Section 4.9 and only structural analysis of the lateral configuration is discussed in this section. As stated in previous section, design for lateral configuration was derived from version 2 of longitudinal configuration.

### 5.7.1 Version 1

The CAD model for this version of PDS was derived from longitudinal configuration version 2. Launch vehicle fixtures were moved from -Z panel in the longitudinal configuration to -Y panel for this configuration. The number of interfaces between PDS and launch vehicle was increased from 4 in previous version to 10 numbers. Increase in interfaces was to accommodate increased surface area on the panel in contact with launch vehicle and to increase frequency of modal excitation.

Total structure mass of this version was 865 grams. Increase of 15 grams compared to version 2 (longitudinal) is expected as -Y panel width is increased to accommodate launch vehicle fixtures. Structural design of the configuration is shown in Figure 74.

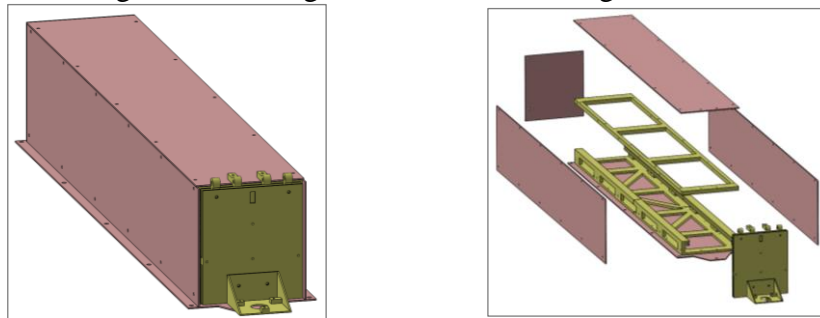


Figure 74: Structural element design lateral version 1.

Modal result summary for lateral version 1 is shown in Table 22, with modal deformations shown in Figure 128. First mode of vibration for this configuration was at 89.7 Hz with highest participation factor. Deformation of this mode as seen in Figure 128 is primarily bending in X direction. With an exception of this mode, all other modes meet the minimum natural frequency requirement. For a similar structure mass, this configuration when compared to the configuration it has been derived from (longitudinal-version 2) reveals higher structural stiffness.

In order to increase frequency of first mode above 135 Hz, the number of fasteners on -Y panel will increased from 10 to 16. Increasing the number of fasteners between -Y panel and guide mechanism would resist bending deformation along X direction which would increase modal frequency.

Table 22: Modal result summary – Lateral Version 1.

Mode Number	Frequency (Hz)
1	89.777
2	166.13
3	175.61
4	223.69
5	238.92
6	295.03

### 5.7.2 Version 2

The overall structural model for this version of lateral configuration is extremely similar to version 1 structure. As mentioned previously, total fasteners between -Y panel and guide mechanism was increased to 16 numbers to resist structural deformation of mode 1. Structure mass for this version was 870 grams.

Modal result summary for lateral version 2 is shown in Table 23, with modal deformations shown in Figure 129.

Table 23: Modal result summary – Lateral Version 2.

Mode Number	Frequency (Hz)
1	146.72
2	196.66
3	231.93
4	236.03
5	307.41
6	403.82

It is evident that increasing the interfaces has stiffened the structure and increased the frequency of 1<sup>st</sup> mode. This version of the PDS meets the minimum frequency requirements with the lowest natural frequency at 146 Hz. However, it is not clear if structure mass could be further reduced.

In order to understand the system natural frequency dependency on structural design variables, a parametric study was performed on this structure. Detailed description of the parametric study is discussed in Section 5.10. Modifications to obtain version 3 single pod lateral configuration structure were based on results obtained from parametric study.

### 5.7.3 Version 3

The changes incorporated for this version were based on parametric study results. As discussed in Section 5.10, during the study, individual parameters were varied from the baseline parameter values. Varying multiple parameters at once would vary system frequencies similar to trends predicted by parametric study. However, the magnitude of change in system frequency would differ from parametric study results.

Modal result summary for lateral version 3 is shown in Table 24. Result summary also includes the changes that were incorporated to structural elements. In the beginning, thickness of  $\pm X$  and  $-Z$  panels were reduced to 0.5 mm each. This change resulted in frequency of mode 1 to drop to 123 Hz. To stiffen structure, 3 vertical ribs were added to  $+X$  and  $-X$  panels on the outside. Further,  $+Y$  panel thickness was reduced to 0.5 mm and total system mass was reduced from 870 to 725 grams based on the changes.



Table 24: Modal result summary – Lateral Version 3.

Changes	$\pm X, -Z$ panel thickness 0.5 mm	Added ribs on $\pm X$ panels	Decreased +Y panel thickness 0.5mm	Increased -Y panel dimensions to accommodate LV interface	Added boss to LV interface
<b>Mass (grams)</b>	750	771	725	735	737
<b>Mode Number</b>	<b>Frequency (Hz)</b>				
1	123.1	138.31	153.3	152.36	156.4
2	174.63	174.72	174.6	211.87	174.57
3	188.68	188.89	184.36	265.92	184.31
4	202.15	213.27	197.84	279.54	193.85
5	247.	253.74	206.6	313.22	197.93
6	252.42	308.74	215.29	326.06	207.45

Upon initial random vibration study on this structure, there was a need to increase launch vehicle fixture distance and a boss of height 2 mm was added to these interfaces. Final structure after all modifications is shown in Figure 75. Structure mass after all modifications was 737 grams. The modal deformations once above mentioned structural changes are incorporated is shown in Figure 130.

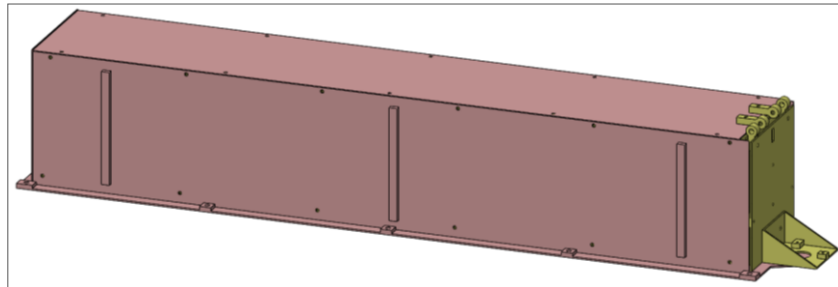


Figure 75: Structure design lateral version 3.

As stated in previous sections, dynamic study results are derived from modal analysis results. For this version of single pod lateral PDS having met the desired natural frequency requirements, static and dynamic load analysis is carried out to verify if member stresses are within desirable range. Excitation loading direction is varied in each axis and result summary is shown in Table 25. It is to be noted that the values recorded in Table 25 are maximum values for all variables. The location of occurrence of these maximum values can be found in Section 11.1.5.

Table 25: Structural analysis result summary single pod lateral.

Direction of Excitation		X	Y	Z
<b>Quasi-Static</b>	Deformation (mm)	0.29007	0.19786	0.12593
	Stress (MPa)	123.16	87.285	41.312
<b>Sinusoidal</b>	Deformation (mm)	0.096316	0.055922	0.033027
	Stress (MPa)	35.547	19.821	10.828
<b>Random</b>	Deformation X (mm)	1.1466	0.059931	0.084836
	Deformation Y (mm)	0.88818	1.0317	0.70273
	Deformation Z (mm)	0.16933	0.40054	0.47371
	Stress (MPa)	375.1	344.87	244.95

The detailed structural response of all analyses are shown in Figure 131 to Figure 145.

Table 26: Design margin of safety – Single pod.

Direction of Excitation	X	Y	Z
Margin of Safety	0.656639	0.039878	0.582012

Based on structural analysis results, margin of safety is calculated for all three excitation axes. Margin of safety is calculated considering cumulative stress values based on all analyses and Equation (51). Table 26 shows the margins of safety in respective directions for single pod PocketQube Deployment System. Margin of safety for all three mutually perpendicular directions are positive, hence, the structure meets the design acceptance criteria.

Having discussed the design progression of longitudinal and lateral configurations of single pod PDS, sensitivity studies are discussed further.

## 5.8 Sensitivity to PQ Mass Distribution

Mass distribution of PocketQubes can vary along the length of the deployer depending on the combinations of PocketQubes housed within. The details of PocketQube combinations which can be accommodated within the deployer envelope is discussed in Section 2.10. Therefore, for structural analysis, it becomes important to study the effect of PQ mass distribution on analysis results.

For this study, 3 different PocketQube combinations in rail were considered namely, 2 PocketQubes of size 3P, 3 PocketQubes of size 2P and 6 PocketQubes of size 1P. The 3 combinations were chosen as any other possible combination will be a combination of one or more these configurations. All PocketQubes were represented as point masses of appropriate mass at their respective CoM as discussed in Section 5.2.2.

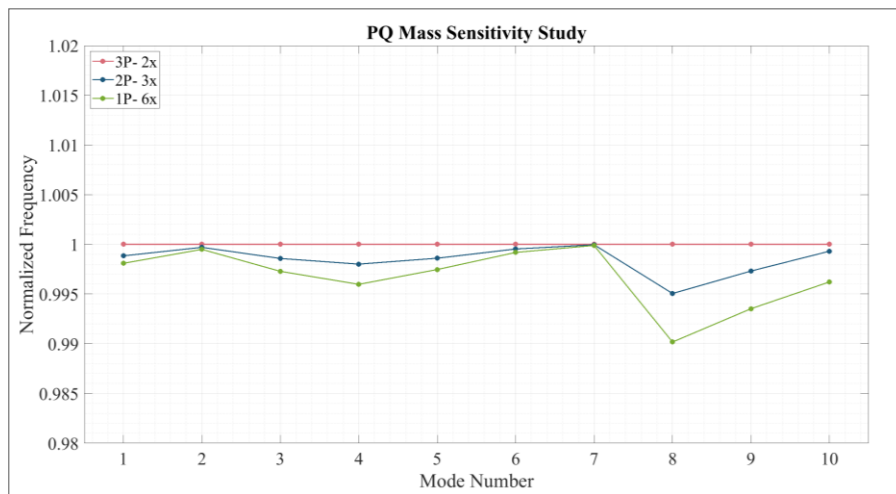


Figure 76: PQ mass distribution sensitivity study.

The analysis was performed on single pod lateral configuration (version 2) model. This model was chosen as it was the first structural model to meet natural frequency requirement. Similar to previous sections, modal analysis was chosen as it is the input step for further FEM analysis. Table 53 shows the results of this study. Change in natural frequency of the structure is negligible for the different PocketQube combinations with a maximum error of 0.98 % for 6 x 1P combination.

Analysis sensitivity to PQ mass distribution is graphically represented in Figure 76. Natural frequency of structure is normalized to 2 PocketQubes of size 3P configuration at different modes to understand the variability of natural frequency with PQ combinations.

Mode number 8 shows highest deviation in system frequency. However, this deviation results in about 1% error in frequency and the net drop in frequency of this mode is about 4 Hz. Frequency deviation for other modes is negligible and therefore, it can be concluded that distribution of PocketQubes along rail does not change stiffness of structure in any significant manner.

Based on this study, it can be inferred that natural frequency of the PDS structure is not sensitive to the size of PocketQube held in pod.

## 5.9 PQ Centre of Mass Sensitivity Study

This section of the study investigates the dependence of system frequencies on location of PQ centre of mass. The location of centre of mass of a given PocketQube is restricted by the PocketQube Standard. According to requirement number '*PQ-Mass-04*', the centre of mass of a given PocketQube must lie within a sphere of radius 1 cm from its geometric centre [2].

The objective of this study was to quantify the change in PDS structural stiffness to changes in location of PQ centre of mass. This study was conducted on the aforementioned structural model mentioned in PQ mass distribution sensitivity study detailed in Section 5.8. Further, 6 PQs of 1P unit size were considered to be placed within the pod. The reason for this decision was that structural sensitivity was greater for this combination than other PQ combinations in rail which was discussed in previous section.

As PQ CoM can lie anywhere within the specified spherical volume around its geometric centre, a total of six discrete points were chosen for this study. For systematic sensitivity study, 6 points are chosen at a distance of 10 mm from geometric centre along +X, -X, +Y, -Y, +Z and -Z directions. In choosing these set of points, the effect on system mass to change in PQ CoM for a particular axis can be quantified.

System natural frequency sensitivity to PQ CoM is shown in Figure 77. Variation of system frequencies are compared to when the CoM is placed at geometric centre for all three axes. It is to be noted that launch vehicle fixture is located on -Y panel for this configuration.

For variation of CoM in X direction, all vibration modes but for modes 3 and 4 are unaffected. Mode 3 drops in frequency whereas mode 4 increases. However, the drop in frequency for mode 3 is not significant to affect the system as natural frequency for this mode is high. It was noted that system frequency is insensitive to direction of movement from geometric centre in X axis as the model is symmetric across this axis.

For variation of CoM in Y direction, three modes show significant sensitivity. Mode 1 and 4 increase in frequency for a CoM shift in -Y direction from geometric centre. As stated previously, the LV fixture is located on -Y panel and translating PQ mass closer to LV fixture therefore stiffens the structure as expected. For CoM shift towards +Y direction, the effect is opposite for modes 1 and 3. Drop in frequency is expected as CoM shifts further from LV fixture. Mode 3 experiences a drop in frequency more significant than X direction case, however, it is still not significant enough to reduce modal frequency below requirement.

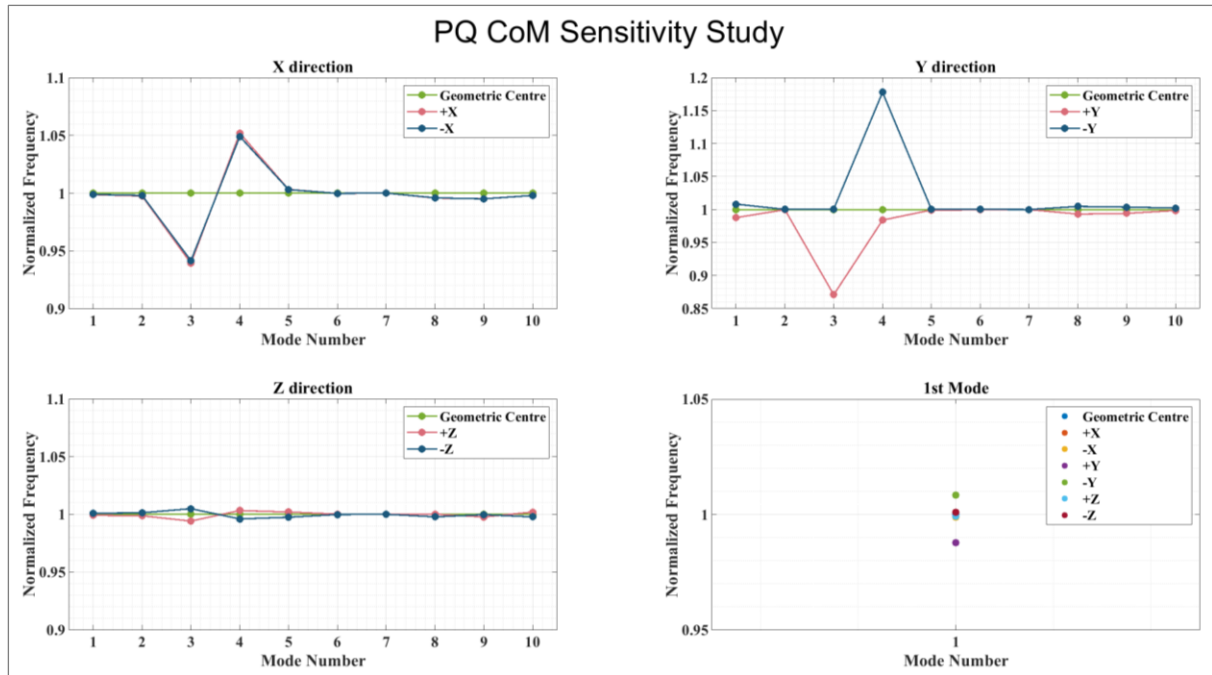


Figure 77: PQ centre of mass sensitivity study.

For variation of CoM in Z direction, there is no significant change in system frequencies. Therefore, it can be concluded that change in PQ CoM in Z direction does not affect structural stiffness.

Based on this study, structural stiffness does not vary for changes in X and Z directions. Adverse effect was observed for CoM translation towards +Y direction and care must be taken to ensure minimum natural frequency is met for this condition as first mode drops in frequency. Additionally, when CoM is translated in both X and Y directions, care must be taken to ensure frequency of mode 3 does not fall below requirement.

It is also important to note that for this study, all 6 PocketQubes (1P) centres of mass housed within the pod are translated in the directions stated. However, in real case scenario not all PocketQubes will have their centres of mass displaced along the same direction. Hence, this study accounts for an extreme case scenario. Based on this study, system designers/integrators can choose PQ combinations within a pod to account for changes in system frequencies.

## 5.10 Parametric Study

The objective of this study is to quantify the variation of lowest PDS natural frequencies to changes in parametric values of different structural members. Each study parameter is individually varied while all other parameters are fixed to a baseline value. By quantifying the system frequency variation, appropriate parameters can be chosen to reduce system mass while aiming to meet system frequency requirements.

Parametric study is conducted on modal analysis as it is the input step for further structural analysis of the system. For this study, the PDS model chosen was version 2 of lateral configuration. The model was chosen as it was the first model to meet the natural frequency requirements described in Table 13. The baseline values of the parameters studied under this section is listed Table 52 with system frequencies in Table 23.

The modal results of the parametric study for -Y panel thickness is shown in Figure 78. While Figure 78 shows the variation of natural frequency of the PDS as a function of -Y panel thickness, it is hard to quantify the change in magnitude of system natural frequency.

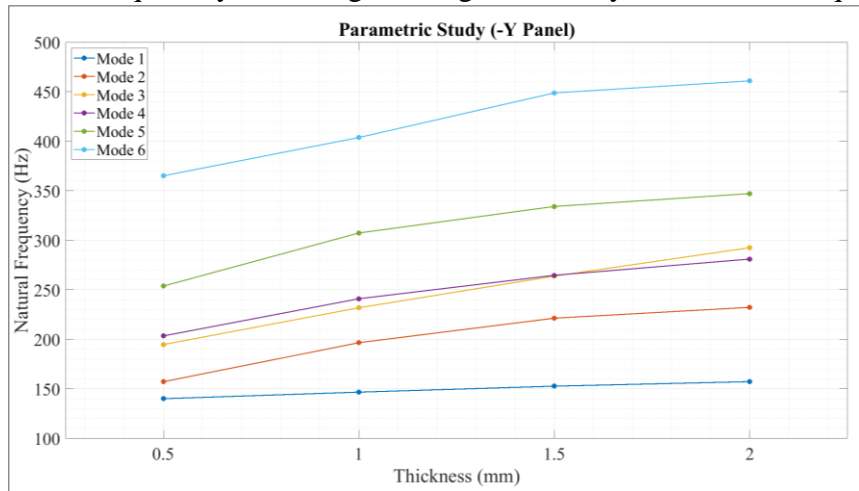


Figure 78: Parametric Study -Y panel thickness.

In order to quantify the magnitude of change in natural frequency of the system with changing parametric values, study results are normalized to the baseline case. Figure 79 shows the normalized natural frequency as a function of -Y panel thickness. For the baseline case, -Y panel thickness was chosen to be 1 mm and in Figure 79 for thickness value of 1, natural frequency of all six modes has been represented as 1.

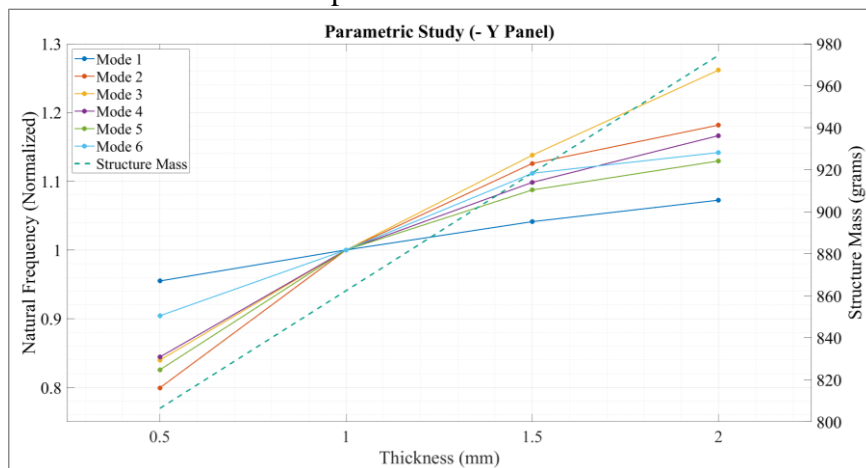


Figure 79: Parametric Study -Y panel thickness.

Such a representation doesn't imply that all 6 modes have the same natural frequency at 1mm thickness. The real value of frequency of different modes for the baseline is shown in Table 23. Comparing modes 1 and 2 in Figure 78 and Figure 79, for a thickness of 0.5 mm, although frequency is dropping for the two modes from the baseline case, drop in frequency of mode 2 is the greatest of all the modes while the drop in frequency of mode 1 is the least. Therefore, representing parametric study data as normalized frequency graph such as in Figure 79, helps in quantifying the drop or gain in system natural frequencies. All further parametric study data is represented as such.

Further, in Figure 79 the vertical axis on the right hand side represents structure mass of the PDS. PDS structure mass for the baseline case was 862 grams and when -Y panel thickness is reduced to 0.5 mm, mass decreases to 806 grams saving about 55 grams. However, the consequence of removing this mass from the structure is that first six natural frequencies drop.

Mode 2 experiences the biggest drop in frequency of about 20% and mode 1 experiences a frequency drop of about 4% to the baseline case.

Similarly, the results of the parametric study for the different parameters are represented from Figure 81 to Figure 86.

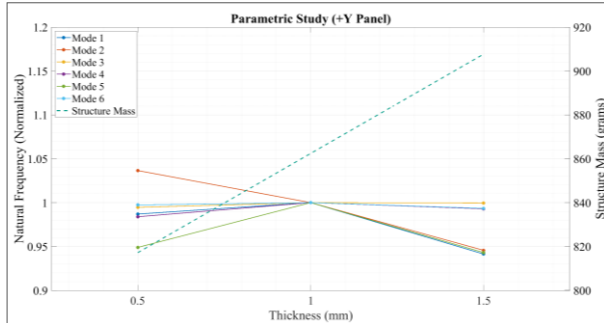


Figure 81: Parametric Study +Y panel thickness.

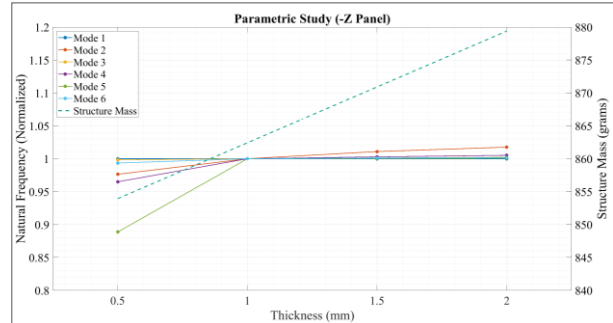


Figure 80: Parametric Study -Z panel thickness.

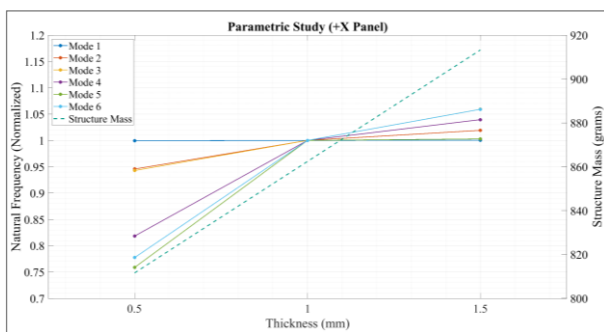


Figure 82: Parametric Study +X panel thickness.

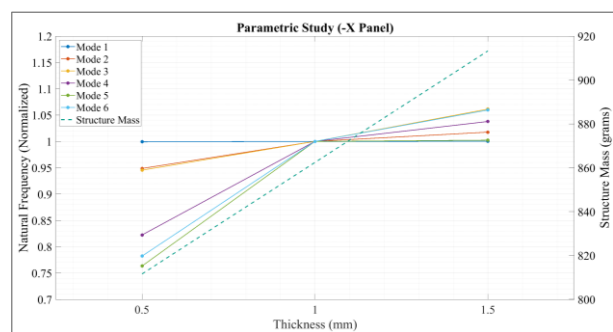


Figure 84: Parametric Study -X panel thickness.

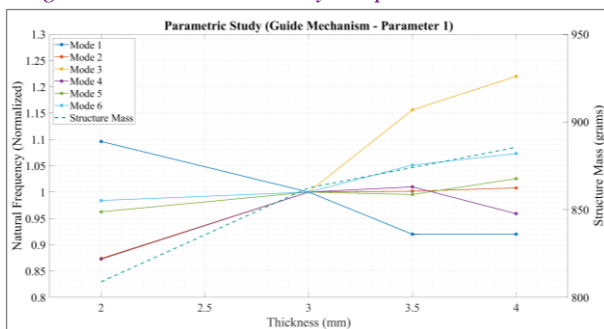


Figure 85: Parametric Study guide mechanism thickness (Parameter 1 & 2).

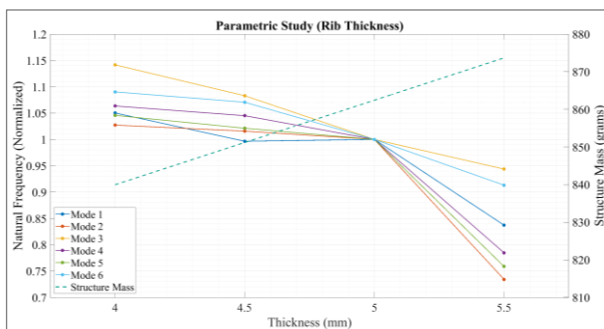
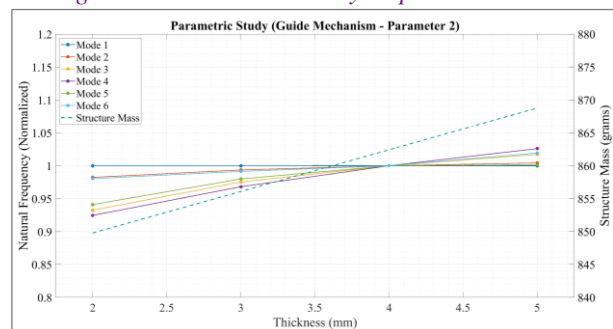


Figure 86: Parametric Study rib thickness.

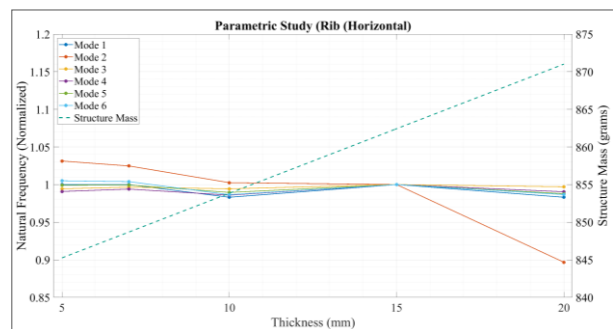


Figure 83: Parametric Study rib horizontal thickness.

### 5.10.1 Result Summary

The individual results for the different parameters are represented in the previous section. However, to gain an overall understanding of the effect of each parameter and their influence

on system natural frequency, a parametric study correlation matrix was generated. The correlation matrix is shown in Figure 87 and its legend in Figure 88.

This depiction uniformly quantifies the variation of system frequency and mass to changes in parameters chosen for the study. To convert the results shown between Figure 79 and Figure 86 to the correlation matrix in Figure 87, the modal variation and structure mass saved are normalized to 1 mm change in parametric thickness.

Parameter	Variation in Natural Frequency (Mode Number)						Mass Saved
	1	2	3	4	5	6	
-Y Panel Thickness	Light Green	Dark Green	Dark Red	Dark Red	Dark Red	Dark Red	Light Cyan
+Y Panel Thickness	Light Green	Dark Green	Light Yellow	Light Yellow	Light Yellow	Light Yellow	Light Cyan
-Z Panel Thickness	Light Yellow	Light Yellow	Light Yellow	Light Yellow	Light Yellow	Light Yellow	Light Cyan
+X Panel Thickness	Light Yellow	Light Yellow	Light Yellow	Light Yellow	Light Yellow	Light Yellow	Light Cyan
-X Panel Thickness	Light Yellow	Light Yellow	Light Yellow	Light Yellow	Light Yellow	Light Yellow	Light Cyan
Guide Mechanism Parameter 1	Light Green	Light Green	Light Yellow	Light Yellow	Light Yellow	Light Yellow	Light Cyan
Guide Mechanism Parameter 2	Light Yellow	Light Yellow	Light Yellow	Light Yellow	Light Yellow	Light Yellow	Light Cyan
Rib Thickness	Light Green	Dark Green	Light Green	Light Green	Light Green	Light Green	Light Cyan
Rib Horizontal Thickness	Light Yellow	Light Yellow	Light Yellow	Light Yellow	Light Yellow	Light Yellow	Light Cyan

Figure 87: Parametric study correlation matrix.

A positive correlation between thickness and modal frequency means that as thickness of a parameter increases, frequency of the respective mode increases. And a negative correlation signifies that frequency increases with decreasing thickness. As a designer we prefer negative correlation as it would mean structural stiffness increases with decreasing thickness implying decreasing component mass.

Modal Relation Legend		Mass Saved per mm change (grams)	
Dark Green	Negative Correlation	Light Cyan	125.00
Medium Green		Light Cyan	107.14
Light Green		Light Cyan	89.29
Very Light Green		Light Cyan	71.43
Light Yellow	Neutral	Light Cyan	53.57
Light Orange	Positive Correlation	Light Cyan	35.71
Dark Orange		Light Cyan	17.86
Dark Red		Light Cyan	0.00

Figure 88: Parametric study correlation matrix legend.

In Figure 87, for a parameter, we are looking for negative correlation (green) or neutral colours in modal relationship and greater saturation in cyan for mass saved. It is evident that decreasing Rib thickness would increase first six structural natural frequencies (indicated by the greens). However, thickness value of 5 mm was chosen due to the constraints of tapped hole required for fasteners attaching +X and -X panels to the rib. Similarly, Guide Mechanism Parameter 1 was fixed to 3 mm to allow for minimum thread engagement length for fasteners attaching -Y panel.

Further, for reducing structure mass, the effect of parameters on mode 1 is considered as it is the natural frequency closest to the cut off frequency of 135 Hz (PDS-LVR-005 & Table 13). Other modes are sufficiently high that even a considerable drop of structural frequency would still result in a frequency above the cut off frequency.

Based on all of the considerations mentioned above, a design decision was taken to reduce thickness of certain parameters. The summary of the changes is enumerated in Table 52.

With the changes mentioned a total structure mass of 178 grams was saved while ensuring first system natural frequency is above cut off frequency. Based on the outcomes of parametric study, version 3 of PDS lateral configuration is derived. Details of which are discussed in Section 5.7.3.

## 5.11 Single Pod Result Summary

Having concluded the discussion on design progression of single pod PDS and analysing the structural stiffness sensitivity in previous sections, a summary of the design is presented in this section.

Modal result summary for single pod structure design is shown in Figure 89. First six modes of vibration are plotted for the versions along with system mass.

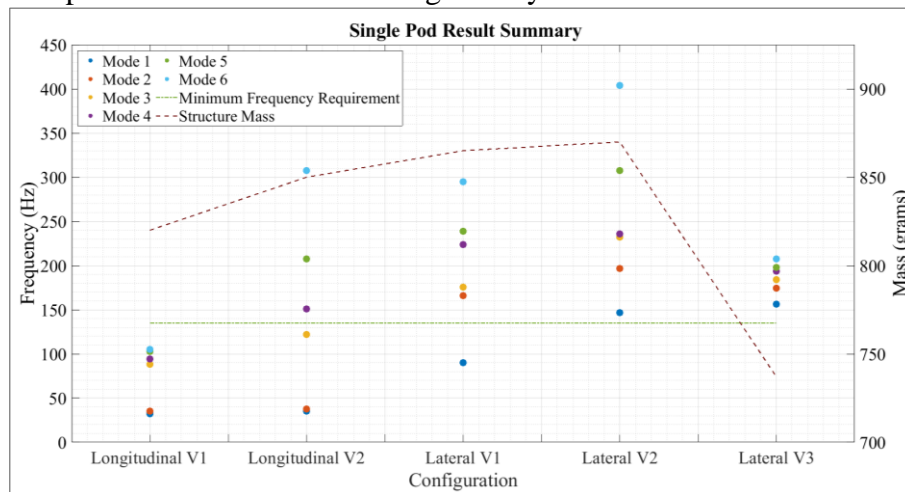


Figure 89: Single pod result summary.

For longitudinal configuration, although frequency of higher modes increased between versions 1 and 2, first two modes do not show any rise in frequency. As discussed earlier, this phenomenon was attributed to behaviour of structure similar to a cantilever beam. This prediction was proved right with structure stiffness increasing with a change in LV mounts in lateral configuration version 1.

Hence, lateral configuration is the preferred configuration for single pod PDS. However, this configuration occupies greater launch vehicle surface area. For typical launchers, this factor would not be limiting in case of launch vehicle selection. However, if minimizing launch vehicle surface area is a priority, lateral configuration can be mounted similar to longitudinal configuration using a large L bracket with stiffening members on its diagonal.

Lateral configuration version 3 mass reduction is possible due to parametric study results. In Section 5.9 it was discussed that first natural frequency of the structure drops when PQ centre of mass shifts away from launch vehicle mounting surface. Taking into account the margin provided by a conservative approach on the FEM methodology discussed in Section 5.3.2, frequency drop is not expected to drop below cut off frequency (135 Hz) for this case.

The discussion on single pod PDS is thus concluded. Structure design progression of multi pod PDS is discussed in further sections.



## 5.12 Multi Pod Design Progression

Having seen the design progression of single pod PDS configurations, this section will detail the design considerations and progression for the multi pod PDS. At early stage of structure design for the multi pod PDS, it was decided to use a quarter symmetric model as structural symmetry was present across X and Y axis. Solving a symmetric FEM model reduces system resources required to obtain the solution. However, it was evident early on that using a symmetric model for modal analysis would not capture all system dynamic characteristics.

Therefore model size reduction was not possible for structural analysis of multi pod PDS. In order to obtain analysis solution for the large model, HPC-12 computation capabilities were utilized. The solution for multi pod PDS was run in Ansys batch mode on distributed Linux machine.

Preceding the discussion on different versions of structural design of multi pod PDS, we define the launch vehicle load characteristics for this system. Quasi-static and harmonic acceleration values are independent of system mass. However, random vibration input PSD levels drop when system mass is greater than 22.7 kg.

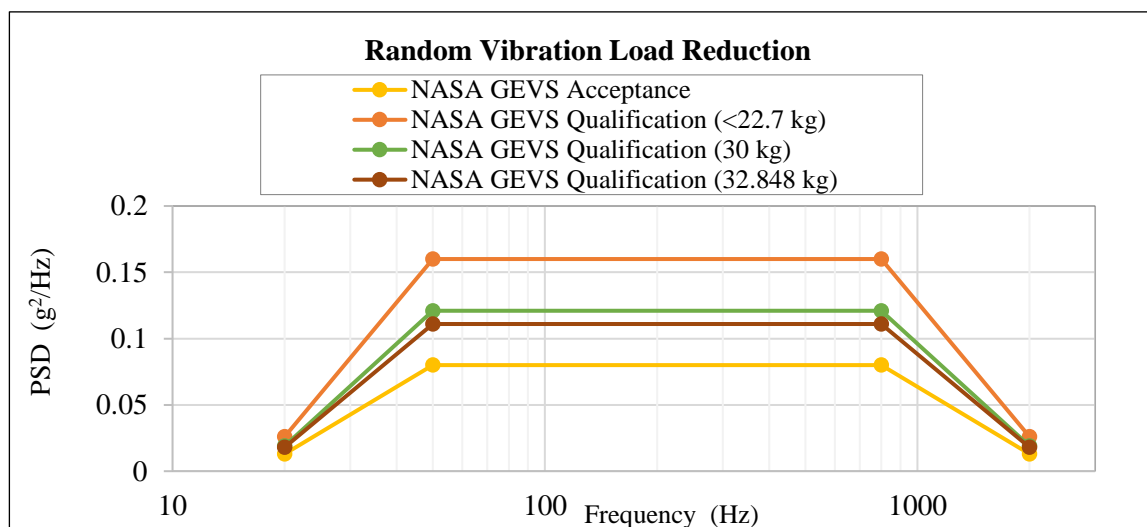


Figure 90: Random input PSD levels for multi pod PDS.

The reduction factor in plateau of random vibration input PSD is dependent on the mass of the multiple pod system and is given by Equation (52). The slopes of input PSD shall remain at  $\pm 6$  dB per octave [51].

$$PSD_{(50-800\text{ Hz})} = 0.16 * (22.7/m_{PDS}) \quad (52) [51]$$

Visual representation of this drop in input PSD is shown in Figure 90.

Some changes had to be incorporated to the multi pod PDS structure to accommodate essential elements. Pod length of the outer pods in Y direction had to be increased by 16 mm in the same direction. This increase was to accommodate hold down of pin puller for the outer pods and door actuation clearance of inner pods. Detailed log of all changes is presented in Section 6.3.1.

It is to be noted that the solution methodology to obtain eigen values and eigen vectors for multi pod modal analysis was changed from an iterative solver to a direct solution method. The change was incorporated as iterative solver convergence criteria was not satisfied for this

model. There was no change in solution accuracy between methods, however, the direct method consumed additional physical memory during solution.

Having discussed relevant differences for structural design, design progression of multi pod PDS is discussed further in detail.

### 5.12.1 Version 1

Version 1 of the multi pod PDS was envisioned to compare and evaluate the optimum orientation of the PDS structure for achieving maximum structural stiffness. Exploded views of the structural elements for this version are shown in Figure 91. Lateral X configuration, lateral Y configuration and longitudinal configuration are shown in Figure 91 respectively. The panels that contain launch vehicle fixture are shown in magenta for ease of distinguishability.

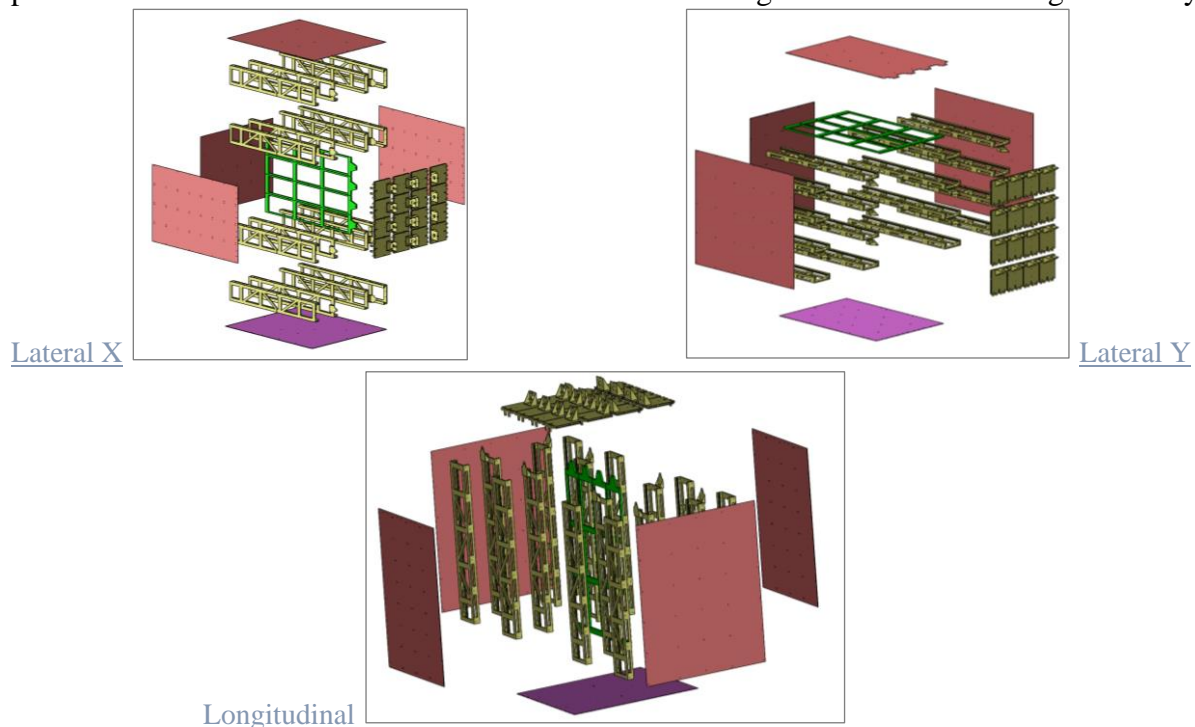


Figure 91: Structural element design multi pod version 1.

Lateral Y structure is based upon configuration 3 from Figure 61 and lateral X, longitudinal structures are based upon configuration 4 from Figure 61. Although configurations 3 and 4 from Figure 61 use the same amount of structural elements, configuration 3 was chosen for lateral Y structure as it reduces the overhang of guide mechanism from launch vehicle fixture. Reducing overhang increases structural stiffness as observed during single pod design in Section 5.7.

Table 27: Configuration results for multi pod version 1.

Multi pod Configuration	Lateral X	Lateral Y	Longitudinal
Mode	Frequency (Hz)		
1	13.222	10.302	26.383
2	20.969	18.754	27.016
3	23.342	20.909	29.388
4	25.084	21.273	34.473
5	37.352	24.866	38.265
6	39.768	31.556	55.802

Further, mass of different configurations were similar and averaged to about 8.6 kg. Having similar system mass for the configurations allows for a direct stiffness comparison between them. All other variables were tightly controlled and system natural frequencies for different configurations are shown in Table 27. Significant modes for the different configurations are highlighted red in Table 27.

It was observed that longitudinal configuration having fixture on -Z panel has the highest stiffness. Stiffness of lateral X and lateral Y configurations are similar with lateral X having marginally higher system frequencies. Based on these results, further structural design of multi pod PDS would be considering the longitudinal configuration because the configuration provided highest stiffness for similar structure mass.

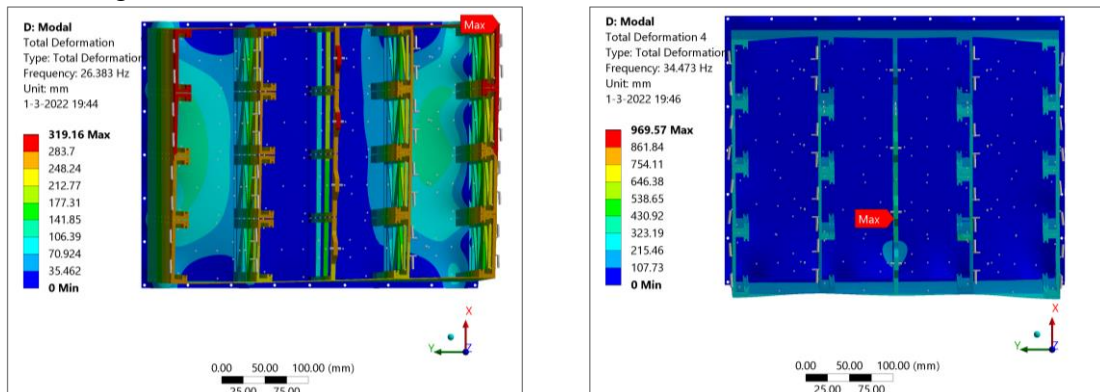


Figure 92: Modal analysis results longitudinal multi pod version 1.

Further, of the system frequencies shown in Table 27, for longitudinal configuration, mode number 1 and 4 at 26.3 Hz and 34.4 Hz are the significant contributors having high participation factors. Deformation of significant modes for longitudinal configuration is shown in Figure 92. Mode 1 had the highest participation, with bending deformation in Y direction. Therefore, stiffening ribs are necessary to limit deformation in this direction.

### 5.12.2 Version 2

For version 2 of the multi pod PocketQube deployer, 2 numbers of side rib are added. Each side rib has a mass of 250 grams and are fixed to +X and -X panels to increase stiffness in Y direction. In order to save mass, thickness of  $\pm X$  panels were reduced to 0.5 mm which saved about 235 grams on each panel. Additionally, mid rib in X direction was combined from four individual elements to a single rib saving about 75 grams. Combining mid rib is expected to limit modal interaction in X direction. The orientation and dimensions of structural elements are shown in Figure 93.

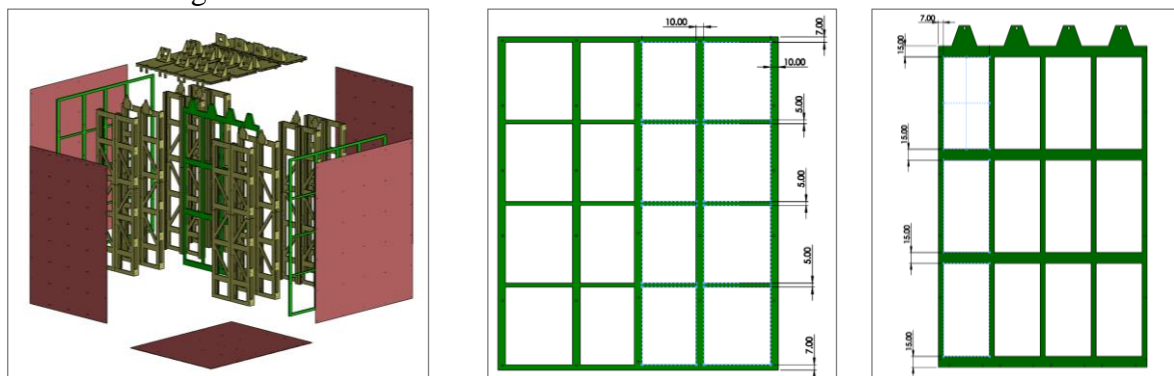


Figure 93: Structural element design multi pod version 2.

As a result of the changes to structure, the frequency of mode increased from 26.3 Hz to 28.12 Hz in Y direction and from 34 Hz to 58 Hz in X direction. The dimensions were varied for the

mid rib and side ribs to observe the changes in structural stiffness. Increasing the thickness of ribs only increased system mass and did not result in significant changes to system frequency.

It is evident from the change in system frequency that structural stiffening increased in X direction due to combining the mid rib in that direction. However, structural stiffness in Y direction did not change in any significance. In order to increase stiffness of the structure in this direction, an additional rib in this direction is envisioned at the middle of PDS structure.

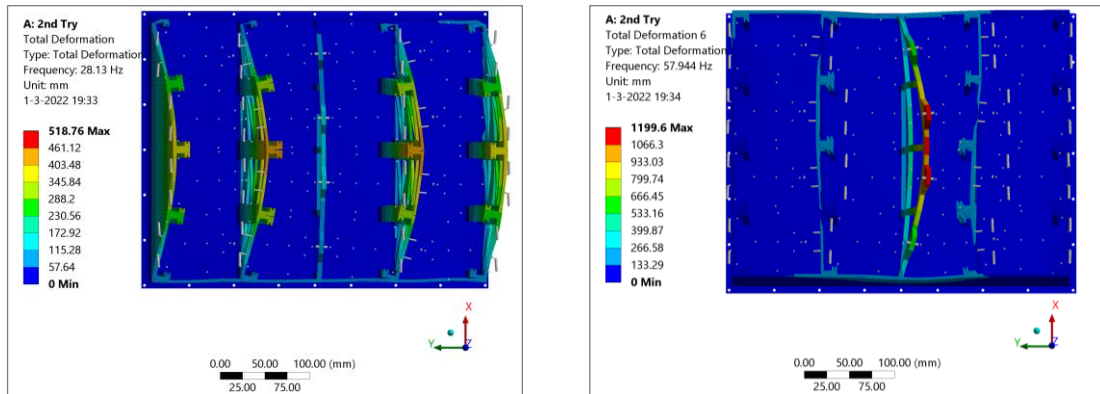


Figure 94: Modal analysis results multi pod version 2.

Further, there is a need for stiffening at the middle of structure in both X and Y directions. A continuous rib was proposed for Y direction as the participation factor for this mode was higher. In doing so the middle rib seen in Figure 93 has to be divided into two ribs to allow for a continuous rib perpendicular to it. Additionally, this rib is renamed to mid rib X and the one perpendicular is addressed as mid rib Y in future versions.

### 5.12.3 Version 3

As discussed in previous section, mid rib Y was to be continuous and mid rib X was split into two elements having equal dimensions. Horizontal width of mid rib X was reduced to 10 mm from 15 mm and diagonal ribs were added to stiffen structure as a compensation for the split. Width of diagonal ribs was 5 mm.

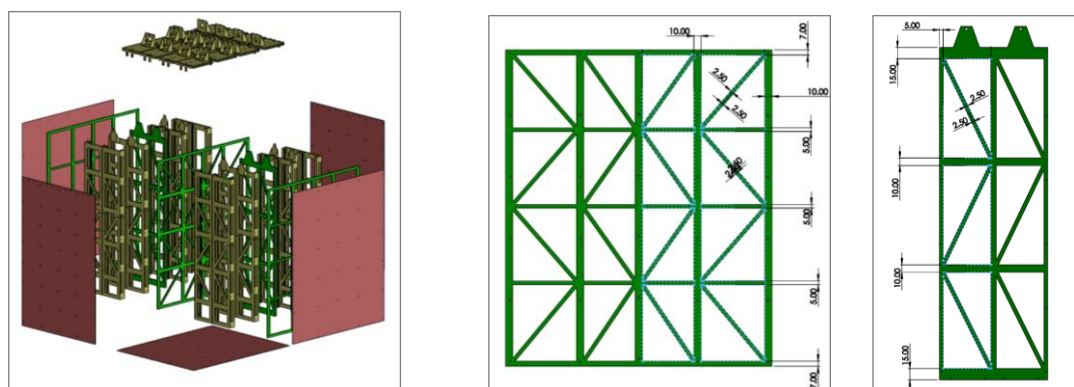


Figure 95: Structural element design multi pod version 3.

As a starting point, mid rib Y had same dimensions as side rib shown in Figure 93. However, frequency of significant mode rose from 28 to 30 Hz while system mass was 8.024 kg. When horizontal rib width of mid rib Y was increased to 15 mm from 5 mm, frequency increased to 35 Hz with system mass of 8.105 kg.

In order to increase modal frequency while not affecting system mass, horizontal width was reduced back to 5 mm and diagonal ribs were added as shown in Figure 95. System mass was 8.11 kg and modal frequency increased to 53.2 Hz in Y direction. However, lowest system



With a decrease in panel thickness, structure mass reduced to 7.956 kg with frequency of primary mode increasing to 98 Hz. As the modal excitation direction was primarily along Y axis in the middle of the structure, mid rib Y ribs were changed from diagonal ribs to x ribs as shown in Figure 97. Width of all x ribs were 5 mm. Adding these additional diagonal ribs increased the system frequency from 98 to 107 Hz with system mass being 8.11 kg.

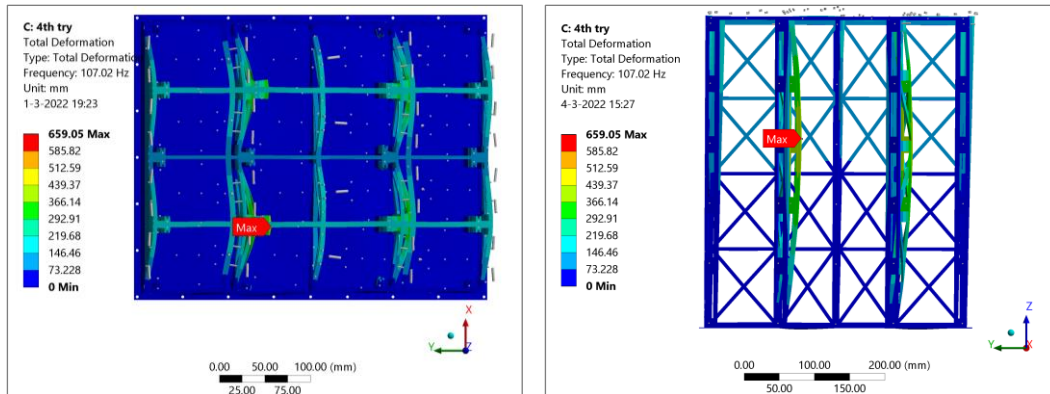


Figure 98: Modal analysis results multi pod version 4.

For primary mode at 107 Hz, maximum modal deformation was displaced from top of structure to middle of guide mechanism. Top rib resists deformation at structure top hence, modal deformation displaces to the middle. The deformation of this mode is shown in side view in Figure 98.

### 5.12.5 Version 5

In order to resist deformation of mode at 107 Hz in version 4, two ribs as shown in Figure 99 were added to the middle of guide mechanism. Holes were provided on guide mechanism to accommodate the ribs.

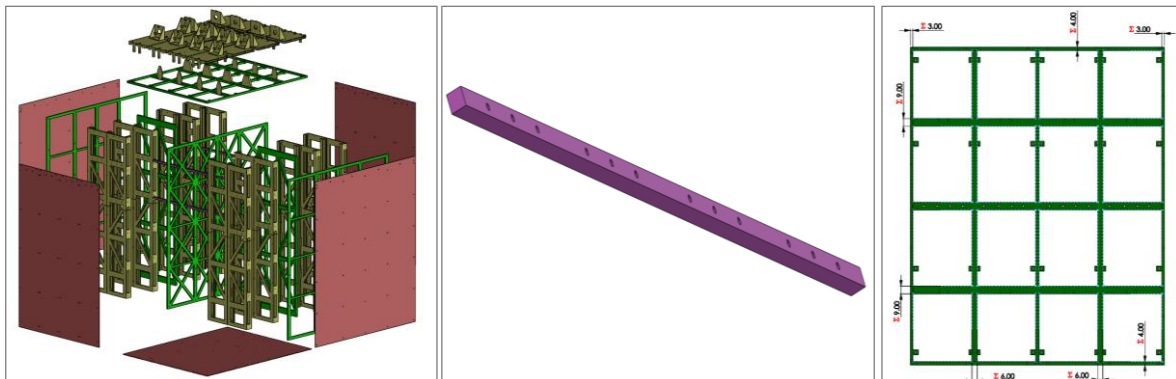


Figure 99: Structural element design multi pod version 5.

Upon addition of the two ribs, modal frequency increased from 107 Hz to 109 Hz. However, modal deformation moved up along the length of the guide mechanism. Hence, two additional ribs of same dimensions were added to this location to resist the said deformation. In total there were four similar ribs and this increased the system frequency to 125 Hz with system mass being 8.2 kg.

It was observed that an insignificant mode was present at 122 Hz after the structural changes mentioned before and significant vibration mode at 125 Hz was in the Y direction which was same as version 4.

In order to increase the frequencies of the two modes, modification of top rib was required. However, a decision was taken not to increase thickness of top rib in Y axis as it would cause

interference with PQ appendage volume. It was possible to increase the thickness of top rib in X axis and it was increased to 9 mm from 6 mm in version 4 with system mass increasing to 8.36 kg.

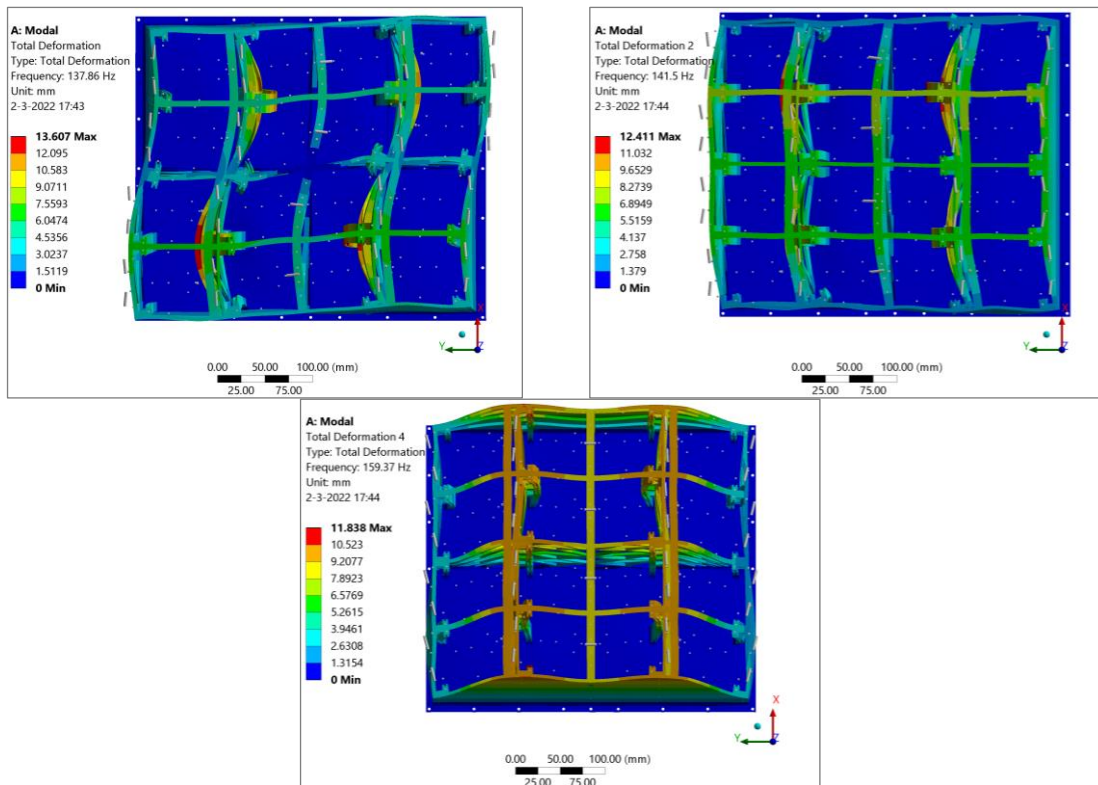


Figure 100: Modal analysis results multi pod version 5.

Increasing top rib thickness in X axis increased system frequency. Insignificant mode increased to 137.8 Hz and significant modes in Y and X directions were at 141.5 Hz and 159.4 Hz respectively. Modal deformations of these modes are shown in Figure 100.

Having made all the described changes to the structure of multi pod PDS, natural frequency requirement is met by this version. Launch vehicle loads were applied to this version of multi pod PDS and the results of these analyses are discussed in Section 5.13.

## 5.13 Multi Pod Result Summary

With detailed discussion on multi pod structural design concluded in previous section, a summary of the design is presented in this section.

Modal result summary for the multi pod design versions is shown in Figure 101. Significant system natural frequencies, lowest frequency and configuration system mass are plotted for the various configurations discussed previously.

It is to be noted that in Figure 101 lowest natural frequency is plotted only for longitudinal configuration versions 3 and 5. It was for these versions that lowest frequency did not coincide with significant mode in a direction. Additionally, for longitudinal configuration versions 4 and 5, significant mode in Z direction is out of range of plot in Figure 101.

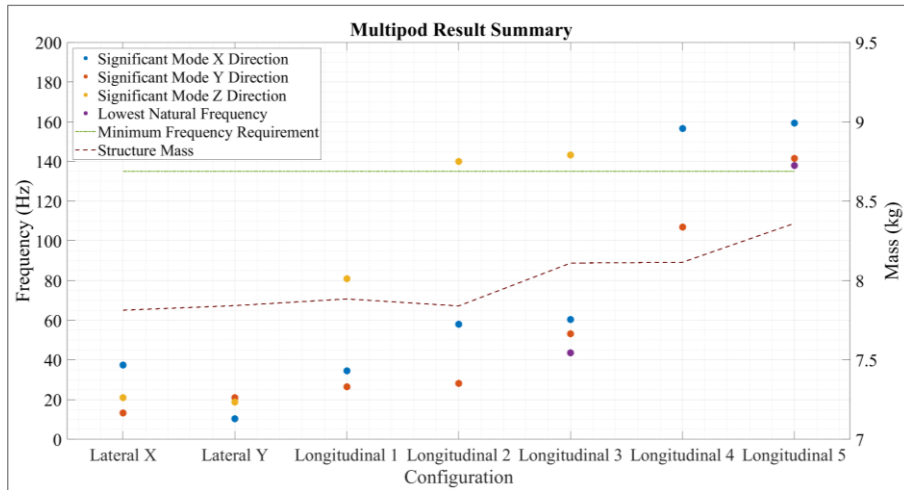


Figure 101: Multi pod result summary.

System mass increases for transition from longitudinal version 2 to 3 due to the addition of mid rib in Y direction and for version 4 to 5 due to addition of 4 ribs at the middle of guide mechanism and thickening of top rib in X direction.

Based on the experience of single pod PDS structural design, version 5 of longitudinal multi pod structure was modified before conducting launch vehicle load analysis. A boss of 2 mm height was added near the launch vehicle mounting locations on -Z panel. The addition of boss did not result in any significant changes to system frequencies. Summary of load analysis in different directions is shown in Table 28. It is to be noted that the values recorded in Table 28 are maximum values for all variables. The location of occurrence of these maximum values can be found in Section 11.1.6.

Table 28: Structural analysis result summary multi pod PDS.

Direction of Excitation		X	Y	Z
Quasi-Static	Deformation (mm)	0.25494	0.30428	0.094096
	Stress (MPa)	118.3	79.971	51.5
Sinusoidal	Deformation (mm)	0.087023	0.13636	0.028895
	Stress (MPa)	25.852	32.535	7.2532
Random	Deformation X (mm)	1.0679	0.40197	0.16402
	Deformation Y (mm)	0.34647	1.4956	0.59069
	Deformation Z (mm)	0.63157	0.52229	0.83749
	Stress (MPa)	387.19	356.64	258.07

The detailed structural response of all analyses are shown in Figure 146 to Figure 157. Based on structural analysis results, margin of safety is calculated for all three excitation axes. Margin of safety is calculated considering cumulative stress values based on all analyses and Equation (51). Table 29 shows the margins of safety in respective directions for multiple pod PocketQube Deployment System. Similar margins of safety were obtained when random input PSD was changed to less than 22.7 kg levels.

Margin of safety is positive for excitation in Y and Z directions. However, MoS is negative for excitation in X direction. The occurrence of maximum stress for this loading axis is at the launch vehicle mounting location holes on -Z panel (seen in Figure 148, Figure 149). Two solutions are proposed to obtain a positive MoS in X direction. To increase height of boss in order to distribute encountered forces over a larger surface or to manufacture -Z panel using



titanium alloy. Increasing the boss height to 3 mm increased system mass by 4 grams and changing the material to titanium increased it by 207.5 grams. Therefore, the preferred solution is to increase height of boss.

*Table 29: Design margin of safety – Multi pod.*

<b>Direction of Excitation</b>	<b>X</b>	<b>Y</b>	<b>Z</b>
<b>Margin of Safety</b>	<b>-0.115447301</b>	0.001820329	0.48347722

Although margin of safety is positive for loading in Y direction, this orientation is not preferred for launch vehicle mounting. In Figure 152, directional deformation in Y direction is maximum (~1.5 mm) near the pin puller mounting location. Although measured deformation is not critical, it increases the likelihood unintended release of door mechanism due to dynamic loading. Hence, this mounting orientation is not preferred and the alternative for this mounting would be coinciding the launch vehicle longitudinal axis with X axis of PDS.

The multi pod PDS structure in its current form meets design acceptance for Z axis and would meet design acceptance in X axis if proposed changes to LV interface boss height are implemented.

The material selection for the different structure components were based on maximum stress experienced by the component. Material selection for the components for single and multi pod configurations are listed in Table 55 and Table 56. Limiting factor for the structure from a launch vehicle load perspective was the random vibration input levels. Response analysis for the shock spectrum consistently yielded stress values lesser than  $3\sigma$  estimations of structure random response.

This concludes chapter discussion on structural analysis of the PocketQube Deployment System. Final design, prototyping and system integration is discussed in further chapters.

# 6.

## Final Design

The chapter is dedicated to discussion on the final design of PocketQube deployment system. PQ stacking, Single pod, and multi pod final designs are discussed followed by discussion of safety and additional features. Mass and cost budgeting for the systems are conducted to estimate total costs for the respective systems.

Deployer ratios of the single and multi pod PocketQube deployers are compared with CubeSat deployers to evaluate overall system performance. Finally, costing of deployers is carried out to evaluate suitable system configuration when PocketQubes deployed per mission is between the capacity of single pod and multi pod system and costs are compared to existing deployers.

### 6.1 PocketQube Order in Pod

In this section, the best permutation for stacking of PocketQubes within the deployer pod is evaluated. For determining the order of spacecraft in deployer pod, two spacecraft properties have to be considered. They are: PocketQube size and PocketQube centre of mass (CoM) with respect to its geometric centre (GC). The sensitivity of system natural frequency to changes in PQ centre of mass was discussed in Section 5.9. Dimensions and mass of different PocketQube unit sizes was discussed in Section 2.2.

Of the two properties mentioned above, change in centre of mass of spacecraft would be considered with higher priority (due to sensitivity of system natural frequency). The allowable change in spacecraft CoM is constrained by the PocketQube standard and has a maximum value of 10 mm in any given direction [2]. If the PocketQubes follow the standard and their CoM are located within the stipulated region around their geometric centre, then the PocketQube order in pod will be dictated by the deployment velocity constraints discussed in detail below.

In Section 4.8, the effect of deployment velocity vector on separation distance was discussed. There it was concluded that, separation distance can be approximated as a product of deployment velocity and time since separation till about 5 minutes post spacecraft separation. Hence, higher deployment velocity indicates greater separation distance between spacecraft and the launch vehicle.

Various combinations of PocketQubes which can be accommodated in deployer pod was discussed in Section 2.10 and shown in Figure 19. Further in Section 4.3.4, it was concluded that the magnitude of deployment velocity not only depended on the size of PocketQube but also on its location in the pod. Of the different combinations shown in Figure 19, we consider the combination containing each of 1P, 2P and 3P PocketQubes for this study.

This combination was chosen because it provides the greatest diversity of PocketQube sizes. Hence, by analysing different permutations of this combination, a holistic perspective of

optimum PocketQube order can be derived for other possible combinations. The said combination offers 6 possible PocketQube stacking orders which are shown in Figure 102.

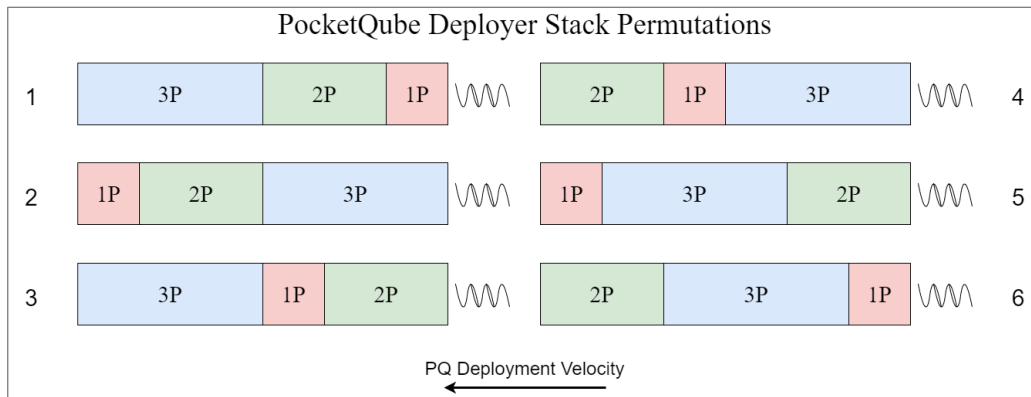


Figure 102: Possible permutations of PocketQubes in deployer (specific case).

For the six stacking orders depicted in Figure 102, deployment velocity is estimated similar to that conducted in Section 4.3.4 accounting spring load reduction after spacecraft separation. Table 54 tabulates the deployment velocity of PocketQubes based on position in pod and stacking order. It is to be noted that the top, middle, and bottom PocketQube in Table 54 is with respect to the location of spacecraft in Z axis and the size of PocketQube changes based on the order at each of the locations.

From values estimated in Table 54, relative velocities between launch vehicle and deployed PocketQubes are calculated. The relative velocities for different PQ order in pod is shown in Figure 103. Relative velocities are calculated as the difference between the respective spacecraft deployment velocities. Any additional relative velocity imparted by the separation springs is not accounted for. Therefore, this study can be considered as a conservative estimate.

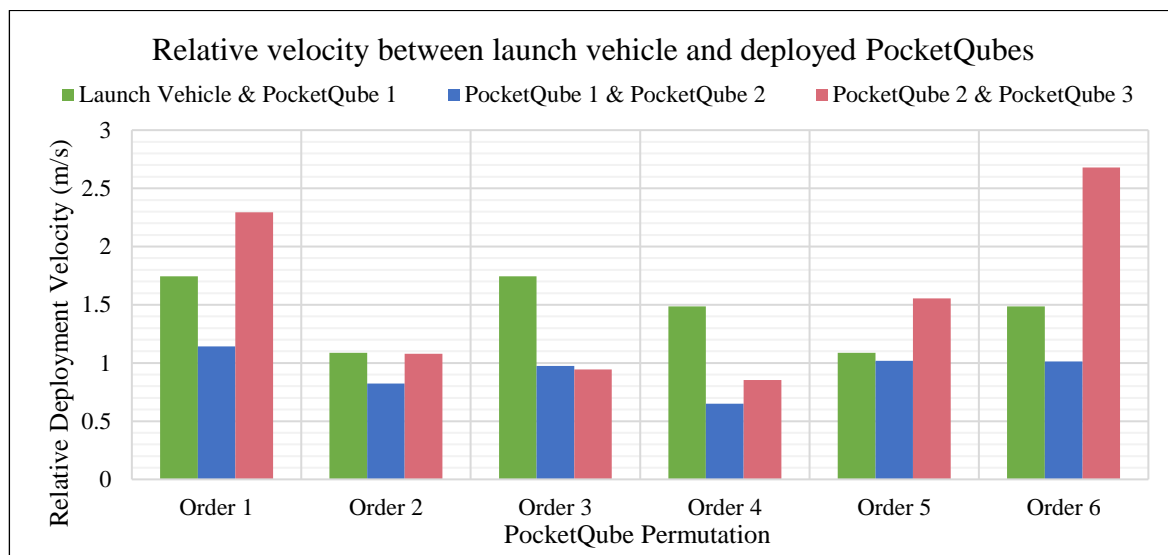


Figure 103: Relative velocities of launch vehicle and deployed PocketQubes (refer Figure 102).

It is the goal of this analysis to provide high relative velocity between objects which ensures greater separation distance. From Figure 103, it is observed that the PocketQube order 1 and 6 depicted in Figure 102 offers highest relative velocity between the considered objects (launch vehicle and deployed spacecraft). However, merely from a deployment velocity perspective, it would be optimum to place 1P adjacent to pusher plate, 2P in the middle and 3P on top of the pod (order 1).

Assuming that centres of mass for the three PocketQubes considered (1P, 2P & 3P) lie at their geometric centre, the different orders described in Figure 102 would have the same stack centre of mass when stacked in the pod. In reality however, it is highly unlikely that the centre of mass and geometric centre of PocketQubes coincide. Therefore, a the decision on order of PocketQube in pod shall be based on the actual centre of mass of PQs.

Further in Figure 33, the mass of PQs considered were assumed to be equal to maximum permissible mass for each type of PQ by the PocketQube standard. A change in PQ mass would also result in change in CoM of the stack. In order to quantify the change in stack centre of mass and relative deployment velocity when PQ masses are not equal, a similar study as mentioned above is reasoned out.

6 numbers of 1P spacecraft are stacked in pod for this study and the mass of these PQs are assumed to be successively reduced/increased by 10 grams each (0.25, 0.24, 0.23, 0.22, 0.21, 0.2 kg). These PQs are stacked in ascending and descending order of their mass in pod. The relative deployment velocities of the two stacks were compared and it was observed that the change in velocity is negligible for the two stack combinations. However, the stack centre of mass changed by a value of 16.59 mm in Z direction (considering CoM at GC). The stack CoM was lower when PQ with higher mass was placed lower in pod and this would be the preferred stack order when PQs of same size but different mass are to be placed in the pod.

In this study, PocketQube mass properties (mass and centre of mass) were individually varied while assuming other parameter to be according to the standard. Centre of mass of the stack of PocketQubes in the pod is given by Equation (53) where,  $CoM_{Stack}$  is the centre of mass of stack,  $CoM_{PQ}$  is the centre of mass of individual PQ, and  $m_{PQ}$  its mass.

$$CoM_{Stack} = \sum_{i=1}^{2-6} \frac{(m_{PQ})_i * (CoM_{PQ})_i}{m_{Stack}} \quad (53)$$

It is seen from Equation (53) that, stack centre of mass is not only dependent on the individual mass and centres of mass of PocketQubes but also on the location of PQ in pod. At this time since the actual mass properties of PocketQubes are unknown, the centre of mass of the stack shall be minimized from the perspective of deployment system stiffness. For the single pod configuration, structure stiffness is sensitive to changes in stack CoM in +Y direction and it is sensitive in +Z direction for the multi pod configuration.

In conclusion, when PocketQubes of same size are stacked in pod, the order in pod is dictated by PQ mass. When PocketQubes of different sizes are stacked in pod, a decision has to be taken on the order of the stack based on PQ size, mass, and centre of mass.

## 6.2 Single Pod

Final design of single pod PocketQube deployer is shown in Figure 104. Harness routing for the system is shown in red. The harness on the launch vehicle end will be terminated with a 9 pin connector. This eliminates any timing electronics as trigger signal would be received from the launch vehicle deployment sequencer. A total of 6 pins would be in use of which 4 will be for deployment trigger signal (2 main, 2 redundant) and 2 for deployment telemetry signal.

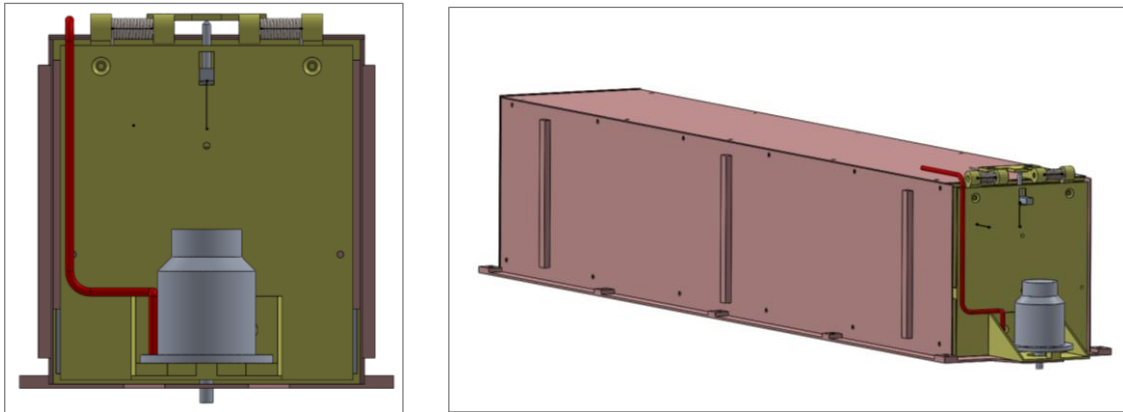


Figure 104: Harness routing single pod.

Venting of gases from within the pod during launch vehicle fairing depressurization in the atmospheric phase of flight has to be accounted for. It was found that the clearance gap between door assembly and pod panels are sufficient for venting.

## 6.3 Multiple Pod

The final design of multi pod PocketQube deployer is discussed in detail.

### 6.3.1 Structural Changes From Single Pod

Certain changes have to be made to the structural design of multi pod system from the single pod design. A list of these changes are based on structural analysis of multi pod system and discussed below.

1. Reduced door length in Y direction by 5 mm because 5 mm thick rib was removed for the configuration (between pods).
2. Attachment for door assembly is moved from rib to guide mechanism. As a result push back assembly is moved towards the door hinge.
3. Increased pod dimensions of eight pods in Y direction by 16 mm to accommodate adjacent door assembly clearance at its deployed position. The pods which have increased dimensions are 1 to 8 (see Figure 108).
4. Guide mechanism length is reduced by 5 mm to accommodate top rib. As a result, Hinge 2 and door retainer plate length was increased by 5 mm.
5. Side ribs of 2 numbers were added adjacent to  $\pm X$  panels, and mid ribs were added between pods in X and Y directions for additional stiffening.

This concludes the list of changes made for the multi pod structure components.

### 6.3.2 Deployer Footprint

The final launch vehicle footprint of multi pod PDS is shown in Figure 105. Final footprint dimensions of multi pod PDS are close to preliminary dimensions estimated in Section 4.10.1. PDS footprint dimensions are similar to multi pod CubeSat deployers. Hence, **PDS-LVR-010** requirement is satisfied enabling multiple launch vehicle adaptability of the deployment system.

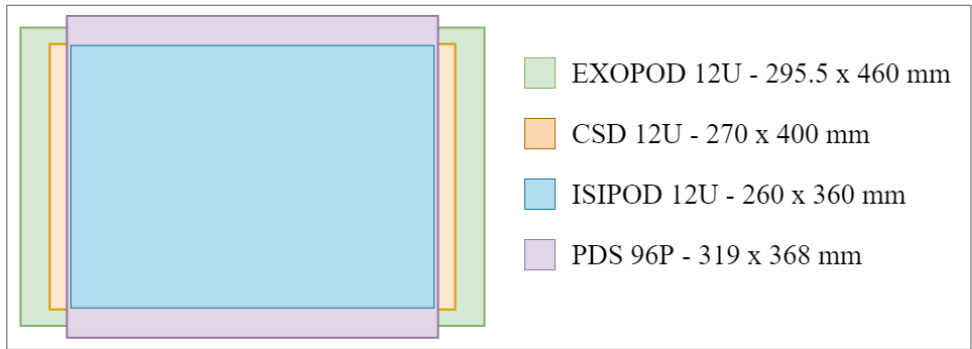


Figure 105: Multi pod deployer final footprint comparison.

### 6.3.3 Deployment Separation

In this section, an understanding on the time delay between successive pod door actuation is considered. Time difference between successive door actuations must be optimized considering adequate separation between spacecraft and total time required for the release of all PocketQubes.

Assumption for this analysis is that PocketQubes deployed from different pods have identical velocity vectors. Separation distance between PocketQubes is calculated as the product of deployment velocity and time between actuation of successive pods based on results discussed in Section 4.8. Note that as PDS would be mounted on final stage of the launch vehicle, the separation distance is the distance between the deployed PocketQubes and launch vehicle upper stage.

Based on Figure 34 where PDS deployment velocity for PocketQubes ranges from 1 to 2.2 m/s, velocity is varied from 1 to 2.4 m/s for this analysis. Figure 106 shows the variation of separation distance with deployment time between pods and PocketQube deployment velocity for stated range.

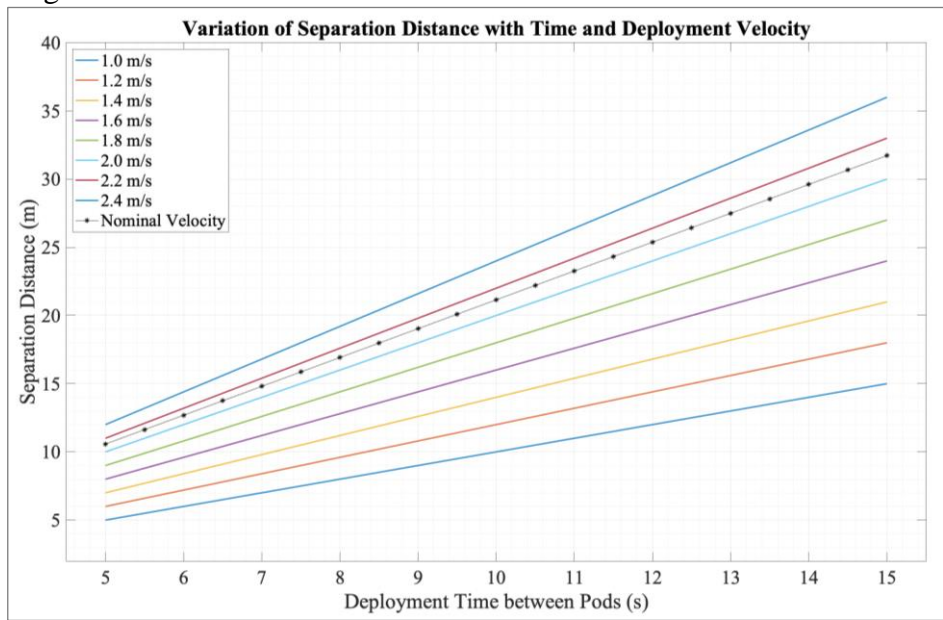


Figure 106: PocketQube separation distance variation.

The goal of this study is to select the time between successive pod door actuations. Ideally, long separation time would be considered, however, as PDS would not be a primary payload, the actuation time between pods shall be as little as possible to ensure injection parameters of the launch vehicle are met for all of its payloads.

A PocketQube of size 3P has a maximum dimension of 192 mm in Z axis. The deployer envelope volume being 6P for a pod, the maximum dimension of PocketQubes will be less than 0.5 m in the direction of deployment (Z axis). Hence, a separation distance of 10 meters is selected which is sufficiently higher than PocketQube largest dimension.

Considering minimum deployment velocity of 1 m/s as a conservative estimate and a separation distance of 10 m, the time between successive pod door actuation is selected to be 10 seconds. In real world scenario, it is highly unlikely that deployment velocity vectors of PocketQubes will be unidirectional. As we have considered worst case magnitude of deployment velocity, the separation distance will be greater than 10 m for most actuations.

Angular separation of deployment velocity vectors between successive deployments can be estimated. For this estimation the assumptions are:

1. Launch vehicle upper stage is in a circular earth orbit. Hence, orbital velocity along is orbit does not vary.
2. Considering upper stage mass is considerably higher than injection spacecraft, velocity change of launch vehicle due spacecraft injection is negligible.
3. Launch vehicle upper stage attitude does not vary during PQ deployment process.
4. PocketQube deployment velocity vectors are tangential to orbital plane and perpendicular to instantaneous orbital radius vector (parallel to LV velocity vector).

Orbital period for an object in circular orbit is given by Equation (54), where  $t_P$  is the orbital period,  $R_E$  radius of earth,  $h_o$  orbital height, and  $\mu_E$  the gravitational parameter for planet Earth.

$$t_P = 2\pi \sqrt{\frac{(R_E + h_o)^3}{\mu_E}} \quad (54)$$

Considering orbital velocity vector rotates an angle of  $360^\circ$  over an orbit, Figure 107 is arrived at for varying deployment time between pods. Angular separation of deployment velocity vectors decreased with orbital height as orbital period increases with height. Angular separation increases as expected for an increase in time between door actuations.

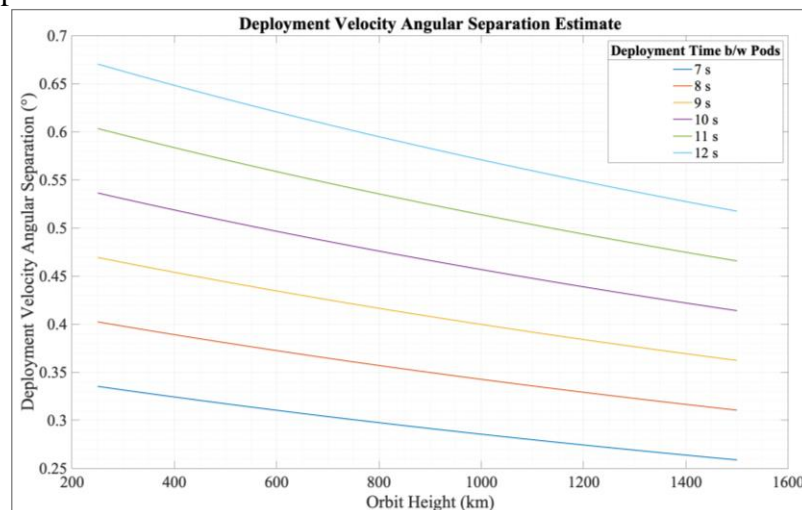


Figure 107: Deployment velocity angular separation estimate.

For a successive pod door actuation time of 10 seconds, it is seen in Figure 107 that the angular separation between PocketQubes of each pod varies between  $0.55^\circ$  and  $0.41^\circ$  for low earth orbits. The angular separation combined with a minimum separation distance of 10 meters is sufficient to ensure separation of the deployed PocketQubes from different pods. Hence, 10

seconds is chosen as the minimum time delay between successive actuations for the multi pod deployment system. Total deployment time would be 160 seconds without considering the time for pin puller actuation. However, it is likely that all PQ deployments will be completed within 180 seconds (3 minutes) under nominal condition.

### 6.3.4 Deployment Sequence

Having discussed the time delay required for safe and efficient deployment of PocketQubes from the multi pod deployer, this section will focus on the sequencing of pod actuation. Deployment sequencing is an important aspect for the multi pod PDS. It has to be carefully planned to ensure there would be no interference between the deploying PocketQubes and deployer structure.

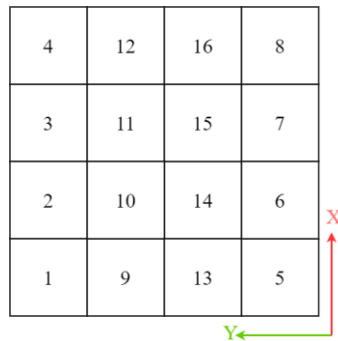


Figure 108: Multi pod deployment sequence.

Sequence of deployment for the multi pod deployer is shown in Figure 108. Outer pods in Y direction are chosen to be actuated first. If inner pods are deployed before outer pods, interference between deployed door assembly and PocketQubes are a concern (due to door assembly locking position). The deployed door would encroach on appendage volume assigned to PocketQubes that are deployed from adjacent pods. Hence, to avoid this scenario, the sequence shown in Figure 108 is preferred. Further, this sequencing pattern would provide a minimum of 40 seconds of time delay (not accounting the time required for pin puller actuation) between actuation of adjacent pods. This delay provides additional temporal margins to further reduce chance of PocketQube collision.

### 6.3.5 Power Requirement

Power requirement of the multi pod PocketQube deployer can be a constraint due to the number of actuations that are demanded. With 16 pods to be actuated by the deployer, electrical energy required for successful deployment of all pods are discussed in this section.

Based on pin puller power requirements (nominal power 1.25 W@ 0.4A for 160 ms) [71], total of 20 W would be required nominally to deploy all 16 release mechanisms present on multi pod deployer. However, energy required for actuation increases with a decrease in temperature. Therefore, a margin has to be considered for actuation in cold temperatures. Actuation time increases from 160 to 330 ms when ambient temperature decreases from 23°C to -65°C. Therefore total energy required to trigger pin retraction would increase by a factor of 2.2 (considering similar deployment current).

Total energy required for deployment is given by Equation (55), where,  $N_d$  is total number actuations,  $P_e$  is power required for actuation,  $T_e$  is time required for actuation, DOD is permissible Depth of Discharge (DOD) for battery, and  $C_B$  is battery capacity required.

$$C_B = N_d(P_e T_e) / DOD \quad (55)$$

Considering a lithium ion battery for its high specific energy density, a recommended DOD is 80% [117]. Based on these factors a total of 8.25 J would be the required capacity for powering the deployment sequence.

The source of this energy would depend on launch vehicle used for the mission. If launch vehicle has sufficient stored electrical energy for the deployment sequence, deployment of PocketQubes can be carried out using launch vehicle battery power. If not, a separate battery can be installed to provide the electrical energy for deployment. The source of deployment



power for the multi pod deployment system would be defined based on the type of launch vehicle used and launch vehicle power margins.

## 6.4 Safety Features

Having discussed the final design of single pod and multi pod PDS, this section is dedicated to the safety features that are incorporated within the design of the deployment system. Safety features are necessary to account for any anomalies that occur during the operation of the deployment system. Different safety features and their functions are discussed below.

### 1. Electrically Redundant Pin Puller Actuation :

Pin puller actuation is the first step in release of PocketQubes from pod. Hence, nominal pin puller release mechanism operation is mission critical. To ensure pin release, two electrically isolated redundant trigger circuits are utilized. By providing two independent trigger signal paths, multiple actuation signals can be routed through them to reduce chance of sub-system failure due to electrical contacts. As pin puller is a procured component, electrical redundancy is a requirement for choosing a suitable pin puller.

### 2. Main Spring Locking Mechanism :

Main spring is the component that provides required PocketQube deployment energy. Unintentional release of main spring would release the PocketQubes held within the pod (provided door is deployed). Main spring locking mechanism is designed to avoid this scenario by incorporating two Remove Before Flight (RBF) fasteners. The RBF fasteners are installed from -Z panel and attaches to bottom of pusher plate guide. When these RBF fasteners are in place, the main spring cannot extend and therefore is locked in place. PocketQube integration into pod is simplified with the main spring locking mechanism and the RBF fasteners can be removed to arm the main spring for flight.

### 3. Door Assembly Locking Mechanism :

In previous sections, the allowable rotation of door assembly was fixed based on the clearance requirement for the deploying PocketQubes. Door assembly locking mechanism is required to lock the door assembly once the assembly has reached its deployed position. The function of this mechanism is to avoid bouncing back of door assembly due to angular momentum imparted to the assembly by the torsion springs. The details of this mechanism was discussed in Section 4.4.1.

### 4. PocketQube Push Back Mechanism :

This mechanism is designed to resist movement of PocketQubes in Z direction during launch phase of a mission. By resisting PocketQube movement within the guide rail, any possible excitation of main spring-PocketQube(s) system to launch vehicle dynamic loads are avoided. Further, restricting movement in rail reduces wear between PocketQube backplate and guide rails. For PocketQubes with FR-4 backplate, this mechanism would ensure delamination of material is limited. The details of this mechanism was discussed in Section 4.4.2.

Having discussed the design safety features, additional features are discussed in the next section.

## 6.5 Additional Features

This section details the additional appendage volume available for PocketQubes. The additional available volume is shown in Figure 109. It is to be noted that this volume is only available for the bottom PQ in a pod and upon request. The additional volume is available due to compactness of main spring and pusher plate assembly design.

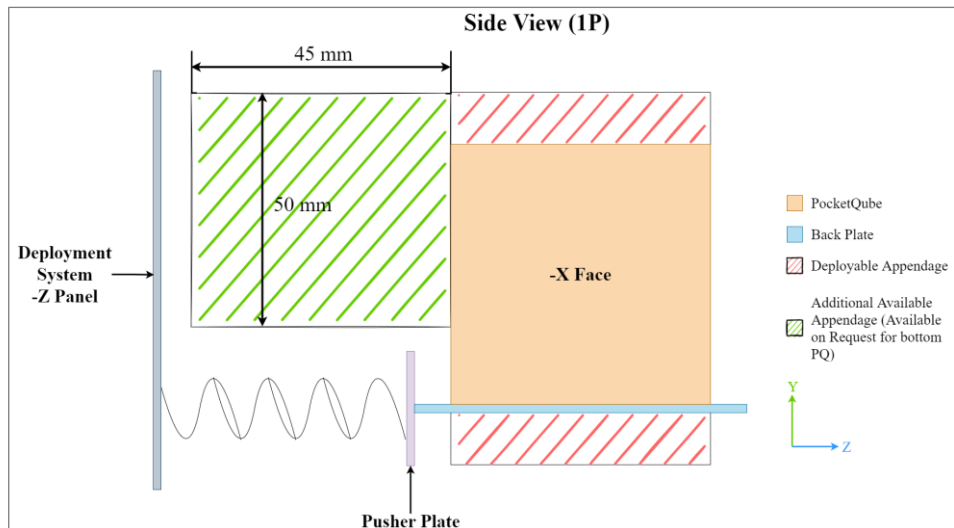


Figure 109: Additional appendage volume in -Z direction<sup>G</sup>.

## 6.6 Mass Budget

Having discussed the final design and features of PocketQube Deployment System, this section details the mass budgets for single and multi pod deployment system. A comparative study between PocketQube and CubeSat deployers is conducted in the Section 6.7.

Mass breakdown for single pod and multi pod PocketQube deployers are given in Table 55 and Table 56 respectively. Total mass for single pod deployment system is about 845 grams. Total mass for multi pod deployment system is 9.67 kg. In order to compare the two systems, mass is normalized using PocketQube units deployed by each system. Deployer electronics mass is budgeted as 30 grams for single pod and 50 grams for multi pod system. For multi pod system, additional mass has to be accounted if separate battery is used for pin puller actuations.

Single pod system with deployer capacity 6P has a mass of 140.3 grams/P unit and multi pod system with deployer capacity 96P has a mass of 100.7 grams/P unit. Multi pod deployer saves about 40 grams in system mass per P unit deployed to orbit. Single pod deployer requires about 40% additional structure mass to deploy same number of PocketQubes as multi pod deployer.

It is evident multi pod deployment system is more efficient with respect to system mass. Mass comparison of PDS with other pod based deployers is carried out in the next section.

## 6.7 Deployer Mass Comparison

Having discussed the mass budgets for PocketQube deployment system, a comparison of pod based spacecraft deployers is carried out in this section. Mass comparison of different deployers is shown in Figure 110. Similar to Figure 16, deployer masses are compared by computing the deployer ratio as discussed in Section 2.7.

Deployer ratio for single pod PDS is 1.8 and for multi pod PDS is 2.5. Single pod deployer ratio is marginally higher when compared to 3 unit CubeSat deployers (except Maxwell). It is evident that the parametric study conducted to reduce structure mass of single pod PocketQube deployer results in a high deployer ratio.

<sup>G</sup> Available on request for bottom PQ in pod.

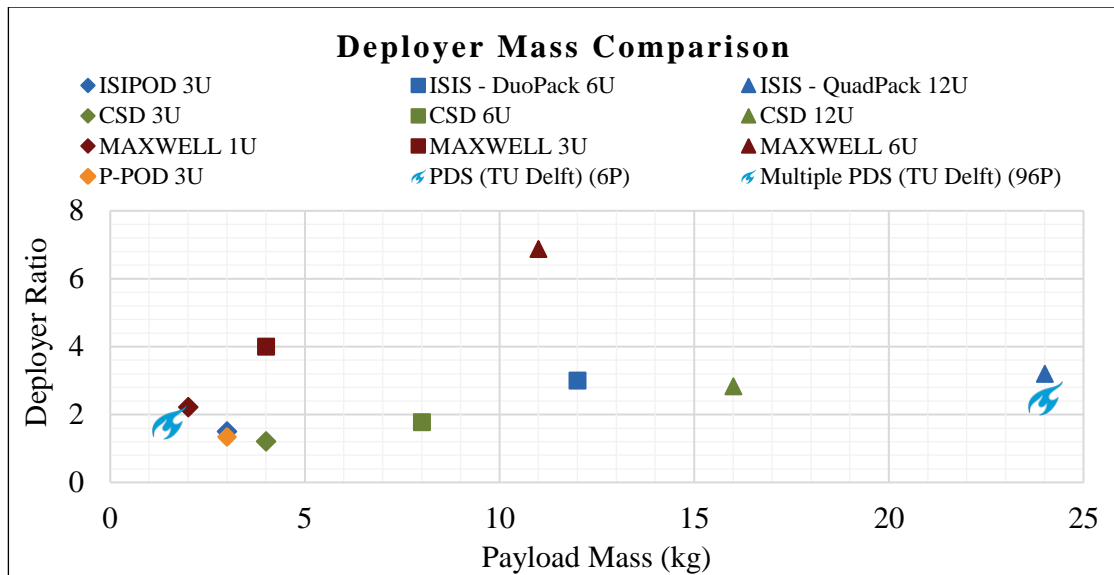


Figure 110: Mass comparison between PocketQube and CubeSat deployers [13], [14], [16], [38].

Multi pod PDS is compared to 12U deployer (ISIS – QuadPack) because both the deployers have equal payload capacity. ISIPOD – 12U has a deployer ratio of 3.2 whereas multi pod PDS has a ratio of 2.5. For equal mass of payload deployed to orbit, ISIPOD – 12U achieves greater system mass efficiency when compared to the multi pod PDS. A possible reason for this discrepancy would be that the spacecraft class for the deployers are different. However, this would account for minor variation in deployer ratios between the two deployers. Further, mass optimization of multi pod PDS structure would increase the deployer ratio for the multi pod PocketQube deployer.

With the comparison between pod based deployers completed, findings on the costs associated for PocketQube deployer configurations are discussed.

## 6.8 Cost Budget

Having discussed the mass budget of PDS and comparing PocketQube and CubeSat deployer mass, we estimate the costs involved for deployment system. System cost is shown in Table 30. Bulk ordering is considered as procurement and manufacturing costs for nonstandard parts would be reduced due to economies of scale. A total of 100 numbers are considered for bulk orders.

Table 30: PocketQube Deployment System Cost Breakdown.

System Cost (€)	Single Order		Bulk Order	
	Single Pod	Multi Pod	Single Pod	Multi Pod
Procurement Cost	5074.23	81025.7	5043.48	80577.7
Manufacturing Cost [80]	3725.79	39531.94	271.17	2179.12
Assembly and Integration Cost	180	1700	180	1700
Environmental Test Cost	25000	25000	25000	25000
Launch Cost	133562.58	1920444.96	133562.58	1920444.96
<b>Total Cost</b>	<b>167542.6</b>	<b>2067702.6</b>	<b>164057.2</b>	<b>2029901.7</b>
<b>Cost / P Unit</b>	<b>27923.77</b>	<b>21538.569</b>	<b>27342.87</b>	<b>21144.81</b>

Procurement and manufacturing costs are based on quotations received from respective manufacturers. Manufacturing costs include raw material, machining and secondary treatment

costs for the different parts. Assembly and integration costs estimates in Table 30 are based on prototyping experience, estimation methodology is discussed in Section 8.3. Launch cost is estimated using system mass and launch cost per kilogram as discussed in Section 2.6.

Procurement cost is driven by pin puller acquisition as it is the biggest contributor. System cost would reduce by a considerable amount if alternative release mechanism like wire cutter would be utilized. However, pin puller costs can be offset if release mechanism will be reused in the future from launch vehicle technology advancement.

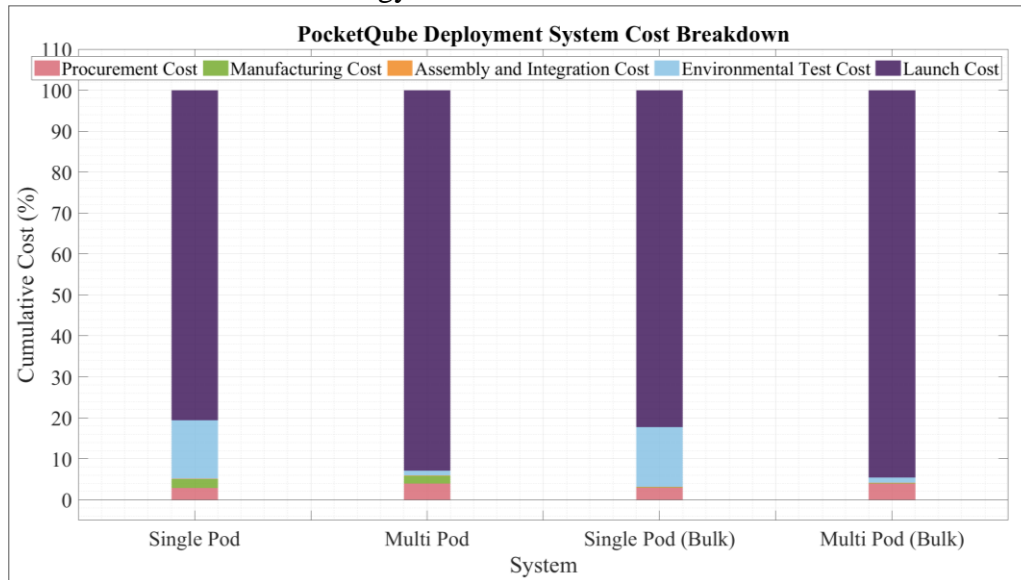


Figure 111: PocketQube Deployment System cost division.

Contribution of the different costs discussed in Section 2.5 to overall system cost is shown in Figure 111. It is evident from Figure 111 that the biggest contributor to system cost would be the launch cost. At least 80% of the total system cost is required for launching spacecraft into orbit. As system mass is the driver for launch cost, it is necessary to optimize deployment system mass to reduce total cost. Hence, increasing the deployer ratio for the multi pod deployer would result in further reduction in system cost for this configuration. Figure 111 also shows that manufacturing costs for both systems reduce as a percentage of overall cost when bulk manufacturing is carried out. Manufacturing cost decreased by 91.73% for the single pod and 94.5% for the multi pod for mass production.

To compare the costs between the single and multi pod deployment system, system cost is normalized to PocketQube units deployed by the respective systems. The normalized cost for the single pod deployer is about 28,000 € whereas for the multi pod deployer it is about 21,500 €. By utilizing the multi pod deployer, about 6,500 € can be saved per P unit of spacecraft mass deployed.

It is important to highlight that the deployer mass for single pod system was reduced by conducting a parametric study, and such a study was not conducted for the multi pod deployer. With launch cost (dependant on system mass) being the largest driver of system cost, optimizing system mass of the multi pod deployer will further reduce normalized cost.

In conclusion, it is observed that multi pod PDS, is cost efficient when considering cost per payload accommodated. The cost breakeven point between single pod and multi pod systems is discussed in the next section.

## 6.9 Deployer Choice

This section is dedicated to discuss the choice of deployer to be utilized when total PocketQubes to be deployed lie between the capacity of a single pod and a multi pod deployer. The choice for deployer is simple when PocketQube numbers lie close to the capacity of each of the deployers (6P & 96P respectively). In the case that total PocketQube units to be deployed is spread in between thus stated capacities, this section addresses which configuration of the deployment system to utilize.

Total cost to orbit for PocketQubes of different capacities is shown in Figure 112 for single pod and multi pod deployment systems. With the current design of deployment system, total system cost would even out if a payload capacity of 66P units are deployed using the multi pod deployer. Hence, if total payload capacity is equal to or greater than 66P units, it is preferred to use the multi pod deployer. For a payload volume lesser than 66P units, total cost would be lower when using multiple single pod deployers.

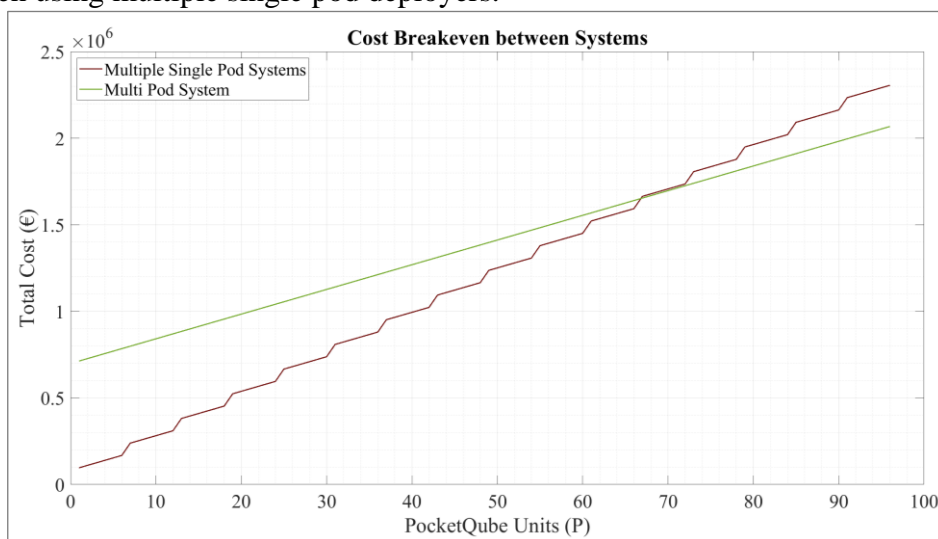


Figure 112: Cost breakeven between systems.

Figure 112 considers the average normalized cost for launch cost estimation. However, based on the launch vehicle selected for a mission the breakeven costs vary. Figure 113 shows the breakeven cost between the single pod and multi pod system for different launch vehicles accounting for their specific launch cost shown in Table 39. Figure 113 shows that the cost breakeven was observed to be at 72P units for most launch vehicles, whereas, for Falcon class launch vehicles it is at 78P units.

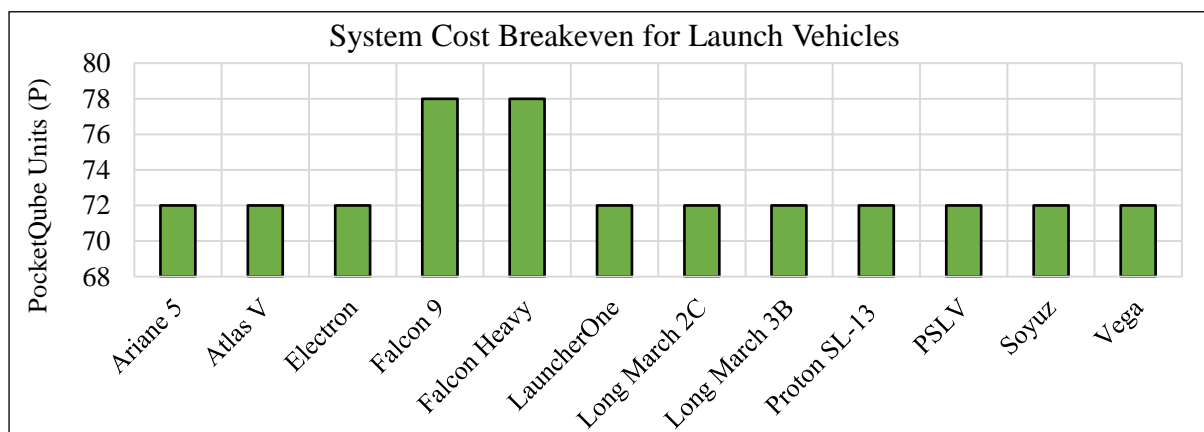


Figure 113: Breakeven cost for different launch vehicles.

As discussed previously, reducing multi pod system mass will reduce its total cost and hence, the cut-off point between the use of multiple single pod systems and multi pod deployer would also decrease.

## 6.10 Deployer Cost Comparison

Having discussed the total system cost and breakeven point between system configurations, this section is dedicated to cost comparison between pod based spacecraft deployment systems. It is a convention that launch service providers only specify the launch cost for spacecraft [118]. The companies provide system level environmental testing (TVAC & Vibration) as a service which would incur additional costs.

In Section 6.8, system costs were estimated for the PocketQube Deployment System. Included in the cost budget (Table 30) was the cost for system level environmental testing. In order to even out the comparison between PDS and commercial launch providers, environmental testing cost is deducted from total cost. The reasoning behind this decision is that the launch provider (TU Delft) can charge spacecraft manufacturers for system level environmental testing before flight and system qualification tests are only a one time cost for the PDS.

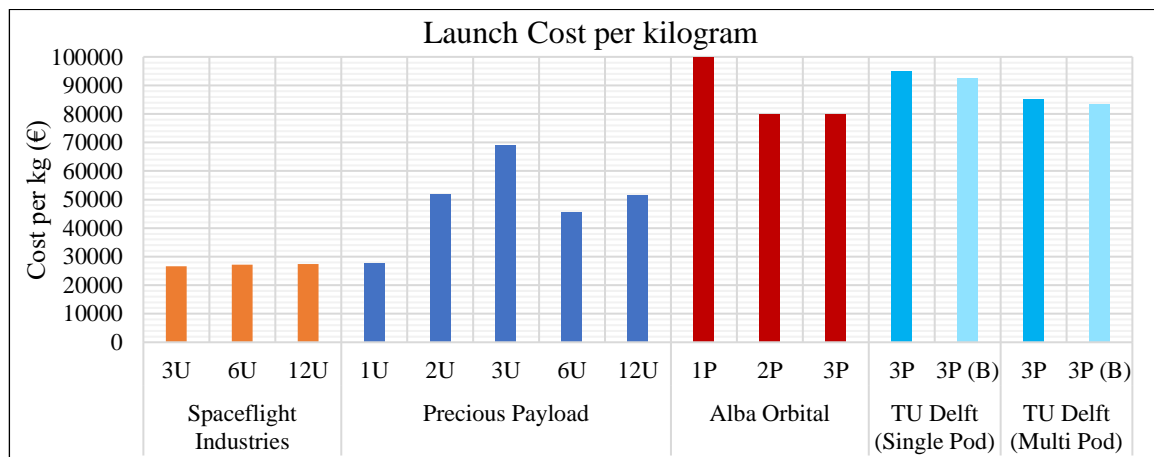


Figure 114: Launch cost comparison per kilogram [118], [119], [120].<sup>H</sup>

Figure 114 shows the launch cost per kilogram of spacecraft launched. As pod based deployers are designed for different spacecraft standards, launch cost per kilogram helps in comparing costs between CubeSat and PocketQube deployers. In Figure 114 it is observed that the launch cost per kilogram for PocketQubes is higher than that for CubeSats. Additionally, the PDS cost is similar to other commercially existing PocketQube deployment system (AlbaPOD). It can therefore be inferred that the launch cost per kilogram estimated in Section 2.6 would be in the range predicted by this study.

Although launch cost per kilogram helps us to compare launch costs of different spacecraft standards, it does not provide an overall perspective into spacecraft mission cost. In order to compare the actual costs for launching the mentioned spacecraft, launch cost per spacecraft is considered. Figure 115 shows the launch cost per spacecraft for different CubeSat and PocketQube unit sizes. Launch cost for the same unit size vary across different manufactures as expected.

<sup>H</sup> Launch costs shown are for LEO.

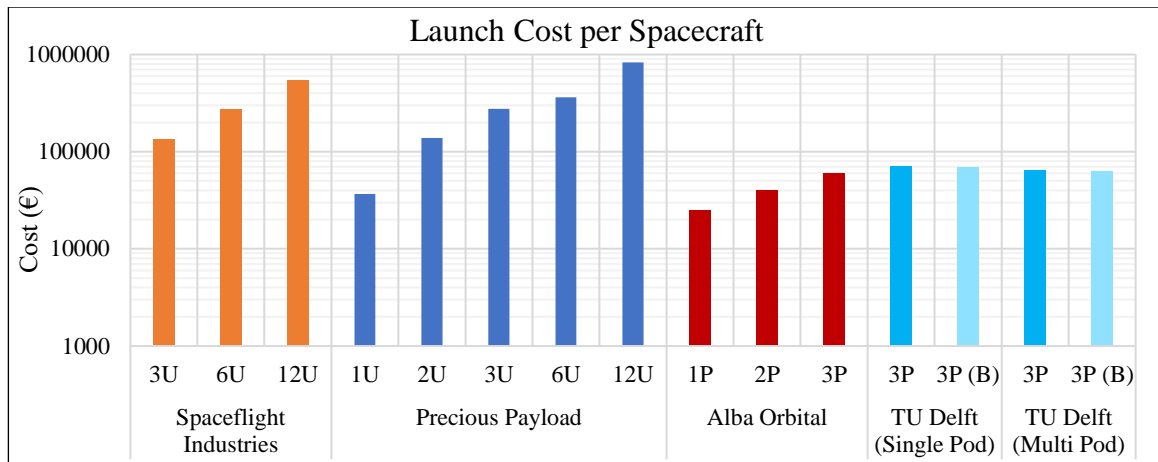


Figure 115: Launch cost per spacecraft comparison per [118], [119], [120].<sup>1</sup>

However, launch cost for PocketQubes are lower than that for CubeSats. As the total cost to launch PocketQubes are lower than that for CubeSats, PocketQubes reduce the entry barrier to space. Further costs can be lowered by utilizing multi pod deployer and performing a structure mass optimization for this system configuration.

This concludes the discussion on final design of the PocketQube deployment system.

<sup>1</sup> Launch costs shown are for LEO.

# 7.

## Prototyping and Testing

The chapter will focus on the discussion of system prototyping, main spring characterization testing and door deployment testing. Structure prototyping was carried out to arrive at a suitable integration procedure for the system.

Main spring characterization testing was performed to characterize spring force along its stroke length. Characterization test is conducted to ensure main spring properties are within its designated window of operation as specified by the manufacturer. Door deployment test was carried out to validate torsion spring model and to predict door deployment time for standard gravity conditions.

### 7.1 Structure Prototyping

Structure prototype was manufactured in order to verify the design of PDS. Additionally, it would also provide a benchmark for system integration and help in detection of potential flaws of the deployment system.

A decision was taken to 3D print all structural members of PDS except the panels. The panels would be manufactured using acrylic sheets and assembled onto the structure. Replicator 5<sup>th</sup> Gen manufactured by MakerBot was used for 3D printing parts for PDS prototyping. The printable volume of this printer was not sufficient to print the parts in whole, hence some modifications had to be made on the model to ensure 3D printing was possible.

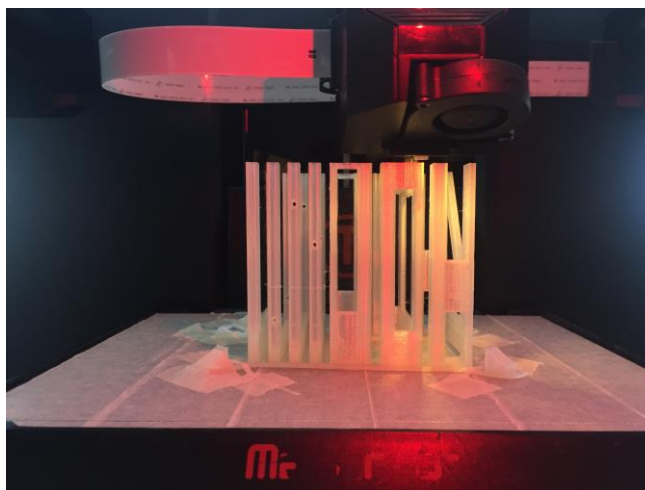


*Figure 116: PDS structure 3D printing.*

Guide mechanism and support rib were split into printable sizes along their length and a number of fasteners were added to fit them together at the end. Print material was Poly-lactic Acid (PLA). Tolerance of certain parts were modified to accommodate for the expansion of the PLA



material after 3D printing. Structural ribs, door assembly and the pusher plate assembly were 3D printed using this method.

The 3D printed parts were subsequently assembled using fasteners. Following which, assembled prototype was used for in-depth analysis of integration constraints and door deployment testing. The lessons learned from integration of PDS prototype will be discussed in Chapter 8.

Having discussed the constraints of deployment system prototyping, characterization testing for the main spring is described.

## 7.2 Main Spring Characterization Test

Main spring is critical sub-system within the PDS as it is the component which provides the necessary force to achieve deployment of PocketQubes. Therefore, it becomes essential to identify, by means of a test, if the spring provides required deployment force. The goal of this test is to verify if the spring force of the compression spring satisfies its designated force-stroke curve in Section 4.3.4. It is expected that the spring force does not exceed the error values as defined by manufacturer tolerance values in Figure 29.

This test investigates the uncertainties that may arise in the manufacturing of the compression spring. By characterization of the spring specimen, confidence is achieved to satisfy the designer that main spring is working within its intended operation window.

### 7.2.1 Test Method and Setup

Initial method planned for the test was to provide spring load with a beaker of water for variable force on the spring. By balancing the beaker containing water vertically on the spring, required force to compress the spring could be generated. In order to alter the characterization force on the compression spring, water level in the beaker could be varied. However, as the maximum force of the spring is 15 Newtons, the required volume of water was approximately 1.5 litres. A suitable beaker of such volume could not be accessed, therefore a change in test plan was needed.

Upon accessing the tools available at the workshop belonging to Space Engineering section of TU Delft, two possibilities were explored. First possibility was the use of spring based weighing scale as a way of producing the required characterization force. However, due the design of the weighing scale (hook on the weighing end), the test apparatus created a force imbalance on the compression spring which introduced a measuring error. Accordingly, another method had to be thought of.

The second possibility was the use of calibrated weights as a method to produce the required characterization force. The total mass of the calibrated weights were 600 grams which was less than needed 1.5 kg. Therefore, a quick solution was found using metal slabs lying around the workshop. The mass of these metal slabs had to be known with sufficient accuracy in order to use them to provide characterization force.

A digital weighing scale was checked for its accuracy using the calibrated weights following which the mass of metal slabs were measured. Apart from the calibrated weights, three metal blocks of mass 875, 240, 250 grams respectively were used. These blocks along with the calibrated weights were used in different combinations to obtain the a range of required

characterization force. Table 57 lists the combinations of weights used and the force applied on the spring.

Additionally, a thick disk with a hole in its centre was 3D printed to balance the weights on top of the spring. Mass of the part was measured to be 36 grams. Centre hole was provided for a cylindrical rod to pass through which provided a balance for the test set up. A measuring tape was attached to a vertical surface in order to measure spring deflection. Figure 117 shows the test setup with weights placed on the 3D printed part resulting in spring deflection.



*Figure 117: Main Spring Characterization Test Setup.*

## 7.2.2 Characterization Test Result

A total of 5 springs were manufactured to order, first, the uncompressed lengths of each specimen were measured. Each spring specimen was then subjected to characterization test, repeating the test three times to ensure no errors are introduced during the test. The difference in spring deflection between trials were within  $\pm 3$  mm. The three trial results are averaged for each specimen and test results are plotted in Figure 118 along with the operation window of the spring.

The apparent outlier of the characterization test results is specimen 1. It is to be noted that specimen 1 was the only spring specimen used for prototyping. Hence, this specimen was compressed and uncompressed multiple times causing it to lose its spring force linearity. The consequence of this effect will be elaborated in Chapter 8 (Specimen 1 was overworked hence the change in properties and irregular behaviour).

It was also observed that other specimen were demonstrating linear behaviour as expected. In order to analyze their bulk behaviour an average deflection between the specimen excluding specimen 1 is plotted. Specimen average closely follows the nominal spring performance until last two sets of data points at 13.25 N and 15.21 N respectively.

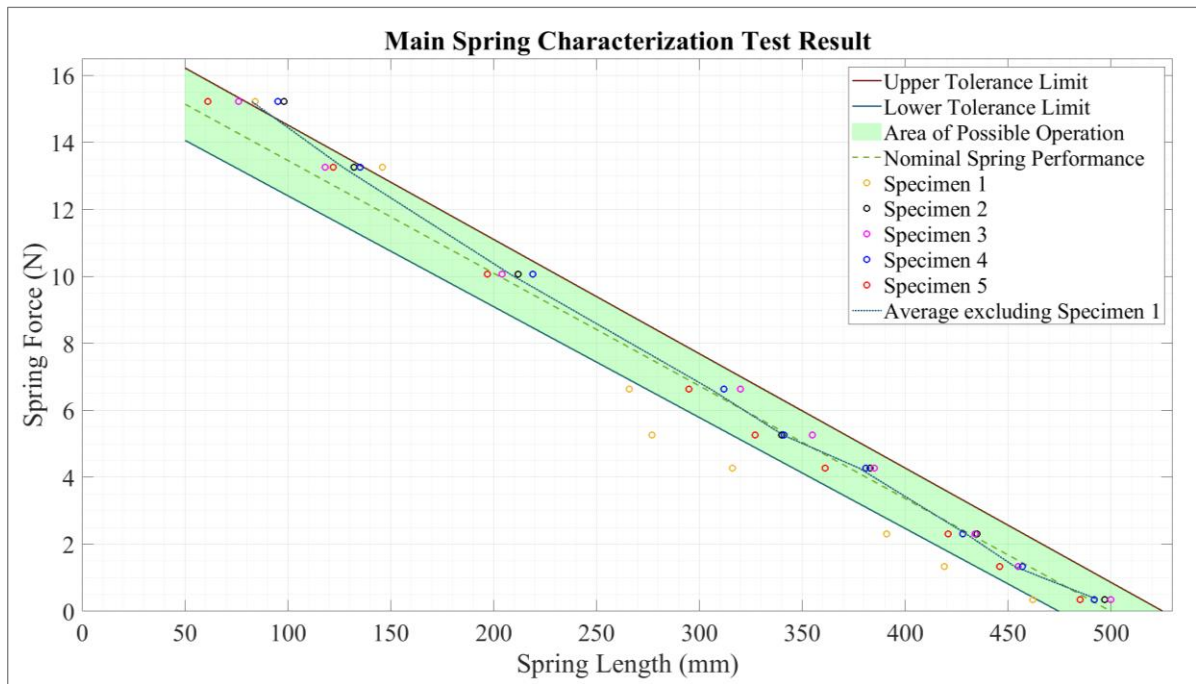


Figure 118: Spring Characterization Test results overlaid on operation window.

For these data points, slope of the average is greater than the slope of the nominal spring. It can be inferred that spring constant of the springs increases at these deflection states which implies that spring force has a value greater than expected. This trend is also seen in specimen 1. One possible explanation for this behaviour is the spiralling of spring observed near its compressed state. This spiralling causes extra potential energy to build up near its compressed state leading to higher than expected spring force.

The trend of increased force close to spring compressed state does not adversely affect the deployment velocity. Hence, it can be ascertained that the custom springs perform as intended and are fit for use in the PDS.

## 7.3 Door Deployment Test

Door deployment test was conducted to measure the time required by the door assembly to actuate from its stowed position to the deployed position. The intension of this test is to experimentally determine the time required for deployment of door assembly and compare experimental results to analytically estimated result in Section 4.3.7. Such a comparison will serve as a validation of analytical results as well as the characterization of torsion springs used on the door assembly.

### 7.3.1 Test Method and Setup

The experiment was conducted using the 3D printed structure of the PocketQube Deployment System. Mass of the 3D printed door assembly was noted down to be 30 grams before the test. A block diagram showing the test sequence and result analysis is shown in Figure 119.

The PDS structure was oriented to a vertical position during the test. The reason for the vertical orientation is that when the structure was placed horizontally, the door due to the effect of gravity would come to rest at a position other than the intended deployment position. This effect was minimized when the structure was oriented in the vertical direction.

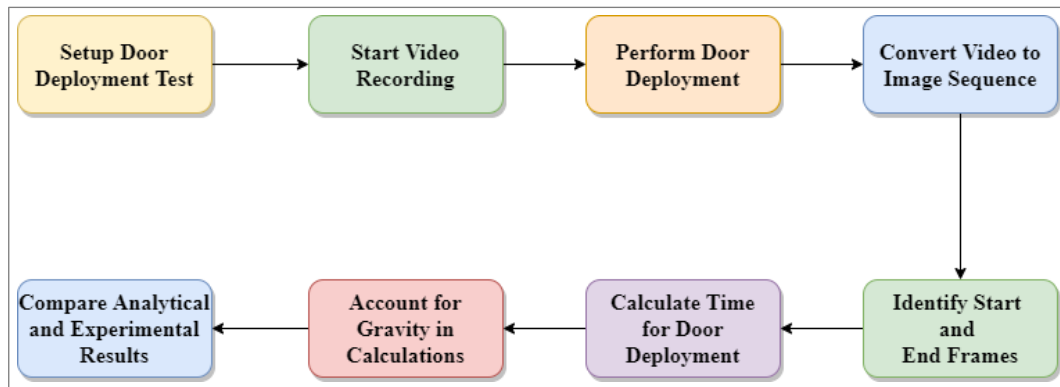


Figure 119: Block Diagram showing sequence of Door Deployment Test.

The difference between the door assembly shown in Section 4.4 and the 3D printed door assembly for this test was the change in material density from aluminium alloy to Polylactic Acid (PLA). However, upon changing the material of door in the CAD assembly to PLA, it was noted that the change in centre of mass (CoM) of door assembly was less than 0.1 millimetres. Therefore, CoM of the 3D printed door assembly is assumed to be at the same location (54 mm) as indicated on the CAD model in Section 4.4.



Figure 120: Images of the setup used for Door Deployment Test.

In order to accurately determine the time of deployment experimentally, a mobile phone was set up to record the deployment video at a high frame rate. The maximum frame rate capable by this device for video recording was 239.84 Frames per Second (FPS). Hence, frame rate close to 240 frames a second was used which, in turn resulted in providing a measuring resolution of 4.17 milliseconds between successive frames.

4.17 milliseconds temporal resolution was acceptable as the time required for deployment was calculated to be 83.6 milliseconds for a door assembly mass of 30 grams in Figure 39. Therefore, the measuring error in time can be 4 milliseconds which was acceptable to correlate the experimental and analytical results.

$$\text{Time for Deployment} = \frac{\text{Total frames between start and end}}{\text{Frames per Second}} \quad (56)$$

Once the test was performed, video recorded at 239.84 FPS now had to be converted into an image sequence in order to identify the start and end frames of deployment. The conversion

from video files to images was carried out using Adobe Photoshop. Having produced the image sequence, the start and end frames of the door deployment were identified. Based on the sequential numbering of frames between the start and end, total frames required for the door deployment was arrived at. The time required for the door deployment can be calculated using the Equation (56).

### 7.3.2 Result

Door deployment test was repeated 3 times to equalize any inconsistencies that may be occur during the test. The test was actuated using a pin to replicate the action of the pin puller mechanism as shown in Figure 121. The different trials of the deployment test showing experimentally calculated door deployment times are tabulated in Table 31.

*Table 31: Experimental results of door deployment test.*

<b>Trial</b>	<b>Start Frame</b>	<b>End Frame</b>	<b>Total Deployment Frames</b>	<b>Door Deployment Time (s)</b>
1	300	325	25	0.104236157
2	58	84	26	0.108405604
3	60	84	24	0.100066711

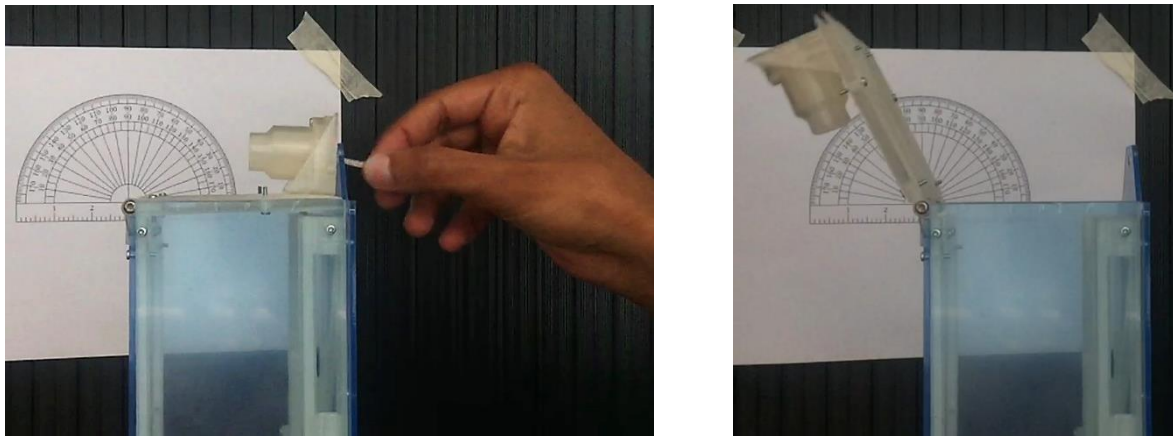


*Figure 121: Start and End frames of Door Deployment Test.*

It can be seen that from Table 31 that the time required for the door deployment is around 0.1 seconds. However, in Figure 39 it was estimated for that the door deployment time for a door mass of 30 grams is around 0.0836 seconds. The discrepancy in the values from the test and the analysis can be attributed to the influence of Earth's gravity during the test. The value of this gravitational force is given by Equation (57).

$$F_g = m_d g \quad (57)$$

Figure 122 shows the component of gravity that opposes the force exerted by the torsion springs on the door. This force is found to have a value of  $F_g \cos \theta$  where,  $\theta$  varies from  $0^\circ$  to  $110^\circ$ . This component is the force countering torsion spring force when the structure is placed in a vertical orientation for the test. As the gravity force opposing the deployment force varies with the door rotation angle ( $\theta$ ), a compensation term is introduced in the analysis tool to account for gravity.

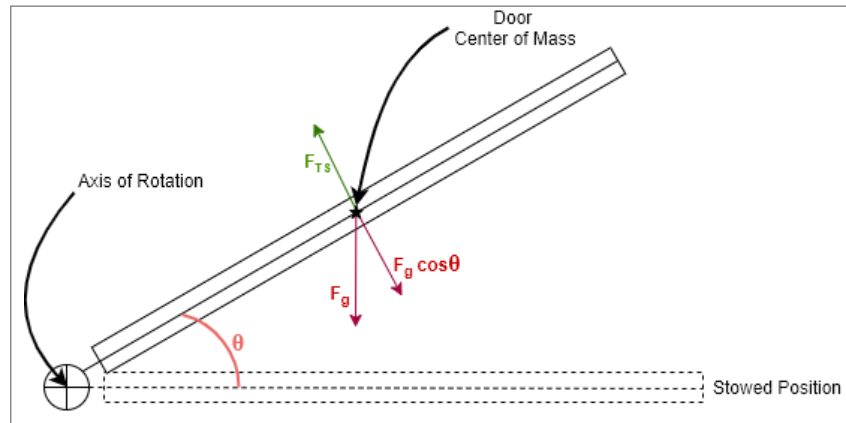


Figure 122: Diagram indicating components of gravity influencing door deployment test.

Figure 123 shows the influence of gravity on door deployment time. The analysis tool having included the effect of gravity, estimates the time for deployment is increased to 0.1 seconds from 0.0836 seconds for a door mass of 30 grams. The test and the analytical results are within the  $\pm 4$  milliseconds temporal resolution that can be obtained from a 240 FPS video recording. Therefore, the experimental results validate the analytical tool. Additionally, as the analysis and the experiment results match, it can be inferred that the commercially procured torsion springs are providing the required force.

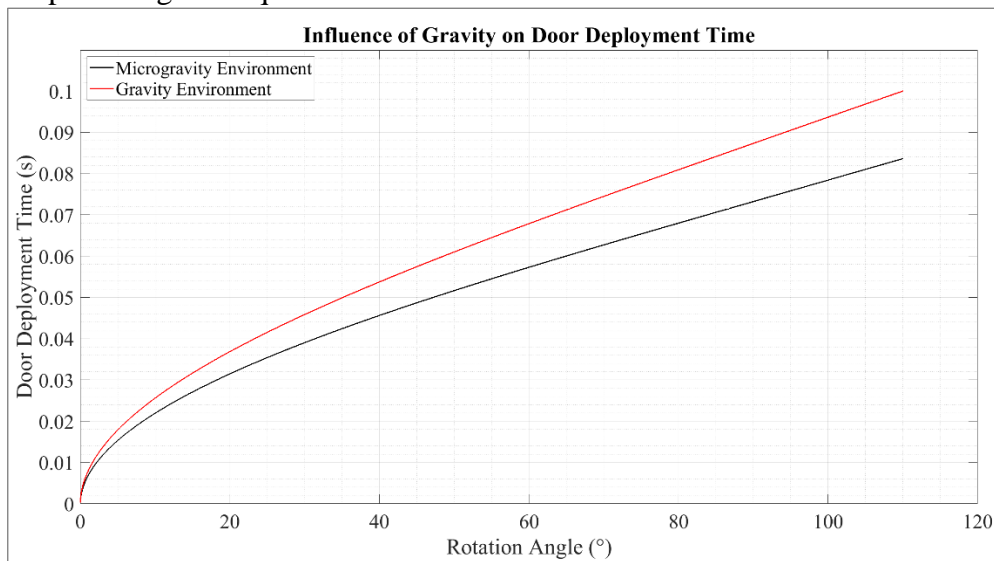


Figure 123: Influence of gravity on time for door deployment.

Further inferences can be drawn using the analysis tool when observing the door deployment force and angular velocity variation. Figure 124 illustrates the effect of gravity on deployment force and angular velocity of door respectively. The door deployment force is reduced by a factor of  $F_g \cos \theta$  between  $0^\circ$  and  $90^\circ$ . However, after  $90^\circ$  it turns positive as the torsion spring force is 0 whereas the gravity component now acts in the direction of door movement. The increase in deployment force results in the increase in angular velocity after  $90^\circ$  of door rotation in the gravity environment as seen in Figure 124. However, in a microgravity environment the angular velocity plateaus after  $90^\circ$  of door rotation as the force exerted by the torsion springs is close to 0 Newtons.

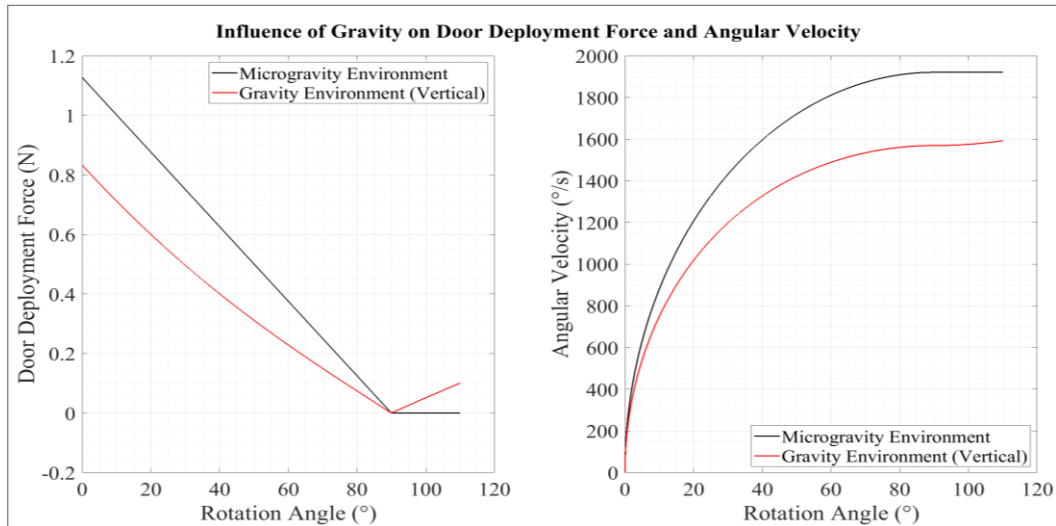


Figure 124: Gravity influence on door deployment force and angular velocity.

Having analyzed the contribution of gravity during the door deployment test in vertical orientation, a comparative study can be carried out between the vertical and horizontal orientations. When the PocketQube Deployment System is tested for door deployment in horizontal orientation, the component of gravity that opposes the force exerted by torsion springs on the door is  $F_g \sin \theta$ . Table 32 compares the door deployment time for vertical and horizontal orientations. Further, it estimates the deployment times if the door is manufactured with aluminium alloy and tested in gravity conditions.

Table 32: Expected results for door assembly made of aluminium alloy.

Deployment Condition	Door Mass (grams)	Door Material	Deployment Time (s)
Micro Gravity	30	PLA	0.08362
Gravity (Vertical)			0.09999
Gravity (Horizontal)			0.09094
Micro Gravity	90	Aluminium Alloy	0.1366
Gravity (Vertical)			0.3194
Gravity (Horizontal)			N/A

It is to be noted that for horizontal orientation with door made of aluminium alloy in standard gravity condition, angular velocity of door reaches 0°/s at an angle of 88.5°. Hence, door assembly would not reach its intended deployed position at 110° for this condition.

The discussion on system prototyping, characterization test, and door deployment test are thus completed.

# 8.

## System Integration and Environmental Test Plan

System integration procedure for single pod and multi pod PocketQube Deployment System is discussed in this chapter. Procedures required for system level environmental tests such as thermo-vacuum test and vibration test are established.

### 8.1 System Integration

System integration is a critical operation for systems intended to operate in space. Care must be taken to ensure that procedures specified for integration are followed to maintain the quality of workmanship and to avoid any challenges at final phase of a project.

For the PocketQube Deployment System, system integration procedure is divided into three sections. Integration of door assembly is discussed at first as it is a common assembly for single and multi pod configurations. It is followed by integration procedures for single pod and multi pod assembly. The detailed procedure for system integration can be found in Section 11.3.

Having discussed the integration procedures for the different system configurations, lessons learned during system prototyping are discussed.

#### 8.1.1 Prototyping Lessons

System integration procedure discussed for different assemblies in Sections 11.3.1, 11.3.2, and 11.3.3 are based on the lessons learned during prototype integration. In this section, changes that were carried out due to the experience of system prototyping and testing are discussed.

Based on main spring characterization test in Section 7.2, it is recommended not to compress the main spring multiple times. The performance (spring constant) of the compression spring changes if it undergoes multiple compression-extension cycles. Hence it must be avoided for spring specimen used in PDS flight model.

Further, for ease of compression of main spring during system integration, a cylindrical concentric collapsible mechanism is conceptualized. The working principle of this mechanism is similar to extendable legs of a tripod. This mechanism will restrict any lateral movement of main spring during integration onto PDS.

Another change that was brought about by prototyping was with respect to integration of door assembly to PDS. Initially, fastener threads were placed on Hinge 2 with clearance holes



present on Rib and +Y panel. The threading direction of this assembly was reversed and clearance holes were placed on Hinge 2 and +Y panel with fastener threads placed on rib. This change was incorporated to ease up system integration.

Having discussed the procedure for system integration of PDS and integration lessons learned by prototyping, fastener tightening procedures are discussed in the next section.

## 8.2 Fasteners

With the discussion on system integration procedures completed, this section will focus on the design of fasteners for PocketQube Deployment System. Fasteners are required to join two members to one another. In systems which are expected to withstand cyclic loads, fastener design must account for cyclic joint loading. Steps must be taken to ensure fastener failure is avoided due to dynamic loading. Fastener pretension increases fatigue resistance of a joint by reducing the alternating stress component induced in a fastener.

Fastener preload is created when torque is applied on the fastener and it is the primary goal when tightening a joint. Tightening the fastener introduces a tensile load on it which, will translate as a compressive load on the joining members. The compressive joint load provides the clamping force which holds the joining members in place. Hence, it is critical for the fastener design to ensure sufficient clamp load is applied on the joint while ensuring stress induced in the fastener is below its material yield strength.

Total load on the fastener will be a sum of joint load and induced preload. Therefore, it is critical to define right amount of preload to be introduced in the fastener based on the joint load experienced by it. Joint load varies if the joint experiences pure axial loading, pure shear loading or a combination of the two. Typical NASA recommended preloads for a fastener is 65% of the yield strength of fastener material [121].

Fastener preload is calculated using Equation (58) to Equation (63).

$$F_j = 0.75 F_p \quad (58)$$

$$F_p = \sigma_p A_t \quad (59)$$

$$\sigma_p = 0.85 \sigma_y \quad (60)$$

$$A_t = \frac{\pi}{16} (d_p + d_r)^2 \quad (61)$$

$$d_p = d - 0.649519 p \quad (62)$$

$$d_r = d - 1.1226869 p \quad (63)$$

$F_j$  is maximum preload applied to a fastener, and  $F_p$  is proof load of fastener material.  $\sigma_p$  is proof stress of fastener material,  $A_t$  is tensile (nominal) stress area on metric fastener,  $\sigma_y$  is yield stress of fastener material,  $d$  is nominal diameter of metric fastener, and  $p$  is pitch of metric thread.

Based on Equation (58) and Equation (60) maximum allowable preload is 63.75% of yield strength which is below NASA recommended preload condition. Equations (64) to (68) must satisfied for all fasteners used on the deployment system structure. Equations (67) and (68) take into account for a fastener failure condition when combined axial, shear and bending loads are applied on it [121].

$$R_t = \frac{F_a}{\sigma_y A_t} \quad (64)$$

$$R_s = \frac{FOS * F_{sh}}{0.577 \sigma_y A_t} \quad (65)$$

$$R_b = \frac{FOS * M_b}{\sigma_y A_t} \quad (66)$$

$$(R_t + R_b)^2 + R_s^3 \leq 1 \quad (67)$$

$$MoS = \frac{1}{\sqrt{(R_t + R_b)^2 + R_s^3}} - 1 \quad (68)$$

The failure criteria for a fastener is met if margin of safety (MoS) calculated using Equation (68) is positive. All fasteners that were selected from manufacturer Jeveka B.V [122] were manufactured from stainless steel material (A4-70) with yield strength of 700 MPa. Axial, shear forces and bending moment on fasteners were obtained from structural analysis results of deployment system discussed in Chapter 5. Based on structural analysis fastener load results, margins of safety for all fasteners on single and multi pod deployment systems met acceptance criteria.

For all fasteners of metric size M2, the pretension as defined earlier would be equal to 923 N, and 2240 N for M3 fastener. Torque to be applied for pre-tensioning of fastener is given by Equation (69).

$$T_b = K F_j d \quad (69)$$

$T_b$  is the torque to be applied on the fastener for pre-tensioning, and  $K$  is nut factor. The nut factor is dependent on friction conditions in torquing elements. For unlubricated fasteners, typical value of nut factor will be equal to 0.2 [121]. Based on Equation (69), fastener torque to be applied for PDS fasteners is equal to 0.37 Nm for M2 and 0.89 Nm for M3.

Fastener torquing (pretension) is the primary locking feature used for fasteners. Care must be taken during fastener pre-tensioning, and torquing procedures specified in reference must be followed to avoid fastener over tensioning [123].

Further, NASA specifies minimum length of thread engagement for tapped holes shall be at least 1 times nominal diameter for fastener. Recommended length is 1.5 times nominal diameter [123] and all tapped holes in PDS structure are designed to meet this specification.

As a secondary locking feature, liquid locking compounds are approved. Thread locking compounds that are approved for use in space environment are Loctite® Threadlocker Red 271™ and Blue 242™ [124]. All fasteners shall have an approved secondary locking feature that is applied during integration.

Having discussed the procedure for system integration of PDS, integration lessons learned by prototyping and fastener tightening procedures, cost estimation methodology for system integration is discussed.

## 8.3 Integration Cost Methodology

Costs incurred due to system integration of PDS was discussed in Section 6.8. This section details the methodology for arriving at the integration costs for single and multi pod PDS. Estimation of PDS integration costs are based on structure prototyping experience and integration costs for single and multi pod systems are listed in Table 30.

System integration of structure prototype was timed to evaluate the total time required for integration. The time required for integration of single pod prototype was measured to be about 6 hours. A factor of 25% is added to the total time to account for torquing of fasteners. Additional factor of 25% is added to this time to account for additional care that must be taken during integration of flight model. Hence, additional 50% is added to total integration time.

Integration cost is calculated based on hourly rates of technician discussed in Section 2.5. For multi pod deployment system, system cost is estimated based on the number of fasteners present in the structure. Based on single pod integration, cost is normalized to cost per fastener and total cost of multi pod PDS is estimated based on number of fasteners on structure.

Having discussed system integration of PDS and the associated methodology for estimating its cost, system environmental testing is discussed next.

## 8.4 Environmental Test Plan

With discussion on system integration completed, this section is focussed on system environmental testing. Environmental test such as vibration and Thermo-Vacuum (TVAC) tests are mandatory for any space system. In this section, test levels for qualification and flight acceptance are discussed and procedures for these tests are established.

Test factors of safety and duration for various loads is listed in Table 33. Vibration test tolerance shall be according to Table 58. For sinusoidal acceleration test, if required acceleration is not achieved for low excitation frequencies (5-20 Hz), the limit shall be based on maximum permissible displacement of vibration test shaker table.

Random vibration tests shall be preceded and succeeded by low intensity sinusoidal frequency sweep. The sweep tests before and after random vibration test shall be used to determine any changes in system natural frequencies. A change in system frequency indicates failure of random vibration test.

*Table 33: NASA recommended test factors and durations [51].*

Test	Prototype Qualification	Protoflight Qualification	Acceptance
<b>Quasi-Static</b>			
Level	1.25 x Limit Level	1.25 x Limit Level	Limit Level
<b>Random Vibration</b>			
Level	Limit Level +3 dB	Limit Level +3 dB	Limit Level
Duration	2 minutes per axis	1 minute per axis	1 minute per axis
<b>Sinusoidal Vibration</b>			
Level	1.25 x Limit Level	1.25 x Limit Level	Limit Level
Duration	2 octave/minute	4 octave/minute	4 octave/minute

$$PSD_{(50-800\text{ Hz})} = 0.08 * (22.7/m_{PDS}) \quad (70)$$

For multi pod PDS random vibration test, acceptance levels are reduced according to Equation (70) with slopes at  $\pm 6$  dB [51].

Further, input level notching shall be carried out for random vibration test for frequency range close to system natural frequency having high modal participation. Notching is carried out to ensure system is not over tested. Notching levels will be determined by system transmissibility factor.

Appropriate fixtures shall be designed for vibration and TVAC tests. Fixture that would be used for vibration test must be designed taking into account the required transmissibility factor by vibration table set up. Thermal cycling for TVAC test will be dependent on launch vehicle flight acceptance requirements. Based on this requirement, a test plan for TVAC at a system level shall be arrived at.

This concludes the chapter on system integration and testing. Thesis conclusion and recommendations for future work is presented in the following chapter.

# 9.

## Conclusion and Recommendations

The chapter provides a summary of the thesis and details the conclusions that were arrived at during the design and prototyping of the PocketQube Deployment System (PDS). Possible enhancements to this study are further listed as recommendations.

### 9.1 Thesis Summary

The research conducted over the course of this thesis on the PocketQube Deployment System was rooted in the objective set in Chapter 1. Based on this objective, a heritage review on spacecraft deployment systems was conducted, design requirements were arrived at, and system level trade-off studies were performed in Chapter 2.

Preliminary cost breakdown for space systems revealed that launch cost is a significant driver of the PocketQube mission cost. In Section 2.6, it was observed that system mass is the major contributor to launch cost. Therefore, by reducing system mass of the PocketQube deployer, launch cost can be reduced, subsequently reducing PocketQube mission cost.

Launch environment was analyzed in Chapter 3 to arrive at suitable design loads and stiffness requirements for the deployment system. System design involves arriving at a custom spring specification to minimize compressed spring length and provide required deployment energy. Guide rail dimensioning was carried out based on the effect of temperature on the tolerance between PocketQube backplate and guide mechanism.

Preliminary configuration study was conducted for the structural design of single and multi pod deployer systems. Based on structural analysis, the best suited configuration for the systems were arrived at. It was observed that the main driver of structure mass was due to structure stiffening to meet natural frequency requirements.

Final design was based on results obtained during structural analysis. Mass budgets and cost budgets were estimated for the deployer system configurations. A mass comparison metric called '*deployer ratio*' was introduced in the study to compare CubeSat and PocketQube deployers. Further, breakeven costs between multiple single pod and multi pod deployers were discussed for different launch vehicles.

System prototyping and testing was conducted to even out system integration procedures and validate spring estimations. Finally, system integration and environmental test procedures were described.

## 9.2 Conclusion

Having discussed a summary of thesis work, the following section enumerates the list of actions to answer the research question in Section 1.2 –

1. *‘What measures are best suited to reduce total cost to orbit for PocketQubes?’*
  - 1.1. Designed a custom compression spring to be used for PocketQube deployment in order to reduce structure mass by minimizing spring compressed length. PocketQube deployment velocity estimate is within CubeSat deployment velocity range found in literature. The spring chosen for deployment has sufficient energy stored to ensure PocketQube deployment velocity is within desirable range for extreme deployment cases<sup>J</sup>.
  - 1.2. A parametric study was conducted on the single pod PocketQube deployer. The goal of this study was to reduce structure mass of the system while maintaining the required stiffness. The study resulted in reduction of system mass by 133 grams (15.8% of total mass) which would save about 7,600 € (5.69% of total cost) in launch cost using the framework described in Section 2.6.
  - 1.3. System cost normalized to P units for the single pod deployer is about 28,000 €, whereas, for the multi pod deployer it is about 21,500 €. By utilizing the multi pod deployer, about 6,500 € can be saved per P unit of spacecraft deployed.
  - 1.4. Cost breakeven point between the single pod and multi pod systems is currently found to be at 66 P units. This signifies that for a PocketQube deployment mission, it is economical to use multiple single pod systems until total PocketQubes to be deployed reaches 66 P units (total of 11 pods). Once total PocketQubes to be deployed are above 66 P units, it is more economical to launch given PocketQubes using the multiple pod deployer.
  - 1.5. System total cost reduces for bulk manufacturing due to economies of scale. Hence, for large scale PocketQube deployments, bulk manufacturing will lead to significant cost savings as discussed in Section 6.8. 3,454.62 € would be saved for single pod system and 37,352.8 € for multi pod system.
  - 1.6. It follows from currently available data that, using a reusable launch vehicle for PocketQube deployment further reduces spacecraft launch cost and thereby its mission cost. For example, it was observed in Section 2.6 that, specific launch cost for falcon class of launch vehicles was lower than its counterparts which are non-reusable.
2. *‘What is the best suited deployer configuration for deployment of one or more PocketQubes?’*
  - 2.1. Structural analysis of single pod deployment system in Section 5.11 revealed that for similar structure mass, the system is better configured using a lateral configuration. The lateral configuration offered high stiffness when compared to longitudinal configuration by reducing mass overhang. Hence, for the single pod deployment system, lateral configuration is the preferred configuration which reduces launch cost by offering higher stiffness to mass ratio.
  - 2.2. Structural analysis of multi pod deployment system in Section 5.13 revealed that for similar structure mass, the system is better configured using a longitudinal

---

<sup>J</sup> Minimum value of 1 m/s.

configuration. Longitudinal configuration offered higher stiffness for the structure when compared to lateral configurations in X and Y directions. Hence, for the multi pod deployment system, longitudinal configuration is the preferred configuration which reduces launch cost by offering higher stiffness to mass ratio.

- 2.3. Based on sensitivity study in Sections 5.8 and 5.9, it was concluded that the structural stiffness (natural frequency) is not dependent on the combination of PocketQubes enclosed in a pod. Further, natural frequency of the deployment system is highly sensitive to shifts in PQ centre of mass (CoM) away from launch vehicle mounting surface. Therefore, care must be taken to accommodate the change in structural stiffness when stack CoM shifts in +Y direction for single pod, and +Z direction for multi pod systems.
- 2.4. System mass per P unit deployed, is lower in case of multi pod system. In Section 6.6 it was observed that single pod deployer requires about 40% additional structure mass to deploy same number of PocketQubes as the multi pod deployer.
- 2.5. Multiple pod deployment system offers higher deployer ratio than the single pod system. Single pod deployer ratio is similar to its peers deploying CubeSats. However, multi pod system deployer ratio is lower than multi pod CubeSat deployers of similar payload capacity.
3. *‘What is the best suited system configuration that can be integrated to multiple launch vehicles?’*
  - 3.1. The design of multi pod deployment system accommodates a total of 96 P units in 4x4 pattern as this configuration offers launch vehicle footprint similar to CubeSat deployers. 4x4 pod pattern was chosen to improve dynamic mass balancing properties of the structure.
  - 3.2. An observation following the study on system configurations was that the breakeven cost between choosing a single or a multi pod system depends on the launch vehicle. System cost is influenced by the total number of PocketQube units deployed in a mission which was discussed in Section 6.9.

## 9.3 Recommendations

Based on the learnings through the design process of the PocketQube deployment system, certain considerations are recommended. They are -

1. Estimation of PocketQube deployment velocity in this study does not account for actual friction between guide rail and PocketQube backplate. Microgravity deployment testing is recommended for the PocketQube deployer to ensure friction losses are lesser than accounted spring margins. Gravitational forces greatly impact the friction between PocketQube and guide rails [125], hence deployment shall be carried out in microgravity.
2. Microgravity PocketQube deployment test would accurately assess frictional losses during deployment. Based on test results, design can be modified to reduce friction coefficient by coating guide rail. Aromatic thermosetting co-polyesters (ATSP) or molybdenum disulphide (MoS<sub>2</sub>) coatings are recommended in the case that frictional losses are high [126].
3. Mass of single pod PocketQube deployer can be minimized by using structure panels manufactured from carbon fibre re-enforced polymers (CFRP). Cost saved by reduction

in system mass may be offset by increase in manufacturing costs. A cost benefit analysis is recommended to study the feasibility of this change.

4. A parametric study is recommended for the multi pod deployment system. Such a study can help identify system parameters that contribute in reducing system mass. Based on such a study, mass optimization of the multi pod deployment system can be carried out. Mass optimization would result in an increase of deployer ratio and hence a decrease in overall system cost.
5. It is recommended to perform a fatigue analysis on structural elements of PocketQube deployment system. Such an analysis will define the maximum number of times PDS structure can be reused in flight before a fatigue failure. The analysis becomes necessary when launch vehicle technology evolves to complete hardware reusability.
6. From structural analysis of PDS, the biggest contributor to system mass is the natural frequency requirement. This requirement is present to decouple PDS structure from launch vehicle harmonic excitations. An active vibration control system can isolate PDS structure from said harmonic loads, allowing for cut off frequency to drop resulting in system mass reduction.

A suitable form of active vibration control is use of piezo-electric isolators [127]. Spacers made of a piezo-electric material can be added during integration of PDS to launch vehicle. These spacers would isolate deployment system from launch vehicle base excitation. By isolating base excitation, system natural frequency can be lowered hence saving mass.

However, such control systems have to be evaluated for reliable use on a mission. Failure of such a system will result in dynamic load amplification and structural failure. A drawback of such a system is that it would not be able to counteract system displacement for low frequency excitations. Low frequency excitation (5-20 Hz) would result in large displacements which are not isolated by piezo-electric spacers.

This concludes the discussion on the PocketQube Deployment System.



# References

- [1] S. Radu, M. S. Uludag, S. Speretta, J. Bouwmeester, E. Gill and N. Foteinakis, "Delfi-PQ: The first pocketcube of Delft University of Technology," in *69th International Astronautical Congress*, Bremen, 2018.
- [2] S. Radu, M. Uludag, S. Speretta, J. Bouwmeester, A. Dunn, T. Walkinshaw, P. K. D. Cas and C. Cappelletti, "The PocketCube Standard (Issue 01)," Delft University of Technology, Delft, 2018.
- [3] T. Villela, C. A. Costa, A. M. Brandão, F. T. Bueno and R. Leonardi, "Towards the thousandth CubeSat: A statistical overview," *International Journal of Aerospace Engineering*, vol. 2019, 2019.
- [4] T. Wekerle, J. B. Pessoa Filho, L. E. V. L. d. Costa and L. G. Trabasso, "Status and trends of smallsats and their launch vehicles—An up-to-date review," *Journal of Aerospace Technology and Management*, vol. 9, no. 3, pp. 269-286, 2017.
- [5] M. Bailey, "Frequent and Reliable Launch for Small Satellites: Rocket Lab's Electron Launch Vehicle and Photon Spacecraft," Springer, 2020, pp. 453-468.
- [6] S. Engelen, C. J. M. Verhoeven and M. J. Bentum, "OLFAR, a radio telescope based on nano-satellites in moon orbit," in *24th Annual AIAA*, 2010.
- [7] NASA, "Marman Clamp System Design Guidelines," Guideline no. GD-ED-2214, 2012.
- [8] C. Lazansky, "Refinement of a Low-Shock Separation System," in *Proceedings of 41st Aerospace Mechanisms Symposium*, Jet Propulsion Laboratory, 11 March 2014.
- [9] \$50SAT Team, "\$50SAT - Eagle2," [Online]. Available: <http://www.50dollarsat.info/>. [Accessed August 2019].
- [10] S. McNeil, "Attitude Determination and Control in the T-LOGOQUBE FEMTO-Satellite Mission," *Advances in the Astronautical Sciences*, vol. 153, 2015.
- [11] E. Kulu, "Nanosats Database," Nanosats Database, [Online]. Available: <https://www.nanosats.eu/>. [Accessed 14 January 2022].
- [12] R. Connolly, "P-POD Payload Planner's Guide," California Polytechnic State University, San Luis Obispo, 2000.
- [13] W. Lan, R. Munakata, R. Nugent and D. Pignatelli, "Poly Picosatellite Orbital Deployer Mk. III Rev. E User Guide," Cubesat Program, Cal Poly, San Luis Obispo, 2014.
- [14] Innovative Solutions In Space B.V, "CubeSat Deployers," Innovative Solutions In Space B.V, Delft, 2015.
- [15] Tristan Prejean, "NanoRacks CubeSat Deployer, Interface Definition Document (IDD)," *NanoRacks LLC*, 2018.
- [16] Planetary Systems Corporation, "CANISTERIZED SATELLITE DISPENSER DATA SHEET," Planetary Systems Corporation, 2018.
- [17] Japan Aerospace Exploration Agency (JAXA), "JEM Payload Accommodation Handbook, Volume 8, Small Satellite Deployment Interface Control Document, Revision B," JX-ESPC-101133-B, January, 2015.

- [18] S. K. Tullino and E. D. Swenson, "Testing and Evaluating Deployment Profiles of the Canisterized Satellite Dispenser (CSD)," in *55th AIAA Aerospace Sciences Meeting*, 2017.
- [19] EXOLAUNCH GmbH, "EXOPOD 12/16U CubeSat Deployment System: User Guide," EXOLAUNCH GmbH, Berlin, Germany, 2021.
- [20] C. Cappelletti, S. Battistini and F. Graziani, "Small launch platforms for micro-satellites," *Advances in Space Research*, 2018.
- [21] Alba Orbital Limited, "AlbaPod ICD v0.1," Alba Orbital Limited, Glasgow.
- [22] news.satnews.com, "SatNews," 20 January 2022. [Online]. Available: <https://news.satnews.com/2022/01/20/fossa-systems-iot-smallsat-launch-accomplishment/>. [Accessed 22 January 2022].
- [23] FOSSA Systems, "FOSSA Systems," FOSSA Systems, [Online]. Available: <https://fossa.systems/>. [Accessed 15 January 2022].
- [24] M. Dubey, M. Kader, K. Shivam, P. V. Ganesh, P. Veeramuthuvel and P. Murugan, "Indian Nano satellite -platform for payloads from ISRO & Universities," *Journal of Spacecraft Technology*, vol. 31, pp. 31-41, 12 2020.
- [25] A. Thurn, S. Huynh, S. Koss, P. Oppenheimer, S. Butcher, J. Schlater and P. Hagan, "A Nichrome Burn Wire Release Mechanism for CubeSats," in *Proceedings of the 41st Aerospace Mechanisms Symposium*, Jet Propulsion Laboratory, 2012.
- [26] P. Cipollo and B. Surrusco, "An Electrically Actuated Pin-Puller for Space Application using Nickel-Titanium Memory Alloy," in *Proceedings of the Small Satellite Conference*, Logan, Utah, 2004.
- [27] A. Toorian, K. Diaz and S. Lee, "The CubeSat Approach to Space Access," in *2008 IEEE Aerospace Conference*, 2008.
- [28] N. Nava, M. Collado, M. Palladino and S. Patti, "A novel hold-down and release mechanism for non-explosive actuators based on SMA technology," in *16th European Space Mechanisms and Tribology Symposium*, Bilbao, Spain, 2015.
- [29] R. Twiggs, "Making it Small," in *Cal Poly Developers' Workshop*, San Luis Obispo, 2009.
- [30] A. Narayanan, "Literature Study: PocketQube Deployment System, Pg. 11-12," TU Delft, Delft, 2019.
- [31] Payscale, "Average Mechanical Technician Hourly Pay," payscale, [Online]. Available: [https://www.payscale.com/research/US/Job=Mechanical\\_Technician/Hourly\\_Rate](https://www.payscale.com/research/US/Job=Mechanical_Technician/Hourly_Rate). [Accessed 21 June 2021].
- [32] Tyvak International, OHB System AG and Politecnico Di Torino, "Multi-purpose Cubesat at the ISS," European Space Agency, 2017.
- [33] C. A. Esionwu, "CubeSat Market Analysis and Cost Breakdown," London, 2014.
- [34] H. Jones, "The recent large reduction in space launch cost," in *48th International Conference on Environmental Systems*, Albuquerque, New Mexico, 2018.
- [35] A. L. Weigel and D. E. Hastings, "Evaluating the cost and risk impacts of launch choices," *Journal of Spacecraft and Rockets*, vol. 41, no. 1, pp. 103-110, 2004.
- [36] Wikipedia, "Polar Satellite Launch Vehicle," Wikipedia, [Online]. Available: [https://en.wikipedia.org/wiki/Polar\\_Satellite\\_Launch\\_Vehicle](https://en.wikipedia.org/wiki/Polar_Satellite_Launch_Vehicle). [Accessed 17 June 2021].

- [37] Wikipedia, "Comparison of orbital launch systems," Wikipedia, [Online]. Available: [https://en.wikipedia.org/wiki/Comparison\\_of\\_orbital\\_launch\\_systems](https://en.wikipedia.org/wiki/Comparison_of_orbital_launch_systems). [Accessed 17 June 2021].
- [38] D. Gillies, "Rocket Lab Rideshare CubeSat Launch in Maxwell," 2018 CubeSat Developers Workshop, Rocket Lab, 2018.
- [39] Matmatch, "Matmatch," Matmatch GmbH, December 2021. [Online]. Available: <https://matmatch.com/>.
- [40] SAE International, "Steel, Corrosion-Resistant, Sheet, Strip, and Plate 19Cr - 9.2Ni (304) Cold Rolled (AMS5910C)," SAE International, 2018.
- [41] M. J. Donachie, Titanium: A Technical Guide, 2nd Edition, Materials Park, OH: ASM International, 2000.
- [42] American Society for Testing and Materials (ASTM) International, "Standard Specification for Aluminum and Aluminum-Alloy Sheet and Plate (Metric)," ASTM International, West Conshohocken, 2014.
- [43] Industries 3R, "FR-4 Data Sheet," [Online]. Available: [http://www.industries3r.com/images/absolucatalog/documents/NEMA%20G10\\_FR4%20-%20Industries%203R%20ENG.pdf](http://www.industries3r.com/images/absolucatalog/documents/NEMA%20G10_FR4%20-%20Industries%203R%20ENG.pdf). [Accessed April 2020].
- [44] SAE International, "Beryllium Near-Net Preforms Standard Grade Hot Isostatic Pressed (AMS7908E)," AMS G Titanium and Refractory Metals Committee, 2018.
- [45] S. Bhowmick and A. T. Alpas, "The role of diamond-like carbon coated drills on minimum quantity lubrication drilling of magnesium alloys," *Surface and Coatings Technology*, vol. 205, no. 23, pp. 5302-5311, 2011.
- [46] P. F. Infante and L. S. Newman, "Beryllium exposure and chronic beryllium disease," *The Lancet*, vol. 363, no. 9407, pp. 415-416, 2004.
- [47] L. S. Newman, M. M. Mroz, R. Balkissoon and L. A. Maier, "Beryllium sensitization progresses to chronic beryllium disease: a longitudinal study of disease risk," *American journal of respiratory and critical care medicine*, vol. 171, no. 1, pp. 54-60, 2005.
- [48] F. Z. Fang, L. C. Lee and X. D. Liu, "Mean flank temperature measurement in high speed dry cutting of magnesium alloy," *Journal of Materials Processing Technology*, vol. 167, no. 1, pp. 119-123, 2005.
- [49] W. Pedersen and M. Ramulu, "Facing SiCp/Mg metal matrix composites with carbide tools," *Journal of materials processing technology*, vol. 172, no. 3, pp. 417-423, 2006.
- [50] S. Chang and S. H. Lamm, "Human Health Effects of Sodium Azide Exposure: A Literature Review and Analysis," *International Journal of Toxicology*, vol. 22, no. 3, p. 175-186, 2003.
- [51] NASA GODDARD SPACE FLIGHT CENTER, "GENERAL ENVIRONMENTAL VERIFICATION STANDARD (GEVS)," GSFC-STD-7000A, Greenbelt, Maryland, April 2013.
- [52] T. Sgobba, Space Safety and Human Performance, Butterworth-Heinemann, 2017.
- [53] Space Exploration Technologies Corporation, "Falcon 9 Launch Vehicle Payload User's Guide," Space Exploration Technologies Corporation, 2015.
- [54] Arianespace, "Small Spacecraft Mission Service VEGA C User's Manual," Arianespace, Paris, September 2020.

- [55] F. Singarayyar, R. Reinhard, C. Asma, J. Thoemel, T. Scholz, C. Bernal, W. Weggelaar, G. Shirville, D. Kataria and M. Richard, "QB50 System Requirements and Recommendations," Issue 7, 2015.
- [56] S. Ramakrishnan, S. V. Sharma and L. Sowmianarayanan, "Small satellite launch opportunities on PSLV," *Cooperation in Space*, vol. 430, pp. 547-556, 1999.
- [57] Rocket Lab, "Electron: Payload User's Guide," Rocket Lab, Long Beach, November, 2020.
- [58] D. Zhao and X. Y. Li, "A review of acoustic dampers applied to combustion chambers in aerospace industry," *Progress in Aerospace Sciences*, vol. 74, pp. 114-130, 2015.
- [59] NASA, "Transient Loads from Thrust Excitation," Langley Research Centre, NASA, Hampton, Virginia, 1969.
- [60] D. T. Harrje, Liquid propellant rocket combustion instability, vol. 194, Scientific and Technical Information Office, National Aeronautics and Space Administration, 1972.
- [61] B. W. Oppenheim and S. Rubin, "Advanced pogo stability analysis for liquid rockets," *Journal of Spacecraft and Rockets*, vol. 30, no. 3, pp. 360-373, 1993.
- [62] L. D. Peterson, E. F. Crawley and R. J. Hansman, "Nonlinear fluid slosh coupled to the dynamics of a spacecraft," *AIAA journal*, vol. 27, no. 9, pp. 1230-1240, 1989.
- [63] F. E. Culick and P. Kuentzmann, "Unsteady motions in combustion chambers for propulsion systems," NATO RESEARCH AND TECHNOLOGY ORGANIZATION NEUILLY-SUR-SEINE (FRANCE), 2006.
- [64] T. S. Chandler and D. Lomen, "Analysis of Fluid Sloshing in Arbitrary Tanks Having Rotational Symmetry-A Correction for Low Gravity Conditions.," Marshall Space Flight Center, Huntsville, Alabama, 1964.
- [65] United Launch Alliance, "Atlas V Launch Services User's Guide," United Launch Alliance, Centennial, Colorado, 2010.
- [66] M. J. Crocker, "The vibroacoustics environment of spacecraft during launch and flight," *Sound and Vibration*, vol. 36, no. 6, p. 5, 2002.
- [67] R. Margasahayam and R. Caimi., "Launch Pad Vibroacoustics Research at the Kennedy Space Center," *Sound and Vibration*, vol. 36, no. 6, pp. 28-33, 2002.
- [68] D. S. Steinberg, Vibration analysis for electronic equipment, John Wiley & Sons New York, 2000.
- [69] R. Slootweg and J. M. P. Garcia, Interviewees, *Designers, ISIS CubeSat Deployers*. [Interview]. 23 January 2020.
- [70] M. Garrison and S. Steffan, "Two-fault tolerant electric actuation systems for space applications," in *42nd AIAA/ASME/SAE/ASEE Joint Propulsion Conference & Exhibit*, 2006.
- [71] Tini Aerospace, "Tini Pin Puller P5," Ensign-Bickford Aerospace & Defence, [Online]. Available: <https://www.ebad.com/tini-pin-puller/>. [Accessed March 2020].
- [72] Catalog: Glen AIR, "Hold Down and Release Mechanisms for Space Applications: HDRM's, Pin Pushers, Pin Puller and other Space Mechanisms," Glen AIR, [Online]. Available: <https://www.glenair.com/space-mechanisms/a.htm>. [Accessed 17 March 2020].
- [73] Deployables Cubed GmbH, "Products," Deployables Cubed GmbH, [Online]. Available: <https://dcubed.space/products/>. [Accessed 20 January 2022].

- [74] Arquimea Ingenieria S.L., "Pin Pullers for Space," Arquimea Ingenieria S.L., [Online]. Available: <https://www.arquimea.com/aerospace-and-defence/pin-pullers/>. [Accessed 20 January 2022].
- [75] R. J. H. Wanhill, R. T. Byrnes and C. L. Smith, "Stress corrosion cracking (SCC) in aerospace vehicles," in *Stress Corrosion Cracking*, V. S. Raja and T. Shoji, Eds., Woodhead Publishing, 2011, pp. 608-650.
- [76] A. D. Juhl, "Overview of anodizing in the aerospace industry," *Metal Finishing*, vol. 2, no. 108, pp. 20-21, 2010.
- [77] R. Canyook, P. Seubsom, J. Sang-ngean, T. Trirujirapapong and K. Taweessup, "Influences of sealing solutions on anodized layer properties of 7075 aluminium alloy," *Materials Today: Proceedings*, vol. 5, no. 3, pp. 9483-9488, 2018.
- [78] N. K. Kuromoto, R. A. Simão and G. A. Soares, "Titanium oxide films produced on commercially pure titanium by anodic oxidation with different voltages," *Materials Characterization*, vol. 58, no. 2, pp. 114-121, 2007.
- [79] G. Bussu and B. D. Dunn, "ESA Approach to the Prevention of Stress-Corrosion Cracking in Spacecraft Hardware," in *Joint ESA-NASA Space-Flight Safety Conference*, 2002.
- [80] Protolabs, "Hubs," 15 March 2022. [Online]. Available: <https://www.hubs.com/>.
- [81] L. A. Mallette and R. Adams, "Introduction to EMI/EMC test requirements for space applications," *IEEE Aerospace and Electronic Systems Magazine*, vol. 26, no. 6, pp. 24-29, 2011.
- [82] P. Richardson, "Pinterest," Pinterest, [Online]. Available: <https://www.pinterest.com/pin/269723465154530738/>. [Accessed 2022 May 09].
- [83] JOHN EVANS' SONS INC., "Spiral Torsion Springs," [Online]. Available: <https://springcompany.com/products/spiral-torsion-springs>. [Accessed 2022 May 09].
- [84] A. Toorian, "Thesis: Redesign of the Poly Picosatellite Orbital Deployer for the Dnepr Launch Vehicle," 2007.
- [85] Tevema B.V., "Tailor made springs," Tevema B.V., [Online]. Available: <https://www.tevema.com/custom-springs/>. [Accessed 30 March 2020].
- [86] G. IONASCU, C. I. RIZESCU, L. BOGATU, L. A. CARTAL and E. MANEA, "Study of Influence of Surface Microtexture and Roughness on Friction Coefficient," 2017.
- [87] G. I. Dumitru, G. Chisiu and A. Tudor, "Tribological Characteristics of Printed Circuit Boards Determinate Through Micro-scratch Test," *UPB Scientific Bulletin, Series D*, vol. 76, no. 4, 2014.
- [88] U. Malayoglu, K. C. Tekin, U. Malayoglu and S. Shrestha, "An investigation into the mechanical and tribological properties of plasma electrolytic oxidation and hard-anodized coatings on 6082 aluminum alloy," *Materials science and Engineering: A*, vol. 528, no. 24, pp. 7451-7460, 2011.
- [89] Y. Lin, J. Chen, Y. Huang and Y. Jian, "Wear and friction characteristics of surface-modified aluminium alloys," *International Journal of Surface Science and Engineering*, vol. 9, no. 2-3, pp. 109-123, 2015.
- [90] I. Ali, M. M. Quazi, E. Zalnezhad, A. A. D. Sarhan, N. L. Sukiman and M. Ishak, "Hard anodizing of aerospace AA7075-T6 aluminum alloy for improving surface properties," *Transactions of the Indian Institute of Metals*, vol. 72, no. 10, pp. 2773-2781, 2019.

- [91] I. Nason, J. Puig-Suari and R. Twiggs, "Development of a family of picosatellite deployers based on the CubeSat standard," in *Proceedings, IEEE Aerospace Conference*, 2002.
- [92] A. Mehrparvar, "CubeSat Design Specification Rev.13," California Polytechnic State University, San Luis Obispo, 2014.
- [93] K. Suzuki, "Introduction of the Small Satellite Deployment Opportunity from JEM," in *3rd Nano-Satellite Symposium*, Kitakyusyu, Japan, 2011.
- [94] P. D. Fleischauer and J. R. Lince, "A comparison of oxidation and oxygen substitution in MoS<sub>2</sub> solid film lubricants," *Tribology international*, vol. 32, no. 11, pp. 627-636, 1999.
- [95] R. R. M. Johnston and A. J. W. Moore, "Water adsorption on molybdenum disulfide containing surface contaminants," *The Journal of Physical Chemistry*, vol. 68, no. 11, pp. 3399-3406, 1964.
- [96] B. D. Dunn, *Materials and Processes for Spacecraft and High Reliability Applications*, Chichester, UK: Springer Praxis Books, 2016.
- [97] M. Kaseem, S. Fatimah, N. Nashrah and Y. G. Ko, "Recent progress in surface modification of metals coated by plasma electrolytic oxidation: Principle, structure, and performance," *Progress in Materials Science*, p. 100735, 2020.
- [98] S. Shrestha and B. D. Dunn, "Plasma electrolytic oxidation and anodising of aluminium alloys for spacecraft applications," in *Surface Engineering of Light Alloys*, Elsevier, 2010, pp. 603-641.
- [99] S. Shrestha, A. Merstallinger, D. Sickert and B. D. Dunn, "Some preliminary evaluations of black coating on aluminium AA2219 alloy produced by plasma electrolytic oxidation (PEO) process for space applications," in *Proceedings of the 9th International Symposium on Materials in a Space Environment*, Noordwijk, The Netherlands, 2003.
- [100] Paul Janu, Christian Neugebauer, Manfred Falkner, Ludwig Supper, Gerhard Mitterbauer, Hannes Weinhappl and Gerhard Traxler, "Electric Propulsion Pointing Mechanism Hold Down & Release Mechanism Design and Breadboard Test Results," in *13th European Space Mechanisms and Tribology Symposium*, Vienna, 2009.
- [101] A. Archuleta and M. Nicolls, "Space debris mapping services for use by LEO satellite operators," in *Proceedings of the Advanced Maui Optical and Space Surveillance (AMOS) Technologies Conference*, Maui, HI, 2018.
- [102] N. V. Bogomolov, A. S. Anfalov, S. V. Borzykh and V. N. Bakulin, "Simulation of process of small satellites separation from deployer installed on cargo spacecraft," *Journal of Physics: Conference Series*, vol. 1392, no. 1, p. 012003, 2019.
- [103] Q. Tu, M. Jiang, W. Qi, Y. Li and Y. Liu, "The Design and Analysis of Picosatellite Orbital Deployer Based on Shape Memory Alloy Release," in *2017 International Conference on Computer Systems, Electronics and Control (ICCSEC)*, 2017.
- [104] ANSYS, Inc, "Module 03: Modal Analysis," ANSYS Mechanical Linear and Nonlinear Dynamics (Release 2019 R2), 2019.
- [105] D. Johnson, "ANSYS Mechanical-APDL Harmonic Analysis Example and Comparison to ANSYS Mechanical results.," PennState Behrend, Erie, Pennsylvania, 2017.
- [106] ANSYS, Inc, "Module 06: Harmonic Analysis," ANSYS Mechanical Linear and Nonlinear Dynamics (Release 2019 R2), 2019.

- [107] O. E. Hansteen and K. Bell, "On the accuracy of mode superposition analysis in structural dynamics," *Earthquake Engineering & Structural Dynamics*, vol. 7, no. 5, pp. 405-411, 1979.
- [108] ANSYS, Inc, "Module 08: Random Analysis," ANSYS Mechanical Linear and Nonlinear Dynamics (Release 2019 R2), 2019.
- [109] P. Rivera, "Thesis: Dynamic Response Validation of CubeSats through Testing and Finite Element Analysis," Cal Poly, San Luis Obispo, California, 2019.
- [110] J. Piattoni, G. P. Candini, G. Pezzi, F. Santoni and F. Piergentili, "Plastic Cubesat: An innovative and low-cost way to perform applied space research and hands-on education," *Acta Astronautica*, vol. 81, no. 2, pp. 419-429, 2012.
- [111] T. Cai, "Thesis: Theoretical analysis of torsionally vibrating microcantilevers for chemical sensor applications in viscous liquids," Marquette University, Milwaukee, Wisconsin, 2013.
- [112] S. P. Chaphalkar, S. N. Khetre and A. M. Meshram, "Modal analysis of cantilever beam structure using finite element analysis and experimental analysis," *American journal of engineering research*, vol. 4, no. 10, pp. 178-185, 2015.
- [113] A. Ampatzoglou, A. Baltopoulos, A. Kotzakolios and V. Kostopoulos, "Qualification of composite structure for cubesat picosatellites as a demonstration for small satellite elements," *International Journal of Aeronautical Science & Aerospace Research (IJASAR)*, vol. 1, no. 1, pp. 1-10, 2014.
- [114] R. Lee and A. C. Cangellaris, "A study of discretization error in the finite element approximation of wave solutions," *IEEE transactions on antennas and propagation*, vol. 40, no. 5, pp. 542-549, 1992.
- [115] N. Naik, V. George and S. Kowshik, "Investigations on mesh discretization error in FEM based structural analysis using ANSYS," *International Journal of Advanced Computational Engineering and Networking*, vol. 2, no. 8, pp. 17-22, 2014.
- [116] J. Kim, J.-C. Yoon and B.-S. Kang, "Finite element analysis and modeling of structure with bolted joints," *Applied Mathematical Modelling*, vol. 31, no. 5, pp. 895-911, 2007.
- [117] M. A. Hannan, M. S. H. Lipu, A. Hussain and A. Mohamed, "A review of lithium-ion battery state of charge estimation and management system in electric vehicle applications: Challenges and recommendations," *Renewable and Sustainable Energy Reviews*, vol. 78, pp. 834-854, 2017.
- [118] Spaceflight Industries, "Pricing Information," Spaceflight Industries, [Online]. Available: <https://spaceflight.com/pricing/>. [Accessed 05 May 2022].
- [119] Precious Payload, "Launch schedule," [Online]. Available: <https://preciouspayload.com/launch-schedule/>. [Accessed 05 May 2022].
- [120] Alba Orbital Limited, "Launch," Alba Orbital Limited, [Online]. Available: <http://www.albaorbital.com/launch>. [Accessed 05 May 2022].
- [121] J. A. Chambers, "Preloaded Joint Analysis Methodology for Space Flight Systems - NASA Technical Memorandum - 106943," NASA, Lewis Research Center, Cleveland, Ohio, 1995.
- [122] Jeveka B.V., "Socket head screws," Jeveka B.V., [Online]. Available: <https://jeveka.com/en/metric-fasteners/socket-head-screws>. [Accessed 30 August 2020].

- [123] J. E. Bennett, "Process Specification for Installation of Threaded and Collared Fasteners," Lyndon B. Johnson Space Center, National Aeronautics and Space Administration, Houston, 2020.
- [124] M. J. Dube and W. R. Gamwell, "Performance Characterization of Loctite (Registered Trademark) 242 and 271 Liquid Locking Compounds (LLCs) as a Secondary Locking Feature for International Space Station (ISS) Fasteners," NASA, Goddard Space Flight Center, 2011.
- [125] S. K. Tullino, E. Swenson and J. Tullino, "Investigative Microgravity Deployment Tests of the Canisterized Satellite Dispenser (CSD)," in *2018 AIAA SPACE and Astronautics Forum and Exposition*, 2018.
- [126] K. Bashandeh, V. Tsigkis, P. Lan and A. A. Polycarpou, "Extreme environment tribological study of advanced bearing polymers for space applications," *Tribology International*, vol. 153, p. 106634, 1 2021.
- [127] M. Makhtoumi, "Active Vibration Control of Launch Vehicle on Satellite Using Piezoelectric Stack Actuator," *Journal of Space Technology*, vol. 8, no. 1, 2018.



# Appendix

Table 34: Material physical properties. <sup>K</sup>

Material	Property	Density (g/cc)	Tensile Strength (MPa)	Yield Strength (MPa)	Young's Modulus (GPa)
Stainless Steel (type 304)		7.8	565	190	210
Titanium (Ti6Al4V Grade 5)		4.45	1200	900	120
Aluminium (7075-T651)		2.81	570	500	72
Beryllium (Structure Grade S-200-F)		1.84	324	241	290
Magnesium		1.78	240	160	45
FR-4		1.85	310	180	24
CFRP (70% carbon fibres in epoxy matrix)		1.6	1500	750	181

Table 35: Sinusoidal acceleration of different launch vehicles.

QB 50		PSLV		Space X Falcon 9		Atlas V		Vega C	
Frequency (Hz)	Acceleration (g)	Frequency (Hz)	Acceleration (g)	Frequency (Hz)	Acceleration (g)	Frequency (Hz)	Acceleration (g)	Frequency (Hz)	Acceleration (g)
5	2.5	5	1.7	5	0.5	5	0.6	5	2.5
100	2.5	8	4.5	20	0.8	20	0.6	70	2.5
100	1.25	100	4.5	35	0.8	20	0.8	70	1.25
125	1.25			35	0.6	30	0.8	110	1.25
				75	0.6	30	0.6	110	1.25
				85	0.9	75	0.6	125	1.25
				100	0.9	75	0.7		
						80	0.7		
						80	0.9		
						100	0.9		

Table 36: Random vibration  $G_{RMS}$  for launch vehicles.

HTV		ATV		Falcon 9		Orbital Cygnus		PSLV	
$G_{RMS}$	Duration (s)	$G_{RMS}$	Duration (s)	$G_{RMS}$	Duration (s)	$G_{RMS}$	Duration (s)	$G_{RMS}$	Duration (s)
4	60	5.84	60	7.25	60	4.4	60	6.7	60
Electron		NASA GEVS Qualification		QB-50		NASA GEVS Acceptance		Vega C	
$G_{RMS}$	Duration (s)	$G_{RMS}$	Duration (s)	$G_{RMS}$	Duration (s)	$G_{RMS}$	Duration (s)	$G_{RMS}$	Duration (s)
4.14	60	14.4	120	8.03	120	10	60	8.8	60

Table 37: Design loads accounting for NASA recommended FOS.

Quasi-Static	Sinusoidal Vibration		Random Vibration <sup>L</sup>	
Acceleration (g)	Frequency (Hz)	Acceleration (g)	Frequency (Hz)	PSD (g <sup>2</sup> /Hz)
16.25	5-100	3.125	20	0.026
			20-50	+6 dB/oct
			50-800	0.16
	100-125	1.5625	800-2000	-6 dB/oct
			2000	0.026
			<b>Overall <math>G_{RMS}</math></b>	<b>14.1</b>

<sup>K</sup> Composite material properties (FR-4, CFRP) are along fibre orientation.

<sup>L</sup> Qualification levels for system with mass less than 22.7 kg. Correction factor to be applied for mass above 22.7 kg.

Table 38: Cost correction to 2021 US\$ accounting inflation.

Launch Vehicle	Specific Launch Cost (US\$/kg)	Inflation Factor	Specific Launch Cost 2021\$ (US\$/kg)
Ariane 5	13100	1.0573	13850.63
Atlas V	6560	1.5902	10431.712
Electron	32700	1.0573	34573.71
Falcon 9	2700	1.0573	2854.71
Falcon Heavy	1400	1.0573	1480.22
LauncherOne	20000	1.0573	21146
Long March 2C	10000	1.0573	10573
Long March 3B	6300	1.0573	6660.99
Proton SL-13	4100	1.0573	4334.93
PSLV	6600	1.0573	6978.18
Soyuz	7600	1.0573	8035.48
Vega	10000	1.0573	10573

Table 39: Launch cost estimate for a kilogram of space hardware<sup>M</sup>.

Launch Vehicle	Specific Launch Cost (US\$/kg)	Average Launch per Annum	Normalised Specific Launch Cost (US\$/kg)
Ariane 5	13850.63	14	193908.8
Atlas V	10431.71	6	62590.27
Electron	34573.71	4.75	164225.1
Falcon 9	2854.71	16.83333333	48054.29
Falcon Heavy	1480.22	0.33333333	493.4067
LauncherOne	21146	2	42292
Long March 2C	10573	1.5	15859.5
Long March 3B	6660.99	3.785714286	25216.61
Proton SL-13	4334.93	12	52019.16
PSLV	6978.18	2.785714286	19439.22
Soyuz	8035.48	12	96425.76
Vega	10573	1.875	19824.38
<b>Average</b>	<b>10957.71</b>	<b>-</b>	<b>61695.71</b>

Table 40: Chemical composition limits for aluminium alloys [42].

Additive	Aluminium Alloy Composition (%)				
	2014	2024	6013	6061	7075
Silicon	0.5-1.2	0.5	0.6-1	0.4-0.8	0.4
Iron	0.7	0.5	0.5	0.7	0.5
Copper	3.9-5	3.8-4.9	0.6-1.1	0.15-0.4	1.2-2
Manganese	0.4-1.2	0.3-0.9	0.2-0.8	0.15	0.3
Magnesium	0.2-0.8	1.2-1.8	0.8-1.2	0.8-1.2	2.1-2.9
Zinc	0.25	0.25	0.25	0.25	5.1-6.1
Titanium	0.15	0.15	0.1	0.15	0.2
Chromium	0.1	0.1	0.1	0.04-0.35	0.18-0.28
Others	0.15	0.15	0.15	0.15	0.15
Aluminium	Balance				

<sup>M</sup> Costs were corrected to 2021 US\$ using the Consumer Price Index (CPI). (CPI Inflation Calculator, 2021)

Table 41: Mechanical Properties of Aluminium Alloy [42].<sup>N</sup>

Aluminium Alloy	Ultimate Strength (MPa)	Yield Strength (MPa)	Young's Modulus (GPa)
2014-T651	460	405	71
2024-T861	480	440	72
6013-T651	370	325	70
6061-T651	290	240	69
7075-T651	540	470	72

Table 42: Specification of Main Spring [85].

Specification	Quantity
Maximum Force	15 N
Stroke	450 mm
Compressed Length	50 mm
Outer Diameter	Around 20 mm
Material	Stainless Steel

Table 43: Deployment velocity based on location in pod.

Location in Pod	Deployment Velocity (m/s)		
	6x1P	3x2P	2x3P
Top	1.088	1.485	1.744
to	1.627		
	2.136	2.354	
	2.718		
	3.535	3.662	2.99
Bottom	5.179		

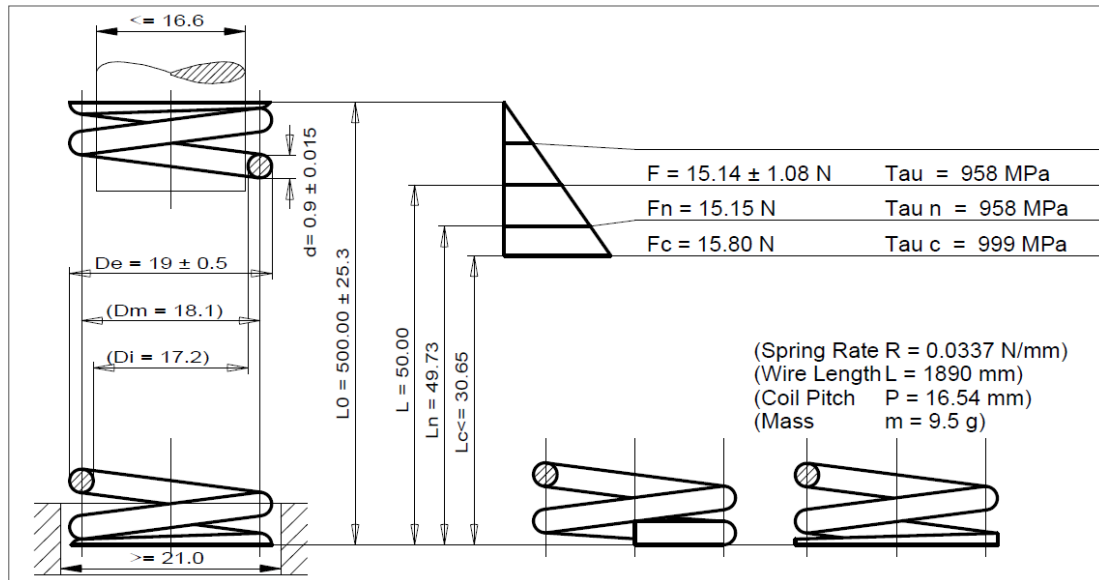


Figure 125: Main spring drawing showing tolerance [85].

<sup>N</sup> Mechanical properties are dependent on tempering (heat treatment) process.

Table 44: Specification of Torsion Springs.

Specification	Quantity
Part Number	TS100990R/L
Position	A
Maximum Torque	54.9 N mm
Maximum Deflection	167 °
Leg Length	9.75 mm
Material	Stainless Steel

Table 45: Specification of door retainer spring.

Specification	Quantity
Part Number	D20944
Maximum Force	5.9 N
Stroke	10.7 mm
Compressed Length	10.3 mm
Material	Stainless Steel

Table 46: Specification of push back spring.

Specification	Quantity
Part Number	D21470
Maximum Force	12.69 N
Stroke	9.78 mm
Compressed Length	8.72 mm
Min Clearance Diameter	6.01 mm
Material	Stainless Steel

Table 47: Minimum separation distance for deployment velocity of 1 m/s.

Location	Separation Distance (m)	
	LEO	GTO
After ½ orbit (deployment parallel to angular momentum)	0.59	4
After 1 orbit (all orientation except deployment along orbital velocity vector)	1.11	35.5

Table 48: Properties of cantilever beam used for solver validation [94].

Property	Value	Unit
Length	0.8	m
Width	0.05	m
Height	0.006	m
Young's Modulus	210 x 10 <sup>9</sup>	Pa
Density	7856	Kg/m <sup>3</sup>
Poisson's Ratio	0.3	-

Table 49: Modal analysis comparison for FEM methods.

Mode Number	Model 1			Model 2		
	Frequency (Hz)		Error (%)	Frequency (Hz)		Error (%)
	Mid-Plane Method	3D Mesh Method		Mid-Plane Method	3D Mesh Method	
1	5.4007	6.0552	12.12	496.53	746.46	33.48
2	34.044	37.784	10.99	504.39	1062	52.51
3	62.427	74.475	19.3	574.11	1096.2	47.63
4	95.877	105.61	10.15	577.94	1384.2	58.25
5	188.73	206.76	9.55	1003.7	1551.5	35.31
6	312.11	341.28	9.35	1009.4	1577.1	36

Table 50: Static and dynamic analysis comparison for FEM methods.

Excitation		Sinusoidal		Random		Quasi-Static	
		Maximum Stress (MPa)	Maximum Deformation (mm)	Maximum Stress (MPa)	Maximum Deformation (mm)	Maximum Stress (MPa)	Maximum Deformation (mm)
Model 1	Mid-Plane Method	869.57	303.55	44.275	3.11	695.98	222.76
	3D Method	203.96	108.49	28.158	3.0045	355.21	182.01
	Error (%)	326.34	179.8	57.24	3.51	95.93	22.39
Model 2	Mid-Plane Method	2.1908	0.0086	89.026	0.5145	6.5248	0.0244
	3D Method	0.8425	0.0037	41.416	0.1742	4.7615	0.015
	Error (%)	61.54	56.98	53.48	66.14	27.02	38.52

Table 51: Comparison of solver results based on beam theory.

Mode	Type	Frequency (Hz)		Error (%)
		Numerical Result	Theoretical Result	
1	Bending	7.6769	7.829942	1.954578
2	Bending	48.1	49.06981	1.976387
3	Bending	63.585	65.24952	2.551006
4	Bending	134.69	137.3979	1.970814
5	Torsion	229.16	229.5667	0.17715
6	Bending	264.01	269.2437	1.943848
7	Bending	391.46	408.9151	4.268631
8	Bending	436.63	445.0763	1.897719
9	Bending	652.62	664.8671	1.842032
10	Torsion	688.89	688.7	0.027584

Table 52: Changes in baseline parameter values based on study.

Parameter	Baseline Value (mm)	Post Study Value (mm)	Thickness Change (mm)	Mass Saved (grams)
+X Panel Thickness	1	0.5	0.5	50.81
-X Panel Thickness	1	0.5	0.5	50.81
+Y Panel Thickness	1	0.5	0.5	45.23
-Y Panel Thickness	1	1	0	0
-Z Panel Thickness	1	0.5	0.5	8.48
Rib Thickness	5	5	0	0
Rib Horizontal Thickness	15	5	10	17.17
Guide Mechanism Parameter 1 Thickness	3	3	0	0
Guide Mechanism Parameter 2 Thickness	4	3	1	6.33
<b>Total Mass Saved</b>				<b>178.83</b>

Table 53: Sensitivity of PQ mass distribution.

PocketQube Combination	3P – 2 Numbers	2P – 3 Numbers	1P – 6 Numbers	Error (%)
<b>Mode</b>	<b>Frequency (Hz)</b>			
1	146.72	146.55	146.44	0.19
2	196.66	196.6	196.56	0.05
3	231.93	231.6	231.3	0.27
4	236.03	235.56	235.08	0.40
5	307.41	306.98	306.63	0.25
6	403.82	403.63	403.49	0.08
7	438.12	438.1	438.07	0.01
8	446.76	444.55	442.37	0.98
9	472.44	471.17	469.38	0.65
10	504.94	504.59	503.03	0.38

Table 54: PocketQube deployment velocity based on position in pod (specific case).

		<b>PocketQube Deployment Velocity (m/s)</b>					
PocketQube Stacking Order (Refer Figure 102)		1	2	3	4	5	6
Position in Pod	Top	1.744	1.088	1.744	1.485	1.088	1.485
	Middle	2.886	1.911	2.718	2.136	2.106	2.499
	Bottom	5.179	2.99	3.662	2.99	3.662	5.179

Table 55: Mass Budget (Single Pod).

Sub-System	Part	Quantity	Material	Specific Mass	Total Mass (grams)
<b>Door Assembly</b>					<b>85.62</b>
	Door Bottom	1	Al-6061	15.71	15.71
	Door Top	1	Al-6061	23.63	23.63
	Door Bracket	1	Al-6061	7.28	7.28
	Hinge 1	2	Al-6061	0.86	1.72
	Hinge 2	2	Al-6061	1.05	2.1
	Door Retainer Pin	1	Al-7075	0.52	0.52
	Door Retainer Plate	1	Al-6061	1.38	1.38
	Push Back Holder	2	Al-6061	0.41	0.82
	Torsion Spring LH	1	SS	0.75	0.75
	Torsion Spring RH	1	SS	0.75	0.75
	Push Back Spring	2	SS	0.4	0.8
	Door Retainer Spring	1	SS	0.16	0.16
	Pin Puller P5	1	-	30	30
<b>Pusher Plate Assembly</b>					<b>37.26</b>
	Pusher Plate	1	Al-6061	5.58	5.58
	Pusher Plate Guide	2	Vespel	8.09	16.18
	Pusher Plate Stopper	2	Al-6061	3	6
	Main Spring	1	SS	9.5	9.5
<b>Structure</b>					<b>688.68</b>
	Guide Mechanism	1	Al-6061	283.29	283.29
	+X Panel	1	Al-7075	58.34	58.34
	-X Panel	1	Al-7075	58.34	58.34
	+Y Panel	1	Al-7075	44.99	44.99
	-Y Panel	1	Al-7075	115.39	115.39
	Rib	1	Al-6061	101.76	101.76
	Bottom Panel	1	Al-7075	8.47	8.47
	Fasteners	1	A4-70	18.1	18.1
<b>Deployer Electronics</b>		1	-	30	30
<b>Total Mass</b>					<b>841.56</b>

Table 56: Mass Budget (Multi Pod).

Sub-System	Part	Quantity	Material	Specific Mass	Total Mass (grams)
<b>Door Assembly</b>		<b>16</b>			<b>1404.48</b>
	Door Bottom	1	Al-6061	13.9	13.9
	Door Top	1	Al-6061	21.34	21.34
	Door Bracket	1	Al-6061	7.28	7.28
	Hinge 1	2	Al-6061	0.86	1.72
	Hinge 2	2	Al-6061	1.31	2.62
	Door Retainer Pin	1	Al-7075	0.52	0.52
	Door Retainer Plate	1	Al-6061	1.52	1.52
	Push Back Holder	2	Al-6061	0.41	0.82
	Torsion Spring LH	1	SS	0.75	0.75
	Torsion Spring RH	1	SS	0.75	0.75
	Push Back Spring	2	SS	0.4	6.4
	Door Retainer Spring	1	SS	0.16	0.16
	Pin Puller P5	1	-	30	30

<b>Pusher Plate Assembly</b>		<b>16</b>			<b>596.16</b>
	Pusher Plate	1	Al-6061	5.58	5.58
	Pusher Plate Guide	2	Vespel	8.09	16.18
	Pusher Plate Stopper	2	Al-6061	3	6
	Main Spring	1	SS	9.5	9.5
<b>Structure</b>					<b>7617.75</b>
	Guide Mechanism	16	Al-6061	279.93	4478.88
	+X Panel	1	Al-7075	221.87	221.87
	-X Panel	1	Al-7075	221.87	221.87
	+Y Panel	1	Al-7075	181.11	181.11
	-Y Panel	1	Al-7075	181.11	181.11
	-Z Panel	1	Al-7075	324.13	324.13
	Side Rib	2	Al-6061	246.6	493.2
	Mid Rib X	2	Al-6061	244.37	488.74
	Mid Rib Y	1	Al-6061	463.44	463.44
	Guide Mechanism Mid Rib	4	Al-7075	19.72	78.88
	Top Rib	1	Al-6061	248.42	248.42
	Mid Lock	4	Al-6061	9.6	38.4
	Door Lock	8	Al-6061	1.55	12.4
	Fasteners	1	A4-70	185.3	185.3
<b>Deployer Electronics</b>		<b>1</b>	<b>-</b>	<b>50</b>	<b>50</b>
<b>Total Mass</b>					<b>9668.39</b>

Table 57: Combination of weights used for spring characterization.

Weight Combination	Mass on Spring (grams)	Applied Force (N)
0	36	0.35316
50+50	136	1.33416
100+50+50	236	2.31516
200+200	436	4.27716
200+200+100	536	5.25816
240+200+100+50+50	676	6.63156
240+250+200+200+100	1026	10.0651
875+240+200	1351	13.2533
875+240+200+200	1551	15.2153

Table 58: Recommended tolerance during testing [51].

Test Type	Variable	Tolerance
Steady-State Acceleration	-	± 5 %
Sinusoidal Vibration	Frequency	± 2 %
	Amplitude	± 10 %
Random Vibration	RMS Level	± 10 %
	Acceleration Spectral Density	± 3 dB
	Duration	+ 10 % / -0 %



# 11.1 Appendix A (Structural Analysis Results)

## 11.1.1 Single Pod Longitudinal Version 1

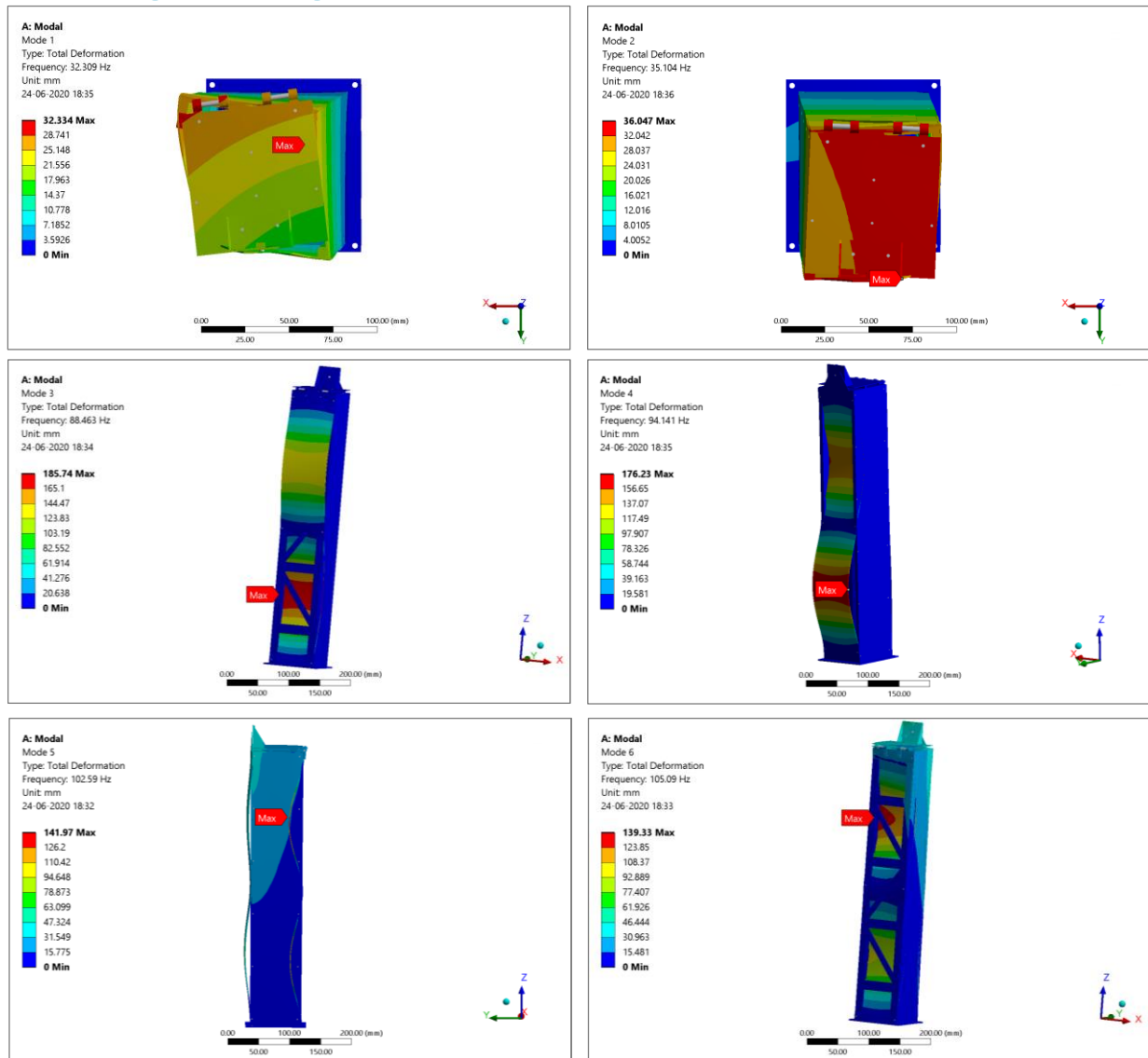


Figure 126: Modal analysis results version 1 – Longitudinal Configuration.

## 11.1.2 Single Pod Longitudinal Version 2

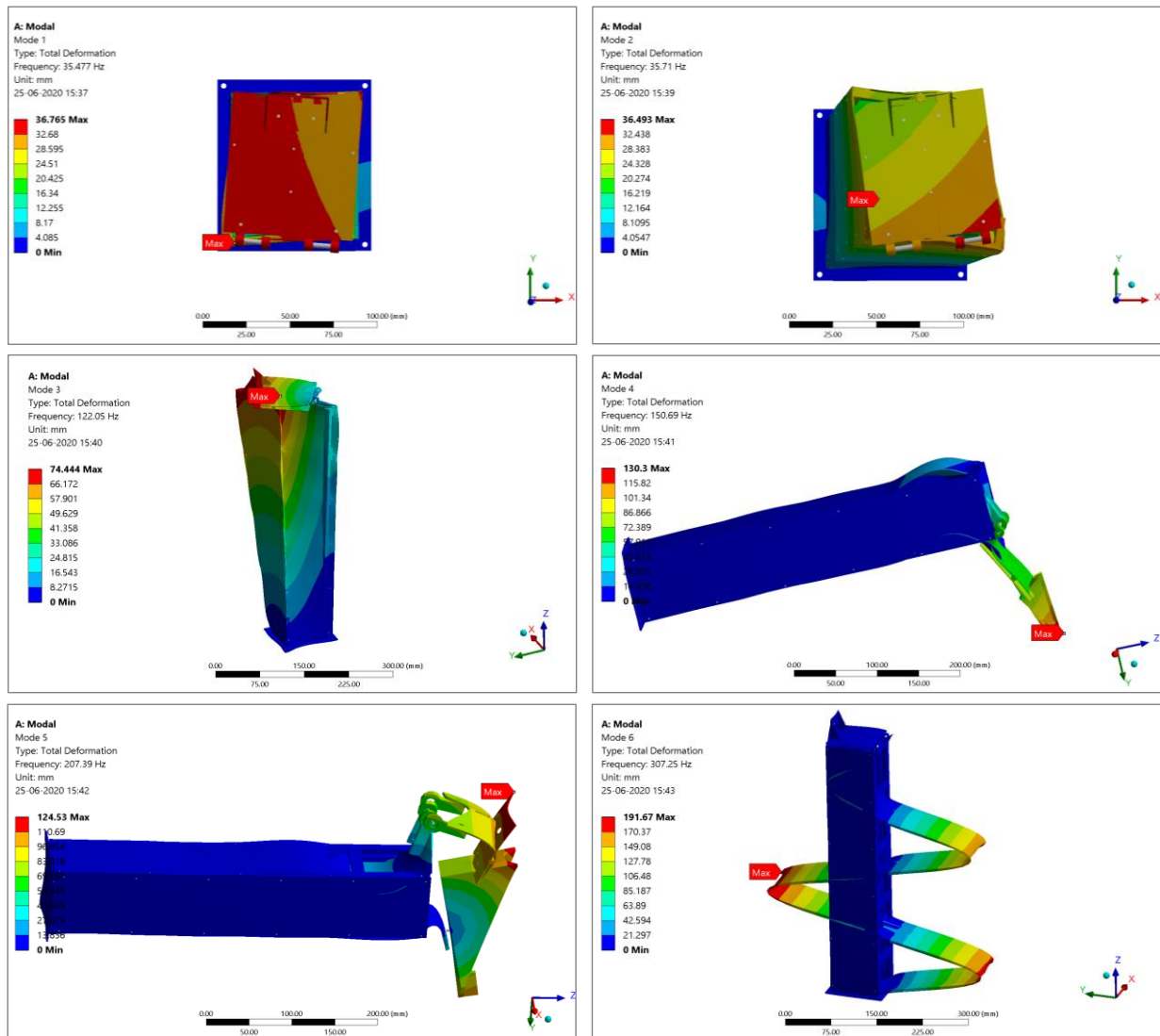


Figure 127: Modal analysis results version 2 – Longitudinal Configuration.

### 11.1.3 Single Pod Lateral Version 1

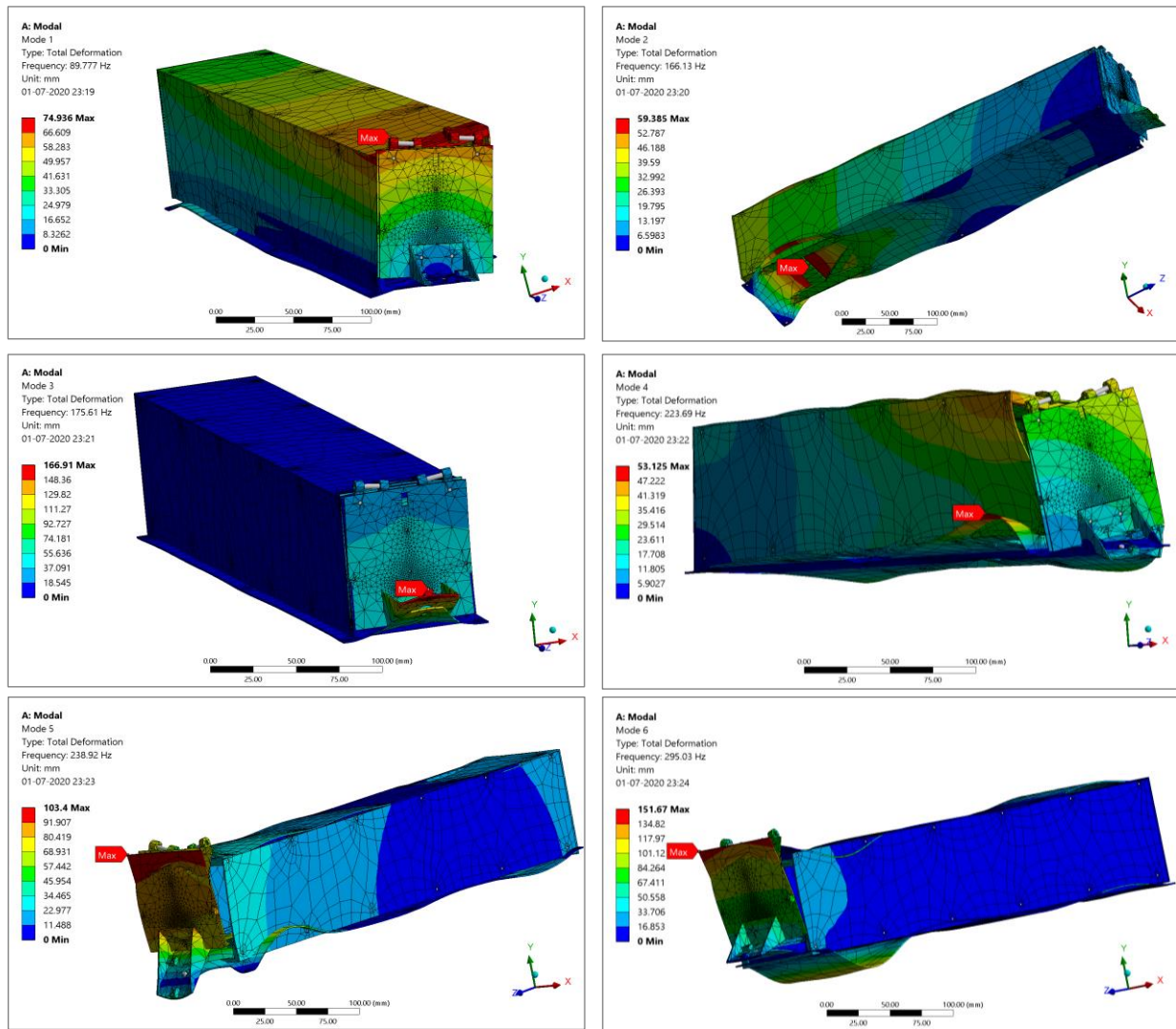


Figure 128: Modal analysis results Version 1 – Lateral Configuration.

## 11.1.4 Single Pod Lateral Version 2

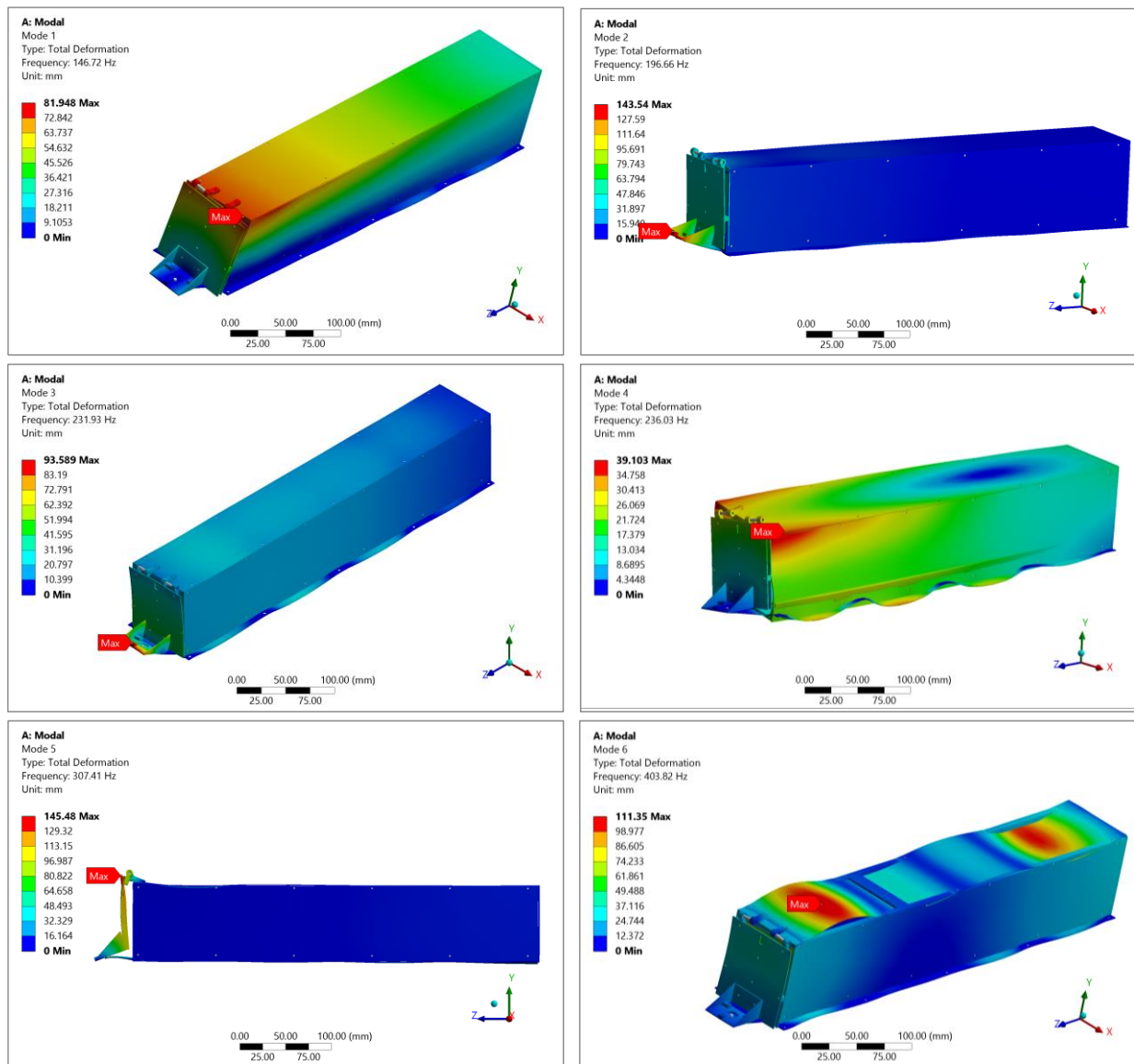


Figure 129: Modal analysis results Version 2 – Lateral Configuration.

### 11.1.5 Single Pod Lateral Version 3

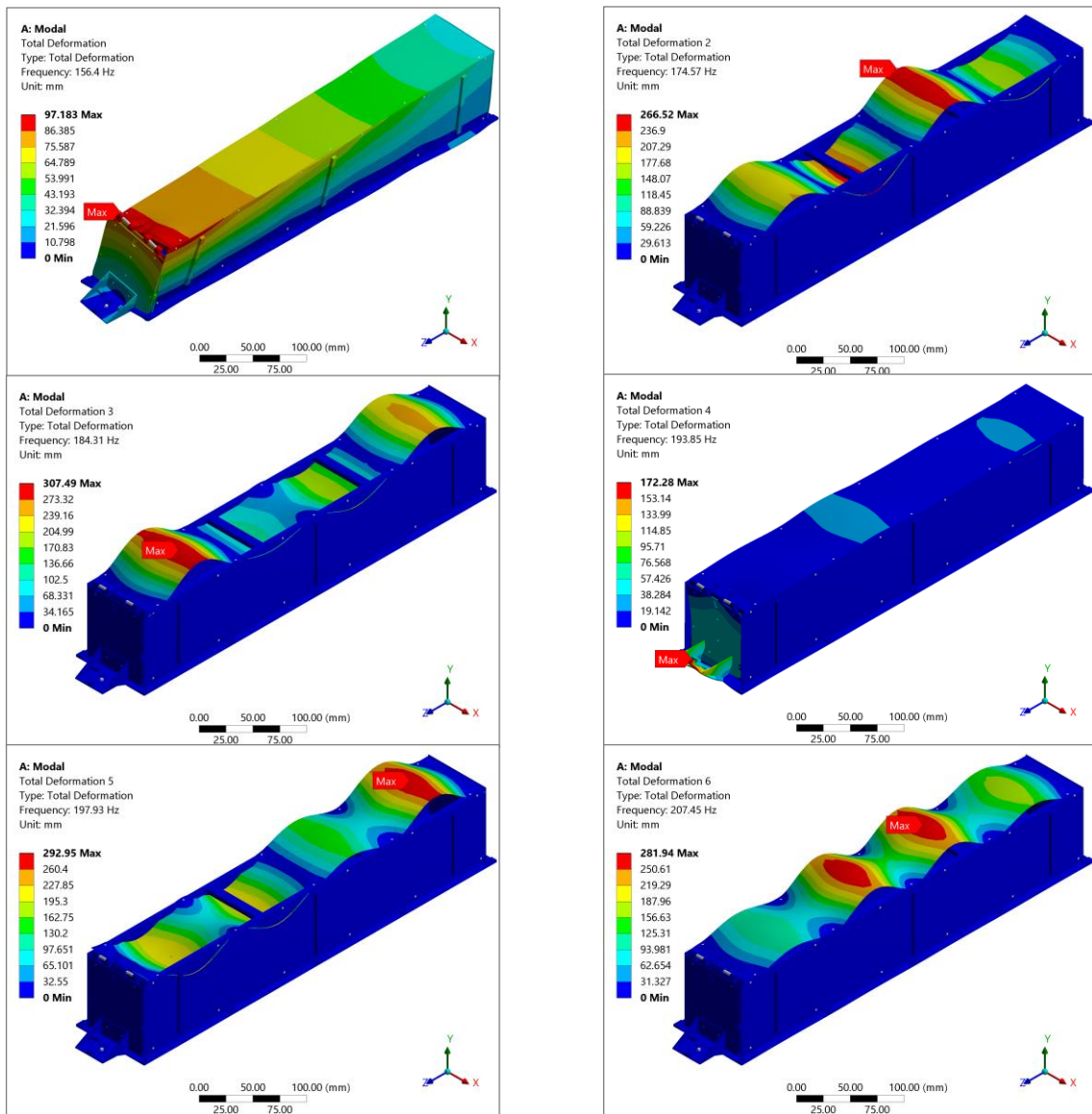


Figure 130: Modal analysis results Version 3 – Lateral Configuration.

#### 11.1.5.1 System Response X Direction

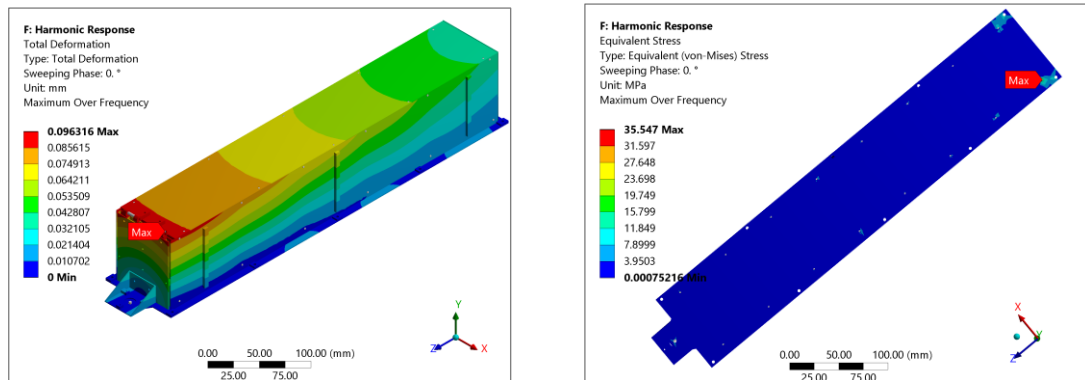


Figure 131: Deformation, induced stress sinusoidal X excitation.

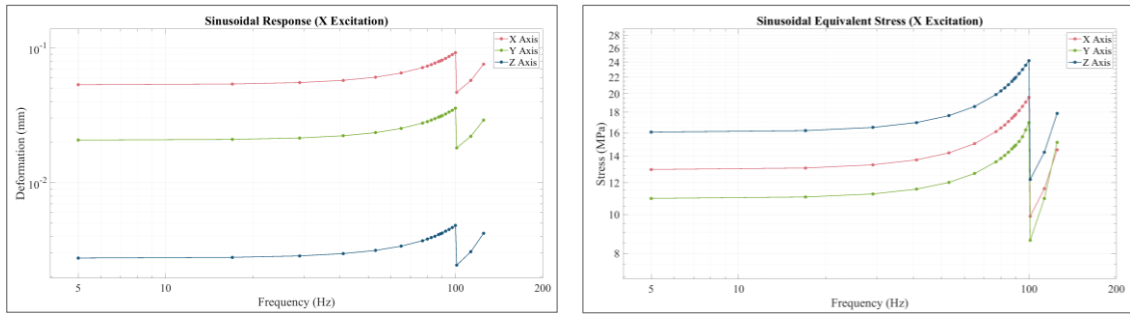


Figure 132: Sinusoidal frequency response X excitation.

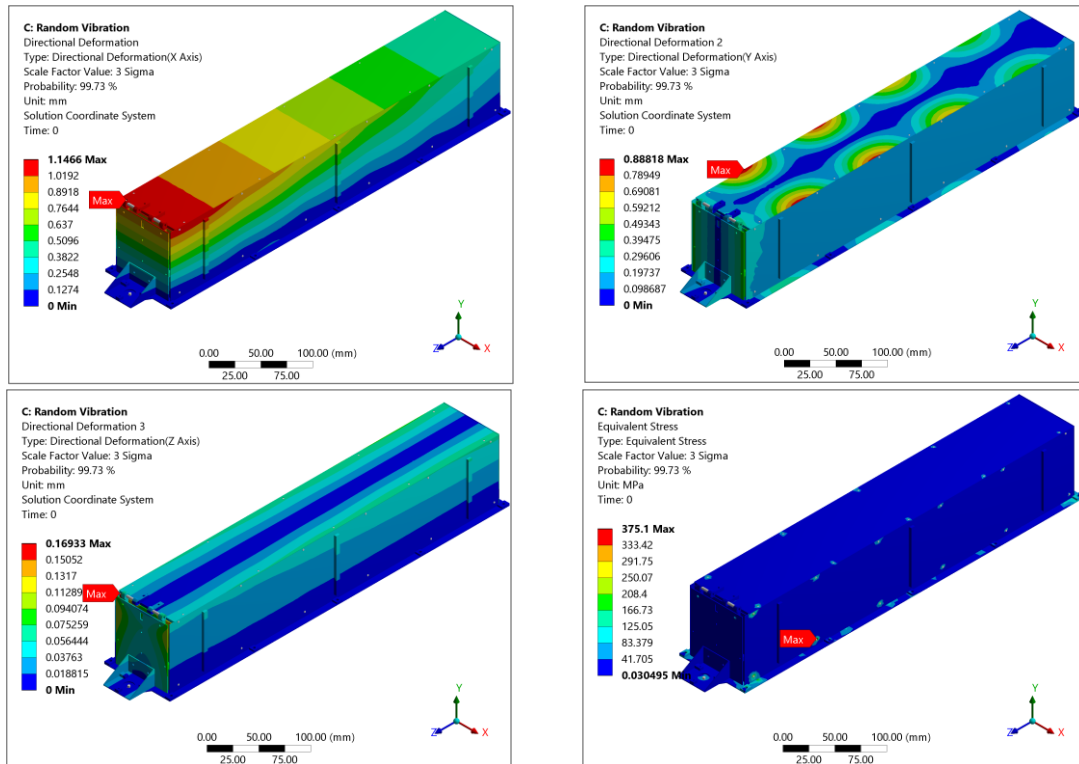


Figure 133: Directional deformation, induced stress random X excitation.

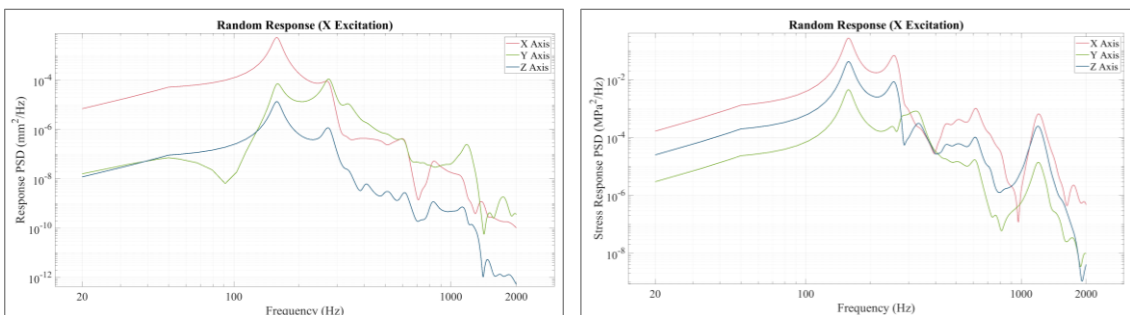


Figure 134: Random frequency response X excitation.

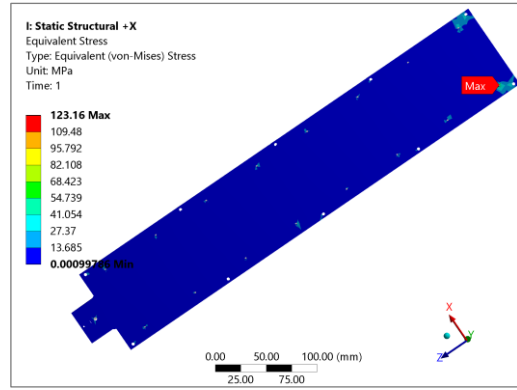
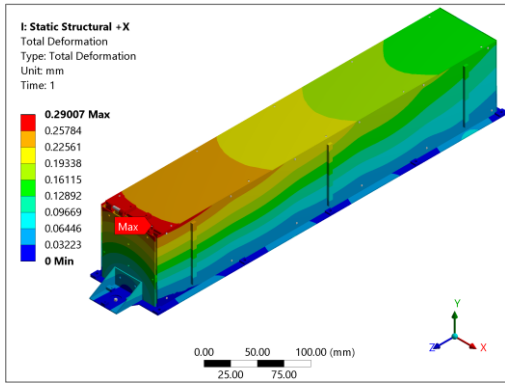


Figure 135: Deformation, induced stress quasi-static X excitation.

### 11.1.5.2 System Response Y Direction

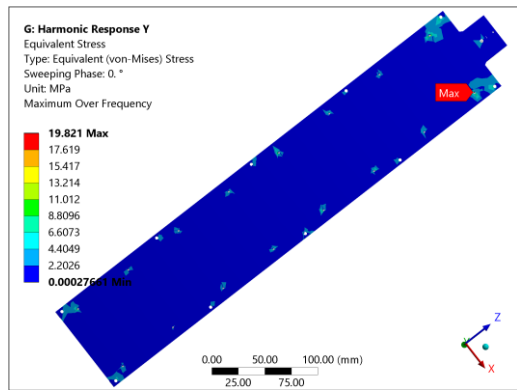
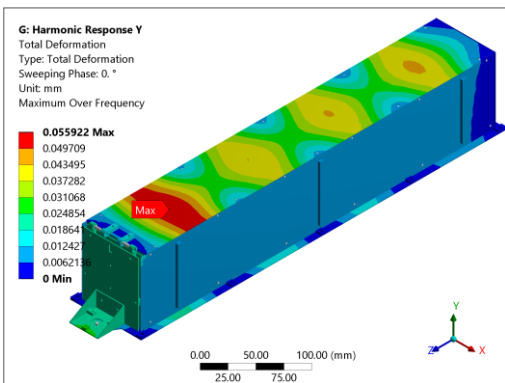


Figure 136: Deformation, induced stress sinusoidal Y excitation.

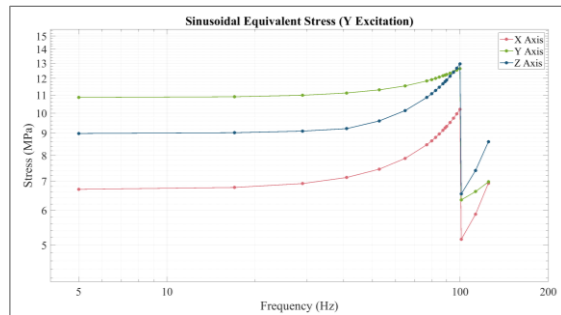
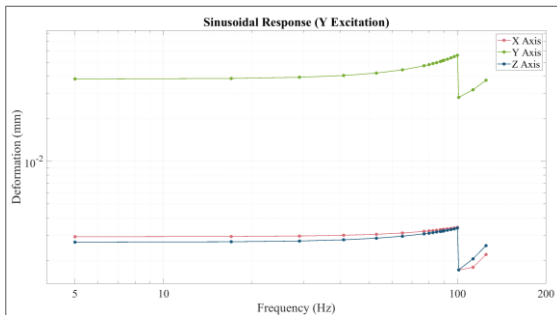


Figure 137: Sinusoidal frequency response Y excitation.

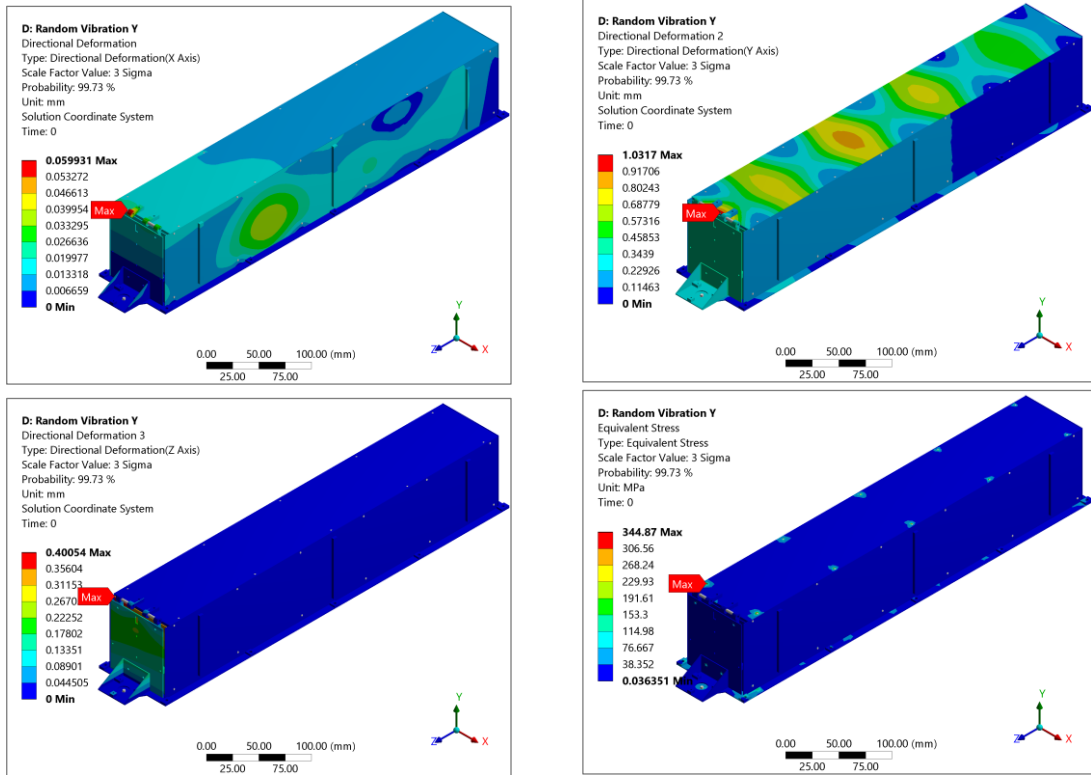


Figure 138: Directional deformation, induced stress random Y excitation.

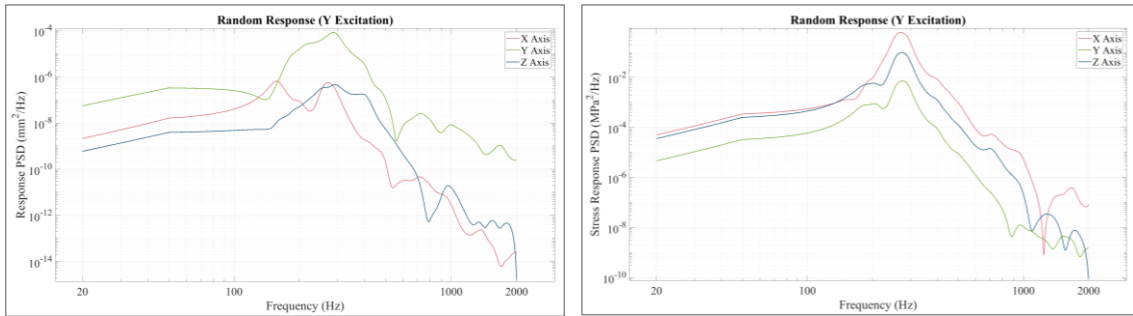


Figure 139: Random frequency response Y excitation.

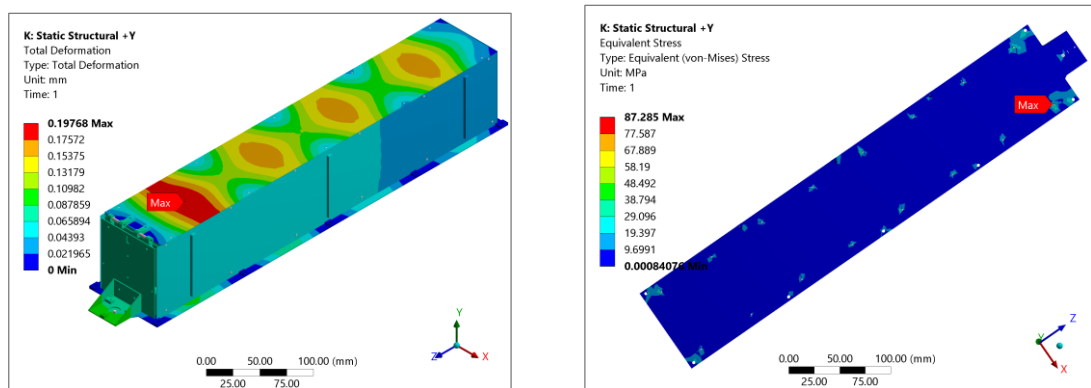


Figure 140: Deformation, induced stress quasi-static Y excitation.



### 11.1.5.3 System Response Z Direction

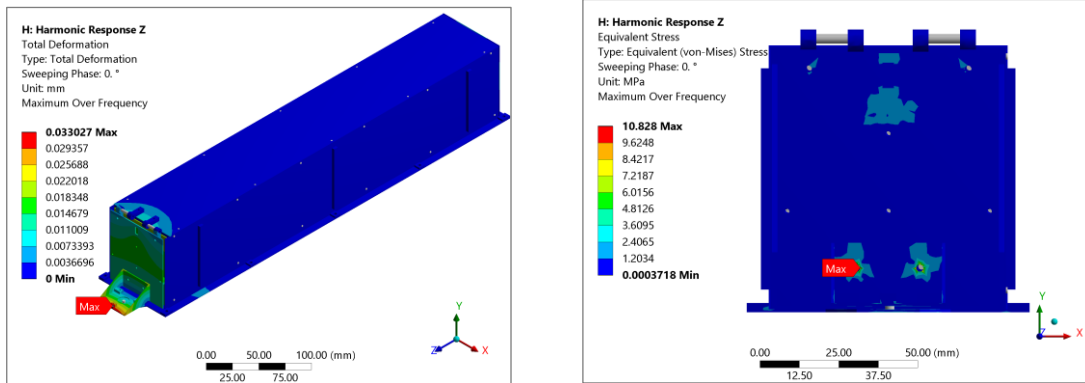


Figure 141: Deformation, induced stress sinusoidal Z excitation.

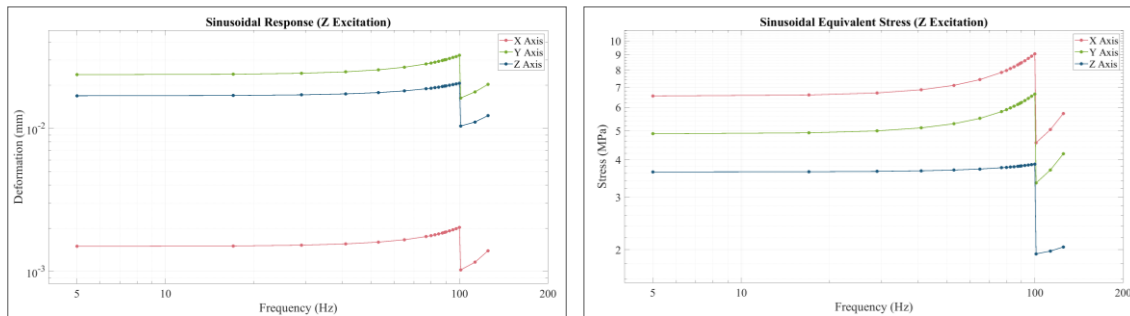


Figure 142: Sinusoidal frequency response Z excitation.

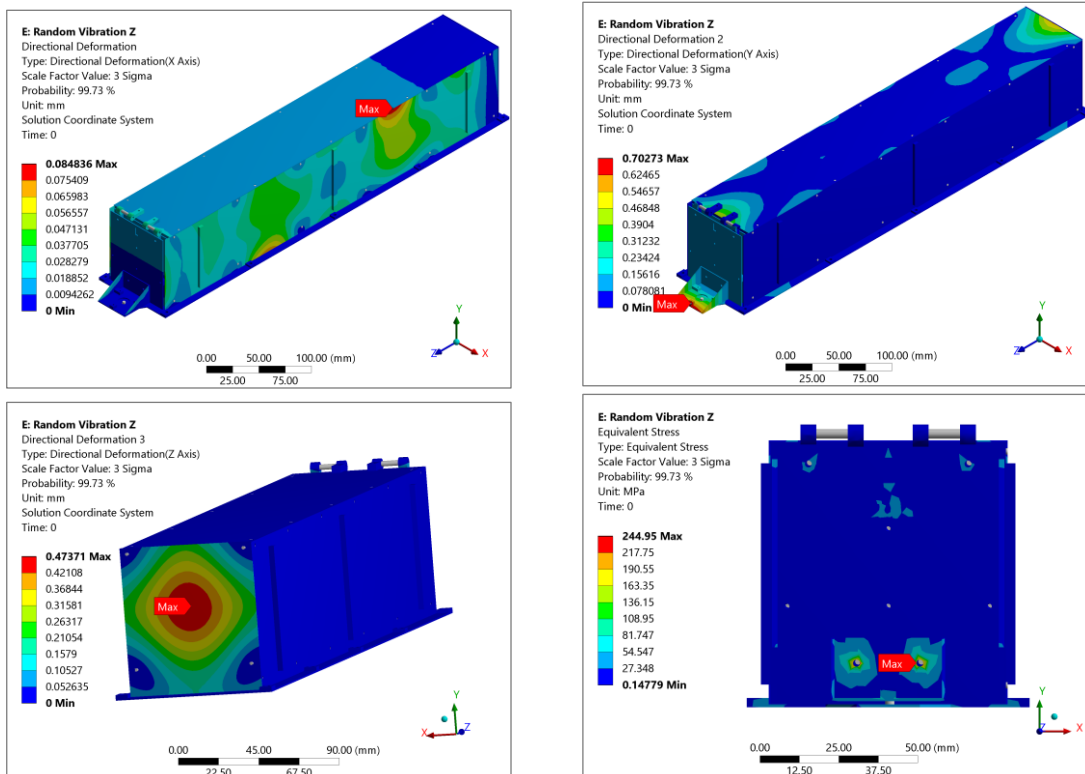


Figure 143: Directional deformation, induced stress random Z excitation.

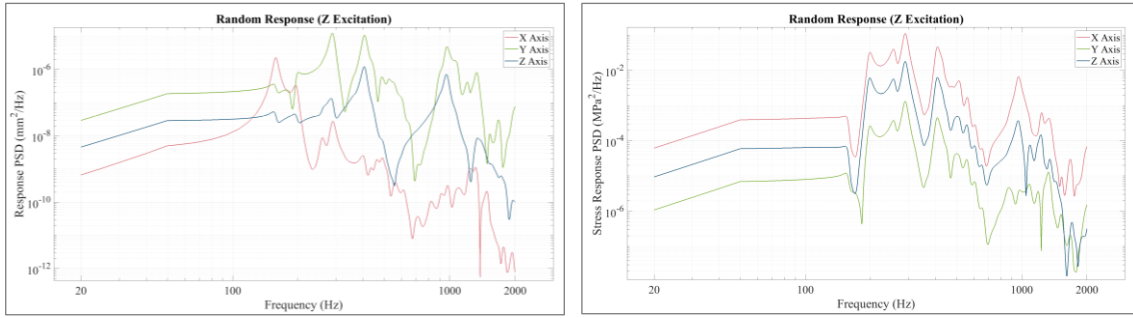


Figure 144: Random frequency response Z excitation.

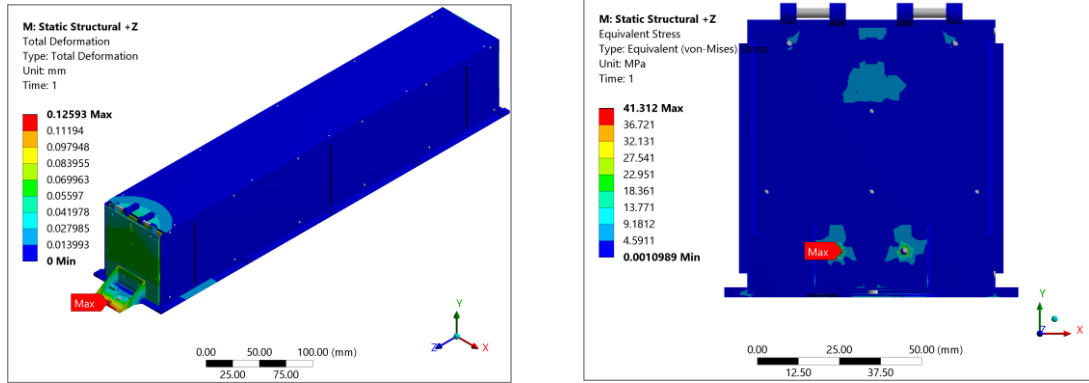


Figure 145: Deformation, induced stress quasi-static Z excitation.

## 11.1.6 Multi pod Final Version

### 11.1.6.1 System Response X Direction

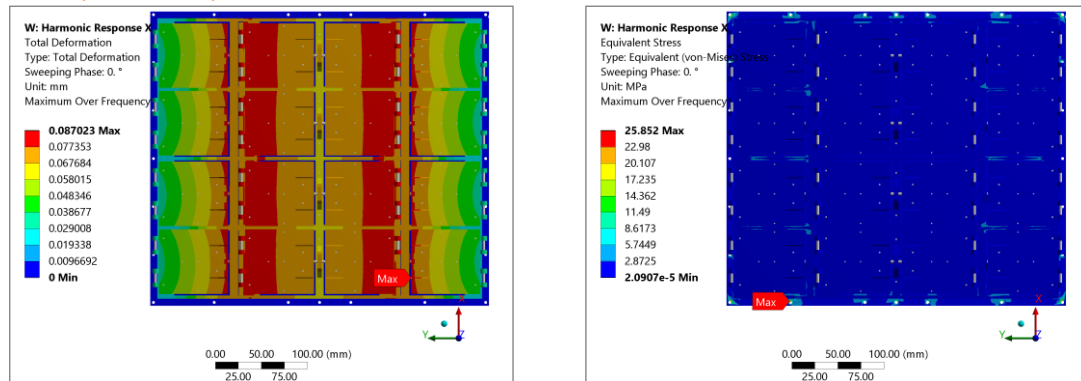


Figure 146: Deformation, induced stress sinusoidal X excitation.

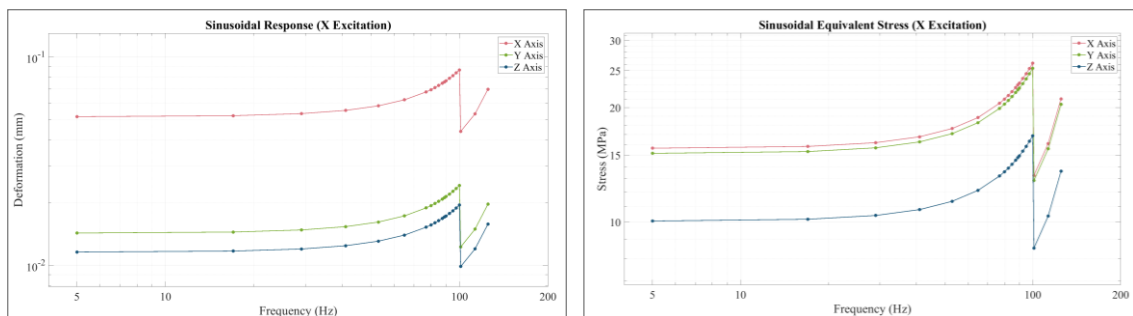


Figure 147: Sinusoidal frequency response X excitation.

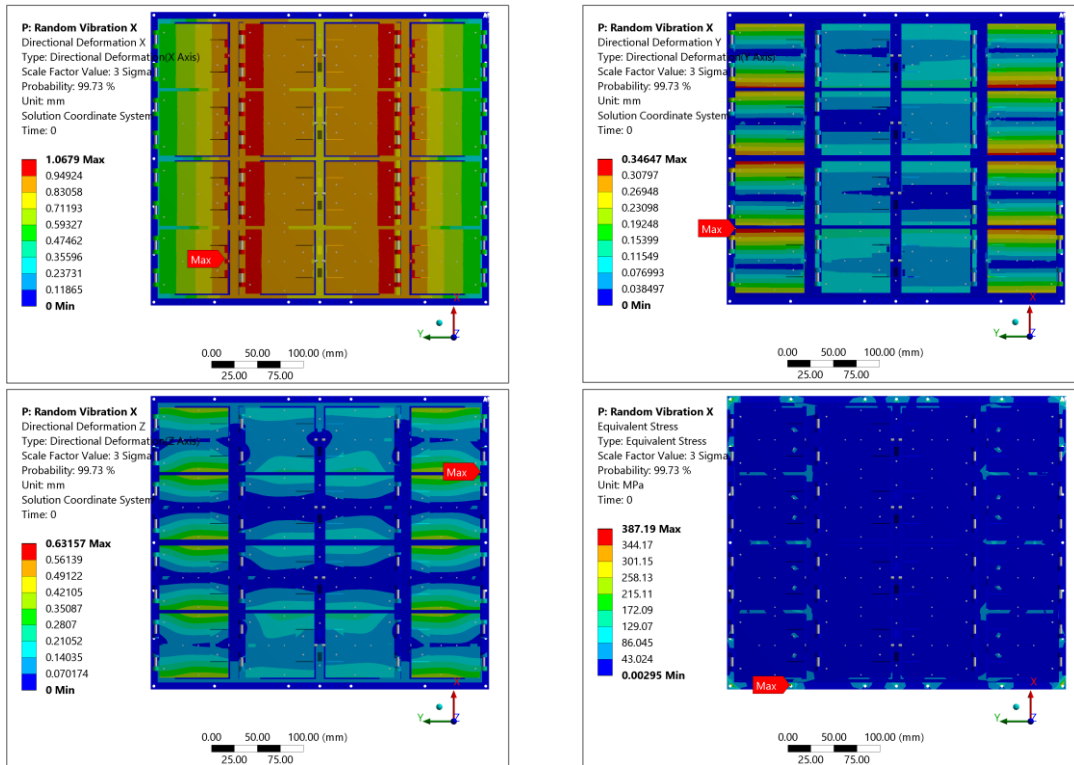


Figure 148: Directional deformation, induced stress random X excitation.

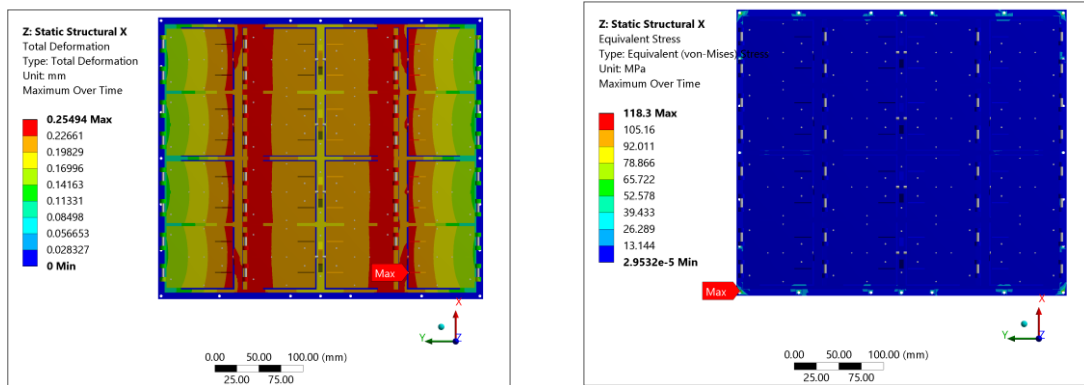


Figure 149: Deformation, induced stress quasi-static X excitation.

### 11.1.6.2 System Response Y Direction

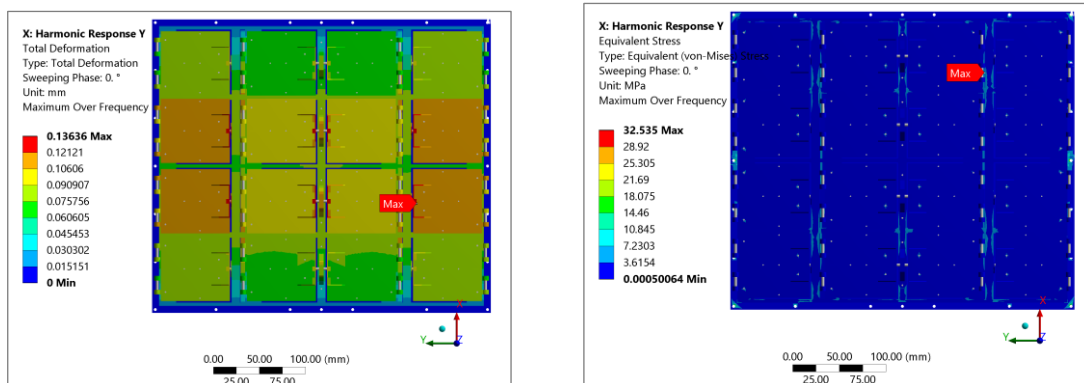


Figure 150: Deformation, induced stress sinusoidal Y excitation.

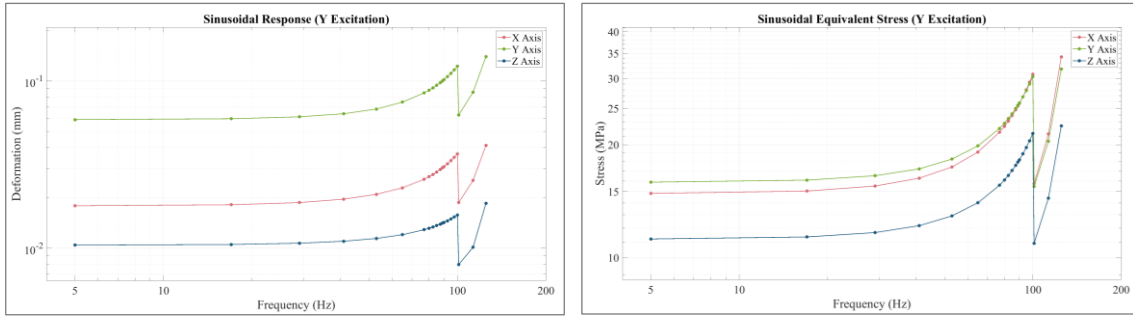


Figure 151: Sinusoidal frequency response Y excitation.

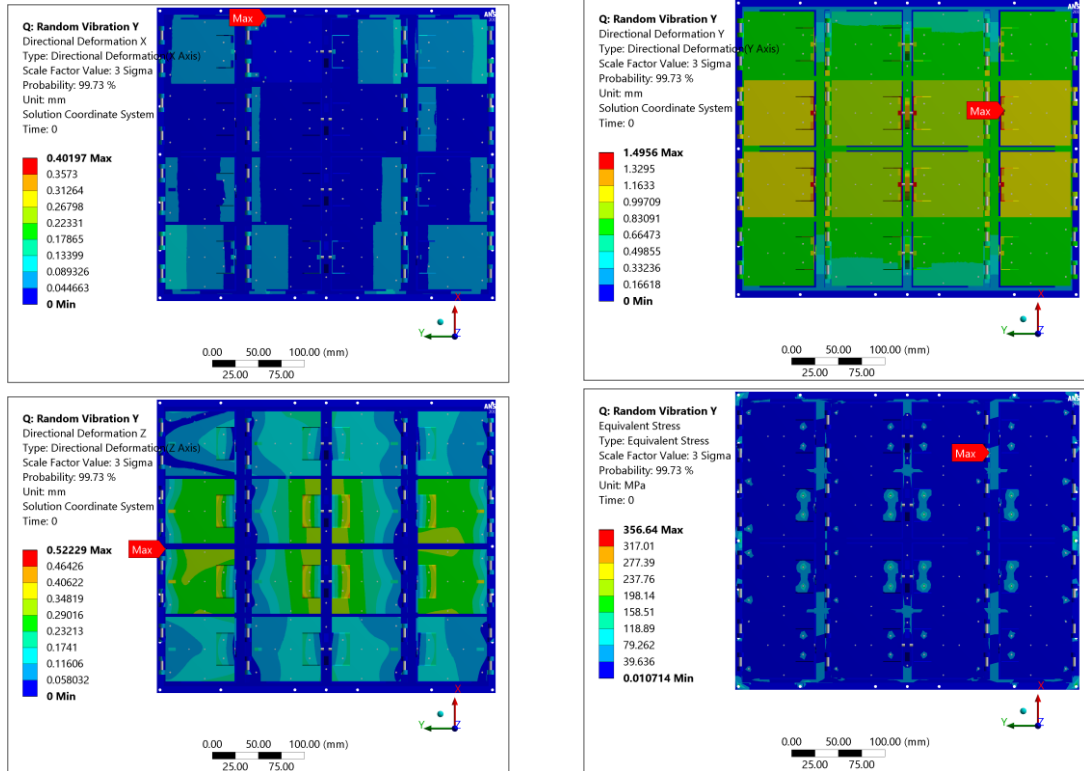


Figure 152: Directional deformation, induced stress random Y excitation.

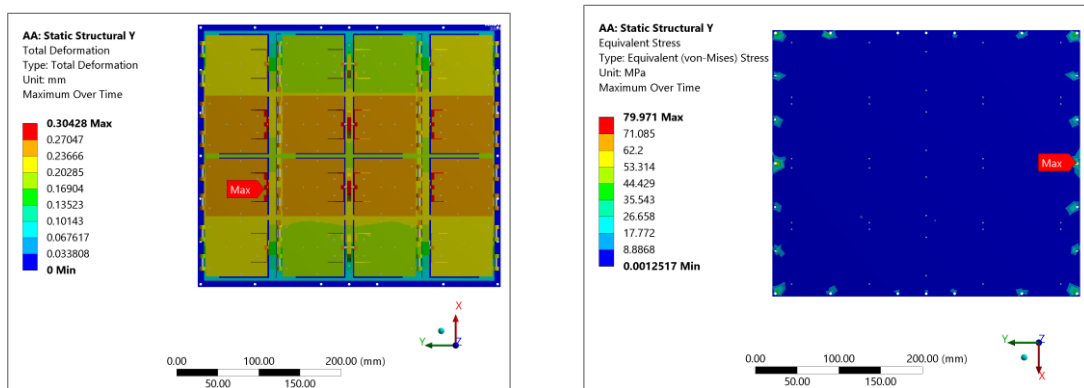


Figure 153: Deformation, induced stress quasi-static Y excitation.

### 11.1.6.3 System Response Z Direction

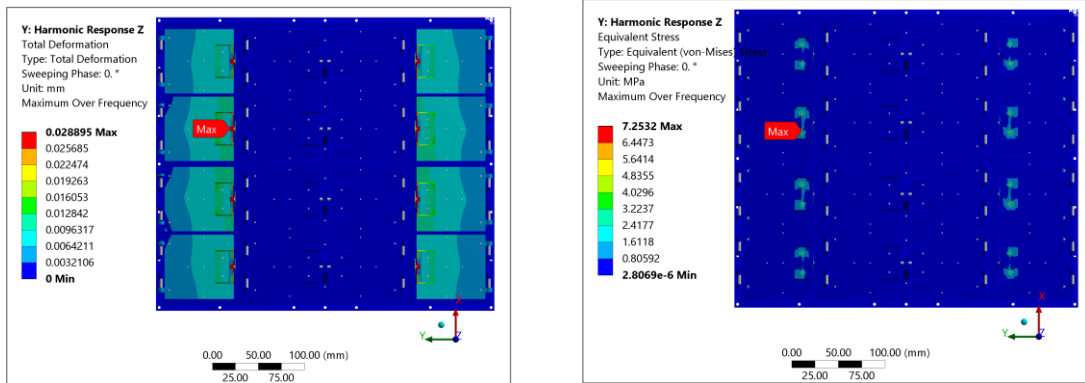


Figure 154: Deformation, induced stress sinusoidal Z excitation.

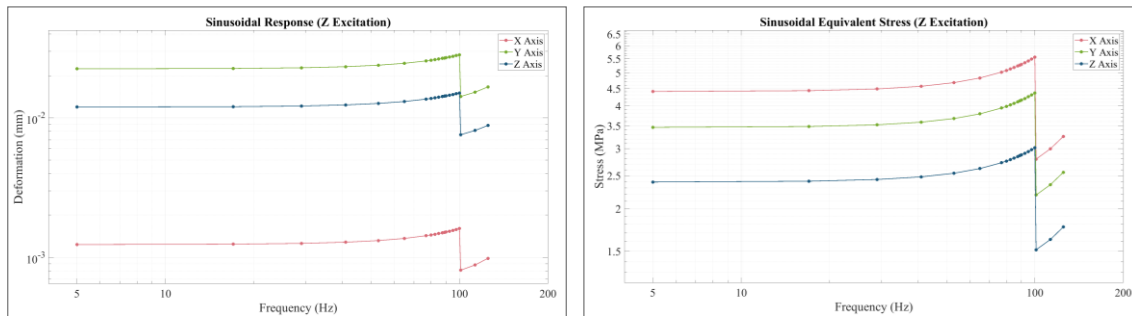


Figure 155: Sinusoidal frequency response Z excitation.

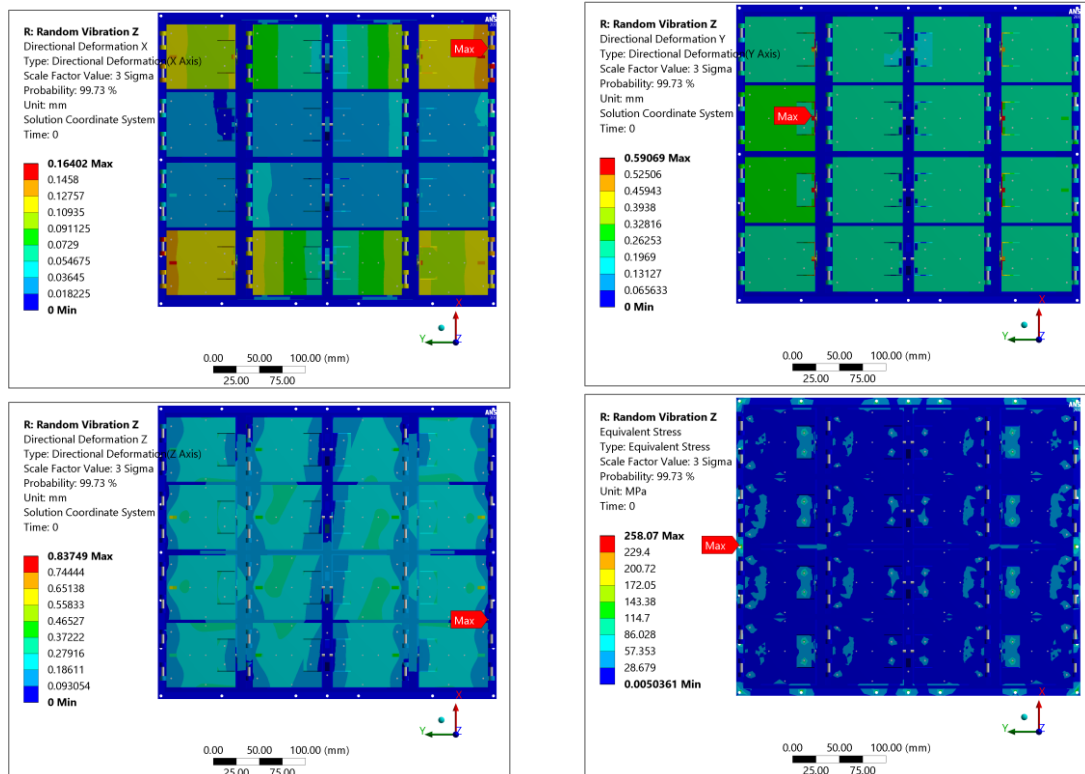


Figure 156: Directional deformation, induced stress random Z excitation.

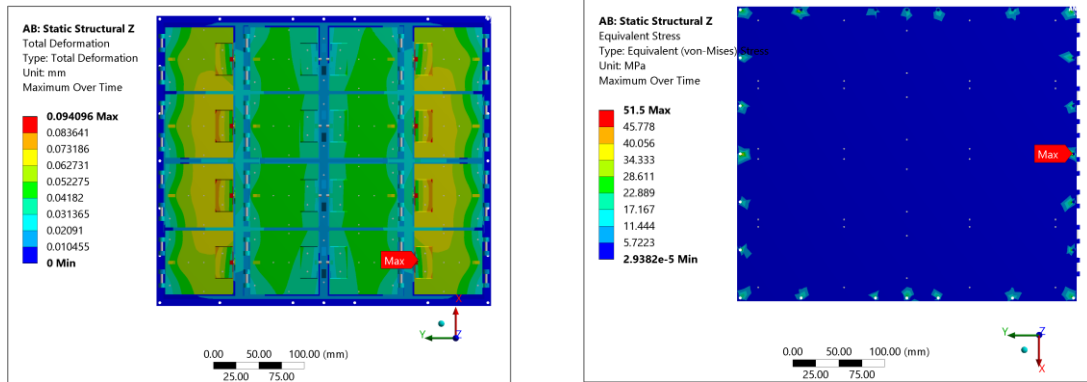


Figure 157: Deformation, induced stress quasi-static Z excitation.

## 11.2 Appendix B (Estimator Scripts)

### 11.2.1 Deployment Velocity Estimator Script

```

% Ashvij Narayanan
% Spring Deployment Velocity Calculation
% May 20,2020
clear
clc


---


%% Initialization
ftol=1.08; % Force Tolerance (N)
ltol=25.3; % Deflection Tolerance (mm)
b=0; % PQ Reduction Factor
f=[15.14+ftol 0]; % Spring Force (N)
m=1.5-(b*0.25); % Satellite Mass (kg)
l=[50 500+ltol]*1e-3; % Compressed & Uncompressed Length (m)
s=390e-3; % Stroke Length of Spring (m)
dx=1e-3; % Discretization
x=(b*64e-3):dx:s;
fs=((f(2)-f(1))*x/(l(2)-l(1)))+f(1);
v=zeros(length(m),length(x)); % Initial Velocity (m/s)
dt=zeros(length(m),length(x));
as=fs./m'; % Instantaneous Acceleration (m/s2)
k=(f(1)-f(2))/(l(2)-l(1)); % Spring Constant(N/m)


---


%% Friction Analysis
mus=0.8; % Static Coefficient of Friction
muk=0.5; % Kinetic Coefficient of Friction
p=10; % Force Percentage
ffr=muk*p*fs/100; % Friction Force (N)
ffr(1)=ffr(1)*mus/muk;
afr=(fs-ffr)./m';
vfr=zeros(length(m),length(x));
dtfr=zeros(length(m),length(x));


---


%% Velocity and Time Calculation
for j=1:length(m)
for i=1:length(x)
v(j,i+1)=sqrt((v(j,i)^2)+2*as(j,i)*dx);
dt(j,i+1)=dt(j,i)+(dx/v(j,i+1));
vfr(j,i+1)=sqrt((vfr(j,i)^2)+2*afr(j,i)*dx);
dtfr(j,i+1)=dtfr(j,i)+(dx/vfr(j,i+1));
end
vdep(j)=v(j,i+1);
tdep(j)=dt(j,i+1);
vdepfr(j)=vfr(j,i+1);
tdepfr(j)=dtfr(j,i+1);

```

```
end
```

---

```
%% Friction Output
```

```
output(1,:)=m;  
output(2,:)=vdepfr;  
output(3,:)=tdepfr;
```

---

```
%% V Theoretical
```

```
vth=sqrt(k*((l(2)-l(1)).^2)-((l(2)-(x+l(1))).^2))./m');  
vth(:,i+1)=NaN;  
er=abs(vth-v);
```

---

```
%% Momentum Balance Check
```

```
output(1,:)=m;  
output(2,:)=vdep;  
output(3,:)=tdep;  
output(4,:)=m.*vdep./tdep; % Equivalent Force (N)
```

---

```
%% Energy Balance Check
```

```
PE=0.5*k*(l(2)-(x+l(1))).^2;  
KE=0.5*m*v.^2;  
TE=PE+KE;
```

---

## 11.2.2 Door Deployment Time Estimator Script

```
%% Torsion Spring Calculation
```

```
clear  
clc
```

---

```
%% Requirement of Torsion Spring
```

```
ar=11; % Acceleration Required (m/s^2)  
md=90e-3; % Door Mass (g)  
fr=md*ar; % Force Required (N)  
d=54e-3; % Centre of Mass of door(m)  
tr=fr*d; % Required Torque (Nm)
```

---

```
%% Actual Spring Calculations
```

```
tot_al=deg2rad(167); % Alpha (rad)  
maxtor=2e-3*54.9; % Torque at alpha degrees (Nm) (2 Nos.)  
stowtor=maxtor*(pi/2)/tot_al; % Torque provided by spring at stowed  
 % position (Nm)  
tottheta=110; % Angle of Rotation required (°)  
dtheta=1e-4; % Discretization (rad)  
theta=0:dtheta:deg2rad(tottheta);  
dep_al=deg2rad(-20); % Alpha when stowed (rad)  
stow_al=deg2rad(90); % Alpha when deployed (rad)  
al=dep_al:dtheta:stow_al;  
k=maxtor/tot_al;
```

---

```
%% Calculation of torsion spring force
```

```
tal=maxtor*al/tot_al;  
tal=flip(tal);  
tal(tal<0)=0;  
fal=tal/d; % Actual Force  
aal=fal./md'; % Actual Acceleration  
I=md*d^2; % Door Moment of Inertia (kgm2)  
alpha=tal./I'; % Angular Acceleration (rad/s2)  
omega=zeros(length(md),length(theta)); % Angular Velocity (rad/s)  
dt=zeros(length(md),length(theta));
```

---

```
%% Test Adjustment for Gravity (Vertical)
```

```
fgv=md*9.81.*cos(theta);  
tgv=fgv*d;  
falgv=fal-fgv;  
talgv=tal-tgv;  
alphagv=talgv/I;  
omegagv=0;  
dtgv=0;
```

---

```
%% Test Adjustment for Gravity (Horizontal)
```

```
fgh=md*9.81.*sin(theta);
```

```

tgh=fgh*d;
falgh=fal-fgh;
talgh=tal-tgh;
alphagh=talgh/I;
omegagh=0;
dtgh=0;
value=0;


---


%% Integrator
for j=1:length(md)
for i=1:length(theta)
    omega(j,i+1)=sqrt((omega(j,i)^2)+(2*alpha(j,i)*dtheta));
    dt(j,i+1)=dt(j,i)+(dtheta/omega(j,i+1));

%% Gravity Compensation
    omegagv(j,i+1)=sqrt((omegagv(j,i)^2)+(2*alphagv(j,i)*dtheta));
    omegagh(j,i+1)=sqrt((omegagh(j,i)^2)+(2*alphagh(j,i)*dtheta));
    dtgv(j,i+1)=dtgv(j,i)+(dtheta/omegagv(j,i+1));
    dtgh(j,i+1)=dtgh(j,i)+(dtheta/omegagh(j,i+1));

end
omegam(j)=omega(j,i+1);
tm(j)=dt(j,i+1);
end


---


%% Momentum Balance
output(1,:)=md*1000;
output(2,:)=d*omegam;
output(3,:)=tm;
output(4,:)=d*md.*omegam./tm;


---


%% Energy Balance
PE=0.5*k*(flip(al)).^2;
PE(flip(al)<0)=0;
PE(i+1)=NaN;
KE=0.5*I*omega.^2;
TE=PE+KE;


---



```

## 11.3 Appendix C (System Integration Procedure)

### 11.3.1 Door Assembly

Integration of door assembly is discussed independently as this procedure is common for single pod and multi pod systems.

Procedure for integration of door assembly is sequentially listed below:

1. Assemble torsion springs between set of Hinge 1 and Hinge 2 - 2 Fasteners.
2. Attach Hinge 1 to Door Top - 2 Fasteners.
3. Rotate Door Top by 180° in X axis, place Door Retainer Spring and Door Retainer Pin.
4. Place Push Back Spring and Push Back Holder on Door Top (2 numbers).
5. Insert Door Bottom on top and apply pressure to compress Push Back Spring.
6. Assemble Door Top to Door Bottom using 5 fasteners.
7. Rotate assembly by 180° in X axis, attach Door Bracket onto Door Top - 2 Fasteners.
8. Assemble Pin Puller on Door Bracket – 3 Fasteners.

This completes the procedure for integration of door assembly.

### 11.3.2 Single Pod

This section details the integration procedure for single pod PocketQube Deployment System. The required steps are sequentially listed below:



1. Attach -Z panel to Guide Mechanism – 2 fasteners.
2. Assemble Pusher Plate assembly – 2 fasteners.
3. Lock main spring at bottom using shim – 2 fasteners.
4. Compress Main Spring using collapsible mechanism, lock spring and pusher plate assembly using 2 RBF screws.
5. Attach Rib to -Z panel – 2 fasteners.
6. Rotate assembly by 90° along X axis.
7. Assemble Guide Mechanism to -Y panel – 16 fasteners.
8. Attach ± X panels to Guide Mechanism and Rib – 24 fasteners.
9. Rotate assembly by -90° along X axis (starting orientation).
10. Assemble Pusher Plate Stopper (2 numbers) onto Guide Mechanism – 2 fasteners.
11. Assemble +Y panel to Rib – 10 fasteners.
12. Attach Door Assembly to + Y panel. Elements attaching for this procedure are Door Retainer Plate, Hinge 2,+ Y panel and Rib respectively in direction of fastener thread.
13. Integrate designated PocketQubes onto PDS.
14. Door Retainer Pin must be compressed to stowed position, followed by rotation of door assembly to stowed position.
15. Pin Puller to be locked by extending its pin using extension mechanism.
16. Attach deployer electronics (components and connectors). Assembly of single pod PDS is complete.
17. Integrate system to launch vehicle using 10 fasteners and required electrical connections. Remove 2 RBF screws from -Z panel.

This completes the procedure for integration of single pod PDS.

### 11.3.3 Multi Pod

This section details the integration procedure for multi pod PocketQube Deployment System. The required steps are sequentially listed below:

1. Assemble required numbers of door and pusher plate assembly (16 numbers).
2. Attach Mid Rib X to Mid Rib Y (2 numbers).
3. Assemble guide mechanisms adjacent to Mid Rib Y to rib (8 numbers).
4. Attach assembly to -Z panel using Guide Mechanism and Mid Rib X fasteners.
5. Assemble remaining guide mechanisms to -Z panel and fasten the fasteners attaching between guide mechanisms (8 numbers).
6. Attach Guide Mechanism Mid Rib to Guide Mechanism (4 numbers).
7. Compress Main Spring using collapsible mechanism, lock spring and pusher plate assembly using 2 RBF screws (16 numbers).
8. Assemble Mid Lock (4 numbers) and Door Lock (8 numbers) onto Top Rib.
9. Assemble Top Rib to Guide Mechanism top (16 numbers) and Mid Rib X (2 numbers). A total of 32 pusher plate stoppers to be included during assembly of Top Rib to Guide Mechanism.
10. Assemble Door Assembly having locking mechanism in middle of structure (Y Axis) (8 numbers).
11. Assemble ± Y panels to Guide Mechanism and Top Rib (2 numbers).
12. Assemble ± X panels to Guide Mechanism, Mid Rib X and Top Rib (2 numbers). (Side ribs to be included)
13. Assemble remaining door assembly to guide mechanism (8 numbers).
14. Integrate PocketQubes to respective pods followed by closing of pod doors and locking of pin pullers.
15. Remove RBF screws to arm main spring of pods (32 numbers).

16. Integrate multi pod PDS to launch vehicle using 24 fasteners.

17. Integrate deployer electronics (components and connectors) with launch vehicle.

This completes the procedure for integration of multi pod PDS.